Understanding Cu2ZnSnS4 as a Photovoltaic Absorber for the Future of Solar Electricity

BOSSON, CHRISTOPHER,JOHN

Understanding Cu_2ZnSnS_4 as a Photovoltaic Absorber for the Future of Solar Electricity

Christopher J. Bosson

University College

Durham University

A thesis submitted in December 2017 to the
Physics Department of the University of Durham
in candidature for the degree of
Doctor of Philosophy

None of the work presented in this thesis has been submitted by the author for any previous degree and it is not being submitted for any other degree.

All the work presented in this thesis was carried out by the author with the following exceptions:

- Inductively coupled plasma mass spectrometry measurements were carried out by Dr Chris Ottley.
- Solid-state nuclear magnetic resonance measurements were carried out by Dr David Apperley.
- The synchrotron experiments at the ISIS Pulsed Neutron and Muon Source were carried out jointly by the author, Prof. Peter Hatton, Dr Douglas Halliday, fourth-year undergraduate students Max Birch and Ruth Zhou, and beamline scientists Dr Kevin Knight and Dr Alexandra Gibbs.
- The synchrotron experiments at the Diamond Light Source were carried out jointly by the author, Prof. Peter Hatton, Dr Douglas Halliday, fourth-year undergraduate students Max Birch and Jack Goodman, and beamline scientists Prof. Chiu Tang and Dr Annette Kleppe.
- Some Raman spectroscopy measurements were carried out by fourth-year undergraduate student Ben Jones.
- Some photoluminescence measurements were carried out by fourth-year undergraduate student Rob Lewis.

Abstract

The world needs solar electricity to replace a large fraction of traditional, fossil-fuel-generated electricity over the coming decades if it is to avoid the worst effects of climate change and continue to meet the needs of an increasingly energy-dependent society. This transition is currently well underway. The installed generating capacity of solar electricity continues to grow exponentially, having reached 307 GW in 2016 (2 % of average global electricity demand), which means that replacing a large majority of fossil fuel use, requiring several terawatts of capacity, in the coming decades is entirely realistic.

Cu_2ZnSnS_4 (CZTS) is a potential material for the absorber layer in photovoltaic solar cells. It has the advantages over silicon, which currently provides 95 % of the solar electricity market, of lower processing costs and a direct band gap, which means much less material is required. Most other alternative absorber materials will ultimately be limited by high material costs, low elemental abundances, or toxicity, but CZTS has none of these problems, making it a very promising material indeed. However, its record photovoltaic efficiency (11.0 %) is well below those of some other materials (>20 %) because of low open-circuit voltage. The outstanding areas of current CZTS research are the absorber-buffer interface, band gap fluctuations caused by point defects, and secondary phases.

This thesis presents work investigating the latter two, primarily using bulk samples fabricated by solid-state reaction. Firstly, compositional, structural, and optoelectronic analysis techniques were used to study the effect of composition on material properties. It was found that the quasi-ternary phase diagram commonly used for CZTS is incorrect; and that no common analysis technique can quantify cation disorder in CZTS, despite Raman spectroscopy commonly being used to do so. Secondly, neutron diffraction was used to study the order-disorder phase transition at around 550 K. It was found that the transition temperature is dependent on elemental composition; and that Cu-Zn disorder is present on all cation lattice sites, not merely the 2*c* and 2*d* sites of the kesterite crystal structure as has previously been assumed. Thirdly, anomalous X-ray diffraction was used to study cation disorder further. It was found that two distinct phases of CZTS can be present in the same sample, with different elemental compositions resulting from the prevalence of different point defect complexes; two new such types of CZTS were identified; and a mechanism of phase formation was proposed. Finally, a fabrication route for thin-film CZTS by sputtering and sulphurisation annealing was established.

Contents

Acknowledgements

This work was financially supported by the UK Engineering and Physical Sciences Research Council (award number 1335920). Experiments at the ISIS Pulsed Neutron and Muon Source were supported by the UK Science and Technology Facilities Council (experiment numbers RB1520091 and RB1620312) and experiments at the Diamond Light Source were supported by the UK Science and Technology Facilities Council and the Wellcome Trust (experiment numbers EE12564 and EE15370).

The author would like to express his sincere gratitude for the excellent support and supervision provided by Dr Douglas Halliday throughout this project, as well as to Dr Aiden Hindmarch for his help and guidance with sputtering and to Prof. Peter Hatton for his help and guidance concerning synchrotron X-ray and neutron diffraction.

Thanks are due to Mr Leon Bowen for training in electron microscopy, to Mr Gary Oswald for training in laboratory X-ray diffraction, to Prof. Andy Beeby for provision of Raman spectroscopy equipment and instruction thereon, to Dr Chris Ottley for performing inductively coupled plasma mass spectrometry, to Dr David Apperley for performing solid-state NMR measurements, to Mr Malcolm Richardson and Mr Aaron Brown for their excellent glassblowing skills, to Mr Duncan McCallum for ensuring nobody died, and to Dr Kevin Knight, Dr Alexandra Gibbs, Prof. Chiu Tang, Dr Annette Kleppe, and all the other scientists at ISIS and Diamond who helped with running experiments there. Help was also appreciated from Max Birch, Jack Goodman, Ben Jones, Rob Lewis, and Ruth Zhou during their fourth-year undergraduate projects.

Personal thanks go to the author's friends and family for their support throughout this project and above all to Anna, for being wonderful in every way.

Publications

Work included in this thesis has been published in the following:

[1] C.J. Bosson; M.T. Birch; D.P. Halliday; K.S. Knight; C.C. Tang; A.K. Kleppe; & P.D. Hatton. 'Crystal structure and cation disorder in bulk Cu_2ZnSnS_4 using neutron diffraction and X-ray anomalous scattering'. *Proceedings of the 43rd IEEE Photovoltaic Specialists Conference*, p.0405, (2016). DOI: 10.1109/pvsc.2016.7749621

[2] C.J. Bosson; M.T Birch; D.P Halliday; K.S. Knight; & P.D. Hatton. 'Cation disorder and phase transitions in the structurally complex solar cell material Cu_2ZnSnS_4'. *Journal of Materials Chemistry A* **5**, p.16672, (2017). DOI: 10.1039/c7ta03603e

[3] C.J. Bosson; M.T. Birch; D.P. Halliday; C.C. Tang; & P.D. Hatton. 'Using high-resolution anomalous-scattering X-ray diffraction to observe off-stoichiometric Cu_2ZnSnS_4 crystal structures'. *Proceedings of the 44th IEEE Photovoltaic Specialists Conference*, (2017).

[4] C.J. Bosson; M.T. Birch; D.P. Halliday; C.C. Tang; A.K. Kleppe; & P.D. Hatton. 'Polymorphism in Cu_2ZnSnS_4 and new off-stoichiometric crystal structure types'. *Chemistry of Materials* **29** (22), p.9829, (2017). DOI: 10.1021/acs.chemmater.7b04010

Understanding Cu_2ZnSnS_4 as a Photovoltaic Absorber for the Future of Solar Electricity

Chapter 1:

Introduction

The world needs solar electricity to replace a large fraction of traditional, fossil-fuel-generated electricity over the coming decades if it is to avoid the worst effects of climate change and continue to meet the needs of an increasingly energy-dependent society. While this transition is already well underway, it can still be eased by improvements in the technology involved.

Photovoltaic solar panels can be based on several different materials. Silicon modules provided 95 % of the solar electricity market in 2016, and CdTe and $CuIn_{1-x}Ga_xSe_2$ (CIGS) provided the remainder with 4 % and 1 % respectively (see Section 2.5). [5] Although silicon solar modules have now reached sufficiently low prices to be economically competitive with other electricity sources, the cost of processing silicon still accounts for a significant proportion of the overall cost, and so a cheaper material technology could significantly reduce the cost of solar electricity. Additionally, the energy-intensive processing of silicon and high volume of material necessary because it is an indirect-gap semiconductor (see Section 2.5.1) mean that silicon solar cells have a higher energy payback time than thin-film solar cells (i.e. those using direct-gap materials like CdTe and CIGS). However, CdTe, CIGS, and most other photovoltaic absorber materials also have problems with toxicity, stability, or element abundance limiting future production volume. The emergence of a new, low-cost, non-toxic, sustainable (i.e. not limited by element abundance) absorber material with lower energy payback time will therefore greatly aid the advance of solar energy.

This thesis presents a study of Cu_2ZnSnS_4 (CZTS), which could be such a material. Its constituent elements are non-toxic and much cheaper and/or more abundant than those of alternative materials (see Section 2.5). However, as a relatively recently developed material, its record photovoltaic efficiency is not yet high enough to make it industrially viable. Many of its basic material properties and their impact on photovoltaic device performance are not yet understood. Hence, the standard fabrication process of CZTS solar cells has not yet been optimised. The effects of fabrication process parameters on material properties, and how these in turn affect solar photovoltaic performance, need to be understood in full before CZTS will be able to contribute to the growth of solar power to supply a significant fraction of global energy use.

To this end, this thesis presents a study of CZTS bulk samples produced by solid-state reaction and thin films produced by sputtering in order to examine the material properties of CZTS and the effects of fabrication thereon.

The major scientific results covered here are presented more concisely in published journal articles, [2,4] and so to give this thesis some purpose beyond gaining its author his PhD, it has been written aimed at those newly entering the field of CZTS research, perhaps starting their own doctoral studies. It aims to be a thorough summary of the current state of CZTS produced by sputtering for photovoltaic solar cells, so that the thorough reader can emerge with most of the relevant knowledge and references its author gained over the four years it took to create.

Because little technical experience or experimental set-up existed in Durham for the fabrication of CZTS by any method prior to this project, much of the work involved was simply to set up such processes and facilities necessary to begin, overcoming the many problems and delays this necessarily entailed. It is a major achievement of this project that any samples were produced at all!

Once fabrication was made possible, there were two main aims of this study:

- Through physical, optical, and electronic characterisation, to achieve a fuller understanding of the material properties and mechanisms behind CZTS working as an absorber layer in solar cells, including the role of defects and impurities, and how fabrication by sputtering affects these.

- Using these results, to find an optimised route for the fabrication of CZTS by sputtering followed by sulphurisation annealing and incorporation into a device structure. This fabrication route should be practically and economically useful for scaling to an industrial level.

This thesis is structured to present the findings of work towards achieving these aims once the reader has been equipped with the relevant context and information to appreciate their significance, covering sequentially by chapter:

1. A general introduction to renewable energy and solar photovoltaics;
2. The physics of solar photovoltaic electricity generation and the current state of its technological development;
3. CZTS, including its properties, issues relevant to its use in solar cells, and the current state of such use;
4. The fabrication of CZTS by sputtering and the current understanding thereof as reported in academic literature;
5. The experimental techniques used to analyse samples in this study;
6. The results of structural and optoelectronic study of bulk samples of CZTS fabricated by solid-state reaction;
7. The results of structural study of bulk samples of CZTS fabricated by solid-state reaction, using neutron diffraction to investigate an order-disorder phase transition;
8. The results of structural study of bulk samples of CZTS fabricated by solid-state reaction, using anomalous X-ray diffraction to investigate cation disorder;
9. The results of structural and optoelectronic study of thin-film samples of CZTS fabricated by sputtering followed by sulphurisation annealing;
10. And finally, the conclusions reached throughout the thesis.

1.1. Motivation for renewable energy

The rapid adoption of environmentally sustainable energy sources is of vital importance to the future of humanity and the rest of Earth's diverse ecosystem. Such sources are numerous; the most common are solar photovoltaic power (i.e. solar electricity), solar thermal power, hydroelectric power, wind power, geothermal power, and biofuels. Each of these has its own strengths and weaknesses, and each will have a part to play.

There are several reasons why the adoption of sustainable energy sources is so important. It is beyond the scope of this thesis to discuss them in detail, but they are summarised here as the context of the research presented in later chapters.

1.1.1. Climate change

Continued use of fossil fuels to supply the majority of society's energy demand will have a significant negative impact on the planet's climate and environment due to the emission of greenhouse gases, such as carbon dioxide (CO_2). These gases increase the trapping of heat in the Earth's atmosphere, raising the average global temperature. This and consequent climate change will have severe negative effects for humanity. These will include significantly reducing crop yields and quality, leading to food scarcity; threatening the supply of fresh water to many people; raising sea levels, thereby destroying much inhabited land and unique animal habitat; increasing desertification; increasing ocean acidification; the extinction of many species; and more frequent extreme weather events. These will cause untold death, destruction, and suffering. [6]

There will also be secondary, non-physical effects. The Stern Review on the economics of climate change, [7] published by the UK government in 2006, discusses the economic effects of global warming and emphasises the importance of acting to reduce its impact. It estimates that 'business-as-usual climate change [i.e. without any effort to combat it] will reduce welfare by an amount equivalent to a reduction in consumption per head of between 5 and 20 %', while 'the costs of mitigation, of around 1 % of GDP, are small relative to the costs and risks that will be avoided', so 'the benefits of strong, early action on climate change outweigh the costs'.

The rise in average annual global temperature is a simple indicator of climate change, measured in reference to a nominally 'pre-industrial' value. This is generally taken as 13.9 °C, the overall average for 1951-1980, but as Figure 1 shows, the global temperature has in fact been increasing rapidly since the beginning of the twentieth century. Without decisive action, current trends in energy use and greenhouse gas emission will lead to an increase in average annual global temperature of around 6 °C. [8] It is generally agreed that to avoid the worst effects of climate change, this global temperature rise should be

restricted to no more than 2 °C. [6] In 2016, the five-year-average had already increased by 0.9 °C. [9] The time for decisive action has been upon humanity for decades already.

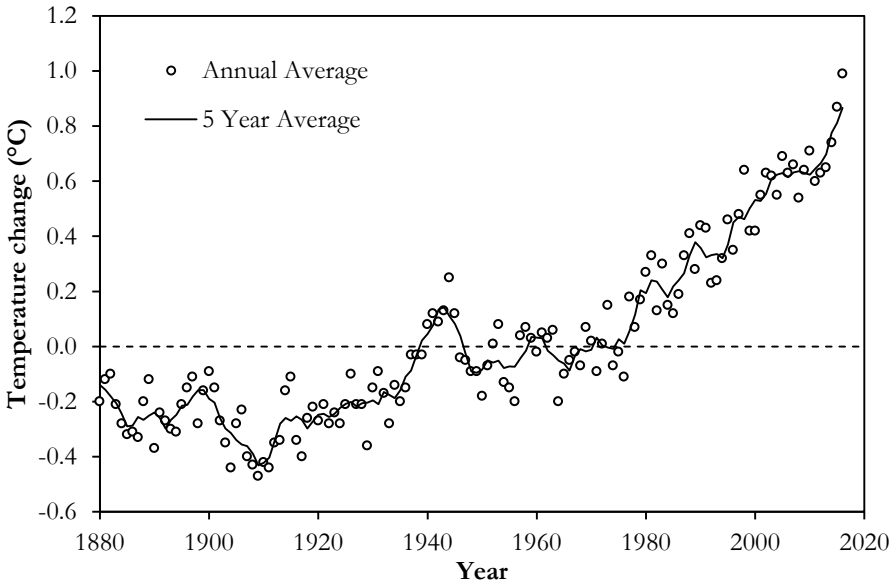

Figure 1: The rise in average global temperature 1880-2016. The dashed zero line represents the nominally 'pre-industrial' average of 13.9 °C. Data from [9].

The dangers of climate change are not merely potential threats to the future; they are measurably occurring now. By 2010, the global average sea level had risen by 19 cm since 1901 (rising at a rate of 3.2 mm per year between 1993 and 2010). [6] Due to oceanic uptake of CO_2, by 2014 the pH of ocean surface water had already decreased by 0.1 from the pre-industrial level: an increase in acidity of 26 %. [6] Wheat yield decreased at an average rate of 2 % per decade from 1960 to 2013 due to climate change. [6] By 2004, the United Nations World Health Organisation attributed 141,000 annual deaths (0.2 % of the global total) to climate change. [10] David King, UK Government Chief Scientific Advisor in 2007, expressed the situation well: 'Avoiding dangerous climate change is impossible; dangerous climate change is already here. The question is, can we avoid catastrophic climate change?' [11]

Climate change is caused by the emission of greenhouse gases above the level at which they can be removed from the atmosphere (for example, through photosynthesis by plants). This increases the amount of energy from the Sun that is retained by the Earth and its atmosphere as heat. Several gases contribute to the greenhouse effect, most prominently carbon dioxide (CO_2), methane (CH_4), and nitrous oxide (N_2O), and others at much lower

levels (although important because they are much more potent) such as hydrofluorocarbons (HFC), fluorocarbons, and sulphur hexafluoride (SF_6). When discussing greenhouse gas emission, they are often measured in units of equivalent CO_2 (CO_2eq), i.e. the amount of CO_2 that would cause the same global warming. For example, the emission of 1 tonne of methane, which has 28 times the global warming potential of CO_2, is reported as 28 tCO_2eq. [6] The global warming potential values of some major greenhouse gases are given in Table 1.

Greenhouse gas:	CO_2	CH_4	N_2O	HFC-152a	CF_4	SF_6
Global warming potential:	1	28	265	138	6,630	23,900

Table 1: The global warming potential of some major greenhouse gases in CO_2eq. [6]

The drastic increase in atmospheric CO_2 content due to human activity since the industrial revolution, plotted in Figure 2, is often used as a warning sign of climate change to come in the imminent future.

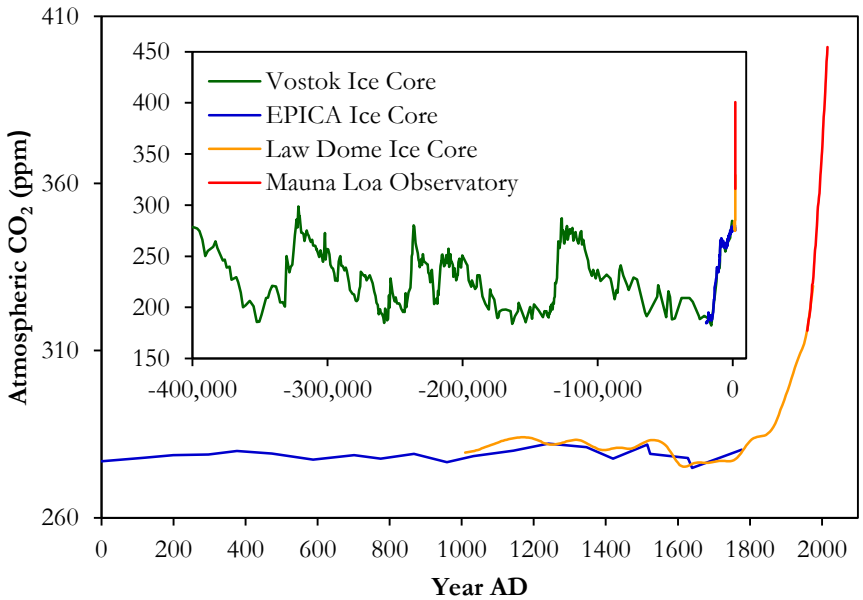

Figure 2: The increase in atmospheric CO_2 content since the industrial revolution (around 1760-1820), with historic data from the last 400,000 years inset for context. This chart is often referred to as the 'hockey-stick curve' because of its long stable level followed by relatively sudden and extremely rapid rise. The inset historical data shows that even before this anthropogenic effect, the Earth was already around its highest point of atmospheric CO_2 content in the last 400,000 years, with the fluctuations of ~100 ppm corresponding to ice age glacial and inter-glacial periods. Data from [12-15].

It has been calculated that to restrict the rise in average global temperature to 2 °C would require the atmospheric CO_2 content to be limited to 450 ppm by the year 2100; it was already approximately 430 ppm in 2010. [6] To put this another way, the cumulative anthropogenic greenhouse gas emissions since 1870 must remain less than 2,900 $GtCO_2eq$; [6] 1,730 $GtCO_2eq$ of this had been emitted by 2015, leaving a buffer of only 1,170 $GtCO_2eq$. [16]

The decline in annual total greenhouse gas emissions necessary to achieve the 2 °C target is illustrated in Figure 3: in 2015 annual emissions were 53.2 $GtCO_2eq$; this will need to be reduced to 42 $GtCO_2eq$ by 2030 and net zero by 2085 to have a >66 % chance of keeping the temperature increase below 2 °C by the end of the 21st century. [17] 'Sustainable Energy Without the Hot Air' by David Mackay [11] is an insightful book for non-specialists that demonstrates the scale of the changes necessary to make a significant impact, and how far humanity still has to go.

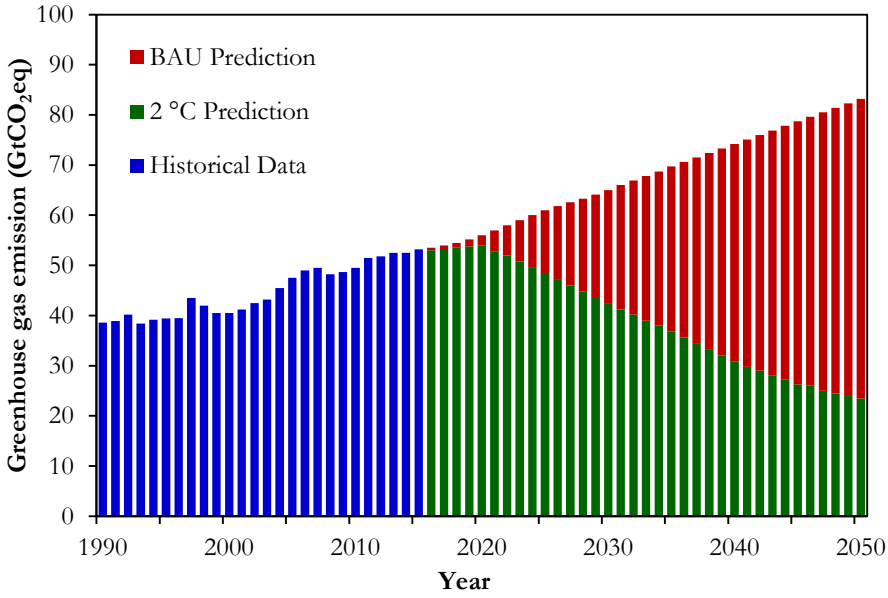

Figure 3: Annual global greenhouse gas emissions 1990-2015, with a business-as-usual baseline projection to 2050 and a projection based on achieving the 2 °C temperature rise target. Data from [17].

Greenhouse gases are emitted by the generation of electricity and many other processes. It is important to emphasise in discussions of climate change and related energy issues that 'electricity' and 'energy', while often used interchangeably, are distinct technical terms. Energy use includes electricity use, but also the direct use of fuels without the energy being

converted to electricity in the process; this includes transport using petrol or other combustion fuel, heating and cooking using gas or biofuel, etc.

The relative contributions of the sources of anthropogenic greenhouse gas emissions are illustrated in Figure 4. Electricity and heat production are the greatest source at 25 %, and agriculture produces almost as much at 24 %, primarily through fertilisers, methane production by cattle, waste from processing, etc.

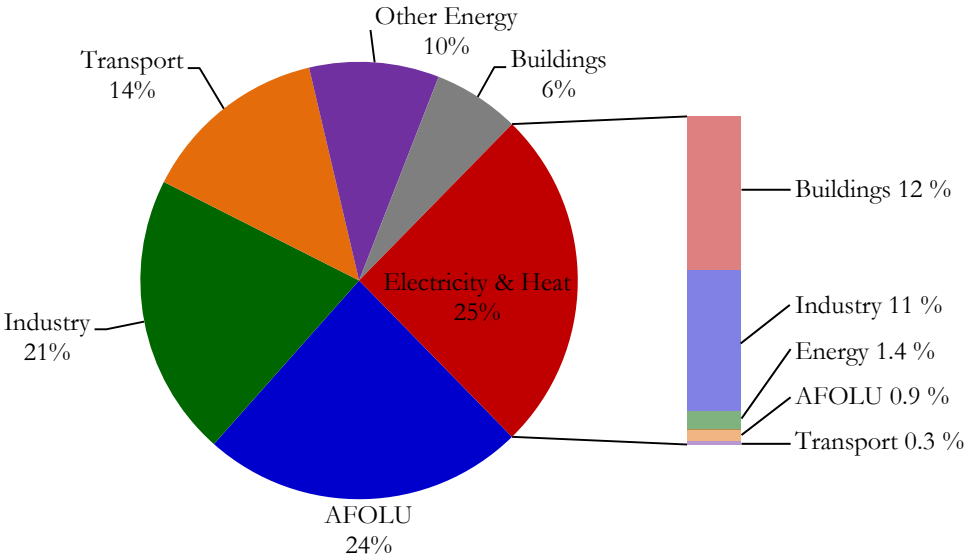

Figure 4: The sources of anthropogenic greenhouse gas emissions in 2010 (49 $GtCO_2$-eq in total). Electricity and 'agriculture, forestry, and other land use' (AFOLU) are the largest sources, accounting for approximately 25 % each. Data from [6].

Both because it will lead to a lower environmental impact and because it will eventually reduce their costs, both transport and 'other energy' are likely to be electrified in the near future. [18,19] Even without any move to sustainable electricity sources, greenhouse gas emission would be cut significantly by powering vehicles using electricity. [11,19] In 2016 only 0.2 % of passenger vehicles were electric, but this is growing exponentially and the International Energy Agency has set targets of 10 % by 2030 and 60 % by 2060, which are supported by national targets set by countries that make up the majority of the current electric vehicle market, in order to achieve the 2 °C global temperature rise target. [19] Including transport and 'other energy' with electricity and heat production means that 49 % of current anthropogenic greenhouse gas emissions can be cut by moving from fossil fuels to sustainable electricity sources.

The regional breakdown of global CO_2 exclusively from fossil fuel use is depicted in Figure 5. In the last decade, these emissions have continued to rise rapidly due largely to the increased industrialisation of China and India, but recent years have seen emissions begin to decrease, largely due to India's efforts. As Figure 3 shows, a much more rapid decrease is now required.

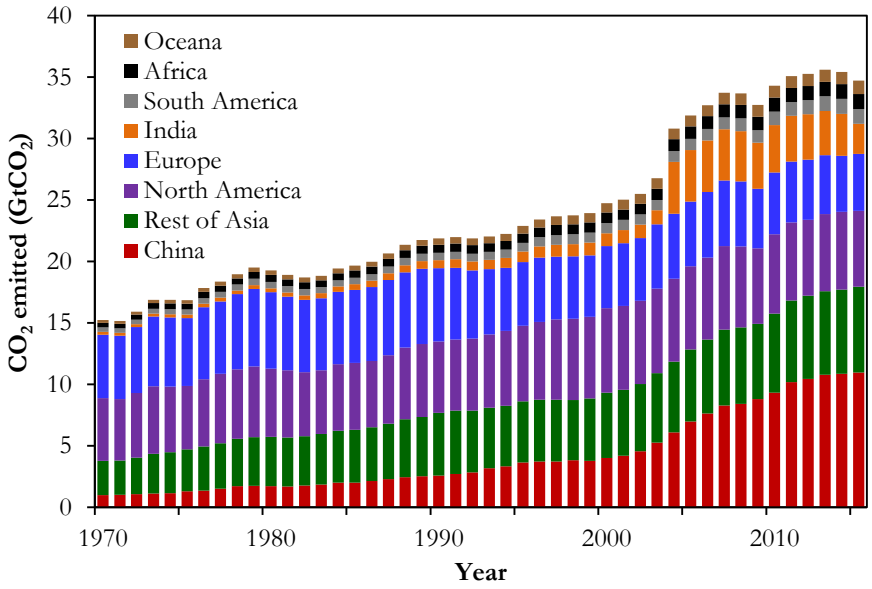

Figure 5: Annual global CO_2 (N.B. not total greenhouse gases as in Figure 3) emissions 1970-2015 from fossil fuel use and industrial processes (excluding biomass burning and 'agriculture, forestry, and other land use'). Data from [20,21].

1.1.2. Fossil fuel scarcity

In 2016, total primary energy use was 57,000 TWh, i.e. the average global power use was 6.5 TW (these numbers are lower than some reported figures because they represent energy used rather than fuel used, the former being a more relevant figure for solar power; a realistic conversion efficiency of 38 % is assumed for fossil fuel, the use of which is simply reported in tonnes of fuel). [22,23] This is expected to increase drastically over the coming decades, reaching around 170,000 TWh (20 TW) by 2050. [24] This has traditionally been met by fossil fuels such as oil, coal, and natural gas (see Figure 6).

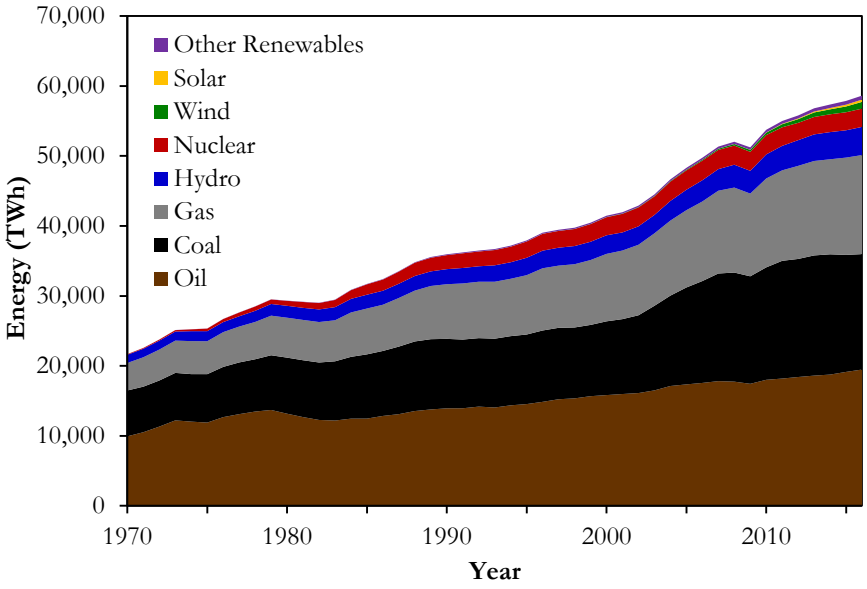

Figure 6: Global primary energy consumption by source. Solar provided 0.57 % of energy (which is 1.8 % of electricity [25]) in 2016. Data from [23].

However, these fossil fuels, as well as contributing to global warming, are in finite supply on Earth and will run out in the coming decades if alternative energy sources are not adopted in their place. It is estimated that there are proven reserves of oil, gas, and coal, to last until approximately 2043, 2045, and 2115 respectively, based on current usage trends and economy of recovery. [26] It is therefore evident that sustainable energy sources must be found and adopted on a global scale well before these years.

1.1.3. Energy security

Increasing use of various sustainable energy sources will also increase energy security, or security of supply, which means the uninterrupted availability of reasonably priced energy. Threats to this include international political instability (a particular concern in many oil-exporting countries), conflicting exporter interests, in-state conflicts (either military or economic, such as strike action), natural disasters, and anything else that can disturb supply or energy markets. Increased provision of power from renewable sources, which of course carry their own risks, often means more power is locally produced and so the international risks to energy security, which are considered the major ones, are significantly reduced. [27]

1.2. Renewable energy progress

In 2016, renewable energy (mainly hydropower, wind, and solar) supplied 24 % of global electricity use, which was equivalent to 10 % of total energy use. [23] This progress has been due to significant global, national, state, and local effort in recent decades to tackle the problems of impending energy shortage and climate change.

1.2.1. International action

At the global level, the United Nations (UN) enacted the Kyoto Protocol [28] in 1997. This was adopted by 197 countries and regions, which thus became the parties to the United Nations Framework Convention on Climate Change, or UNFCCC. The Kyoto Protocol sets binding obligations to reduce emissions of greenhouse gases, particularly on developed countries.

The Copenhagen Accord [29] is a more recent UN agreement, made in 2009 at the 15th Conference of the Parties to the UNFCCC (known as COP15), but is not legally binding. It emphasises the importance of tackling climate change and posits the long-term goal of limiting climate change to a rise in the average annual global temperature of no more than 2 °C from the pre-industrial value.

The Paris Agreement, [30] made at the 21st Conference of the Parties of the UNFCCC (COP21) in December 2015, was much more successful. It emphasises again the commitment to limit the rise in global temperature to no more than 2 °C above the pre-industrial level, makes it officially binding, and outlines international cooperative efforts instigated to facilitate this. These include the 'intended nationally determined contributions' (INDCs), submitted by over 160 countries, representing over 90 % of both global energy-related emissions and global population, which determine how each country intends to reduce its greenhouse gas emissions, and which will be updated every five years. [31] The withdrawal of the United States of America (USA) from the Paris Agreement in 2017 will undoubtedly hinder global progress, but will not prevent it.

1.2.2. Significant national action

At the national level, 60 % of total global greenhouse gas emissions in 2015 came from China (29 %), the USA (14 %), the European Union (10 %), and India (7 %) alone. [21]

The energy markets of developing nations like China and India are growing at an unprecedented rate and will be very important to global climate change. China's CO_2 emissions increased by over 300 % and India's by over 250 % from 1990 to 2015. [32] Due to China's high dependence on coal, its energy supply has been the most carbon-intensive of all regions for the past two decades, and India used five times more coal for electricity generation in 2013 than in 1990. [32] However, developing countries often have the largest potential for green energy: the sustainable energy generation capacity installed in China in 2013 composed over half of that globally, [32] and China is planning to introduce an emissions trading scheme in an effort to reduce the demand for coal. [33] India has pledged that 40 % of its electricity generation capacity will not use fossil fuels by 2030. [33]

The USA enacted its Clean Power Plan in 2015, which requires states to reduce CO_2 emissions from existing fossil fuel generators and extends tax credits to wind and solar energy. It aims to reduce CO_2 emissions from electricity generation by 32 %, relative to 2005 levels, within twenty-five years. This is the first time the USA has set a national limit on carbon pollution produced from power plants. [21,34] The extent of the damage to the USA's progress by the actions of President Trump remains to be seen.

The European Union (EU) committed in 2007 to reduce its emission of greenhouse gases by 60-80 % by 2050. This will start with a 20 % reduction, along with a 20 % improvement in energy efficiency, and a 20 % share of total energy provision by sustainable sources, all by 2020: the 20-20-20 goals. [35] The fraction of total energy use supplied by renewable sources, including nuclear, reached 24.4 % in 2016, [23] already well surpassing the 20 % target.

Emissions per capita, shown in Figure 7, is a useful metric for measuring each country's progress in climate change mitigation. It can be seen that the worst performers are the USA, Canada, Australia, Saudi Arabia, the United Arab Emirates, Kazakhstan, Turkmenistan, and Estonia.

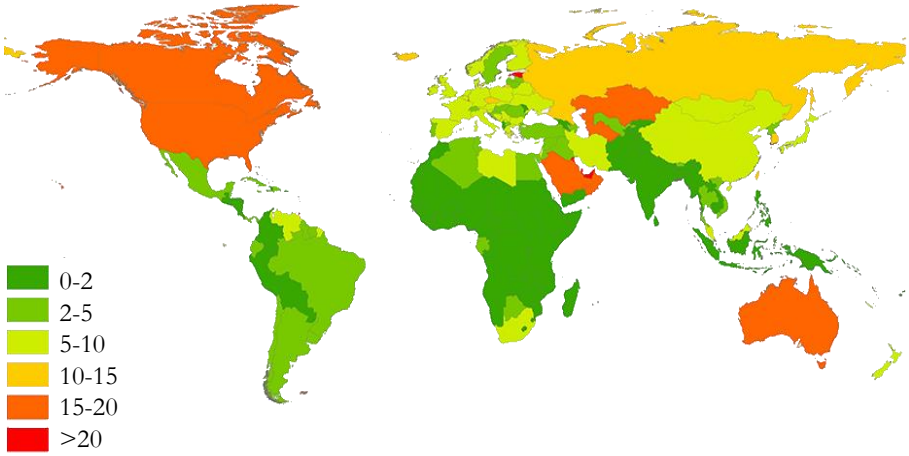

Figure 7: The 2015 greenhouse gas emissions per capita of each country in tCO_2eq. From [20].

1.2.3. Progress evaluation

Progress and development so far, especially the achievements of the Paris Accord, have made a promising start to tackling climate change and the related energy problems. However, the various targets and aims for the future will be difficult to achieve, and even doing so would be insufficient. The International Energy Agency (IEA) reported in 2016 [16,32] that the world is not on track to achieve the 2 °C temperature rise target. The UN concurred, reporting that even with the INDCs determined at COP21, global greenhouse gas emission in 2030 will still be 12 $GtCO_2eq$ above that necessary to achieve the 2 °C target, being likely to give an increase of 3.4 °C. [17] The Energy Institute similarly reported that the commitments made at COP21 are unlikely to be enough to meet the 2 °C target. [36] Clearly more progress is needed.

1.3. Solar power

Photovoltaic solar power has the potential capacity to provide a significant fraction of global energy demand. This is different to thermal solar power, which provides heat rather than electricity. Thermal solar power is often known as 'concentrating solar power' (CSP), which can be confusing as some photovoltaic solar power installations concentrate light using large optical arrays; this is still photovoltaic solar power.

The power incident on Earth in the form of sunlight is 1.4×10^{17} W (on average, 1.366 kW·m^{-2}) [37]. Assuming only 10 % photovoltaic efficiency, this means that around 5×10^{4} km^2 (approximately 0.03 % of the Earth's land surface) of solar panels would be required to satisfy the 2016 global power consumption (6.5 TW [22,23]). This is not unrealistic, as solar panels are either fitted to existing surfaces such as roofs, or are installed as large facilities in little-used land such as deserts.

Photovoltaic installations can be classified as domestic, i.e. traditional small-scale rooftop systems producing power on the kW scale, or utility-scale, sometimes known as 'solar farms' (see Figure 8), producing power on the MW-GW range. Domestic installations currently represent 60 % of installed photovoltaic capacity and utility-scale 40 %, [8] but the share of the latter is growing: it composed 72 % of capacity newly installed in 2016. [38]

Figure 8: Left, a domestic solar photovoltaic system; and right, a utility-scale installation (the 550 MW Desert Sunlight Solar Farm, covering 16 km^2 in California, USA). Photo credits: SolarWorld & First Solar.

While seemingly modest, domestic installations can have a dramatic effect on global electricity supply. As an example, the average UK household roof area is 94 m^2, [39] so around 12.8 kW of power could be generated by 10 % efficient photovoltaic cells at peak performance, giving approximately 10.6 MWh per year, accounting for varying irradiance over the course of a day, weather, etc. [40] An average UK household uses 3.9 MWh of electricity per year, [41] so domestic photovoltaic installations could provide more power than is used domestically, which accounts for 37 % of the UK's total energy use. [41] However, most current domestic installations do not cover all available roof space, and only produce on average 2.3 MWh of power per year. [40]

Large utility-scale photovoltaic installations have a peak generating capacity of several hundred megawatts, and are typically located in deserts as this land is in low demand for any other use and is highly solar-irradiated. They facilitate a much faster growth of photovoltaic capacity and decrease in electricity price, as they require less market development. [42,43]

The distributed nature of photovoltaic generation makes it particularly suited to providing electricity to the population of developing countries without a full grid system in place, bypassing a significant barrier faced by traditional generation sources. [44]

1.3.1. Growth

In 2016, the world's cumulative photovoltaic capacity reached 307 GW, having supplied 375 TWh of electricity that year (1.8 % of average global electricity demand). [25,38]

The global installed capacity, plotted in Figure 9, is increasing exponentially (76.6 of the total 307 GW was installed in 2016 [25,38]). This is due to the exponential increase in annual installations, plotted in Figure 10, which demonstrates the rapid growth of the photovoltaic industry and market as solar energy is increasingly recognised as a viable, sustainable, and mainstream power source.

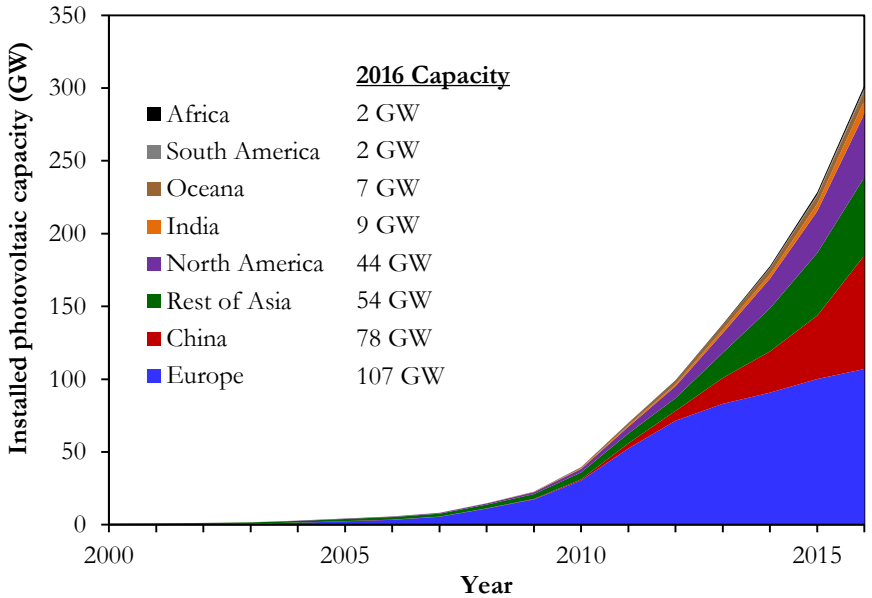

Figure 9: The cumulative installed photovoltaic capacity 2000-2016. Data from [25,43].

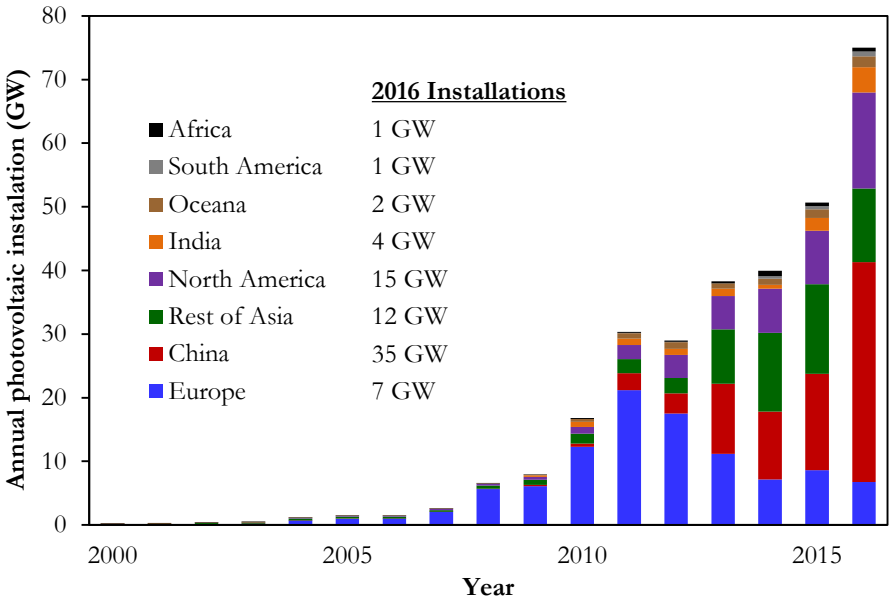

Figure 10: The annual installation of new photovoltaic capacity 2000-2016. Data from [25,43].

However, while this growth is impressive, much remains to be done if solar energy is to make a significant contribution to meeting the UN's 2 °C global temperature rise target. To achieve this, it is predicted that 720 GW of capacity must be installed by 2050. [8] This would require a significant capital expenditure on the order of half a trillion USA dollars annually, [45] or 44 trillion dollars of total additional spending (although this investment is more than offset by over 115 trillion dollars in fuel savings). [8] However, SolarPower Europe is optimistic, predicting in its latest annual global photovoltaic market outlook [38] that 700 GW will be installed as soon as 2021.

Greater consideration of non-technical factors is becoming evident as the industry grows, and will of course help its development. For example, aesthetic considerations are increasingly being catered to for domestic installations: building-integrated photovoltaics such as solar shingles and solar tiles negate the objection that traditional solar panels mar the aesthetic appearance of a building. These are illustrated in Figure 11 in contrast to standard unsympathetically designed panels that are simply added on to a building. [46]

Figure 11: Left, a building-integrated photovoltaic system (Tesla's Solar Roof textured tiles); and right, a traditional rack-mounted domestic photovoltaic system. Photo credits: Tesla & SolarWorld.

1.3.2. Cost and price

Historically, the primary reason solar power was not a major energy source was its cost. Electricity produced from fossil fuels was in many cases cheaper, so was still commercially dominant.

The cost of electricity, and particularly solar electricity, is not easy to define or compare. 'Levelised cost of electricity' (LCOE) is a useful and common concept that includes all investment and operational costs, such as fuel consumption, equipment replacement, etc., over the entire lifetime of the system. This allows the actual cost of producing a kWh of electricity to be compared between different generation technologies, taking account of the different lifetimes and risks of different systems and specific factors such as the installation location and irradiance for solar. LCOE is calculated as [47]

$$\text{LCOE} = \frac{\text{capital expenditure} + \text{net operation \& maintenance costs}}{\text{net total electricity production (in kWh)}}. \qquad (1)$$

Another important concept for solar power (as for all renewable electricity sources) is that of dynamic grid parity. This refers to the point at which the LCOE for solar electricity is equal to the average price of grid electricity over the lifetime of the photovoltaic system. This is relevant to domestic installations and any others in which the owner of the system uses at least some of the electricity produced themselves in place of electricity purchased from the grid; i.e. when an electricity consumer becomes a 'prosumer', both producing and consuming their own electricity. [48]

'Generation value competitiveness' is the equivalent to grid parity for utility installations, which will become independently commercially viable when the LCOE for solar drops to that for conventional energy sources. This is lower than the cost for grid parity, as the later includes the profit made by corporate energy suppliers on traditionally supplied electricity. However, utility-scale solar has a lower LCOE than domestic installations because of economies of scale. [48]

Exemplar levelised costs of electricity generated by various technologies are listed in Table 2. They can be compared to the average domestic retail price of electricity, which in 2012 varied from 90.08 $\$\cdot MWh^{-1}$ in Mexico to 403.12 $\$\cdot MWh^{-1}$ in Denmark, with the UK value being 255.66 $\$\cdot MWh^{-1}$. [22] The values in Table 2 are average or representative prices; in advantageous areas solar has reached as low as 24 $\$\cdot MWh^{-1}$. [38]

Generation technology	**Cost ($\$\cdot MWh^{-1}$)**
Geothermal	43.3
Onshore wind	52.2
Natural gas (advanced combined cycle)	56.5
Hydroelectric	66.2
Solar photovoltaic	66.8
Nuclear (fission)	99.1
Biomass	102.4
Coal	123.2
Offshore wind	145.9
Solar thermal	184.4

Table 2: The levelised cost of electricity by generation source. Data from [47].

The costs that contribute to that of an installed photovoltaic system include the materials (which can further be broken down into the separate layers of the device, see Section 3.8); fabrication process; 'balance of system' costs such as the device housing structure and an inverter (which enables connection to a distribution grid); installation (which includes project development, administration, planning, and installation labour); and end-of-life management, i.e. removal and disposal or recycling. A breakdown of the price components of a typical commercial photovoltaic solar installation is given in Figure 12.

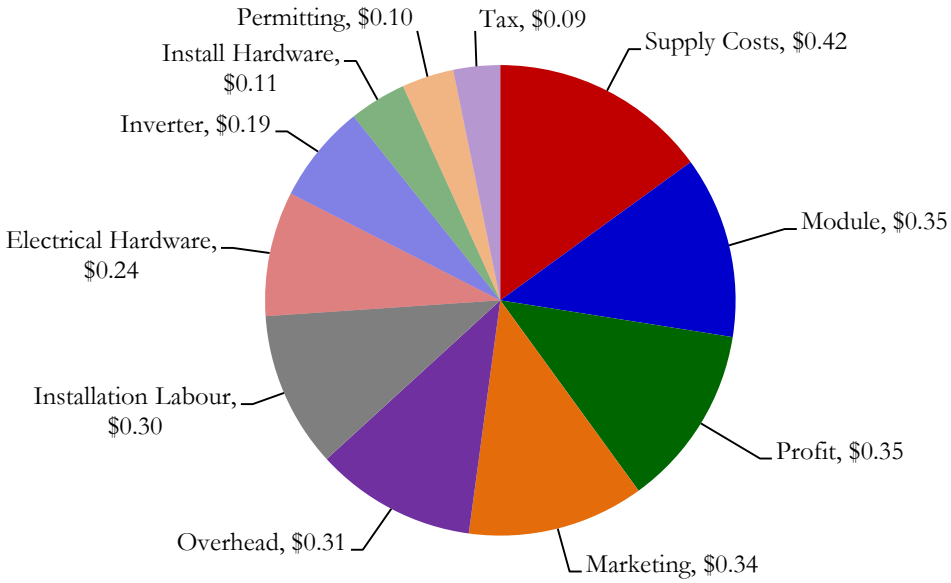

Figure 12: The breakdown of price components of a typical 5.7 kW residential monocrystalline silicon solar panel installation, costing 2.80 $\$\cdot W^{-1}$, in 2017. Data from [49].

The price and breakdown thereof is of course different for every photovoltaic technology and even between products using the same technology. Additionally, building-integrated photovoltaics (i.e. solar cells designed as a fundamental component of a building rather than added on as a separate installation) could cost around 10 % less than traditional rack-mounted photovoltaics as the cost of module-mounting hardware and labour is less and the cost of traditional building materials is offset. [46]

As the photovoltaic industry grows and economies of scale, production experience, infrastructure, and public perception develop, the price of solar electricity naturally falls, as well as with developments in technology that make devices more efficient and cheaper to produce. [50] This drop in module price is plotted in Figure 13.

It has been observed that the price of photovoltaic modules has decreased by approximately 20 % for every doubling of cumulative installed capacity, which has equated to the price halving roughly every 10 years. This relation is referred to as Swanson's Law (named after Richard Swanson, the founder of SunPower Corporation) as a parallel to Moore's Law for transistor density in integrated circuits. [8] Figure 14 shows Swanson's Law depicted graphically.

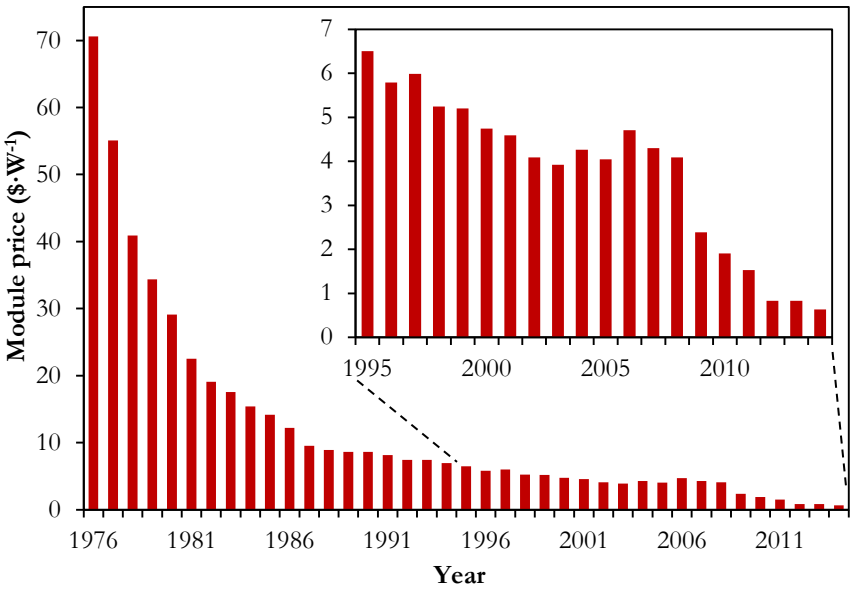

Figure 13: The annually averaged silicon photovoltaic module price 1976-2014. Data from [8].

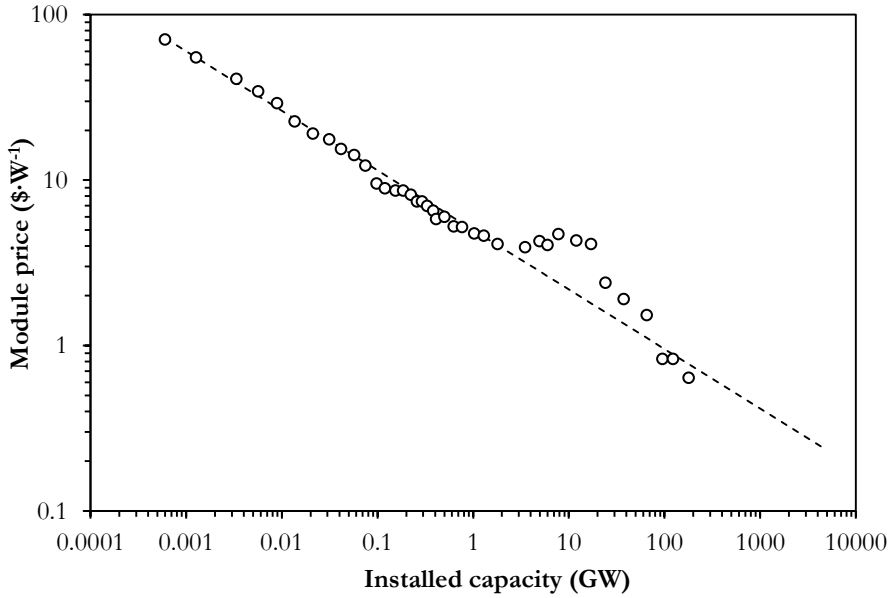

Figure 14: Swanson's Law: the ~20 % decrease in module price with doubling cumulative installed capacity. Note the logarithmic scales. The bump at 10 GW corresponds to the 2008 financial recession. Data from [8].

1.3.3. Challenges

While solar photovoltaic power may have the potential to provide the amount of power used by humanity, its variability over the course of a day and its reliance on weather conditions mean that achieving this will be very challenging. However, with the integration of electricity storage and improvements in output prediction, it will become an important and significant component of the energy mix of the future.

Connecting solar panels to existing national or large-scale grids can be problematic due to the required grid flexibility. Existing systems were designed to connect large, relatively consistent generating units via high-voltage power lines to large consumers, and to substations for distribution to smaller consumers using lower-voltage distribution lines. A large number of much smaller distributed generators such as photovoltaic modules will be much more difficult to manage because of the variability of their production capacity, and because they cannot be controlled centrally, i.e. they are not 'dispatchable'. [51]

The voltage and frequency of electricity supplied by large-scale grids must remain within acceptable limits to avoid damage to components. To achieve this, grid generation must always closely match demand. While most of the electricity currently produced is provided by 'baseload' power plants, which run constantly, 24 hours a day all year round, many large generators are dispatchable, i.e. their output is controlled in real-time by a 'transmission system operator' to ensure that supply always matches demand and that the system is stable. These dispatchable generators are split into two categories: cycling plants, which are used to meet predicted increased demand over the course of each day, and flexible plants, which can vary their output very rapidly, often within seconds, and so are used to deal with smaller, more rapid fluctuations in demand (such as the famous spike in UK electricity demand due to tea-making during television commercial breaks). [51]

Provided that solar photovoltaic generation can be predicted with reasonable accuracy on a timescale long enough for more dispatchable generators or energy storage to adapt their output, the non-dispatchable nature of solar electricity does not prevent it from forming a significant contribution to electricity supply. Such forecasting of photovoltaic electricity production (based on weather prediction, usage habits, etc.) does exist, but is still in its

infancy and will need to be further developed by transmission system operators for large-scale integration of solar electricity into large electricity grids. [51]

Another challenge for photovoltaic solar energy is that, even on entirely sunny, cloudless days, when variability is not a problem, solar panels produce electricity only during the daytime, while the largest peak in electricity consumption is in the evening. Reducing the daytime demand from grid electricity by the deployment of a significant amount of distributed solar generation can therefore necessitate a much greater ramp rate in grid electricity provision than currently seen, as dispatchable power stations must be brought into use very quickly to account for the rise in demand just as solar panel output drops. This is illustrated in Figure 15, a plot known as the 'duck curve' for its apparent resemblance to a duck facing to the right. The need for such steep ramping of grid provision could be problematic for many grids, which currently contain too high a proportion of conventional base-load power stations, which are not dispatchable on such timescales.

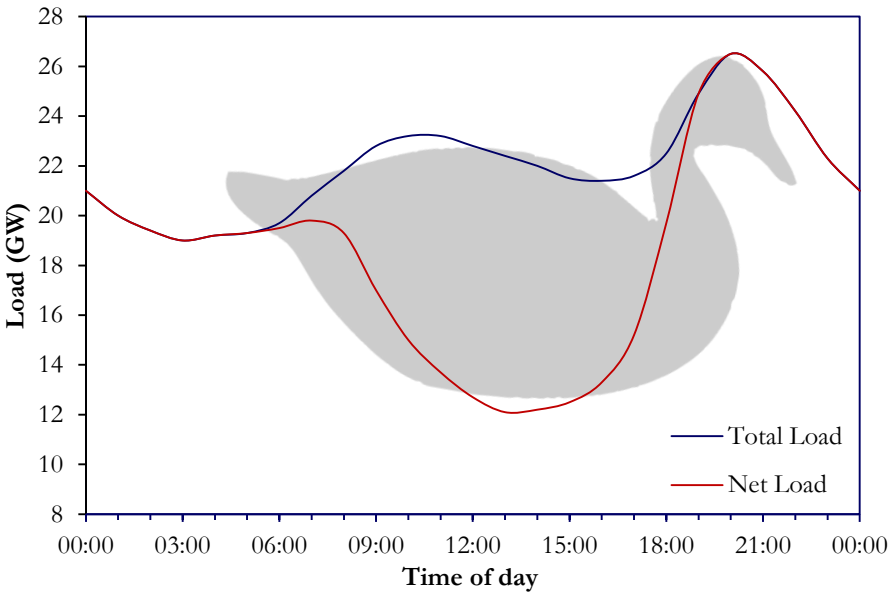

Figure 15: The 'duck curve', showing the effects on the grid demand of a high proportion of electricity coming from distributed solar. Specifically, this data is a prediction for a typical spring day in California in 2020. The net load shows the electricity provided by dispatchable sources (i.e. excluding solar and wind). The steep ramp around 18:00 could be problematic for grid operators. Data from [8].

Integrating local storage capacity within the system is a simple way to tackle these problems. Such storage could operate on the scale of individual photovoltaic installations (e.g. batteries) or much larger (e.g. pumped hydro storage), and could store energy for periods from a few minutes to months. Fuel production, e.g. hydrogen from water, is a promising option for energy storage as it could take place on any scale from domestic to large industrial plants, and could also be used for non-electrical energy uses, such as transport and heat, without the need for electrical technology incorporation. New storage technologies are currently advancing rapidly, and will allow currently non-dispatchable renewable generators like solar panels to be managed in a more controlled way, by meeting local demand and storing excess energy when not needed locally, rather than having to be incorporated into a large grid. [52]

1.3.4. The future

The European Photovoltaic Industry Association is, unsurprisingly, optimistic about the place of photovoltaic electricity in the energy mix of the future, stating that 'large-scale photovoltaic integration in the European grid is technically feasible with a high level of security of supply, even under the most extreme weather and load conditions. With the right measures in place, system reliability can be ensured.' [51] They estimate that by 2030, it could provide up to 25 % of electricity demand in Europe without any adverse effects on electricity grids.

There is certainly a great commitment to making the large-scale adoption of solar power a reality in the future, including academic research on the topic, commercial investment, and government policy at all levels. For example, in 2007 the European Union set a target in its 'Strategic Research Agenda for Photovoltaic Solar Energy Technology' [35] for solar power to be economically competitive with conventional electricity generation methods by 2020. The United States of America (USA) set a similar 'SunShot target' in 2011, for the cost of photovoltaic electricity to be less than that of conventional fossil fuel electricity by 2020. In concrete terms, this has been defined as 1 $\$\cdot W^{-1}$ for utility-scale photovoltaic systems, 1.25 $\$\cdot W^{-1}$ for commercial rooftop systems, and 1.50 $\$\cdot W^{-1}$ for residential rooftop systems. If this is achieved, it is envisioned that solar power alone will provide 14 % of USA electricity by 2030 and 27 % by 2050. [53]

Progress has been quicker than expected in recent years. The International Energy Agency (IEA) reported that this economic competitiveness was already happening in 2014, predicting that solar could supply 16 % of global electricity by 2050. [8] In another IEA report [54] the 'next generation' phase of solar energy (technological maturity and economic competitiveness with tens of percent of electricity coming from solar) was said to be imminent, and indeed already present in some countries in 2016.

Simply adding new renewable generation sources to the electricity mix using the model of the past will cause problems. For a high penetration of solar electricity to work successfully, an energy system transformation is necessary, including advances like an integrated smart grid, automatic demand management, local energy storage, and the electrification of heating and transport. This transition is now underway. [8,54,55]

Chapter 2:

Photovoltaic solar cells

2.1. Introduction

Solar panels are modules composed of individual photovoltaic cells. Photovoltaic cells convert power incident in the form of light to electrical power by exploiting the photovoltaic effect. They typically use inorganic semiconductors to achieve this, but devices using organic and other novel materials have also been successful. This chapter details the physics of solar photovoltaic cell designs and related general issues.

2.2. Fundamental physics

The working of a solar cell is dictated by the absorption of light to generate a potential difference using the photovoltaic effect, and the fundamental behaviour of the p-n junction around which the cell is designed in order to separate electrical charges and drive them in opposite directions.

2.2.1. Optical absorption in semiconductors

A photon incident on a semiconductor can only be absorbed if its energy is greater than the band gap; i.e. the material is transparent to photons with energy less than the band gap. The energy from an absorbed photon promotes a negatively charged electron from the valence band of the semiconductor to the conduction band, leaving a positive 'hole' in the

valence band. In this context, a hole is a missing electron in the semiconductor lattice, considered as a quasiparticle with existence of its own.

The absorption of light by a semiconductor as a function of energy is thus determined by its band gap and the three-dimensional density of states in the energy bands. The absorption coefficient, α, more often expressed as a function of frequency, is given by the Tauc equation,

$$\alpha = \frac{\mathrm{A}\sqrt{\mathrm{h}f - E_g}}{\mathrm{h}f} \ , \qquad (2)$$

where A is a constant determined by the electronic band structure, h is the Planck constant, f is the frequency of the light, and E_g is the band gap of the material.

The absorption coefficient can be calculated experimentally using the relation

$$\alpha = \frac{1}{d} \cdot \ln\left(\frac{2TR^2}{\sqrt{(1-R)^4 + 4T^2R^2} - (1-R)^2} \right), \qquad (3)$$

and measured values of the semiconductor thickness, d, reflectance, R, and transmittance, T, over a range of incident light energy. [56] The optical band gap of a semiconductor can then be found using Equation (2), by extrapolating the linear region of a plot of the absorption squared as a function of energy down to zero absorption. This is known as a Tauc plot. Slightly below the band gap value, this relationship often shows exponentially rather than linearly decreasing behaviour due to Urbach tailing, but an accurate band gap value is obtained if this is discounted and only the linear region is extrapolated to zero. [57]

2.2.2. The photovoltaic effect

The photovoltaic effect is the generation of a potential difference, or photovoltage, when two materials, at least one of which is a semiconductor, are in contact and exposed to light. The effect was first observed in 1839 by Becquerel, [58] in experiments involving electrolytic cells. Attempts were first made to use the phenomenon to produce useful power after its observation in selenium in 1873. [59] The first patent for such a device was filed in 1887. [60]

In a lone semiconductor the electrons and holes produced by absorption of light recombine with each other, either radiatively or non-radiatively. However, if the semiconductor is in contact with another material, an internal electric field at the interface can allow selective transport across the junction, giving charge separation. This allows a photovoltage to be sustained, which can be used to do work if connections to opposite sides of the junction through an external resistive load are made to allow a photocurrent to flow.

Two types of semiconductor junction can be used to exploit the photovoltaic effect:

- Schottky junction: a semiconductor in contact with a metal.
- p-n junction: two layers of semiconductor in contact, doped in different ways such that they have different majority carrier types; i.e. one is n-type and the other p-type.

If the two layers of a p-n junction are of the same semiconductor (still doped to be different types), they are a homojunction, and if they are different, a heterojunction.

Figure 16 shows schematic band structure diagrams of these junctions. The p-n junction is of most relevance to thin-film photovoltaic solar cells, and so will be detailed below.

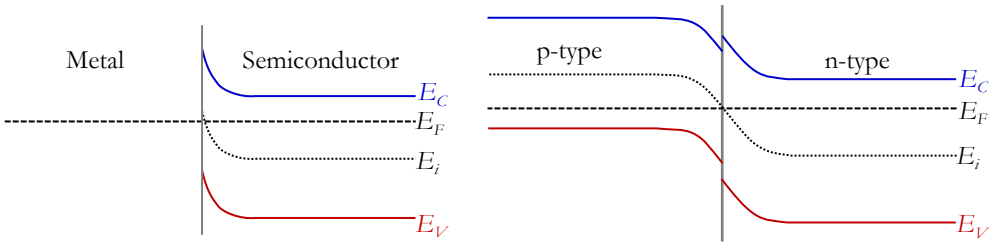

Figure 16: Band structure diagrams of, left, a Schottky junction, and, right, a (type II) semiconductor p-n heterojunction, in which the band gaps of the p-type and n-type semiconductors are different. E_C and E_V represent the edges of the conduction and valence bands in the semiconductor respectively, E_i is the intrinsic Fermi level, and E_F the actual (equilibrium) Fermi level.

2.2.3. The p-n junction

The band structure model of p-n junctions was proposed in 1962. [61] When p-type and n-type semiconductors are in direct contact to form a p-n junction, their band structures are realigned such that the Fermi level (which would be higher in the n-type than the p-type

material if they were separate) is constant across them both (see Figure 16). This is due to a dynamic equilibrium between drift and diffusion currents.

The diffusion current is due to the movement of electrons from the n-type to the p-type region and holes in the opposite direction due to the concentration gradients between the two. Once the carriers have diffused across the junction, they are minority carriers, and so very quickly recombine, leaving a region very close to the interface in which the dopant atoms are ionised and very few carriers exist. This is called the depletion region.

The drift current occurs in the opposite direction to the diffusion current and is caused by the electric field due to this build-up of ions with no carriers to balance their charge in the depletion region. The drift and diffusion currents achieve an equilibrium in which they exactly cancel each other. Alternatively, the electric field across the junction can simply be considered as discouraging further diffusion, until at equilibrium there is no current across the junction.

The electric field across the junction and the band bending caused by the realignment of the Fermi level gives a built in potential difference between the two regions given by

$$V_{bi} = \frac{\left(W_p - W_n\right)}{\mathrm{e}} \,, \tag{4}$$

where W_p and W_n are the work functions (i.e. the thermodynamic work required to remove an electron from the Fermi level of the material to a rest state in a vacuum) of the p- and n-type regions respectively, and e is the magnitude of the charge on an electron.

This model assumes an abrupt interface between the two sections, with the carrier concentrations changing suddenly at the edges of the depletion region. The extent of the depletion region in the n- or p-type section of the junction can be calculated by solving Poisson's equation relating the electrostatic potential $V(x)$ to the charge density $\rho(x)$ (a detailed derivation can be found in [62]), which gives:

$$x_n = \sqrt{\frac{2N_a\varepsilon_n\varepsilon_p V_{bi}}{\mathrm{e}N_d\left(\varepsilon_p N_a + \varepsilon_n N_d\right)}} \,, \tag{5}$$

and

$$x_p = \sqrt{\frac{2N_d\varepsilon_n\varepsilon_p V_{bi}}{eN_a\left(\varepsilon_p N_a + \varepsilon_n N_d\right)}}\ , \tag{6}$$

where N_a and N_d are the acceptor density (essentially equivalent to the hole density) in the p-type region and the donor density (essentially equivalent to the free electron density) in the n-type region respectively, and ε_n, and ε_p are the dielectric permittivities of the n-type and p-type regions respectively. The total width of the depletion region is

$$w = x_n + x_p = \sqrt{\frac{2\varepsilon_n\varepsilon_p V_{bi}\left(N_a + N_d\right)}{eN_a N_d}}\ . \tag{7}$$

In actuality, one region is often much more heavily doped than the other (in solar cells the n-type buffer layer is often designed to be the more heavily doped), giving a carrier concentration several orders of magnitude higher, in which case ($N_d \gg N_a$) Equation (7) can be simplified to

$$w = \sqrt{\frac{2\varepsilon_n\varepsilon_p V_{bi}}{eN_a}}\ . \tag{8}$$

When a bias voltage is applied across the junction, the width of the depletion region is adapted from Equation (8) to

$$w = \sqrt{\frac{2\varepsilon_n\varepsilon_p\left(V_{bi} - V_B\right)}{eN_a}}\ , \tag{9}$$

where V_B is the applied bias voltage. Under forward bias the depletion region width decreases, and under reverse bias it increases.

When devices are illuminated, the charge carriers created by the photovoltaic effect mean that the device is no longer in a static equilibrium. The extra carriers created by photoexcitation thermalise within each band much quicker than they recombine across the band gap, meaning that the carrier populations in each band are described by quasi-Fermi levels (specific to each band), rather than the single equilibrium Fermi level.

The difference in each band edge position across the junction separates the carriers, driving the two types selectively in opposite directions. Electrons move preferentially from the p-type to the n-type material (to a lower energy) across the junction, and holes in the opposite direction (to a higher energy) across the junction. If the two sections of the junction are connected by an external circuit, electrons from the n-type region recombine

with holes from the p-type region through the circuit, giving a photocurrent from the p-type to the n-type region (the direction of positive charge movement). The difference in band levels forms a potential difference between the two sides of the p-n junction, so work can be done. [63-65]

2.2.4. Band offsets

The relative positions of the band edges in the p-type and n-type semiconductors can significantly affect the ability of the charge carriers to cross the junction, and so can help or hinder charge separation.

If the conduction band edge of the n-type material is higher than that of the p-type material, the conduction band offset (CBO) is said to be 'spike-like', and electrons are faced with an energy barrier in moving from the p-type material to the n-type. However, if the conduction band edge of the n-type material is lower than that of the p-type, the conduction band offset is said to be 'cliff-like', and the electrons can pass easily from the p-type material to the n-type. This is also true vice versa for the valence band edges.

In type-I ('straddling gap') band alignments the material with the higher conduction band edge has the lower valence band edge, i.e. its band gap extends both higher and lower than that of the other material. In type-II ('staggered gap') alignments, the material with the higher conduction band edge has the higher valence band edge. Figure 17 depicts these band alignment types for a p-n junction graphically. Type-II junctions are the best for photovoltaic devices, as they encourage charge separation without either charge carrier facing an energy barrier.

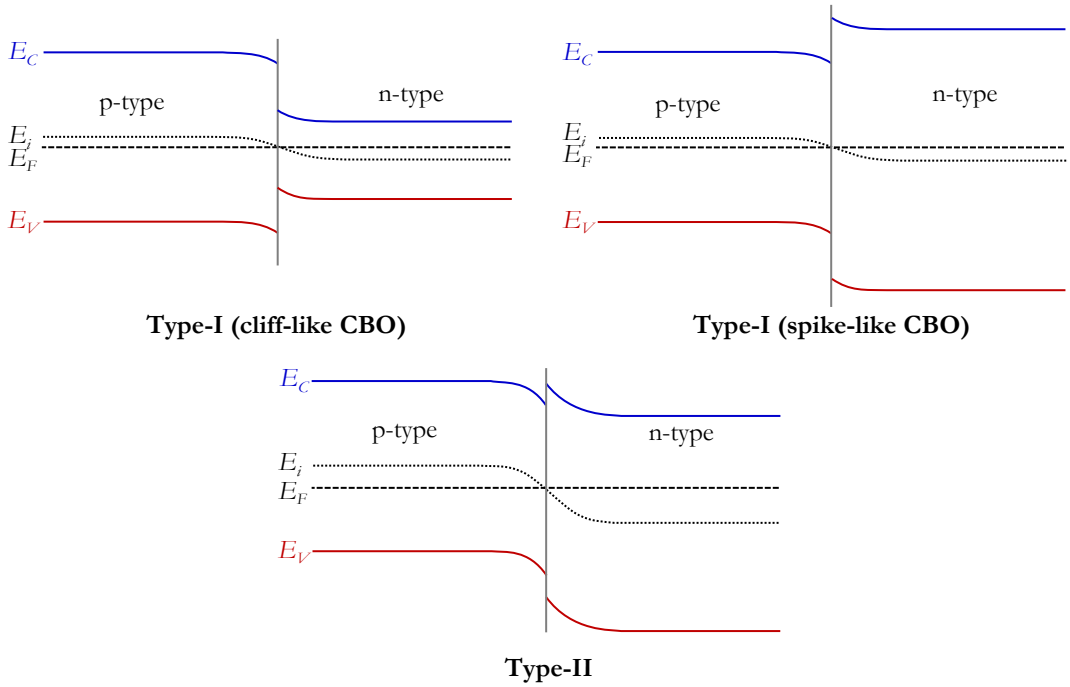

Figure 17: The various band alignment types of a p-n junction.

2.2.5. Capacitance-voltage characteristics

Capacitance is defined as the ratio of a change in stored charge to the associated change in potential,

$$C = \frac{\mathrm{d}Q}{\mathrm{d}V}\,, \tag{10}$$

and so arises in p-n junctions due to the charge stored in the depletion region, where there are no charge carriers to balance the charged dopant ions. The capacitance per unit area of the junction under bias is given by

$$\frac{C}{A} = \frac{\varepsilon_p}{w}\sqrt{\frac{\mathrm{e}N_a\varepsilon_p}{2\varepsilon_n\left(V_{bi}-V_B\right)}}\,. \tag{11}$$

The values of V_{bi} and N_a can hence be found experimentally by measuring $(\mathrm{C/A})^{-2}$ as a function of V_B: the gradient of this relation is N_a and the V axis intercept is V_{bi}. [62]

2.2.6. Current-voltage characteristics

Because of the directionally preferential charge transport across p-n junctions, they behave as diodes. Their current-voltage behaviour is described by

$$I = I_0\left(\frac{eV_B}{Ak_BT} - 1\right), \tag{12}$$

where I is the current, I_0 is the saturation current, e is the magnitude of the charge on an electron, V_B is the applied bias voltage, k_B is the Boltzmann constant, T is the temperature, and A is the 'diode ideality factor', a constant for each device, which is 1 for an ideal junction (one in which transport is not limited by recombination) and between 1 and 2 for real junctions. Under illumination, the photovoltaic effect generates a photocurrent, I_L, which acts in the opposite direction within the junction to the current generated by a forward bias voltage, so Equation (12) becomes [63-65]

$$I = I_0\left(\frac{eV_B}{Ak_BT} - 1\right) - I_L \,. \tag{13}$$

This current-voltage behaviour for an ideal junction is shown graphically in Figure 18, both under illumination and in the dark. This illustrates several parameters that can be used to define photovoltaic device performance, in addition to the power conversion efficiency: the short-circuit current, the open-circuit voltage, and the fill factor.

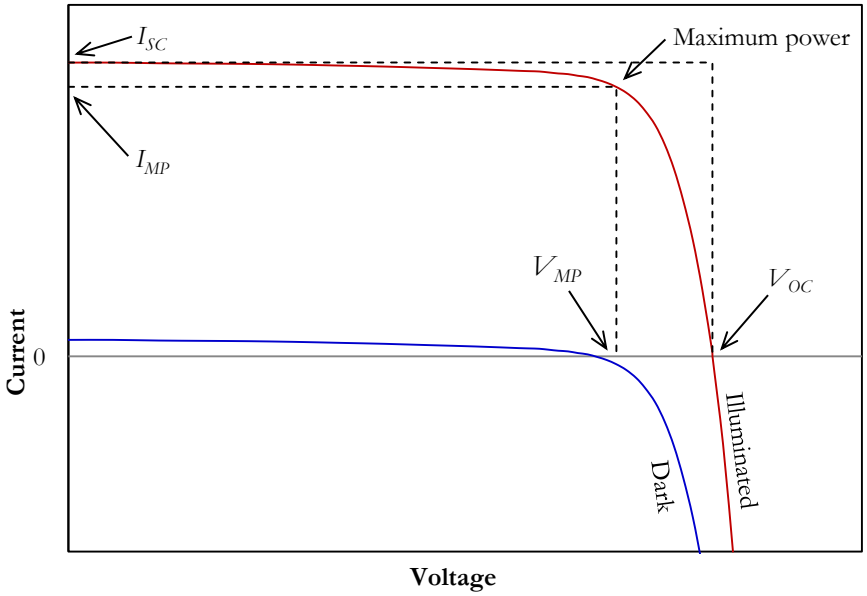

Figure 18: The current-voltage behaviour of a p-n junction under illumination and in the dark. Marked points show the short-circuit current (I_{SC}), maximum-power current (I_{MP}), open-circuit voltage (V_{OC}), and maximum-power voltage (V_{MP}). The fill factor is the area of the smaller dashed rectangle as a fraction of the larger, i.e. the maximum power as a fraction of $I_{SC} \times V_{OC}$.

The short circuit current, I_{SC}, is given by the intercept with the I axis of the curve for the junction under illumination; i.e. the current when $V = 0$, a short circuit.

The open-circuit voltage, V_{OC}, is given by the intercept with the V axis of the curve for the junction under illumination; i.e. the voltage when $I = 0$, an open circuit. This is theoretically equal to the built in potential, but in real devices various shunt and series resistances limit it to $V_{OC} \sim 0.7 V_{bi}$. [63-65]

The fill factor, FF, is the largest-area rectangle possible under the curve, as a fraction of $I_{SC} \times V_{OC}$. It represents how much of the power theoretically possible from the device can actually be produced.

2.3. Device structure

Photovoltaic solar cells are primarily minority-carrier devices: their behaviour is defined by the ability of minority carriers (usually electrons in the p-type absorber layer) to cross the p-n junction to become majority carriers in the opposite semiconductor and be extracted. The minority carrier diffusion length is the distance a minority carrier is likely to travel in the material before it recombines with a majority carrier, given by

$$L = \sqrt{D\tau} \ , \tag{14}$$

where D is the diffusivity and τ is the minority carrier lifetime. This is determined by the concentration of majority carriers and the rate of recombination. [63-65]

Only electrons and holes generated within, on average, the diffusion length of the material from the junction contribute to the net current. Minority carriers generated further from the junction are likely to combine with a majority carrier before reaching the oppositely doped material, and so the energy of both will be lost. Once a minority carrier crosses the junction and becomes a majority carrier, it is much more likely to avoid recombination, and so can be extracted. Because of this, the two sides of junctions used for solar cells should be no thicker than the diffusion lengths of the respective materials, and the easiest way to achieve this with a significant surface area is for the whole cell to be a layered junction, with the top contact obscuring as little of the surface as possible. The cell must, however, be thick enough that most of the incident light is absorbed, which means that it must have a very high absorption coefficient.

In many materials currently used for solar cells, the diffusion length is only a few microns. Devices on this scale would clearly not be robust enough for practical use, so a substrate (sometimes a superstrate) is used to add stability and for ease of fabrication. This is generally a layer of glass coated in a metal such as molybdenum for an electric contact, on which the layers of p-type and n-type semiconductors are deposited to form the junction, followed by a grid of thin metal wires drawn on the surface to collect the charge carriers. Such a basic structure is depicted in Figure 19. Actual cells tend to have several more layers and other features with specific functions to increase the photovoltaic performance of the device (see Section 3.8).

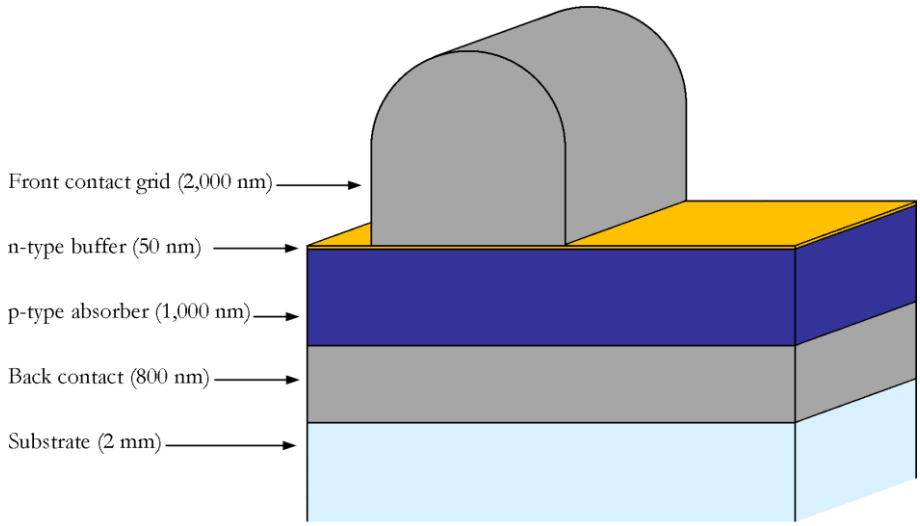

Figure 19: The basic design of a photovoltaic cell structure.

The less heavily doped semiconductor layer is much thicker than the more heavily doped one, and is known as the absorber or base layer, as it is designed (by choice of band gap, absorption coefficient, and thickness) to be where most absorption occurs. The more heavily doped layer is known as the buffer or emitter layer, and is chosen to have a larger band gap than the absorber layer so that it transmits as much light as possible to be absorbed there. As the absorber layer is the thickest in the device and its material properties have the largest effect on performance, devices are usually referred to simply by the material used for the absorber layer. [63-65]

Solar cells typically produce a low voltage of around 1 V, so individual cells are connected in series to add their voltages together, usually up to around either 12 V or 24 V. One or more of these strings of connected cells are sealed to protect them from the environment, and wired as a single unit ready for installation, which is called a module or panel. Several

of these modules are often mounted together on a single rack as an array, usually in parallel but for very large arrays sometimes partly in series. This assembly is illustrated in Figure 20. [63-65]

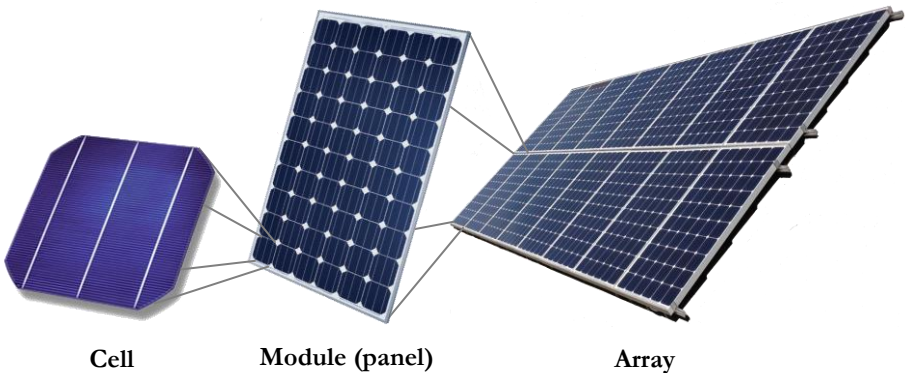

Figure 20: The place of a photovoltaic solar cell in a module or panel, and in an installation of several modules on a single rack as an array. The thick vertical metal bars on the front surface of the cell are called busbars, and collect the current from the many much thinner horizontal wires on the surface. The busbars of one cell are then connected to the back contact of the next cell in the module, creating a string of cells in series. The modules in an array are usually connected in parallel. Image credits: SolarWorld.

Because photovoltaic solar cells produce a direct current (DC), but distribution networks and most appliances use an alternating current (AC), an inverter is required to transform the DC electricity to AC, with a frequency of 50 Hz or 60 Hz depending on region. Invertors for grid-connected systems also increase the voltage of the solar electricity to match that of the distribution grid; 230 V and 120 V are the most common values. The electricity from a whole solar array is usually passed through a single invertor, but micro-invertors are becoming more popular. These are small invertors attached to individual panels, giving the benefit of better output optimisation. [63-65]

2.4. Efficiency

Low conversion efficiency is one of the ubiquitous problems of solar photovoltaics. Most current research in the field is aimed at increasing it. However, even in ideal devices there are unavoidable, fundamental sources of loss.

The efficiency of solar cells is officially tested under standard Air Mass (AM) spectra: that of the Sun's radiation (similar to that of a black body at 5,800 K) after passing through the Earth's atmosphere, where absorption of particular wavelengths occurs. AM1.5G (depicted in Figure 21) is the most common, corresponding to 1 $kW \cdot m^{-2}$ of light incident at 48 ° to the surface normal, which passes through approximately 1.5 times the atmosphere that a direct beam (AM1.0) would. The G stands for Global, and means that the spectrum includes emitted and scattered light from the surrounding area (assumed to be a light, sandy soil). The spectrum outside the Earth's atmosphere is referred to as AM0. [63-65]

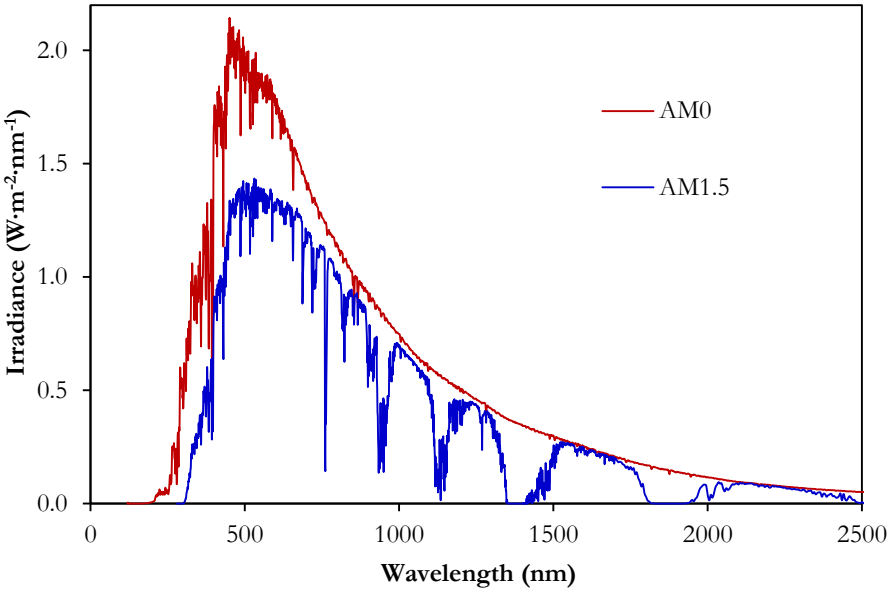

Figure 21: The solar spectrum outside Earth's atmosphere (AM0) and at the surface of the Earth, having travelled through the atmosphere at 48 ° and undergone the resulting absorption (AM1.5). Data from [66,67].

2.4.1. The Shockley-Queisser limit

The fundamental thermodynamic limit on the efficiency of solar cells, known as the Shockley-Queisser limit, is due to several factors. Considering the device as a Carnot engine, at 300 K with the Sun at 5,800 K, gives a starting, truly fundamental efficiency of around 95 %. Angular entropy, or Boltzmann loss, reduces this by around 9 % due to the fact that the cell emits in all directions but only receives sunlight in one. Spontaneous recombination in pure semiconductor material gives a further loss of around 1 %. The band gap of the absorber material gives the largest limitation: photons with energy less than the band gap cannot excite valence electrons, so are not absorbed, giving a loss of around

25 %; and free electrons and holes created by photons with more energy than the band gap value quickly thermalise, i.e. decay to the band edges by emitting phonons, so their excess energy is also lost, contributing a loss of around 30 %. Figure 22 shows the relative contribution of these sources to the fundamental losses as a function of band gap. [68-70]

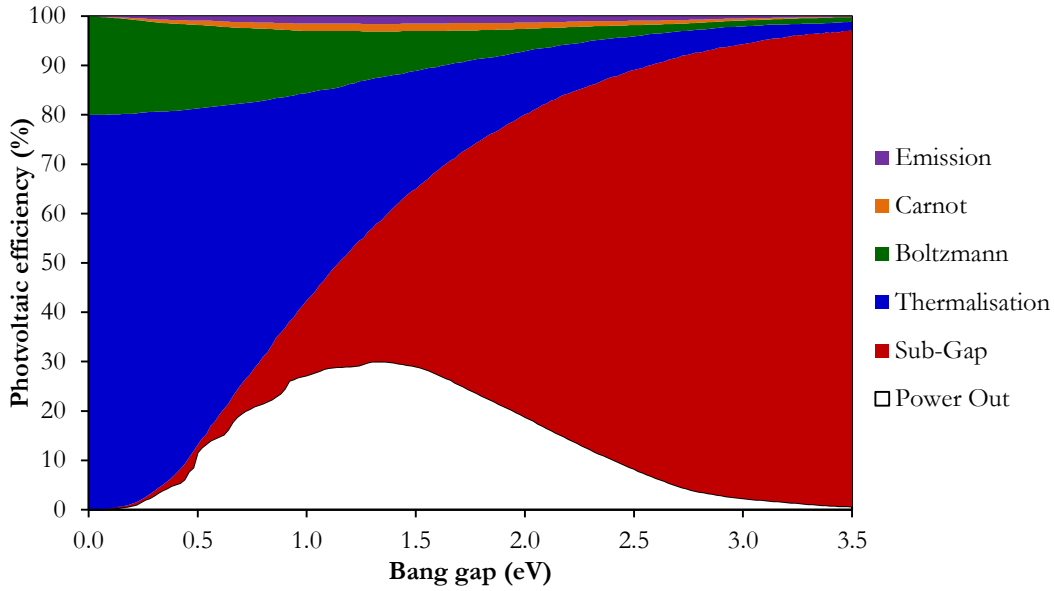

Figure 22: The Shockley-Queisser limit as a function of band gap with the sources of fundamental loss as a function of band gap. Data from [69,70].

Together, these fundamental losses give the Shockley-Queisser limit of up to 33.4 % for a single-layered cell under standard AM1.5G conditions. This limit varies with band gap (see Figure 22), and so is different for every material. The optimal band gap for terrestrial operation is around 1.3 eV (Shockley and Queisser initially concluded it was 1.1 eV, but different assumptions, e.g. on the exact temperature of the Sun, are used now). [63-65]

Specifically for CZTS (taking E_g = 1.48 eV), a detailed balance calculation to find the Shockley-Queisser limit gives 32.4 %, with the optimum device parameters being J_{SC} = 29.6 mA·cm^{-2}, V_{OC} = 1.21 V, and FF = 89.9 %. [71]

It is possible to use technical design features to overcome some of the Shockley-Queisser limitations. For example, light trapping techniques use anti-reflection coatings or refraction and internal reflection to increase the internal path length of light to give greater absorption. [72] Multi-junction tandem cell designs are another particularly successful example, in which cells of two or more different absorber materials are combined to use

more band-gap values, so more energy can be extracted from the incident spectrum. [73] Hot-carrier cells (in which electrons and holes are extracted before they thermalise to the band edges), multiple exciton generation, singlet fission, and thermal up-conversion of low-energy photons have also been investigated. [74-83] However, while these are all active areas of current research, the Shockley-Queisser limit remains fundamentally the best possible photovoltaic efficiency for a standard single-junction cell.

The principle of using the photovoltaic effect and a p-n junction to convert power from solar radiation to electricity is relatively straightforward, but, as should be expected, it is notoriously difficult to approach the limit of theoretically possible efficiency in practice. Materials never initially come close to the ideal Shockley-Queisser limit due to practical phenomena such as recombination and resistance within the cell.

2.4.2. Recombination

If a free electron and a hole combine before they are extracted, the energy of the electron, which could otherwise be extracted as useable electricity, is lost as it decays from the conduction band to the valence band, which lowers the photovoltaic efficiency of the solar cell. There are many possible recombination channels for a free electron and a hole. These are illustrated in Figure 23.

Simple radiative band-to-band recombination (sometimes referred to as free-to-bound, because the free conduction-band electron becomes bound to a specific atom in the valence band) is unavoidable, but not as harmful as other channels because a photon of the band-gap energy is emitted, which can be reabsorbed, meaning the energy is not necessarily lost. [63-65]

However, if a defect with energy level in the band gap is involved in the recombination, the energy is lost because two or more photons are emitted, as the electron and hole are trapped at the defect(s) separately. Each of the photons has less energy than the band gap and so cannot be reabsorbed. This is known as Shockley-Read-Hall recombination or trap recombination, and is usually the dominant recombination type in real devices. Similarly, recombination involving excitons or tail states from fluctuations in potential (see Section 3.7.7) will only result in photons of insufficient energy to be reabsorbed. [63-65]

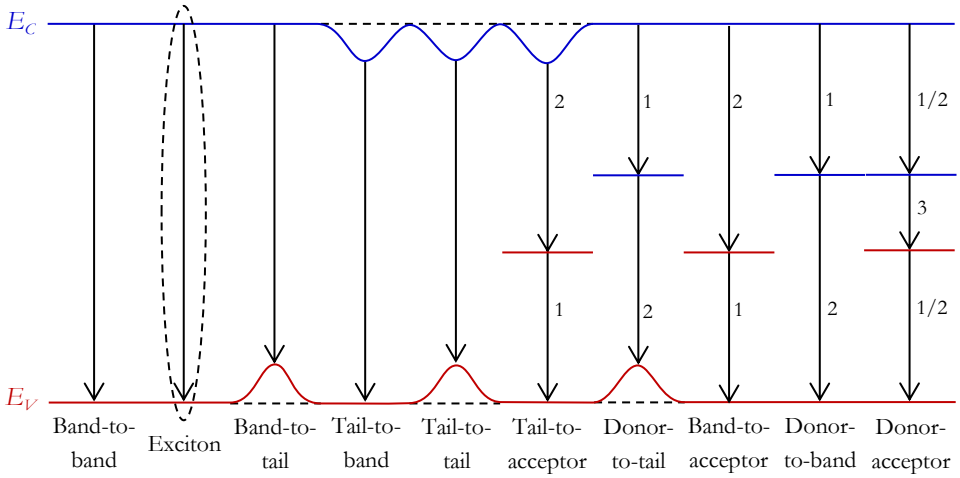

Figure 23: Possible recombination channels. The arrows mark the movement of an electron; the equivalent movement of a hole is in the opposite direction for each step. Each recombination can either occur radiatively (by the emission of a photon) or non-radiatively (by the transfer of energy to another charge carrier, which then rethermalises, losing the energy as phonons; this is known as Auger recombination). [63-65]

Additionally, recombination through any channel, even band-to-band, can occur non-radiatively, meaning the energy cannot be reabsorbed and so is lost. This involves the energy difference being given to another conduction-band electron or valence-band hole, which then thermalises to the band edge again and so the energy is lost as phonons. This is known as Auger recombination. [63-65]

2.4.3. Resistance losses

Series resistance, R_S, is often found at interfaces between the various layers of the cell and at the metal contacts due to the formation of non-Ohmic junctions. It reduces the fill factor, and so the efficiency, of devices by causing additional voltage drop, which decreases the gradient of the forward-bias current-voltage curve. It is typically in the range 0.5 to 10 $\Omega \cdot cm^2$. [84]

Finite shunt resistance, R_{Sh}, is found at grain boundaries in polycrystalline materials and other potential leakage paths. In an ideal cell it would be infinite to prevent alternate paths for current to flow, but in real devices it often is not, which also decreases the fill factor. It is typically in the range 1 to 2 $k\Omega \cdot cm^2$. [84]

A solar cell including these parasitic resistances can be modelled by the equivalent circuit shown in Figure 24. The effects of series and shunt resistances on the current-voltage behaviour of a photovoltaic cell are depicted in Figure 25.

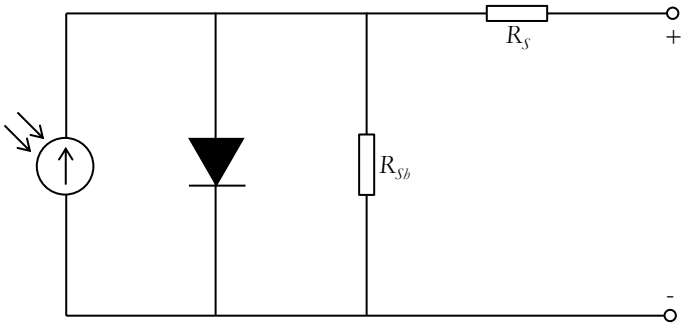

Figure 24: The equivalent circuit to a solar cell.

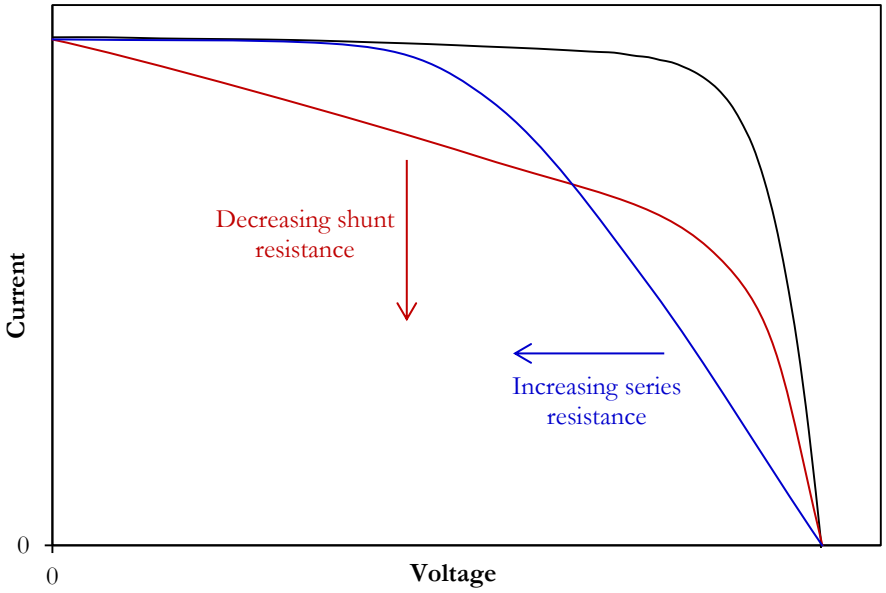

Figure 25: The effect of non-infinite shunt resistance and non-zero series resistance on the current-voltage behaviour of a photovoltaic solar cell.

2.5. Materials

Many materials have been successfully used as the absorber layer in a solar cell, and several of these are available in commercial modules. [85] The record photovoltaic efficiencies achieved by some of the most successful materials are listed in Table 3.

Material	Best efficiency	Year	Reference
GaAs	28.8 %	2012	[86]
Monocrystalline silicon	26.7 %	2017	[87]
InP	24.2 %	2012	[88]
CIGS ($Cu_2In_xGa_{1-x}Se_2$)	22.6 %	2016	[89]
CdTe	22.1 %	2015	[88]
Perovskite	22.7 % (unstable)	2017	[88]
Multicrystalline silicon	22.3 %	2017	[90]
GaInP	21.4 %	2016	[88]
Dye-Sensitised	13.0 %	2014	[91]
CZTSSe ($Cu_2ZnSn(S_{1-x}Se_x)_4$)	12.6 %	2013	[92]
Organic	12.1 %	2017	[88]
CZCTS ($Cu_2Zn_{1-x}Cd_xSnS_4$)	11.5 %	2017	[93]
CZTS (Cu_2ZnSnS_4)	11.0 %	2017	[88]
Quantum dots	10.6 %	2016	[94]
Amorphous silicon	10.2 %	2013	[95]
CZTGSSe ($Cu_2ZnSn_{1-y}Ge_y(S_{1-x}Se_x)_4$)	9.4 %	2015	[96]
CTS (Cu_2SnS_3)	4.6 %	2015	[97]

Table 3: The best solar cell and submodule efficiencies achieved by various materials. See the regularly updated solar cell efficiency tables by Green et al. [88]

When materials are first developed as solar cells, they typically have efficiencies of below 10 %, often much less, but those that have been investigated for the longest are now well over 25 %, not far from the Shockley-Queisser limit. Green et al. publish regularly updated solar cell efficiency tables, [88] and the USA National Renewable Energy Laboratory (NREL) maintains a chart of the advances over time in photovoltaic efficiency of various solar cell technologies, including their current records (given in Figure 26, with single-junction information summarised in Figure 27). The two sometimes differ on record efficiencies because of different standards, definitions, and requirements for inclusion.

Silicon is the most common material for commercially available solar panels, supplying 95 % of the market in 2016. [5] It is used in single-crystal, polycrystalline, and amorphous form, with single crystals giving the highest efficiencies but costing the most, amorphous layers being the cheapest but with the lowest efficiencies, and polycrystalline layers falling in between the two. Polycrystalline silicon supplied 70 % of the global solar power market in 2016, monocrystalline 24 %, and amorphous 1 %. [5]

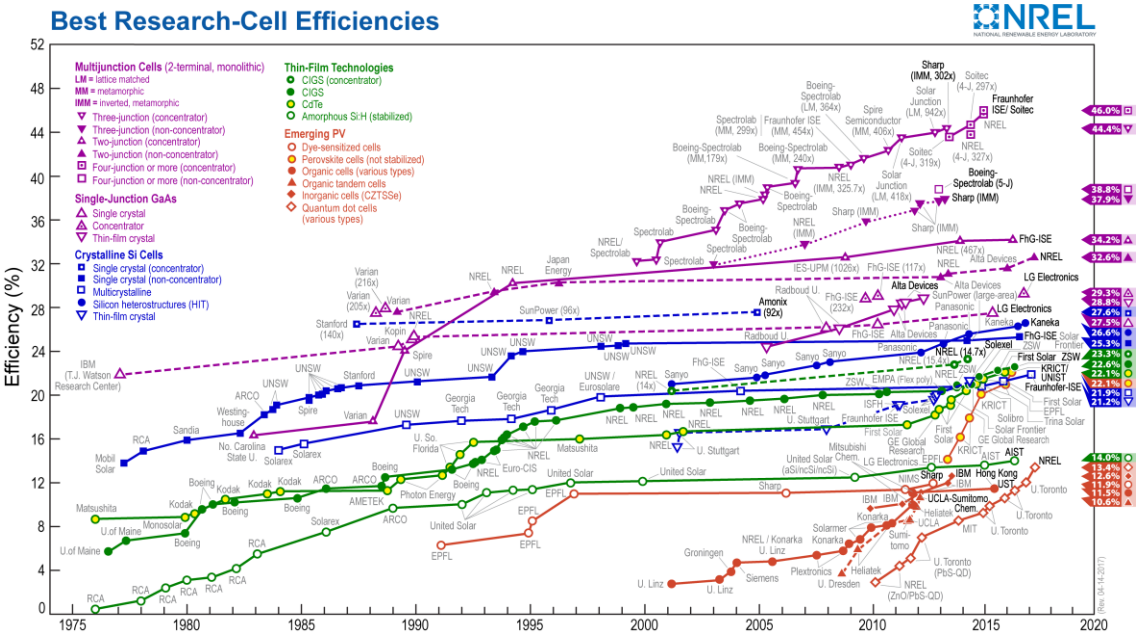

Figure 26: A chart of the advances in photovoltaic efficiency of various solar-cell technologies maintained by the USA National Renewable Energy Laboratory. [98]

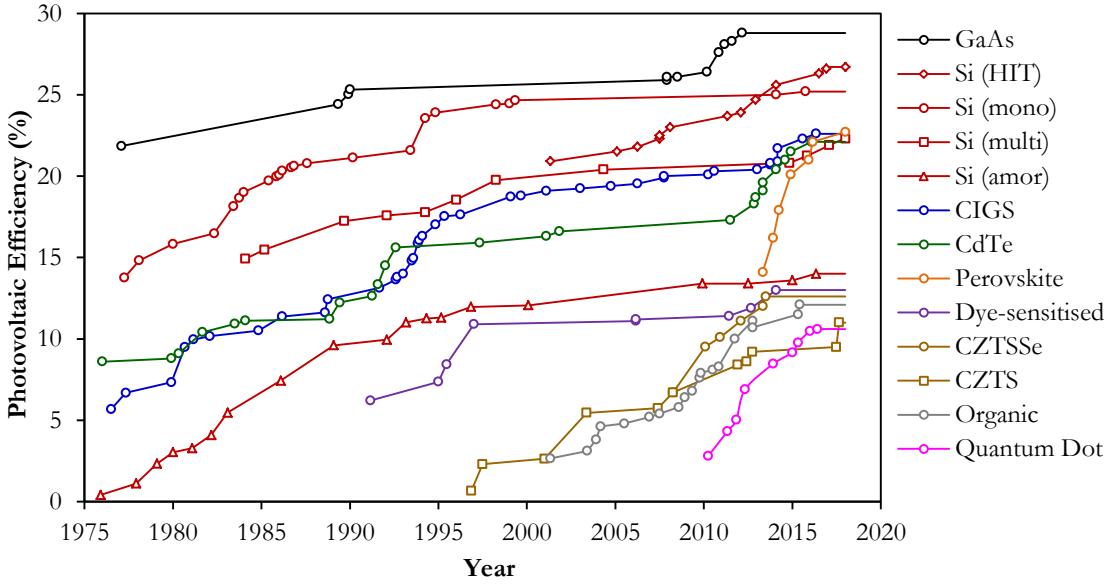

Figure 27: A clearer depiction of solely the single-junction technologies from Figure 26 including more detailed data for CZTS from Figure 30.

'Thin-film' materials (which include GaAs, InP, CdTe, CIGS, GaInP, and CZTS) make up most of the rest of commercial production (CdTe 4 % and CIGS 1 % [5]), and are the fastest-growing sector of the photovoltaic industry as well as currently being the focus of much academic research. These are direct-gap compound semiconductors, meaning that unlike silicon, an indirect-gap semiconductor, the absorption or emission of a phonon is

not required to accompany the absorption of a photon. This gives these materials a much higher absorption coefficient (>10^4 cm^{-1} [37]), meaning solar cells can be much thinner than conventional silicon ones (the order of a few microns [37]) while still making use of most incident radiation, so devices can be much less material-intensive. Thin-film materials are also much more tolerant to defects and grain boundaries than crystalline silicon, so there is less restriction on useable crystal quality, and because they are compounds, they can be grown in many different ways. [99]

Other photovoltaic technologies currently being researched and developed include organic semiconductors, [88] perovskites (which are hybrid organic-inorganic materials), [100] dye-sensitised solar cells, [91] and low-dimensional materials: both two-dimensional [101] and one-dimensional (i.e. quantum dot solar cells). [94]

2.5.1. Problems

Even when a photovoltaic technology has demonstrated a usefully high efficiency in the laboratory, the practical challenges of reproducing this on an industrial scale can be just as preventative to large-scale adoption as any other barrier.

Many materials presently used in commercial solar cells, and many that are still emerging, are too expensive to produce economically competitive electricity. This can be because the raw materials are expensive, which is particularly true for gallium, indium, selenium, and tellurium, or because the processing costs involved are very high, which is particularly true for silicon. [102,103] While silicon itself is relatively cheap, much more of it is required for a solar cell than is of thin-film materials (around 400 μm, compared to around 1 μm), because silicon has an indirect band gap and so relatively low absorption. It additionally requires extended high-temperature processing to achieve the required crystalline purity. The material costs of some elements used in leading solar cell absorber materials are compared in Figure 28.

Several elements used in solar-cell absorber materials are simply not abundant enough on Earth to make sufficient solar cells to provide the order of 10 TW of power required to make a significant contribution to global demand, particularly as they are in high demand for use in other technologies. [102-104] For example, the scarcity of tellurium is expected

to limit production of CdTe solar cells to around 20 GW of output capacity per year by 2020 and CIGS will be similarly constrained by indium and selenium to 70 GW per year. [105] The global abundances of some elements used in leading solar cell absorber materials are compared in Figure 28.

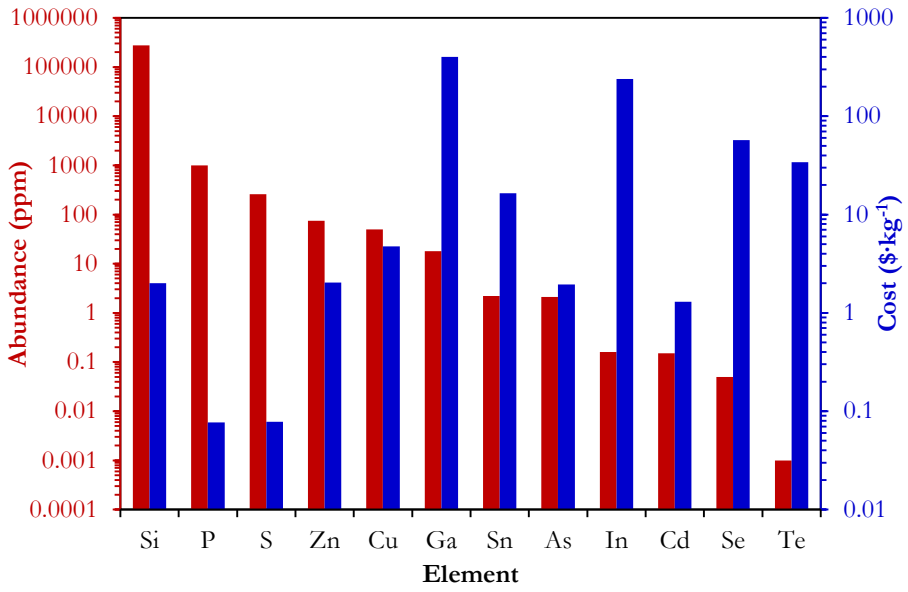

Figure 28: Natural abundance in the Earth's crust and 2016 prices of some elements used in leading solar cell absorber materials. Note the logarithmic scales. Data from [106,107].

In addition, the high toxicity of some materials, particularly cadmium and selenium, is a problem. [108] It is worth noting here that the hydrazine sometimes used in the fabrication of CZTS by solution methods, and the H_2S often used in its sulphurisation stage (see Section 4.3.5), are both toxic. This is less important than material toxicity, however, as processing toxicity can easily be contained and neutralised within the controlled environment of fabrication factories; it is only the possibility of leakage from the modules during operation in situ, due to accident, breakage, or simply seepage over time, that poses danger to the environment or people.

Stability is an issue for many new photovoltaic technologies, such as organic and perovskite cells. Although many of these exhibit high record efficiencies, the devices often degrade significantly over several hours or days, and so are currently unsuitable for industrial use. [100]

CZTS does not suffer from any of these drawbacks; its constituent elements have high abundances and low costs, and toxicity is not an issue. This makes it an ideal candidate for use as the absorber layer in solar cells.

Chapter 3:
Cu_2ZnSnS_4 (CZTS)

3.1. Introduction

Cu_2ZnSnS_4 (CZTS) is a thin-film photovoltaic absorber-layer material with a direct band gap well matched to the solar spectrum (1.5 eV) and high absorption coefficient ($>10^4$ cm^{-1}). It is of particular interest because all its component elements are cheap, abundant, and non-toxic (see Figure 28), and it is relatively cheap and straightforward to manufacture.

CZTS is a covalent semiconductor, but its atoms display significant ionic behaviour, having elemental charges of Cu^+, Zn^{2+}, Sn^{4+}, and S^{2-}. Several related materials have been used to make solar cells: binary II-VI materials such as CdTe and ZnS, and ternary materials of the form A(I)-B(III)-$X(VI)_2$ where, for example, A = Cu or Ag; B = Al, Ga, In, or Tl; and X = S or Se. These are often referred to collectively as chalcogenides, because they contain a chalcogen, i.e. a Group 16 element (S, Se, or Te), as their anions. CZTS is derived from this ternary structure by replacing the trivalent cation (B) alternately with a cation of lower and of higher valence. Its structure is often considered as based on that of CIGS ($CuIn_xGa_{1-x}Se_2$), with the expensive and relatively rare indium and gallium (both valency III) replaced with the much cheaper and more abundant zinc and tin (II and IV), and selenium replaced with sulphur for a band gap closer to the optimum. [109] This relationship between materials is shown graphically in Figure 29.

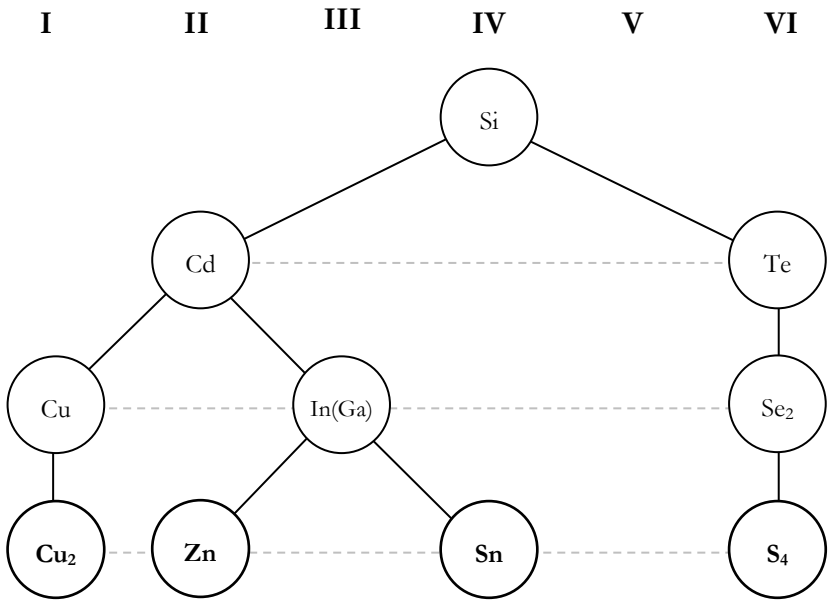

Figure 29: The quaternary structure of CZTS in relation to similar elemental, binary, and ternary/quasi-ternary materials (Si, CdTe, and CIS/CIGS) used in photovoltaic solar cells.

The maximum power conversion efficiency achieved with CZTS is 11.0 %. [88] The main issue currently limiting its performance is low open-circuit voltage (784 mV is the highest reported, [110] i.e. a deficit of around 716 mV with respect to the band gap of 1.5 eV). The two largest contributing factors to this deficit have been found to be hetero-interface recombination (see Section 3.8.5) and band-gap fluctuations in the bulk material (see Section 3.7.7), which contribute around 235 mV and 200 mV respectively. [111] The presence of secondary phases in CZTS is another major issue (see Section 3.7.1), so there are currently three key areas for further research in order to improve the performance of CZTS: interface optimisation, defect characterisation, and phase stability. [112]

Several review articles, [112-127] doctoral theses, [128-145] and books [146-148] have been published in recent years on the progress and remaining challenges of CZTS.

3.2. History

CZTS occurs naturally with significant iron content as the mineral kesterite ($Cu_2Zn_{1-x}Fe_xSnS_4$). [149] Pure CZTS was first fabricated in 1967, by Nitsche et al., [150] by chemical vapour deposition. The photovoltaic effect was first observed in it by Ito &

Nakazawa, [151] in 1988, using a heterodiode including a CZTS thin film fabricated by atom-beam sputtering on a stainless steel substrate. It was first reported in a solar cell in 1996 by Katagiri et al., [152] who set the first record photovoltaic efficiency at 0.66 %. Its subsequent improvements in efficiency are plotted in Figure 30. The early progress of CZTS solar cells is reviewed by Katagiri et al. [153]

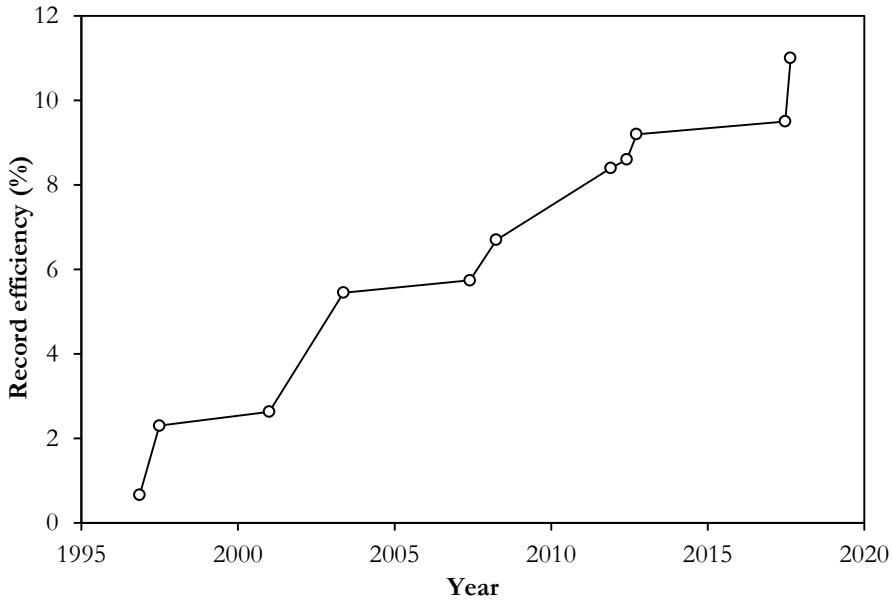

Figure 30: The historical improvement of the record photvltaic efficiency for CZTS solar cells. [88,152-162]

3.3. Variations

CZTS is often doped or compounded with other elements to give more complex I_2-II-IV-VI_4 compounds. Adachi [147] provides a more detailed discussion of these variations and their properties.

Selenium is often incorporated into CZTS to form $Cu_2ZnSn(S_{1-x}Se_x)_4$, known as CZTSSe, or simply CZTSe for $x = 1$. This has given a record photovoltaic power conversion efficiency of 12.6 %. [92] CZTSSe allows the band gap to be tuned using the S:Se ratio and exhibits shallower defect energy levels than pure CZTS, [163-165] but has the disadvantage that selenium is rarer and more expensive than sulphur and is toxic. [166]

$Cu_2ZnSn_{1-y}Ge_y(S_{1-x}Se_x)_4$, or CZTGSSe, has been used successfully, achieving a maximum efficiency of 9.4 % with $y = 0.3$. [96] However, the process of incorporating germanium

often involves hydrazine, [167] which is explosive, hepatotoxic, and carcinogenic. [168,169] Additionally, germanium is lost during processing as easily as tin, which is a significant problem during the fabrication of CZTS (see Section 4.3.2), so the same problems with defects are present. [96]

$Cu_2Zn_{1-x}Cd_xSnS_4$, or CZCTS, has achieved a maximum efficiency of 11.5 %. [93] The substitution of cadmium for some zinc allows the band gap to be tuned between 1.55 and 1.09 eV, reduces the formation of ZnS as a secondary phase, reduces Cu-Zn disorder (see Sections 3.5 and 3.7.3), and increases the grain size. For $x > 0.3$, the material adopts the stannite rather than the kesterite crystal structure (see Section 3.5). [93,170-174]

$Cu_2Zn_{1-x}Fe_xSnS_4$, or CZITS, is the naturally occurring mineral form of CZTS, but of no use to photovoltaic applications. [149]

$(Cu_{1-x}Ag_x)_2ZnSnS_4$, or CSZTS, has been found to exhibit less disorder than pure CZTS. Substituting silver for some copper reduces disorder because the formation energy of Ag_{Zn} antisite defects is much larger than that of Cu_{Zn} defects. This gives an increase in open-circuit voltage of 50 mV, and an increase in efficiency of 2 % absolute. [173]

$(Cu_{1-x}Li_x)_2ZnSnS_4$, or CLZTS, has also been found to have much lower Cu-Zn disorder than CZTS. [175]

The simpler form Cu_2SnS_3, or CTS, has also been used successfully, giving a maximum efficiency of 4.6 %. [97,176]

Only the pure form of CZTS is studied in this thesis.

3.4. Material properties

CZTS has a band gap that is predicted theoretically as 1.56 eV for the kesterite crystal structure and 1.42 eV for the stannite (see Section 3.5), [177] both close to the optimum value for solar cell applications. [63-65] However, practically it ranges from 1.36 eV [178] to 1.78 eV, [179] increasing with decreasing Cu/(Zn+Sn) ratio, [180] although the tin content has a much more significant effect than that of zinc. [181] The band gap is also

dependent on temperature: it decreases with increasing temperature due to increasing phonon population giving more carrier-phonon interaction. [182]

The band structure of CZTS has been modelled using density functional theory by several groups and is illustrated in Figure 31. The valence band is formed from a hybridised antibonding linear combination of S-3*p* and Cu-3*d* states (copper has a higher *d* orbital energy than zinc and tin), and the conduction band is formed from hybridised S-3*p* and Sn-5*s* states (tin has a lower *s* orbital energy than the other cations). [177,183-189]

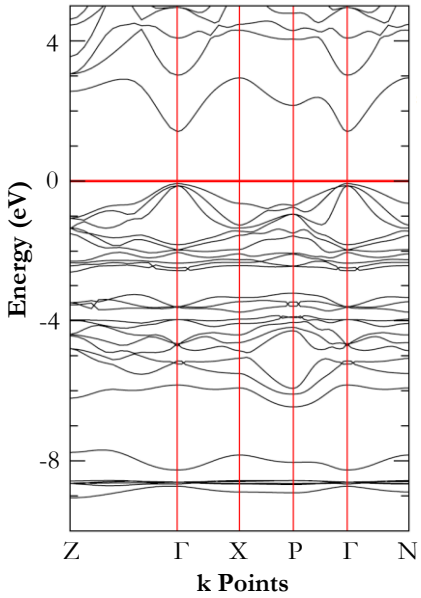

Figure 31: The band structure of CZTS as calculated using density functional theory. From [184].

CZTS has an absorption coefficient >10^4 cm^{-1}, [151] and it is inherently p-type due to the presence of Cu_{Zn} antisite defects, [190] making it ideal for the absorber layer of a solar cell. Reported values of the inherent acceptor density vary over several orders of magnitude, from 3.2 ×10^{15} cm^{-3} [191] to 1 ×10^{20} cm^{-3}, [192] and it has been found to increase linearly with increasing Cu:Zn ratio. [193] It has been calculated that a linear carrier concentration gradient across the CZTS layer improves performance; it gives enhanced carrier separation by extending the distribution of the built-in electric field to the back contact. The optimal gradient has been calculated to be from 6.7 ×10^{17} cm^{-3} at the CZTS-buffer interface to 1 ×10^{20} cm^{-3} at the back contact. [194] Other relevant material parameters are summarised in Table 4.

Quantity	Value	Reference
Lattice parameter a	5.430 Å	[147]
Lattice parameter c	10.845 Å	[147]
Density, ρ	4.61 g·cm^{-3}	[195]
Band gap, E_g	1.36 - 1.78 eV	[178] - [179]
Absorption coefficient, a	>10^4 cm^{-1}	[151]
Carrier concentration (room temperature), p	3.2 ×10^{15} - 1 ×10^{20} cm^{-3}	[191] - [192]
Minority carrier diffusion length, L	170 - 519 nm	[196] - [197]
Minority carrier lifetime, τ	1.7 ns	[198]
Minority carrier mobility, μ	0.09 - 57.6 cm^2·V^{-1}·s^{-1}	[199] - [191]
Refractive index, n	2.07	[156]
Dielectric constant, ε	7 ε_0	[111]
Electrical conductivity, σ	4.6 S·cm^{-1}	[200]
Thermal conductivity, κ	4.0 W·m^{-1}·K^{-1}	[201]
Specific heat capacity, C_p	23 J·mol^{-1}·K^{-1}	[147]
Melting temperature, T_M	1259 K	[147]
Bulk modulus, K	78.4 GPa	[202]
Young's modulus, Y	55-58 GPa	[147]
Shear modulus, G	30.63 - 33.18 GPa	[203]
Speed of sound, v_s	3573 m·s^{-1} (kesterite)	[202]
Debye temperature, θ_D	302 - 394 K	[204] - [202]

Table 4: Various material parameters of CZTS.

3.5. Crystal structure

Under usual photovoltaic device operating conditions, CZTS has been calculated to be most stable in the kesterite $I\bar{4}$ crystal structure (space group no. 82), with enthalpy of formation -361.9 kJ·mol^{-1}. [205] However, the stannite $I\bar{4}2m$ structure (no. 121) is almost as stable, with enthalpy of formation -359.9 kJ·mol^{-1}, [205] which is only 1.3 [177] to 2.9 [183] meV per atom more than the kesterite. The eskebornite $P\bar{4}2c$ structure (no. 112) has been reported to be the next-most stable, with enthalpy of formation only 1.7 meV per atom more than the kesterite structure, [206] although it has rarely been considered. The primitive mixed CuAu-like (PMCA) $P\bar{4}2m$ structure (no. 111) then has enthalpy of formation 3.2 [183] to 7.8 [206] meV per atom more than the kesterite structure.

Despite reports sometimes claiming stannite as the most commonly adopted structure under standard conditions, [207,208] experiments have now conclusively confirmed that

this is kesterite, with various degrees of disorder. [209-217] At high-temperatures (>1050 K) CZTS changes to the sphalerite $F\bar{4}3m$ structure (no. 216, also called zinc blende). [218] Nanoparticles of CZTS, different to its bulk or thin-film form, adopt the wurtzite $P6_3mc$ structure (no. 186). [219]

All these crystal structures of CZTS are shown in Figure 32 and described in Table 5. Their mineral names come from the naturally occurring forms of $Cu_2Zn_{1-x}Fe_xSnS_4$ (kesterite), Cu_2FeSnS_4 (stannite), $CuFeSe_2$ (eskebornite), CuAu (PMCA), ZnS (sphalerite), and less commonly ZnS (wurtzite).

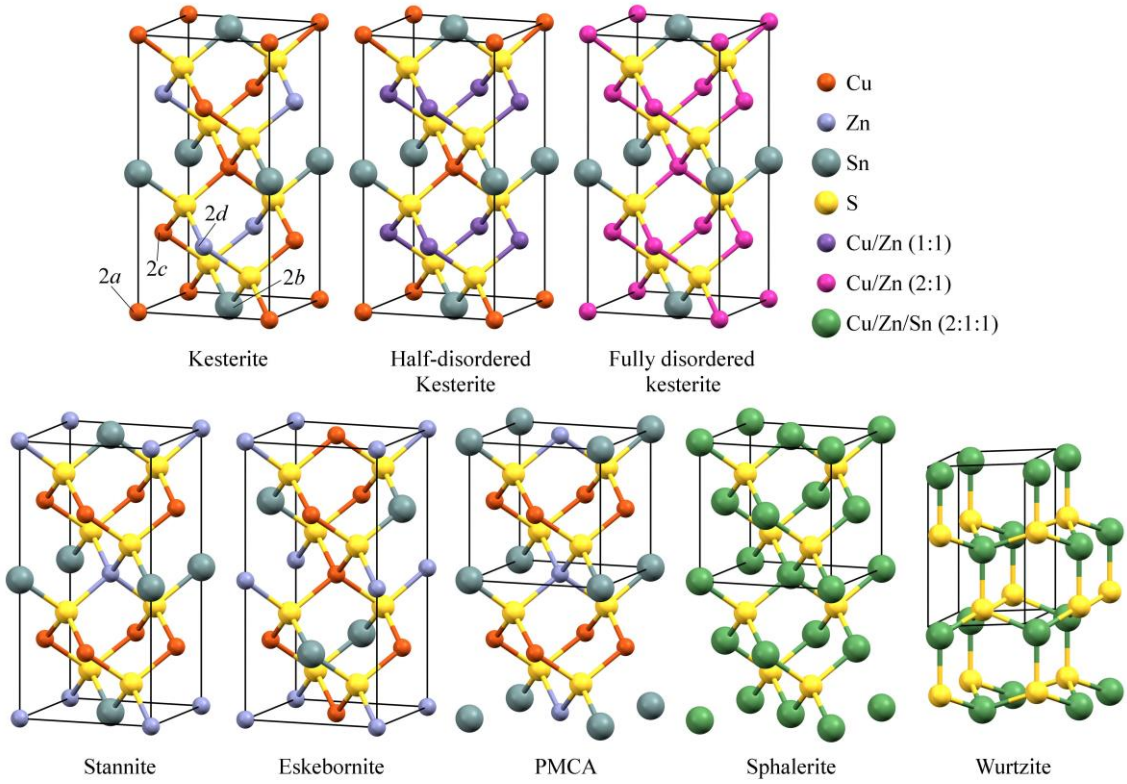

Figure 32: Crystal structures of CZTS. [206,218-220]

The band gaps of the stannite, eskebornite, and PMCA structures have been calculated as less than that of kesterite, at 1.30, 1.46, and 1.21 eV respectively, [184] making the kesterite structure the best for photovoltaic performance. However, despite kesterite being the most stable, it is possible for the structure within a sample to not be well defined, with grains of two or more structures present. [221-223] Such mixing of kesterite and stannite phases has given variations in the band gap of around 100 meV, which could contribute to limiting the open-circuit voltage in CZTS cells. [224] However, diffraction experiments have all found the structure to be exclusively kesterite with various degrees of disorder. [209-217]

Crystal structure	Space group	Wyckoff label	Atomic position	Elements
Kesterite	$I\bar{4}$ No. 82	2*a*	(0, 0, 0)	Cu
		2*b*	(0, 0, ½)	Sn
		2*c*	(0, ½, ¼)	Cu
		2*d*	(0, ½, ¾)	Zn
		8*g*	(x, y, z)	S
Stannite	$I\bar{4}2m$ No. 121	2*a*	(0, 0, 0)	Zn
		2*b*	(0, 0, ½)	Sn
		4*d*	(0, ½, ¼)	Cu
		8*i*	(x, x, z)	S
Eskebornite	$P\bar{4}2c$ No. 112	2*b*	(0, ½, ¾)	Sn
		2*d*	(0, ½, ¼)	Cu
		2*e*	(0, 0, 0)	Zn
		2*f*	(½, ½, 0)	Cu
		8*n*	(x, y, z)	S
PMCA	$P\bar{4}2m$ No. 111	1*a*	(0, 0, 0)	Sn
		1*d*	(½, ½, 0)	Zn
		2*f*	(0, ½, ½)	Cu
		4*n*	(x, x, z)	S
Sphalerite	$F\bar{4}3m$ No. 216	4*a*	(0, 0, 0)	Cu + Zn + Sn
		4*c*	(¼,¼,¼)	S
Wurtzite	$P6_3mc$ No. 186	2*a*	(⅓, ⅔, z)	Cu + Zn + Sn
		2*b*	(0, 0, z)	S

Table 5: Descriptions of the crystal structures that CZTS can be found in. [206,218-220]

Early descriptions of the disordered kesterite model had full copper occupancy remaining in the $z = 0$ plane of the kesterite structure (the 2*a* Wyckoff position), with the copper and zinc atoms randomly mixed only in the $z = ¼$ and ¾ planes (the 2*c* and 2*d* Wyckoff positions). [209] This is the 'half-disordered kesterite' $I\bar{4}2m$ structure (no. 121) depicted in Figure 32. However, disorder can also be present on the 2*a* site: the formation energies of a Cu_{Zn} defect at the 2*a* and 2*c* site were theoretically calculated to be different by less than 0.02 eV per atom, [190] and zinc has been found experimentally to substitute for copper on the 2*a* site as the Cu/(Zn+Sn) ratio decreases. [212] This means that a fully disordered kesterite model with complete random mixing of copper and zinc on the 2*a*, 2*c*, and 2*d* sites is more accurate than the half-disordered kesterite model. This is the 'fully disordered kesterite' $I\bar{4}2m$ structure (no. 121) depicted in Figure 32. Cation disorder is discussed in more detail in Sections 3.6, 3.7.3, and 3.7.4.

The preferred crystal orientation of surfaces is along (112)/($\bar{1}\bar{1}\bar{2}$), [225] with ($\bar{1}\bar{1}\bar{2}$) being much more stable than (112) in Cu-poor, Zn-rich conditions. [226]

3.6. Phase transitions

At room temperature the ordered kesterite crystal structure is the most energetically favourable form of CZTS. A second-order phase transition to a disordered kesterite structure has been observed at 533 ± 10 K using Raman spectroscopy [224] and 552 ± 2 K using neutron diffraction. [227] The associated expansion of the *c* lattice parameter has been observed in situ by synchrotron X-ray diffraction. [218] The same transition has been observed in CZTSe at 473 K. [228,229]

Historically, the half-disordered kesterite model was favoured over the fully disordered model (see Section 3.5), and so disorder in CZTS could be quantified by a simple order parameter, *S*, defined as

$$S = 2Cu_{2c} - 1 , \quad (15)$$

which ranges from 1 for full copper occupancy of the 2*c* site and assumed full zinc occupancy of the 2*d* site, to 0 for a full and equal occupancy by copper and zinc of both sites. [224] This is an incomplete description as it does not account for disorder on the 2*a* site, vacancies, or non-stoichiometric compositions, but is useful in considering order in relation to annealing and the order-disorder phase transition.

Figure 33 illustrates such ordering during annealing, showing that below the critical temperature of the order-disorder transition, a longer anneal time at a given temperature raises the order parameter closer to the equilibrium value.

The same general behaviour applies for the fully disordered kesterite model. The equilibrium state is the fully ordered structure significantly below the transition temperature, and the fully disordered structure above it. An order parameter is harder to define for three lattice sites though, as there are multiple possible states of equal intermediate disorder, especially if vacancies are also considered.

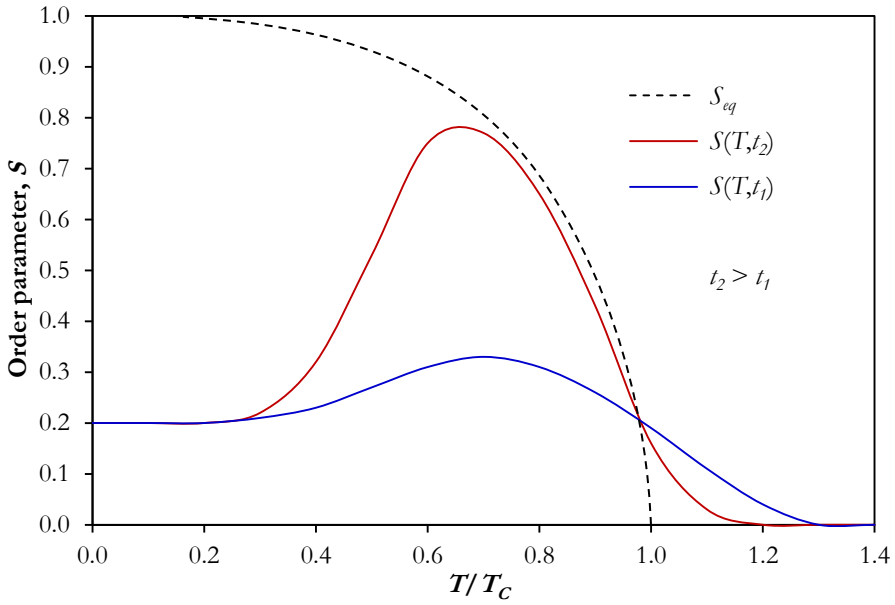

Figure 33: The degree of order, S, in a material with an order-disorder transition at critical temperature T_c. The dashed line indicates the equilibrium value (calculated using the Vineyard model [230]), which would be reached after an infinite time at the relevant temperature. The solid lines show the effect of annealing initially disordered samples for fixed time periods $t_2 > t_1$. [224]

Disorder is detrimental to photovoltaic performance, as it introduces defect levels in the band gap that act as carrier recombination centres (see Sections 3.7.3 and 2.4.2), decreases the band gap by up to 300 meV, and increases band gap fluctuation (see Section 3.7.7). [231,232] However, despite these effects, disordered CZTS has also been shown to produce better-performing photovoltaic devices than comparable ordered CZTS, with efficiencies of 8 % and 4 % respectively. [231]

As photovoltaic device synthesis usually involves an annealing stage at around 1070 K (see Section 4.3), the disordered structure is formed initially and only during a lengthy cooling process below the critical temperature can ordering of copper and zinc occur, often leaving a significant [Cu_{Zn}^{-} + Zn_{Cu}^{+}] defect complex presence (see Section 3.7.4).

The disorder of CZTS samples can thus be controlled using the cooling time below the transition temperature, approximately 550 K. This has been shown experimentally: 50 % antisite population at the 2*c* and 2*d* sites in water-quenched samples (i.e. 'complete' disorder in the half-disordered model, $S = 0$) was reduced to 30 % ($S = 0.4$) in samples with a controlled cooling rate. [210] This effect has been shown to have a direct effect on the open-circuit voltage, which was larger by an average of 40 ± 10 mV for samples that had

undergone slow cooling compared to standard cooling; however, this was concluded to be because the band gap itself had increased rather than because the open-circuit voltage deficit had decreased, and so the efficiency of the corresponding devices was no higher. [123]

It may take an impractically long cooling time to achieve a sufficient degree of order, however: it has been calculated that to reach $S = 0.7$ would take 4.5 days, and $S = 0.8$ would take 1 year. [233] Therefore alternative solutions are preferable, such as passivation of disorder by the introduction of $[V_{Cu}^{-} + Zn_{Cu}]$ defect pairs. [234] These have been shown to aggregate with $[Cu_{Zn}^{-} + Zn_{Cu}^{+}]$ defects, reducing the structural energy and magnitude of band-gap potential fluctuations, and therefore limiting the reduction in band gap. [235]

Additionally, as CZTS becomes more ordered, the dominant radiative recombination mechanism changes from band-to-tail to deep trap related recombination. The latter is more detrimental to photovoltaic performance, and so reduces the positive effect of ordering. [110]

A further, first-order, phase transition from the tetragonal disordered kesterite to the cubic sphalerite structure has been reported at 1149 K , with a two-phase region between 1139 and 1156 K in which both phases exist. [120,218] However, this is of little relevance to the use of CZTS as a photovoltaic absorber because fabrication procedures do not require such high temperatures.

3.7. Impurities

3.7.1. Secondary phases

It has been shown theoretically and confirmed experimentally that only a very small region of the equilibrium composition phase diagram supports the formation of single-phase CZTS; secondary phases are therefore nearly always present in samples. [236-240] These have a significant effect on photovoltaic device performance. Particular elemental compositions during fabrication will inevitably favour the formation of certain secondary

phases, so composition is an important factor in optimising the production of CZTS for solar cells (see Section 4.2.4).

The region around the pure CZTS phase in a quasi-ternary phase diagram is shown in Figure 34. Such a diagram relies on the assumption that sulphur is always present in the correct amount, which is not always the case, despite generally being considered so. Indeed, sulphur concentration has been reported as the main factor determining the phases in a sample, with a sulphur-to-metal ratio > 1 required to fabricate CZTS-dominated material. [192] The phase diagram is misleading in other ways too: some of the secondary phases it predicts are not typically observed in samples, such as $Cu_2ZnSn_3S_8$, and there are several secondary phases not accounted for in the phase diagram that are reported in samples, such as tin sulphides and $Cu_4Sn_7S_{16}$. [129,240,241]

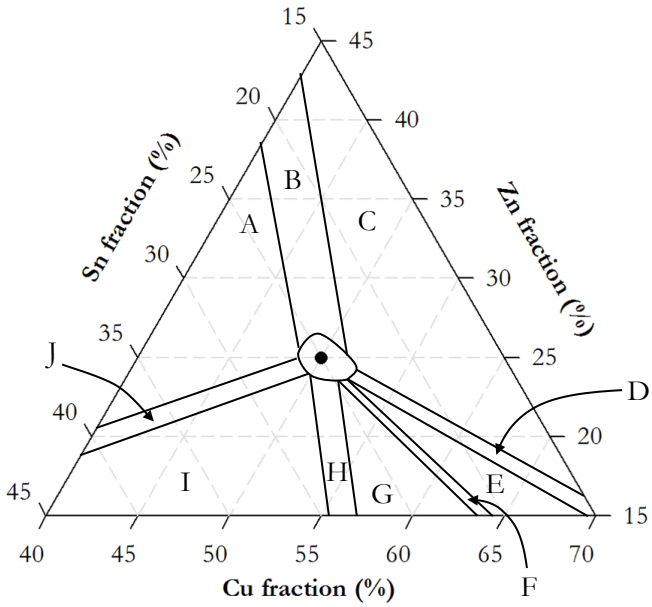

Phase regions:

A: $ZnS + Cu_2ZnSn_3S_8$

B: ZnS

C: $ZnS + Cu_2S$

D: Cu_2S

E: $Cu_2S + Cu_4SnS_4$

F: Cu_4SnS_4

G: $Cu_4SnS_4 + Cu_2SnS_3$

H: Cu_2SnS_3

I: $Cu_2ZnSn_3S_8 + Cu_2SnS_3$

J: $Cu_2ZnSn_3S_8$

(Cu_2ZnSnS_4 is expected in all)

Figure 34: Quasi-ternary composition phase diagram of CZTS and some of its secondary phases (only the region of interest around the pure phase is shown). The central phase is of pure CZTS, with the point in the centre at the stoichiometric ratio of Cu:Zn:Sn = 2:1:1. The regions marked around it are annotated with the major secondary phases that are stable there in addition to CZTS. [128,237,242]

Secondary phases are in general a significant problem for CZTS. They can act as recombination centres and so decrease the conductivity and efficiency of cells, and those with band gaps lower than that of CZTS decrease the open-circuit voltage. The band gaps and crystal structure information of common secondary phases in CZTS are listed in Table

6. However, although secondary phases are in general detrimental to the photovoltaic efficiency of CZTS, some may be beneficial. For example, those with crystal structures compatible with CZTS, such as ZnS, can segregate to grain boundaries and form heterointerfaces with small misfit strain, giving a low recombination velocity; i.e. they passivate the grain boundaries, which is beneficial to device performance. [243,244]

Secondary phase	**Band gap (eV)**	**Crystal structure**	**Lattice parameters**	**Reference**
CZTS	1.5 eV	Tetragonal kesterite $I\bar{4}$	a = 5.424 Å c = 10.869 Å	[245]
CuS	1.0 eV	Hexagonal covellite $P6_3/mmc$	a = 3.795 Å c = 16.34 Å	[246]
Cu_2S	1.2 eV	Monoclinic chalcocite $P2_1/c$	a = 15.246 Å b = 11.884 Å c = 13.494 Å β = 116.35 °	[247]
ZnS	3.8 eV	Cubic sphalerite $F\bar{4}3m$	a = 5.409 Å	[248]
SnS	1.3 eV	Orthorhombic herzenbergite $Pnma$	a = 3.98 Å b = 4.33 Å c = 11.18 Å	[249]
SnS_2	2.2 eV	Hexagonal berndtite $P\bar{3}m1$	a = 3.6297 Å c = 5.9402 Å	[250]
Sn_2S_3	2.1 eV	Orthorhombic ottemanite $Pnma$	a = 8.869 Å b = 3.748 Å c = 14.021 Å	[251]
Cu_2SnS_3	1.4 eV	Tetragonal stannite $I\bar{4}2m$	a = 5.413 Å c = 10.824 Å	[252]
Cu_3SnS_4	1.2 eV	Tetragonal stannite $I\bar{4}2m$	a = 5.445 Å c = 10.75 Å	[253]
Cu_4SnS_4	1.2 eV	Orthorhombic herzenbergite $Pnma$	a = 13.52 Å b = 7.67 Å c = 6.43 Å	[254]
$Cu_4Sn_7S_{16}$	0.8 eV	Rhombohedral pseudospinelite $R\bar{3}m$	a = 7.372 Å c = 36.010 Å	[255]
$Cu_2ZnSn_3S_8$	?	Tetragonal rhodostannite $I4_1/a$	a = 5.435 Å c = 10.825 Å	[237]

Table 6: The band gaps and crystal structure information of secondary phases found in CZTS.

CuS can act as a metallic conductor, creating a shunting pathway within cells, which reduces the photovoltaic efficiency. [246]

Cu_2S is a p-type semiconductor and has been used as the absorber layer of solar cells itself, so is not as harmful as other secondary phases. However, it easily forms a Cu-poor variation referred to as $Cu_{2-x}S$, which is degenerate due to the large number of copper vacancies and therefore more detrimental because it can short-circuit the cell. [129,247]

ZnS is one of the main secondary phases in CZTS because it is particularly stable (enthalpy of formation -205 $kJ \cdot mol^{-1}$ [238]). It is a semiconductor, but has a much larger band gap than CZTS, so acts as a resistive barrier to carriers, [244,256] and has also been found to increase the series resistance of cells and reduce the open-circuit voltage. [257] ZnS has been found to segregate to the bottom of thin-film samples of CZTS, at the Mo/CZTS interface. [258-261]

SnS exhibits p-type conductivity and has also been considered for use as the absorber layer of solar cells, so does not have as detrimental an effect as other secondary phases. [249] It is found only on the surface and at the Mo/CZTS interface, not in the CZTS bulk. [145,261] On the surface, it is detrimental to photovoltaic performance, whereas at the Mo/CZTS interface it can be beneficial because it passivates defects there. [262]

SnS_2 is an n-type semiconductor that can act as a barrier to charge collection from CZTS. [122]

Sn_2S_3 has a larger band gap than CZTS, so will present a resistive barrier to charge carriers. [251]

Cu_2SnS_3 is another of the main secondary phases as it is particularly stable (enthalpy of formation -178 $kJ \cdot mol^{-1}$ [238]). It has a smaller band gap than CZTS, so acts as a recombination centre, [244,256] but has been used as a solar-cell absorber material itself. [97,176]

Cu_3SnS_4 has been found to segregate to the top of thin films of CZTS. [258] It has a very similar structure and band gap to Cu_2SnS_3, and so has a similar effect in CZTS. Cu_2SnS_3 has been shown to form preferentially under 770 K and Cu_3SnS_4 above it. [253]

Cu_4SnS_4 has also been successfully used as a solar cell absorber layer and so is not expected to have a significantly detrimental effect on CZTS. [254]

$Cu_4Sn_7S_{16}$ is not commonly found in CZTS, but is an n-type semiconductor and has a very small band gap, so would introduce significant shunting and reduce photovoltaic efficiency. [240,255,263]

$Cu_2ZnSn_3S_8$ could have beneficial absorber properties, but little is known about this phase as it is rarely observed and has not been studied in detail. [237,240]

Post-fabrication etching is often used to remove unwanted secondary phases (see Section 4.3.12). An aqueous KCN solution has been found to remove Cu_xS impurities, [264-266] and to enhance the energetic barrier to recombination across the CZTS/buffer interface. [267] An aqueous HCl solution has been found to remove ZnS impurities and significantly increase photovoltaic efficiency. [268] Tin-based secondary phases have proved more difficult to eliminate by etching, although Na_2S has been found to remove SnS. [269] A final soak in deionised water for 10 minutes has been found to preferentially eliminate any metal oxide impurities. [158]

3.7.2. Grain boundaries

CZTS, like CIGS and CdTe, has been found to produce more efficient solar cells in polycrystalline than single crystal form. [270] This is not usually the case, as impurities normally gather at grain boundaries and present a barrier to charge transport, acting as recombination centres. [271,272]. The efficiency of polycrystalline solar cells therefore usually increases with grain size in the absorption layer. [273]

In CZTS, CIGS, and CdTe, however, the defects and impurities that segregate to grain boundaries (particularly passivating secondary phases; see Section 3.7.1) trap majority carriers, creating an electric field that acts as a potential barrier to prevent holes reaching

the grain boundary, while encouraging electron collection there. The boundary defects are thus electrically benign and so do not act as recombination centres as they usually would. Instead, boundaries can enhance minority carrier collection by providing a path for them to the buffer layer. However, this increase in current is at the expense of voltage because of recombination at grain-boundary defects, so is not generally beneficial. [270,274-276]

The grain boundaries in CZTS have been found to act as double Schottky barriers with a height of 0.1 eV, and to feature a depletion region 19 nm thick on both sides. [277] It has also been found that charge separation occurs specifically at the interface between the grain and the grain boundary, rather than throughout the whole grain boundary. [278]

3.7.3. Point defects

It is possible for three types of point defect to form in CZTS: antisites, vacancies, and interstitials. An antisite defect is a cation of copper, zinc, or tin present in the crystal lattice where one of the other two cationic elements should be. A vacancy is an unoccupied space in the crystal lattice where an atom (of any of the four elements) should be. An interstitial is an excess atom present in between those of the defect-free structure. These point defects are often referred to as disorder within the crystal lattice. Their formation energies and the defect energy levels they give rise to in the CZTS band gap are primarily attained by computational modelling. [190,279-288] Exemplar values are given in Table 7, and defect energy levels are depicted in Figure 35. However, there is often a significant difference between reported values based on the calculation method used. The formation energies are a function of chemical potential, which is strongly affected by chemical environment, itself largely determined by the elemental composition of the CZTS.

Cu_{Zn} antisite defects are responsible for the inherently p-type nature of CZTS. [190,289] However, a high concentration of these has been found to have a detrimental effect on devices, as their acceptor level is relatively deep. [190,285] This means they encourage trap-assisted recombination, which has been found to be the most significant loss mechanism in CZTS. [290] Cu_{Zn} and Zn_{Cu} are often found together, and are the most common type of disorder experimentally reported. [209-217] Cu_{Zn} and Zn_{Cu} cation disorder is thought to be one of the most significant factors affecting device performance (see Section 3.5), and so is one of the areas of most current research. [291]

Defect	Donor/Acceptor	Defect level (eV)	Formation energy (eV)
Cu_{Zn}	Acceptor	0.15	-0.32
Cu_{Sn}	Acceptor	0.59	0.16
Zn_{Cu}	Donor	-0.11	2.42
Zn_{Sn}	Acceptor	0.28	0.22
Sn_{Cu}	Donor	-1.12	6.54
Sn_{Zn}	Donor	-1.00	4.01
V_{Cu}	Acceptor	0.03	0.21
V_{Zn}	Acceptor	0.26	0.39
V_{Sn}	Acceptor	0.90	1.77
V_S	Donor	-0.74	0.99
Cu_i	Donor	-0.10	3.13
Zn_i	Donor	-0.63	5.92
Sn_i	Donor	-0.76	8.11
S_i	Acceptor	?	?

Table 7: The possible intrinsic point defects in CZTS. Defect levels are positive for acceptor levels above the valence band, and negative for donor levels below the conduction band. Formation energies vary with chemical composition; the values given here are the lowest within the region of phase-pure CZTS. Data from [190,283].

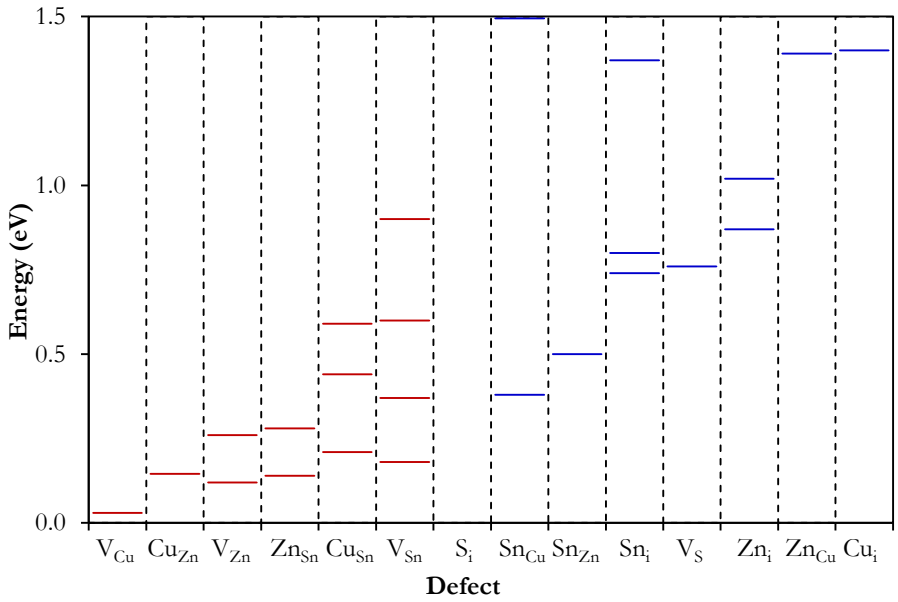

Figure 35: The defect energy levels of point defects within the band gap of CZTS. Data from [190,283].

Cu_{Sn} is theoretically predicted to be one of the most harmful antisite defects, as it has one of the deepest acceptor levels. [283,285] Experimentally, it is not usually found in

significant concentrations for stoichiometric or Cu-poor compositions, but becomes prevalent as the Cu/(Zn+Sn) ratio increases. [212] This is a potential explanation for Cu-poor devices giving the best photovoltaic performance (see Section 4.2.4). [162]

Zn_{Cu} antisite defects have been predicted to be relatively benign in themselves, having one of the shallowest donor levels. [283,285] However they are often found with Cu_{Zn} defects, together the most common crystalline disorder in CZTS. [209-217] This is one of the most significant factors affecting device performance (see Section 3.5). [291] Zn_{Cu} defects can form on both the 2*a* and 2*c* kesterite lattice sites, with formation energies different by less than 0.02 eV per atom. [190]

Zn_{Sn} antisite defects have a reasonably deep defect level, [283] but have been reported as 'benign', [285] although no reasoning for this was given. They will be relatively common for the Cu-poor, Zn-rich compositions that give the best photovoltaic device performance (see Section 4.2.4). [162]

Sn_{Cu} antisite defects have been found to be detrimental, as they have the deepest donor level, [283,285] but tin has been found experimentally to exhibit negligible disorder for stoichiometrically correct tin content, so Sn_{Cu} defects are rarely prevalent. [292]

Sn_{Zn} antisite defects have also been found to be detrimental due to extremely deep defect levels. [283,285] Sn_{Zn} has been theoretically calculated to be a significant deep trap, occurring at densities of around 10^{16} cm^{-3}. [289] However, experimentally tin exhibits negligible disorder for stoichiometrically correct tin content, so Sn_{Cu} defects are rarely prevalent either. [292]

Copper vacancies, V_{Cu}, have a low formation energy and are much better than Cu_{Zn} defects for achieving high-efficiency solar cells, as their defect level is the shallowest of all acceptors. [283,285] This is confirmed by the fact that the best cell efficiencies have been achieved with Cu-poor and Zn-rich CZTS (see Section 4.2.4), [162] in which the copper vacancy will be more prevalent than the Cu_{Zn} antisite. In samples with high Cu-Zn disorder copper vacancies have been calculated not only to be less detrimental than other defects, but to actively increase the band gap by 0.2-0.3 eV. [286,287] This counters the decrease usually caused by local potential fluctuations and thus can increase the open-circuit voltage

of devices. Hence, V_{Cu} is the preferred acceptor defect for providing the p-type behaviour of CZTS, but the material must be engineered for it to dominate.

Zinc vacancies, V_{Zn}, have a relatively deep defect level, and can be formed relatively easily, so care must be taken to minimise their occurrence. [283,285]

Tin vacancies, V_{Sn}, have the deepest acceptor level and so must be avoided. [283,285]

Sulphur vacancies, V_S, have been calculated to be unstable, so do not practically contribute a defect level. [288] However, they have also been calculated to occur with a concentration of around 10^{13} cm^{-3}, and so to act as important deep traps. [289]

Copper interstitials, Cu_i, have a relatively low defect level, but a very high formation energy, so are not expected to occur significantly. [190]

Zinc interstitials, Zn_i, have a much deeper defect level than copper interstitials, so are significantly worse for photovoltaic performance, but they also have a very high formation energy, so are not expected to occur significantly. [283]

Tin interstitials, Sn_i, have a very deep defect level, so must also be avoided. Their very high formation energy makes this easy as they are unlikely to be naturally prevalent. [283]

Sulphur interstitials, S_i, are rarely considered and so are difficult to find values for.

3.7.4. Point defect complexes

When certain point defects with opposite charge are formed in close spatial proximity, their formation energies are lowered due to the Coulomb attraction between them, and the relief of strain in the crystal lattice. These are self-compensated charge-neutral defect complexes. The combined energy levels of these defect complexes are much shallower than those of the individual defects due to charge compensation (i.e. the charges of the two individual defects cancel). They are therefore generally beneficial, as they passivate the individual deep defect levels, reducing Shockley-Read-Hall recombination. However, they can also be detrimental, as they can significantly reduce the band gap. The formation energies of some

common point defect complexes in CZTS are given in Table 8, and their defect levels and effects on the band gap are illustrated in Figure 36.

Defect complex	Formation energy (eV)
$[Cu_{Zn}^{-} + Zn_{Cu}^{+}]$	0.21
$[2Cu_{Zn}^{-} + Sn_{Zn}^{2+}]$	0.18
$[Cu_{Zn}^{-} + Cu_{i}^{+}]$	0.79
$[Cu_{Sn}^{3-} + Sn_{Cu}^{3+}]$	>1.5
$[Zn_{Sn}^{2-} + 2Zn_{Cu}^{+}]$	0.83
$[Zn_{Sn}^{2-} + Sn_{Zn}^{2+}]$	0.86
$[Zn_{Sn}^{2-} + Zn_{i}^{2+}]$	>1.5
$[V_{Cu}^{-} + Zn_{Cu}^{+}]$	0.47
$[2V_{Cu}^{-} + Sn_{Zn}^{2+}]$	1.11
$[V_{Zn}^{2-} + Sn_{Zn}^{2+}]$	1.11

Table 8: The formation energies of some common defect complexes in CZTS. Data from [283].

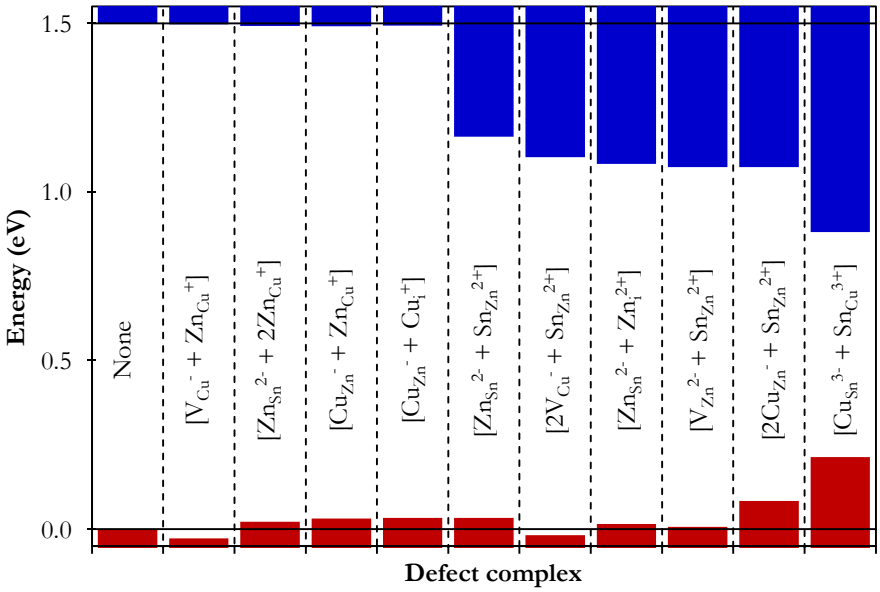

Figure 36: The calculated valence (red) and conduction (blue) band edges, shifted by different defect complexes in CZTS at a concentration of one in a 128-atom supercell. Data from [283].

$[Cu_{Zn}^{-} + Zn_{Cu}^{+}]$ decreases the band gap slightly. At high density, they contribute to band gap tailing and lower the open-circuit voltage. [293] One such cation disorder pair per eight unit cells gives a band gap fluctuation of 40 meV. [234]

[$2Cu_{Zn}^{-} + Sn_{Zn}^{2+}$] is common in Cu-rich and stoichiometric CZTS, and causes a local decrease in band gap of 0.35 eV, which has a significant detrimental effect on the open-circuit voltage of cells. [294]

[$Cu_{Zn}^{-} + Cu_{i}^{+}$] is relatively benign, giving only a small decrease in band gap, and has a relatively high formation energy, so is unlikely to be prevalent in under standard conditions anyway. [283]

[$Cu_{Sn}^{3-} + Sn_{Cu}^{3+}$] significantly reduces the band gap of CZTS, but is generally found only in low concentrations. [190]

[$Zn_{Sn}^{2-} + 2Zn_{Cu}^{+}$] is beneficial because it gives a very small decrease in band gap, whereas the uncompensated defects have deep defect levels, which are very detrimental. It is particularly prevalent in Cu-poor, Zn-rich material. [284]

[$Zn_{Sn}^{2-} + Sn_{Zn}^{2+}$] significantly reduces the band gap of CZTS, but is generally found only in low concentrations. [190]

[$V_{Cu}^{-} + Zn_{Cu}^{+}$] increases the band gap, but is often correlated with [$Cu_{Zn}^{-} + Zn_{Cu}^{+}$] complexes, which decrease it. The presence of one lowers the formation energy of the other in close proximity; hence these two complexes compensate and stabilise the band gap in Cu-poor CZTS. [235] [$V_{Cu}^{-} + Zn_{Cu}^{+}$] complexes restrain the random distribution of Cu_{Zn} and Zn_{Cu} antisite defects found in CZTS, and so promote long-range order in samples. [295,296]

[$2V_{Cu}^{-} + Sn_{Zn}^{2+}$] has a very large formation energy, so is unlikely to form in significant concentrations. [283]

[$V_{Zn}^{2-} + Sn_{Zn}^{2+}$] also has a very large formation energy, so is unlikely to form in significant concentrations. [283]

3.7.5. Off-stoichiometric composition types

Charge-neutral defect complexes can congregate to produce long-range order within CZTS, to the point of individual grains within a sample having different compositions due to the presence of ordered defect complexes. Six such complexes have been identified and are given in Table 9 along with the letter used to designate the type of CZTS produced by them as defined by Lafond et al. [213], Gurieva et al. [297], and Valle Rios et al. [298]

CZTS type	Defect complex	Stoichiometry
S-type	$[Cu_{Zn}^{-} + Zn_{Cu}^{+}]$	Stoichiometric
A-type	$[V_{Cu}^{-} + Zn_{Cu}^{+}]$	Cu-poor, Zn-rich
B-type	$[Zn_{Sn}^{2-} + 2Zn_{Cu}^{+}]$	Cu-poor, Zn-rich
C-type	$[2Cu_{Zn}^{-} + Sn_{Zn}^{2+}]$	Zn-poor, Cu-rich
D-type	$[Cu_{Zn}^{-} + Cu_{i}^{+}]$	Zn-poor, Cu-rich
E-type	$[2V_{Cu}^{-} + Sn_{Zn}^{2+}]/[V_{Zn}^{2-} + V_{Cu}^{-} + Sn_{Cu}^{3+}]$	Cu-poor, Sn-rich
F-type	$[Zn_{Sn}^{2-} + 2Cu_{i}^{+}]/[Cu_{Sn}^{3-} + Zn_{i}^{2+} + Cu_{i}^{+}]$	Sn-poor, Cu-rich

Table 9: The types of CZTS with the defect complexes that cause them. [213,297,298]

The cationic compositions that can be formed by the incorporation of these defect complexes are plotted in Figure 37. The region of stability of single-phase CZTS is extended beyond that calculated in the usual ternary phase diagram (see Section 3.7.1) by the stability provided by these off-stoichiometric defect complexes. [299]

The different compositions of individual grains of CZTS can be observed directly using very spatially precise Raman and XRD measurements. However, standard characterisation procedures only investigate large, multi-grain areas of the sample at a time, so an average composition over many grains is usually all that is found for CZTS samples. This gives misleading information about the sample, and so it has been suggested that microstructural characterisation must become standard to properly investigate the structural properties of the material, which is necessary to improve the low open-circuit voltage. [300]

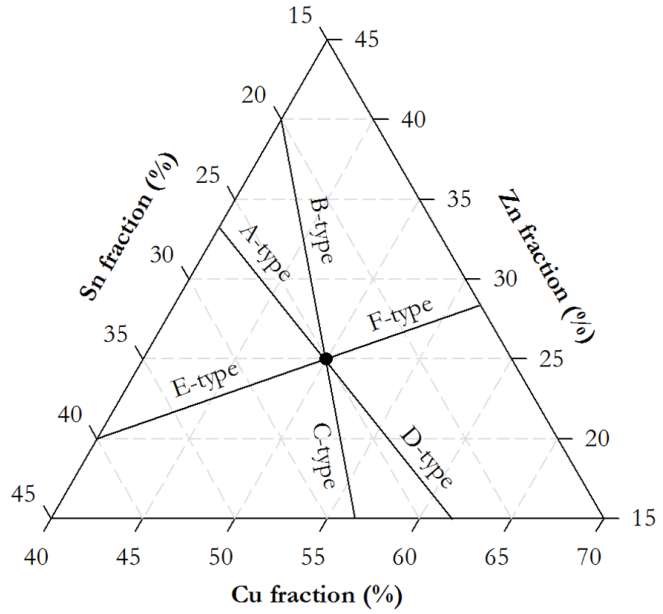

Figure 37: The compositions of the defect-complex-defined types of CZTS. S-type lies only on the stoichiometric point at the centre and the other types lie along the labelled lines, with the exact location along the line determined by the density of the respective defect complex. [213,297,298]

3.7.6. Sodium doping

Sodium and, to a lesser extent but with the same effect, potassium are often found to diffuse into the CZTS layer of solar cells from the soda lime glass usually used as a substrate (see Section 3.8.1). Conveniently this is beneficial to device performance. [133,136,301-316]. Sodium doping up to 1 % is optimal, [311] but only 0.08 at.% has been measured as naturally occurring. [304] Additional sodium is therefore sometimes actively provided to make use of its beneficial effect: the inclusion of a layer of NaF as a sodium source on top of the CZTS precursor layers for the annealing stage has been shown to increase the photovoltaic efficiency of a cell (from 1.5 to 2.8 %). [314]

Sodium can substitute for any of the three cations in CZTS (copper, zinc, and tin) to form an antisite defect. The formation energy of Na_{Cu} defects have been calculated to be close to zero or negative, so sodium doping is controlled simply by the availability of sodium. Na_{Cu} is an isovalent replacement and so does not contribute to the conductivity of CZTS. Na_{Zn} also has a low formation energy and is a shallow acceptor, which does contribute to the conductivity of CZTS, and is therefore very beneficial to conversion efficiency. Na_{Sn} has a

deep defect level in the band gap and acts as a hole trap. However, its formation energy is high, so it is not found in significant concentrations. [285]

Sodium in CZTS is thought to concentrate at grain boundaries, having been measured there at 1 % (atomic) while negligible in grain interiors. [310] It passivates boundary defects, reducing interface recombination (see Section 3.7.2). [136,301,312]

Such sodium doping was also found to improve the crystallinity of CZTS, decrease the intrinsic defect density, significantly increase grain size, and lead to better electronic properties, including enhanced carrier lifetime, hole concentration, mobility, and shunt resistance. [133,301-316]

The presence of sodium from soda lime glass substrates has also been found to lower the temperature necessary to complete the formation of CZTS from precursor materials (see Section 4.3): this was reduced from around 870 K for substrates without sodium such as quartz, to around 670 K for soda lime glass. [133]

However, excess sodium above that required to passivate the grain boundaries acts a detrimental defect, either remaining in the absorber layer or diffusing into the buffer or window layer. Excess sodium defects trap minority carriers and reduce the open-circuit voltage, short-circuit current, and fill factor, [312] and have also been reported to act as a catalyst for the dissociation of CZTS into Cu_2S, ZnS, and SnS. [316] An annealing process after the deposition of the buffer and window layers has been shown to reduce the excess sodium content, improve the stability of the open-circuit voltage as a function of temperature, and give improved device performance. [312]

3.7.7. Fluctuations in band gap and electrostatic potential

Spatial variation in the band gap and in electrostatic potential due to variation in the conduction and valence band edges can have a significant effect on recombination. These two phenomena are illustrated in Figure 38. These fluctuations cause band tailing, which is the most critical cause of low photovoltaic efficiency in CZTS, due to the deficit in open-circuit voltage it causes. Potential fluctuation has been calculated to account for this deficit almost fully, with band-gap fluctuation having a much less significant effect. [317]

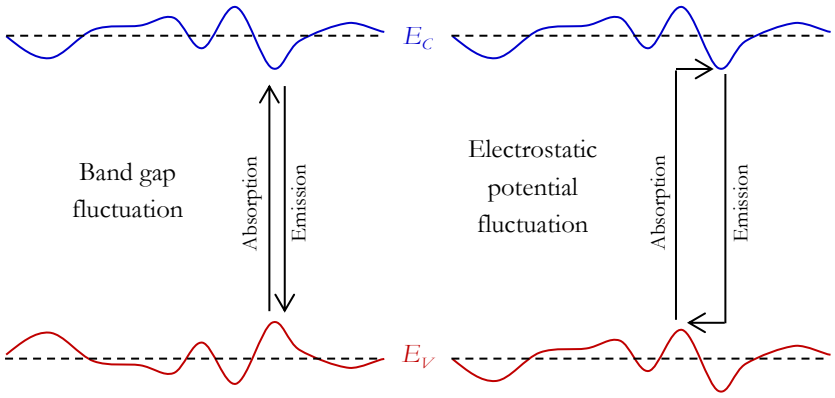

Figure 38: The difference between band-gap fluctuation and electrostatic potential fluctuation. The former is symmetric: maxima in the valence band correspond spatially with minima in the conduction band, so absorption and recombination occur at these points with a smaller effective band gap. The latter is antisymmetric: maxima in the valence band correspond spatially to maxima in the conduction band; sub-band-gap absorption and recombination is possible between maxima and minima in different locations via tunnelling.

Band-gap fluctuation is caused by the presence of the various point defects discussed in Sections 3.7.3 and 3.7.4, which perturb the local structure. [234] It lowers the open-circuit voltage, and so is particularly detrimental to photovoltaic device performance. The magnitude of band gap fluctuations in CZTS has been reported as 120 meV. [111]

Electrostatic potential fluctuation occurs over a larger scale and is caused by deviations in the density of such impurities. This leads to deviations in carrier concentration, which produce Coulomb screening of the band-edge states. This results in a fluctuating potential on the band edges, with no spatial variation in band gap as both band edges follow the same fluctuations. If the magnitude of these fluctuations is larger than the binding energy of impurity states, potential fluctuations become the dominant recombination trap. For a low degree of doping this is not the case, as interaction between defects is not significant, so defect levels in the band gap are relatively discrete. However, for a higher degree of doping, the fluctuating potential model better describes recombination behaviour. This has been confirmed to be the case even in intrinsic CZTS. [318-330] Potential fluctuation is detrimental to photovoltaic efficiency because it leads to the broadening of discrete defect levels into small bands due to the Pauli Exclusion Principle. These defect bands, called Urbach band tails, extend into the band gap, which can be a significant cause of open-circuit voltage reduction. [57] It has been calculated that the maximum theoretical efficiency of a device decreases by 1.7 % (absolute) for fluctuations of magnitude 50 meV

and by 6.1 % (absolute) for 100 meV, with respect to a uniform band gap. [331] Magnitudes between 11 meV [332] and 172 meV [318] have been reported for CZTS.

The magnitude, i.e. average depth, of fluctuations in potential on the band edges is given by

$$\gamma = \sqrt{2\pi N_T r_D} \cdot \frac{e^2}{\varepsilon} \quad , \tag{16}$$

where N_T is the total charged impurity (both acceptors and donors) concentration, e is the magnitude of the charge on an electron, ε is the dielectric permittivity of the material, and r_D is the Debye screening radius, given by

$$r_D = \left(\frac{a_0}{4}\right)^{1/2} \cdot \left(\frac{\pi}{3n}\right)^{1/6} \quad , \tag{17}$$

where a_0 is the Bohr radius and n is the concentration of free charge carriers. [318,333]

The fluctuations in potential result in an absorption coefficient below E_g given as a function of frequency, f, by

$$\alpha = \exp\left(-\frac{2}{5\sqrt{\pi}} \cdot \left(\frac{E_g - hf}{\frac{1}{2}\gamma}\right)^{5/4}\right) , \tag{18}$$

where h is the Planck constant and γ is the amplitude of the potential fluctuations relevant for optical transitions, given by

$$\gamma = \left(\frac{e^2}{4\pi\varepsilon}\right)^4 \cdot \frac{N_T^2 \hbar^2}{m_r} \quad , \tag{19}$$

where e is the magnitude of the charge on an electron, ε is the dielectric permittivity of the material, N_T is the total charged defect density, ħ is the reduced Planck constant, and m_r is the reduced electron/hole mass,

$$m_r = \frac{m_e m_h}{m_e + m_h} \quad . \tag{20}$$

Hence once the bandgap is known, the absorption can be used to find the magnitude of the potential fluctuations. [321]

3.8. Device structure

An example CZTS solar cell architecture is illustrated in Figure 39. This is very similar to the standard CIGS design, from which it was developed. It features a molybdenum back contact on a glass substrate, sometimes a thin Al_2O_3 passivation layer to prevent the formation of MoS_2, then the inherently p-type CZTS absorber layer, n-type CdS as the buffer layer, undoped ZnO as a window layer, a transparent conducting layer such as Al-doped ZnO or indium tin oxide (ITO), an aluminium grid as the top contact, and often an anti-reflection coating layer such as MgF_2. The roles of these nine layers are detailed below.

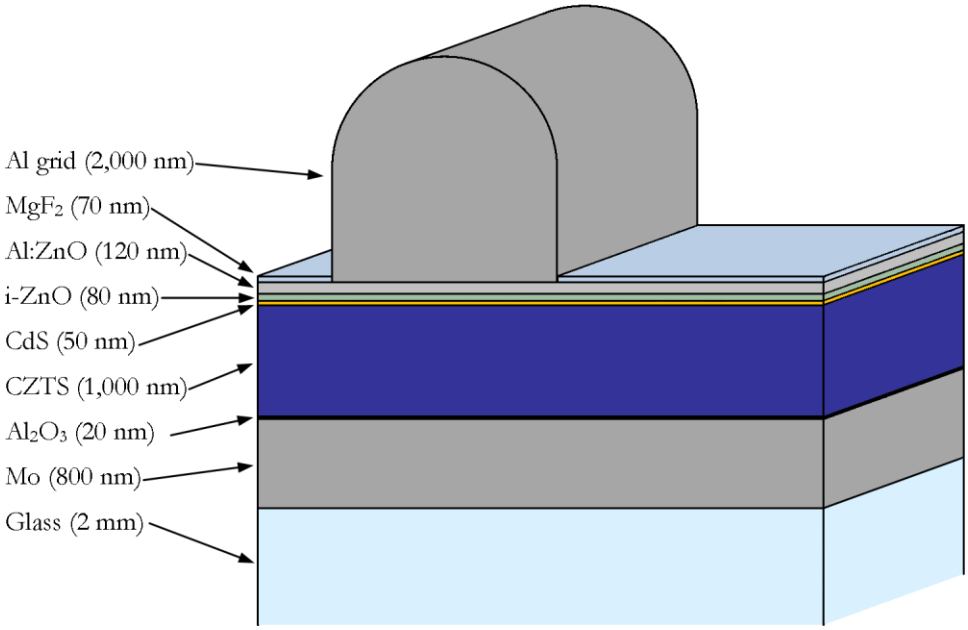

Figure 39: A schematic design of a CZTS solar cell cross section.

3.8.1. Substrate

Soda lime glass is the most commonly used material for the cell substrate, as it is low-cost, stable at high temperatures (up to 870 K), and can easily have a sufficiently smooth surface on the microscopic scale. Additionally, and quite serendipitously, soda-lime glass has a beneficial effect on device performance due to sodium doping of the absorber layer (see Section 3.7.6).

Other materials have been used, including boroaluminosilicate glass, [301] Pyrex, [305] quartz, [305] sapphire, [186,334-336] silicon, [337-340] ZnS, [223] and flexible materials

such as polyamide, [341] polyimides, [342] Willow glass, [343] and foils of aluminium, [344] molybdenum, [344] stainless steel, [315,344] and titanium. [345] These were all successful, and while flexible substrates have the potential to open a wider range of applications, soda lime glass is still preferred for standard, flat-cell applications because of its low cost.

3.8.2. Back contact

Around 800 nm of sputtered molybdenum is most often used for the back contact layer because it has a sufficiently low resistivity (125 nΩ·m [346]) and high chemical inertness, melting point, and mechanical hardness.

Other materials have been used, including aluminium, [347,348] cobalt, [347] gold, [347,349] iron, [347] magnesium, [347] nickel, [347,349] palladium, [347,349] platinum, [349] silver, [348] titanium, [347] and tungsten. [349] These were found to be potentially successful as alternative back contact materials, although none performed as well as molybdenum.

However, molybdenum is not problem-free as a contact layer. It can be unstable in contact with CZTS during annealing and so can produce an intermediate layer of MoS_2. [350] This is an n-type semiconductor and has a high resistivity, so can act as a barrier to carrier extraction and have a significantly adverse effect on the performance of devices. MoS_2 also encourages the formation of other secondary phases at the Mo/CZTS interface. [351,352]

Numerical modelling has shown that MoS_2 layers as thin as 50 nm are sufficient to show detrimental effects [353] and layers from <10 nm [354] to 500 nm [355] thick have been found experimentally. The sulphurisation stage is thus a trade-off between improved crystallinity of the CZTS layer and the formation of a thicker MoS_2 layer; a MoS_2 thickness of 350 nm has been calculated to be the optimum compromise. [356]

Similar detrimental effects have been found for the p-type $MoSe_2$ in CZTSe [357] and CIGS, [358] although in the latter a thin $MoSe_2$ layer is considered necessary to prevent delamination. Numerical modelling for CZTS using a p-type MoS_2 layer rather than n-type found the layer to improve V_{OC} and give better device performance, with 100 nm being the optimal thickness. [359]

3.8.3. Back passivation layer

Intermediate layers of around 10-20 nm of a variety of materials have been used between the molybdenum back contact and CZTS absorber layer to reduce the formation of MoS_2, including Al_2O_3, [360] silver, [136,361] bismuth, [362] carbon, [363] TiB_2, [364] TiN, [365] and ZnO. [136,366,367] These were all successful in doing so; however, most also had detrimental effects.

Al_2O_3 has been utilised in the 'passivated emitter rear contact' (PERC) structure, i.e. with a regular grid of nano-sized point openings to act as contacts (the PERC structure is used as standard in the most efficient silicon solar cells [368]); this gave increased open-crcuit voltage, short-circuit current, and fill factor as well as reducing the formation of MoS_2. [360] Al_2O_3 has been found to self-organise into such a nano-patterned structure from an initially continuous layer during the sulphurisation stage of CZTS formation. [369] 3 nm has been found to be the optimum thickness, with 1 nm having no positive effect and >5 nm causing delamination of the CZTS layer. [369]

Silver reduced the series resistance, recombination, and the presence of voids at the Mo/CZTS interface and of SnS_2 at the CZTS surface; and it increased short-circuit current, fill factor, open-circuit voltage, and efficiency (from 2.3 % to 4.4 % [136]); but it also degraded the crystallinity of the CZTS. [136,361]

Bismuth gave better CZTS crystallinity with larger grains, and less ZnS formed as a secondary phase. [362]

Carbon gave a ~20 % improvement in short-circuit current due to the aggregation of carbon at the inner wall of voids and reconnection of CZTS with the back contact. [363]

TiB_2 degraded the CZTS crystal quality, which is detrimental to open-circuit voltage and so to device performance. [364]

TiN enhanced photovoltaic efficiency, but the TiN/CZTS interface contributed to a high series resistance that reduced the fill factor. [365]

ZnO is consumed during sulphurisation, the zinc being absorbed into the CZTS layer, which reduces the formation of voids. It has also been observed to reduce the series resistance and increase the shunt resistance, increasing the photovoltaic efficiency (from 1.1 % to 4.3 % [136]). However, it can reduce the fill factor. [136,366,367]

3.8.4. Absorber layer

This is the layer for which CZTS is used, in which most absorption of light occurs. It is generally around 1,000 nm thick, which has been found to be optimum [360,370] despite only around the first 450 nm contributing to the photogeneration of charge carriers. [371]

It has been found that splitting the absorber layer into two, with CZTS of slightly different compositions in each, is beneficial. The first layer, next to the molybdenum contact, should have a high copper concentration and the second should have a lower copper concentration. This double-absorber-layer structure forms a carrier concentration gradient similar to that in a p-i-n cell, which aids carrier separation and increases the open-circuit voltage. [372] However, such a double CZTS layer has also been found to exhibit more severe fluctuations in band gap or electrostatic potential, which causes band tailing that negatively affects photovoltaic performance. [373]

3.8.5. Buffer layer

The buffer layer (sometimes called the emitter layer) is much thinner than the absorber layer, having been calculated to be optimal at 40-50 nm. [374,375] It serves to make the p-n junction and allow charge separation.

Absorber-buffer interface recombination has been found to be one of the most significant loss mechanisms in CZTS solar cells, [267,376,377] as the carrier lifetime in CZTS is quite long: up to a few nanoseconds. [378] The interface recombination velocity has been measured as $\sim 10^5$ $cm \cdot s^{-1}$ in a CZTS cell. [111]

CdS is generally used as the buffer layer, as this is the best material found for it in CIGS cells, the structure of which has largely been adopted directly for CZTS cells. Chemical bath deposition has given the best device performance to date. [161] The large band gap of

CdS means it gives a high transmission of light to the absorber layer, [379] and it has been found that cadmium atoms have the additional benefit of passivating point defects at the absorber-buffer interface. [380] However, in general the band gap at the CZTS/CdS interface is narrowed by localised states increasing the valence band maximum in CZTS, which explains the dominance of interface recombination in CZTS solar cells. [142]

Other materials have also successfully been used as the buffer layer with CZTS, including CeO_2, [142] In_2S_3, [381-384] InS_2 and TiO_2, [385] amorphous silicon, [386] ZnO, [387] ZnS, [388-392] $ZnO_{1-x}S_x$, [381,393] $Zn_{1-x}Cd_xO_{1-y}S_y$, [394] and $Zn_{1-x}Cd_xS$. [162,392,395]

The conduction band offset at the absorber-buffer interface is very important to device performance, as it can potentially form a barrier to carrier transport. If the conduction band edge of the buffer-layer material is higher than that of the absorber (i.e. the junction is 'spike-like'), electrons are faced with an energy barrier in moving from the absorber to the buffer. However, if the conduction band edge of the buffer material is lower than that of the absorber (i.e. the junction is 'cliff-like'), the narrowing of the 'interface bandgap' increases recombination and reduces the open-circuit voltage. A small spike in the conduction band offset of 0.1-0.2 eV is the best compromise, as this is not large enough to present a significant barrier to electrons, inhibits interface recombination, and does not reduce the open-circuit voltage. [381]

The offsets for some materials used as buffer layers with CZTS are shown in Figure 40.

The CZTS/CdS interface forms a type-II or 'staggered gap' alignment (i.e. the material with the higher conduction band edge has the higher valence band edge). [381,396-399] The conduction band offset at the CZTS/CdS junction has been reported as negative (i.e. 'cliff-like') with values of -0.05 eV, [398,399] -0.24 eV, [381] -0.32 eV, [397] and -0.33 eV. [396] The valence band offset has been reported as -0.95 eV, [399] -0.98 eV, [398] -1.14 eV, [381] -1.19 eV (reduced to -0.91 eV by KCN etching), [267] and -1.22 eV. [397] The values cover such a large range as the band alignment is very sensitive to the absorber-buffer interface, so variations in the CZTS surface and any treatment (e.g. etching to remove secondary phases) prior to deposition of the buffer layer affect it. The depletion region width (unilluminated and at short-circuit) has been measured as 93 nm for a CZTS/CdS junction. [383] CdS is still considered one of the best buffer layer materials with CZTS.

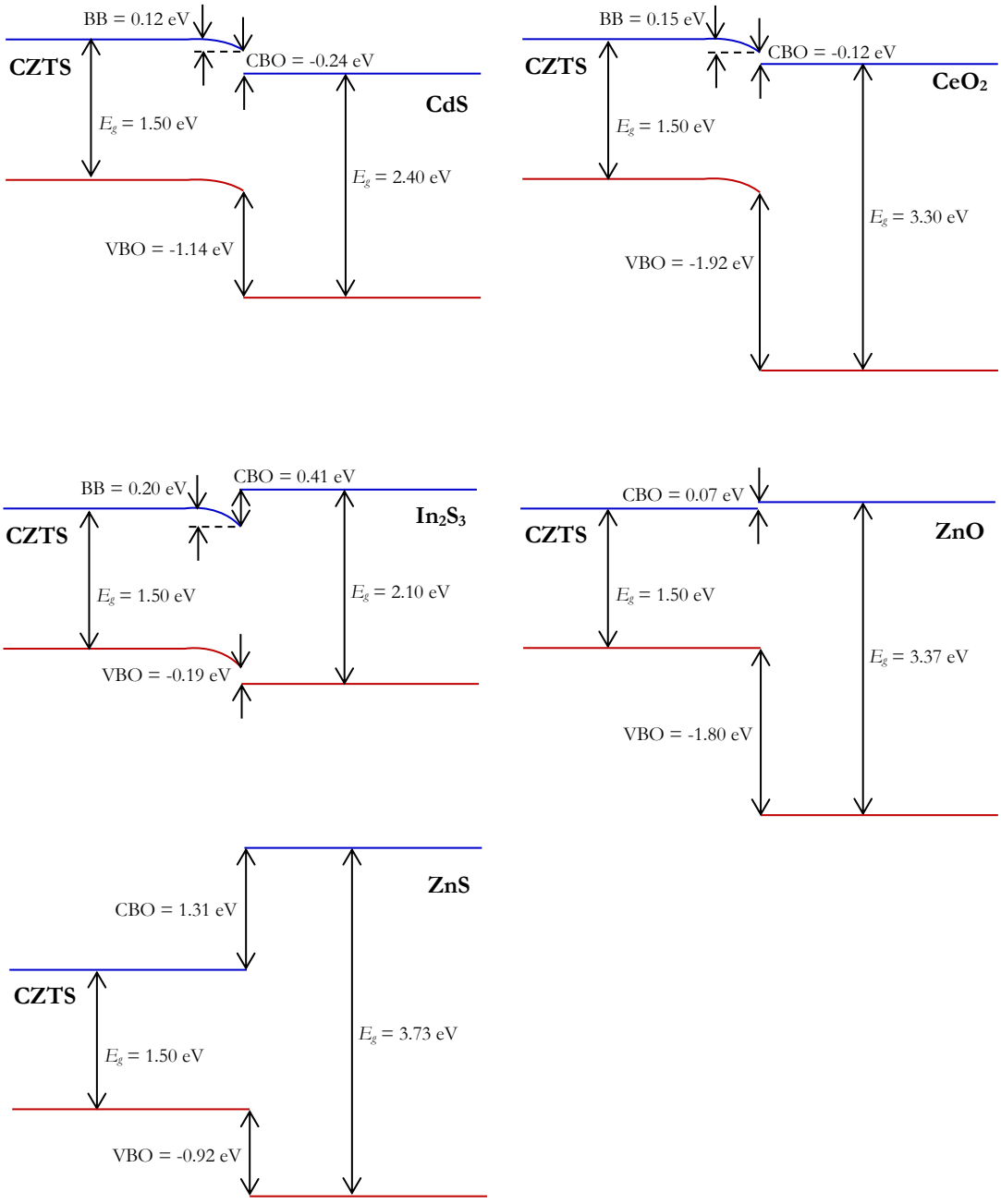

Figure 40: The conduction band offsets (CBO), valence band offsets (VBO), and band bending (BB) for CZTS/CdS, CZTS/CeO_2, CZTS/In_2S_3, CZTS/ZnO, and CZTS/ZnS junctions. [142,381,387,388]

CeO_2 has a nearly perfect lattice match with CZTS and has a wide indirect band gap of 3.3 eV. It also forms a type-II band alignment with CZTS, with a conduction band offset of -0.12 eV, which is very promising for photovoltaic performance. However, unfortunately a CeO_2 buffer layer completely blocks current flow in the cell due to poor transport properties of its conduction band, so the photovoltaic effect is not observed. This can be overcome by using a thickness of only 1-5 nm, so inserting a thin CeO_2 layer

between the CZTS and a CdS buffer is still useful: it alleviates interface recombination and increases the open-circuit voltage of the cell. [142]

In_2S_3 forms a type-I band alignment with CZTS (i.e. the material with the higher conduction band edge has the lower valence band edge; its band gap extends both higher and lower than that of the other material), with a relatively large positive conduction band offset of around 0.41 eV. [384] This value has been found to decrease with increasing deposition temperature of the In_2S_3 layer from 0.41 eV at 370 K to 0.01 eV at 470 K. [384] Using In_2S_3 as the buffer layer gives an increased carrier concentration in CZTS due to indium doping, and a larger open-circuit voltage than CdS; however, the conduction band offset spike is higher than the optimum, which prevents the flow of electrons from the CZTS layer, giving a low short-circuit current and fill factor. [381-383] The depletion region width (unilluminated and at short-circuit) has been measured as 61 nm for the CZTS/In_2S_3 junction. [383] It has been found that the photovoltaic efficiency of a cell is higher for a buffer of In_2S_3 followed by a layer of CdS than one with only In_2S_3 or only CdS. [382]

ZnO forms a type-I band alignment with CZTS, with a small positive 'spike-like' conduction band offset of 0.07 eV, [387] making ZnO one of the best simple binary materials for the buffer layer with CZTS.

ZnS forms a type-I band alignment with CZTS, with extremely large conduction and valence band offsets. This means ZnS presents a large barrier to electrons, and so is not a suitable buffer material. [388]

$Zn_{1-x}Cd_xS$, $Zn_{1-x}Cd_xO_{1-y}S_y$, and $ZnO_{1-x}S_x$ all form a type-I band alignment with CZTS, with a positive 'spike-like' conduction band offset. For the first two, this can be engineered to the optimum value using the Zn:Cd ratio, making these very promising materials for the buffer layer. [162,394] This effect has even been observed for pure CdS buffer layers that have been annealed at 600 K, causing inter-diffusion of zinc from the CZTS layer into the CdS and cadmium from the CdS into the CZTS, giving a beneficially positive band alignment. [400] The conduction band offset for $ZnO_{1-x}S_x$ is 0.92 eV, [381] which is so large that it blocks all flow of electrons from the CZTS layer. [381]

A thin In_2S_3 layer deposited on top of a CdS buffer layer, referred to as a dual or hybrid buffer, has been shown to give an increase in open-circuit voltage of about 70 mV. [123] This improvement is due to enhancement of the hole density by indium diffusing into the CZTS layer. [401]

3.8.6. Window layer

The window layer is a thin (around 80 nm), highly resistive, transparent layer usually incorporated between the buffer and transparent conducting layer. The purpose of this layer is to reduce the effect of pin-holes in the buffer layer, which could otherwise provide a connection between the absorber and the top contact, and to allow a reduction in the thickness of the buffer layer necessary to give a useful open-circuit voltage. The mechanism by which the window layer does the latter is still unclear. [69] Intrinsic ZnO (i-ZnO) is most commonly used for this layer.

The buffer-window interface can have just as significant an effect on performance as the absorber-buffer one, for the same reasons. The CdS/ZnO interface forms a type-II band alignment, as shown in Figure 41. [398]

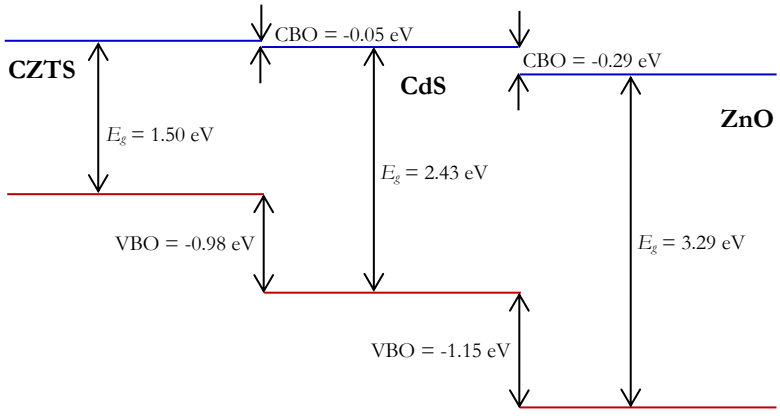

Figure 41: The conduction band offsets (CBO) and valence band offsets (VBO) of the absorber/buffer/window layer structure CZTS/CdS/ZnO. [398]

3.8.7. Transparent conducting layer

The transparent conducting layer, generally made of a transparent conducting oxide (TCO), serves to collect the charge carriers and transport them to the collection grid. Its optimum

thickness has been calculated as 120 nm. [374] Indium tin oxide (ITO) and aluminium-doped ZnO (Al:ZnO) are the most common materials, because they have high transmission (>80 % over the visible spectrum) and low resistivity (<20 nΩ·m). [109]

3.8.8. Front contact

A grid of aluminium, each finger a few microns thick and wide, is most often used as the front electrical contact of the cell. This must balance collecting as many of the carriers from the transparent conducting layer as possible with covering as little of the cell area as possible, as this shading reduces the area that can absorb sunlight.

3.8.9. Anti-reflection coating

Anti-reflection coatings can increase the overall photovoltaic efficiency of a device by reducing the loss of photons by Fresnel reflection at the device surface. Most simply, the anti-reflection coating can be a thin layer of dielectric material of thickness such that light reflected from the semiconductor below and from the anti-reflection coating surface interfere destructively and cancel each other out. Around 70 nm of MgF_2 is commonly used. [402] A less simple but more effective method is to use light-trapping nanostructures; sub-wavelength gratings produced by holographic lithography or dry etching have emerged as a particularly suitable option. [403]

3.9. Fabrication methods

CZTS has been fabricated using several methods, under both vacuum and non-vacuum conditions. Vacuum deposition generally gives higher-quality samples, but is more expensive. Almost all fabrication methods involve an initial deposition stage followed by sulphurisation annealing, because a high temperature is required to crystallise CZTS (~850 K), which in turn requires a high partial pressure of sulphur, which is typically incompatible with the actual film deposition. [365] However, some single-stage processes have been reported. A list of fabrication methods and the best photovoltaic efficiencies achieved using them are given in Table 10. Ramasamy et al. [115] and Song et al. [120] have published useful reviews of the various fabrication methods.

Fabrication method	Vacuum/ Non-vacuum	Sulphurisation stage?	Best efficiency	Year	Reference
Sputtering	Vacuum	Yes	11.0 %	2017	[88]
Thermal evaporation	Vacuum	Yes	9.2 %	2012	[161]
Electrodeposition	Non-vacuum	Yes	7.3 %	2012	[404]
Molten flux recrystallisation	Vacuum	Yes	7.3 %	2017	[110]
Sol-gel spin coating	Non-vacuum	Yes	6.7 %	2016	[405]
Replacement reaction	Non-vacuum	No	6.2 %	2014	[200]
Chemical vapour deposition	Either	Yes	6.0 %	2012	[406]
Electron beam evaporation	Vacuum	Yes	5.5 %	2003	[156]
Pulsed laser deposition	Vacuum	No	5.2 %	2016	[141]
Hot-injection spin coating	Non-vacuum	Yes	3.6 %	2013	[407]
Spray pyrolysis	Either	Yes	1.0 %	2013	[348]
Screen printing	Non-vacuum	No	0.5 %	2010	[341]

Table 10: Various CZTS fabrication techniques, and the best photovoltaic solar cell efficiencies achieved with them.

Sputtering is the method that has been used to produce devices for this project, and will be covered in more detail in Chapter 4.

Thermal evaporation is a type of physical vapour deposition, and is carried out under vacuum. Hot metallic sources evaporate and the vapour particles travel directly to the substrate, where they condense. This is followed by sulphurisation annealing to give crystalline CZTS. It has been used to produce several of the highest-efficiency CZTS devices. [161]

Electrodeposition (often referred to as electroplating or electrochemical deposition) is a popular method as this is common for the parallel material CIGS. [37] It is a non-vacuum process in which precursors are deposited from an electrolytic solution of metal salts, followed by sulphurisation. It is inexpensive and can produce larger areas of film than other methods. However, there are no suitable stable sulphur precursors for direct CZTS deposition, which is why metallic layers are deposited that then undergo sulphurisation annealing. [404]

Molten flux recrystallisation, or monograin layering, involves the growth of monograins from the reaction of sulphide precursors (CuS, ZnS, SnS, and elemental S) in a molten flux of potassium iodide, and then the deposition of these monograins as a thin film. The

precursors and potassium iodide are mixed by grinding the desired amount of each together in an agate mortar. The powder is then sealed in an evacuated quartz ampoule and annealed at around 1010 K for around 120 hours, during which grains of CZTS form. The potassium iodide flux is removed by leaching with deionised water, then the resulting CZTS monograin powder is dried and sieved to select monograins of the desired size, 60-75 μm (much larger than the usual CZTS layer thickness of 1-2 μm). To be incorporated into a solar cell structure, the grains are embedded in a layer of epoxy resin with thickness two-thirds of the grain diameter. This method differs in a number of ways from the typical route of physical vapour deposition or solution deposition followed by sulphurisation annealing, but has achieved relatively high efficiency remarkably quickly. [110]

Spin coating is a solution deposition method. It usually involves creating a colloidal solution of precursors, i.e. a 'sol-gel'; e.g. $Cu(CH_3COO)_2 \cdot H_2O$, $ZnCl_2$, $SnCl_2 \cdot 2H_2O$, and thiourea in dimethyl sulphoxide. Drops of this solution are applied to the substrate, which is rotated to ensure the solution is spread evenly over it. The solvent then evaporates, leaving a film of nanoparticles, which can then undergo sulphurisation annealing to improve the crystallinity. This is a very cheap method as no vacuum is required, but non-uniform coverage can be an issue and so far it has achieved limited success. [405]

Replacement reaction fabrication, a non-vacuum technique that doesn't require a separate sulphurisation stage, has only been achieved relatively recently and has produced remarkably efficient devices for such a recent development. It involves chemical bath deposition of ZnS, followed by submersion in a solution of copper, tin, and sulphur salts in glycerol (water, several alcohols, and acetone have also been used) for ~10 minutes to form CZTS by ionic substitution in the film. [200]

Chemical vapour deposition (sometimes referred to as chemical vapour transport or vapour phase transport) is very similar to thermal evaporation, but a chemical transport agent, bonded to the material to be deposited, is used to encourage reaction upon reaching the substrate. Chemical vapour deposition can be carried out either under vacuum or under open atmosphere, with the latter currently giving the higher record efficiency. Using iodine as a transport agent for the metallic precursors has historically been the most popular method, but $Cu(C_5H_7O_2)_2$, $Zn(C_5H_7O_2)_2$ and $Sn(C_5H_7O_2)_2$ have recently been used most

successfully as raw materials. Precursor deposition is followed by sulphurisation annealing. [406]

Electron beam evaporation is a type of physical vapour deposition, and is carried out under vacuum. The metal or sulphide sources are positively charged and sequentially bombarded with an electron beam produced by a charged tungsten filament under high vacuum. This ejects atoms from the sources, which then precipitate onto the substrate, leaving layers of the source materials. This is followed by sulphurisation annealing. This method has the advantage of a very high deposition rate and good control of stoichiometry in alloy films, but is more expensive than many of the alternative methods. [156]

Hot injection is a solution-based method of fabricating CZTS nanoparticle ink, which is deposited and then annealed to form useable thin films. A highly concentrated precursor solution containing copper, zinc, tin, and sulphur in e.g. oleylamine is injected into a hot (around 570 K) solution containing a capping ligand such as triphenylphosphate (TPP) to form CZTS nanocrystals. After the reaction, the nanocrystal solution is repeatedly washed using standard precipitation and suspension techniques. The CZTS nanocrystal ink is deposited by spin coating or another solution deposition method and the films then undergo sulphurisation annealing. The high volatility and toxicity of most solvents used for this method are problematic, and it generally results in CZTS of low crystal quality because of impurities left from the solvents or capping ligends, and so has not yet produced high-efficiency cells. [407]

Pulsed laser deposition is a vacuum process in which a pulsed laser beam is focused onto a sintered CZTS target pellet made by solid-state reaction of precursors, e.g. Cu_2S, ZnS, and SnS_2 powders. Ablated fragments from the target are deposited on the substrate, then the film is annealed in nitrogen. The advantages of this method are congruent transfer from the target to the film, clean deposition, and flexibility in system engineering. [142]

Ultrasonic spray pyrolysis is a type of thermochemical deposition. It takes place at a high temperature in the absence of oxygen, but not necessarily under vacuum. An atomised vapour of precursors is sprayed onto a heated (~600-800 K) substrate using an ultrasonic nozzle. This uses high-frequency sound to induce capillary waves in a film of liquid on the nozzle surface. When the amplitude of these capillary waves becomes too large to be

sustained, tiny droplets are ejected from each wave, resulting in atomisation. After deposition, the sample undergoes sulphurisation annealing. The advantages of this deposition method include its simplicity, inexpensiveness, and relatively high deposition rate, but it has so far produced only devices with low photovoltaic efficiencies. [348]

Screen printing is a non-vacuum solution deposition technique that doesn't require sulphurisation annealing. CZTS microparticles are prepared from elemental copper, zinc, tin, and sulphur by a four-step method of wet ball milling, isostatic pressing, sintering, and wet ball milling again, then made into a paste with ethyl cellulose in isopropanol. This is printed onto the substrate using nylon monofilament fabric. It is simple, fast, low-temperature, cheap, and versatile, but it has historically been very difficult to achieve, and so is still far behind other fabrication techniques in record photovoltaic efficiency. [341]

Films have also been grown for study, without being used in solar cell devices, by chemical bath deposition, [408] photochemical deposition, [409] and solution dip casting [178]. Bulk single crystals have been grown from a liquid by the traveling heater method [410] and by chemical vapour transport. [411] Bulk polycrystalline samples have been grown by solid-state reaction, [412] high-pressure sintering, [413] and by substitution involving the $2(CuInS_2)$-Cu_2ZnSnS_4 system. [245] Although bulk samples cannot be used in thin-film solar cells, they are useful to study material properties.

Chapter 4:

Fabrication of CZTS by sputtering and sulphurisation annealing

4.1. Introduction

Sputtering is a method of physical vapour deposition for growing thin films. It entails material being ejected from one or more targets by ion bombardment and deposited onto a substrate nearby. An inert gas such as argon is usually used as the ion source. Magnetron sputtering uses a magnetic field to confine sputtering-gas ions near the surface of the target, increasing the deposition rate (typically around 0.1 $Å \cdot s^{-1}$) and reducing the amount of gas used.

Sputtering is a very promising method of fabrication for CZTS because of the reasonable photovoltaic efficiencies achieved so far and the ability to scale the process to an industrial level when required. Fabrication of CZTS by sputtering generally involves two stages: the sputtering itself, in which the copper, zinc, and tin (and sometimes some sulphur) are deposited, followed by sulphurisation annealing, in which the sulphur is added and the crystalline CZTS compound is formed from the precursor materials. The latter is not always necessary if enough sulphur is deposited during the sputtering stage, but it almost universally gives better crystal quality in any case. The details of both processes will be discussed in this chapter.

There are several distinct methods of producing CZTS by sputtering, which are listed along with the record photovoltaic efficiencies achieved using them in Table 11.

Sputtering method	Sulphurisation?	Best efficiency	Year	Reference
Co-sputtering	Yes	11.0 %	2017	[88,162]
Layered sputtering	Yes	9.1 %	2016	[400]
Reactive co-sputtering	Yes	7.9 %	2013	[365]
Single-target sputtering	Yes	6.5 %	2011	[414]
Co-sputtering	No	5.5 %	2014	[415]
Single-target sputtering	No	2.9 %	2014	[416]
Reactive co-sputtering	No	1.4 %	2010	[337]

Table 11: The best photovoltaic efficiencies achieved using various sputtering routes to fabricate CZTS.

Co-sputtering involves several targets being sputtered at once to deposit an amorphous mixture of elemental or sulphide precursor materials. This crystallises during the sulphurisation annealing stage, when sulphur is added if not included in the precursors in sufficient quantity. Alternatively, the deposition can take place on a heated substrate, which results in a crystalline layer without the need for annealing. [415,417] Co-sputtering has been found by direct comparison to give better crystallinity and less secondary phase formation than layered sputtering. [132]

Layered sputtering involves the copper, zinc, and tin being deposited sequentially in separate layers. They then inter-diffuse during the sulphurisation annealing stage, when they react to form the crystalline CZTS. This method has the advantage that the relative amounts of each metal can be controlled very precisely during deposition, but the inter-diffusion can be incomplete, resulting in secondary phases or element loss due to evaporation. [400]

Reactive sputtering means a sulphur-containing gas (usually H_2S) is used to sputter the targets instead of the usual inert argon, so that the metallic elements are partially or completely sulphurised during deposition. This means either that there is less structural disruption during the sulphurisation stage due to the incorporation of extra material, or that no sulphurisation stage is needed at all. [337,365] However, maintaining stable targets and film stoichiometry is problematic using this process. [418-421] Reactive sputtering is usually only used for co-sputtering, as layer sputtering requires an annealing stage anyway

to complete the diffusion of the precursor material. However, reactive layered sputtering has been used to achieve a 'petal' structure, which has been reported to give absorption an order of magnitude higher than regular thin films due to surface effects. [422]

Single-target sputtering uses a pre-fabricated CZTS target (made for example by solid-state reaction) or one consisting of finely mixed sulphide precursors. It is less common than layered and co-sputtering, but has been of increasing interest in recent years. Like co-sputtering, single-target sputtering reduces the need for inter-diffusion of the elements during a sulphurisation annealing stage. It has been shown by direct comparison to give fewer voids than co-sputtering, and so to give a higher photovoltaic efficiency, [423] but despite this, multi-target co-sputtering and layered sputtering continue to produce higher efficiencies than single-target sputtering. Using a single target does not allow fine-tuning of the stoichiometry of the CZTS produced, and the elemental composition of the deposited films is often significantly different to that of the target. [414,416,424-429]

4.2. The sputtering process and its parameters

Sputtering is carried out under ultra-high vacuum. The substrate is mounted in the sputtering chamber above the targets, a flow of argon is provided to each target as the sputtering gas, and a potential difference between the target and the casing (see Figure 42) ignites the gas into a plasma. The targets are pre-sputtered for several minutes with a shutter in front of the substrate to remove contaminants from their surfaces. The deposition rate is measured for each target using a crystal monitor in front of the sample, and used with the desired thickness to calculate the required growth time. The crystal monitor is then removed and the shutter is opened for the required time to deposit the precursor layer. If layer sputtering, this process is repeated for each layer using a single target each time. The sample is rotated by at least one full revolution during one monolayer's growth, in order to avoid directionality developing in the sample. The sample is usually removed to be sulphurised in a separate furnace.

Figure 42: A mounted sputtering target, with open shutter. The target and casing are electrically insulated from each other, and are connected to opposite poles of the power supply. A small gap of around 1 mm exists between them, so the sputtering gas ionises to complete the circuit. The plasma is trapped by a magnetic field generated by a magnetron beneath the target and thus sputters the target material.

Several parameters of the sputtering fabrication process have been examined in detail to determine their effects on the CZTS produced, and on the efficiency of photovoltaic devices using it. These are discussed individually in this section. It should be noted that many of the investigations into these parameters reported in academic literature use an inadequate number of samples, often drawing trends from merely two or three samples. Any such study that is to be really useful in informing an industrial growth process for CZTS solar cells needs to examine all parameters with enough samples to give a high resolution in observing trends, which are quite likely to not be linear over the possible range of values, and to study each parameter as a function of every other one, as their effects are of course highly related.

4.2.1. Substrate and back contact

A 2 mm thick wafer of soda lime glass, ~1 cm × 1 cm in area, is a typical substrate for the growth of laboratory-scale research CZTS cells. They are usually coated in around 800 nm of molybdenum, itself deposited by sputtering (see Sections 3.8.1 and 3.8.2).

With increasing molybdenum sputtering power, the electrical conductivity of the molybdenum increases, the lattice stress within the film changes from tensile to compressive, and the surface grain morphology of the film changes from pyramidal to cigar-shaped. The optimum sputtering power has been found to be 300-600 W. [430]

With increasing sputtering pressure, the electrical conductivity of the molybdenum film decreases, the tensile stress increases, and the grain size decreases. The optimum sputtering pressure has been found to be around 0.7 Pa. [430]

It can be difficult to deposit molybdenum films for the back contact with both sufficiently low resistivity and good substrate adhesion. A two-pressure deposition scheme has been found to be effective at this. It entails a thin layer of molybdenum being sputtered at high pressure (~1 Pa) to give good adhesion, followed by a layer deposited at low pressure (around 0.1 Pa) to achieve good sheet resistance. [431,432]

Rapid thermal annealing of the molybdenum-coated substrate in an inert nitrogen atmosphere (at a peak temperature of between 823 K [433] and 923 K [434] for 10 min) prior to deposition of the absorber layer has been found to be beneficial. This increases the density of the molybdenum, reduces the formation of a resistive MoS_2 layer, and leads to high-quality CZTS. [434] Such pre-annealing also increases sodium doping of the CZTS layer (see Section 3.7.6), because it increases sodium diffusion into the molybdenum from the soda lime glass. [435] Increasing the pre-annealing temperature results in a thinner MoS_2 layer, because it increases both the oxygen and sodium content in the molybdenum layer, so the molybdenum reacts less readily with sulphur during the sulphurisation anneal. [433] However, while having an overall beneficial effect, pre-annealing the molybdenum-coated substrate has been found to enhance the formation of voids and secondary phases in the CZTS layer, and can lower the absorption coefficient and short-circuit current slightly. [434]

4.2.2. Targets

Several groups have used exclusively elemental metallic targets (Cu, Zn, and Sn), but binary sulphide targets for zinc and tin (ZnS and SnS) are also frequently used.

Elemental targets have been found to give larger grain size (1.2 μm for elemental targets; 0.5 μm for sulphide), [242,436] and elemental zinc targets have been found to produce better-performing CZTS solar cells than ZnS, with smoother surfaces and less ZnS between the CZTS and Mo layers, giving better junction characteristics and electrical properties, and ultimately a better photovoltaic efficiency (5.1 % using Zn; 1.0 % using ZnS). [436]

However, the presence of sulphur in the precursors by using sulphide targets minimises the volume expansion during sulphurisation, which improves adhesion between the film and the substrate. [437] Sulphur-containing precursors also give more uniform films with fewer voids and eliminate the formation of secondary phases, which is better for device performance (e.g. 0.1 % and 4.1 % photovoltaic efficiencies have been reported for directly comparable cells using elemental Sn and SnS respectively). [242,438]

Sulphide targets are therefore concluded to be preferable because of the better adhesion, more compact morphology, and reduced secondary phase presence they give, despite elemental targets giving larger grain size.

4.2.3. Layer order

For layered sputtering, the order in which the elemental layers are deposited can have a large impact on the physical properties of the CZTS produced, and so on photovoltaic performance.

The bottom precursor layer (i.e. that at the molybdenum side) should not be copper, as this migrates easily, meaning Kirkendall void formation would be inevitable at the Mo/CZTS interface. [128,439] Similarly, CuS has been found to introduce severe interfacial defects and voids as the bottom precursor layer. [440,441] Zinc is better as it ensures good diffusion throughout the CZTS layer and controls the size of ZnS clusters, [442] but a ZnS bottom precursor has been found to accumulate at the Mo/CZTS interface. [440,441] SnS is the most successful bottom precursor layer; it reduces phase segregation, improves compositional homogeneity and morphology, and leads to improvements in photovoltaic performance. [440,441]

A sulphide bottom precursor layer followed by metallic layers has been referred to as a 'self-constituent buffer layer', i.e. a back passivation layer that becomes absorbed during the CZTS growth, [440,441] but the distinction is somewhat arbitrary.

For metallic precursors, copper should be deposited in between zinc and tin because it easily mixes and alloys with both, while zinc and tin do not readily do so with each other. [346,443] Separating copper and tin has been found to give a particularly large number of voids. [439]

The top layer, or capping layer, has been found to have the largest effect on the resulting film, as it determines the change in composition due to element loss (see Section 4.3.2), which in turn affects the film morphology. Stacks capped by zinc or tin lose significant amounts of these elements during sulphurisation as expected, leaving a rough and cracked morphology. Element loss is significantly reduced for copper-capped precursors, which also give the best resulting film morphology (closely-packed larger surface grains and a very dense structure without any voids). [140,444] A copper capping layer has also been found to give larger grain size, reduce void formation, prevent delamination, produce the largest band gap (1.45 eV as opposed to 1.35 or 1.1 eV), and prevent the formation of $Cu_{2-x}S$, SnS_2, SnS, and ZnS. [445-447]

The preferred layer order is therefore glass/Mo/SnS/Cu/ZnS/Cu.

Additionally, it has been found that the performance of CZTS cells increases with the number of precursor layers; e.g. glass/Mo/SnS/Cu/ZnS/Cu/SnS/Cu/ZnS/Cu is better than glass/Mo/SnS/Cu/ZnS/Cu for the same overall thickness. Specifically, open-circuit voltage improves due to reduced pin-hole formation and short-circuit current increases due to better crystallinity and a reduction in series resistance. [448-450] Increasing the number of precursor layers converges on co-sputtering, giving the advantage of improved crystallinity due to less diffusion being necessary during sulphurisation, but for a relatively small number of layers retains the advantage of layered sputtering that the elemental ratios can be controlled more precisely.

4.2.4. Stoichiometry

It is widely accepted that Cu-poor, Zn-rich samples, with precursor element ratios of Cu/(Zn+Sn) ~ 0.8 and Zn/Sn ~ 1.2, give the best device performance.

This could be due to secondary phases. A higher Cu/(Sn+Zn) ratio has been reported to give a higher percentage of CZTS in the final sample, [451,452] suggesting that the presence of some secondary phases is beneficial. As detailed in Section 3.7.1, the secondary phases formed in a sample are heavily dependent on its elemental composition. For example, SnS has been shown to be the main secondary phase for Cu-poor compositions, and Cu_2SnS_3 for Cu-rich, [453] and so the presence of the former or the absence of the latter could be the cause of Cu-poor samples giving the best photovoltaic performance. Cu_2S could also be responsible; it is formed on the film surface for Cu-correct and Cu-rich, but not Cu-poor, precursors. [439]It is not simply the Cu/(Zn+Sn) ratio though, but the Cu/Sn ratio that must be lower than the stoichiometric value of 50 % to suppress the formation of Cu_2S; depending on the Cu/Sn ratio, Cu_2S can even grow in Cu-poor compositions and can be suppressed in Cu-rich concentrations. [454,455]

The better performance of Cu-poor, Zn-rich samples is more likely to be due to point defects, the formation of which is also affected by the stoichiometry of the sample as detailed in Section 3.7.3. For example, in Cu-poor samples the copper vacancy, V_{Cu}, is likely to replace the Cu_{Zn} antisite as the most common defect in CZTS and become responsible for its inherently p-type nature. [279,456] The concentration of holes is largely unaffected by variation of the chemical composition and this change from Cu_{Zn} to V_{Cu}, however. [289]

Morphology or electrical behaviour could instead be responsible. Grain size has been shown to be smaller for Cu-poor samples than Cu-rich [453,457,458] (although the opposite has also been reported [459]) and the band gap has been shown to increase with decreasing copper content, [456] which is beneficial; however, resistivity has also been shown to increase, [460] which is detrimental. The open-circuit voltage has been shown to increase with increasing zinc content. [461]

Tin content also has an effect on material properties and so photovoltaic performance. It has been shown that as tin content increases grain sizes increases, the band gap increases

by up to 150 meV, and sub-gap absorption decreases by up to two orders of magnitude. [135,292] Excess tin has also been shown to lead to high concentrations of tin-related point defects that limit open-circuit voltage, minority carrier lifetime, and device performance (see Section 3.7.3). [461,462]

The sulphur content has been shown to significantly affect the formation of secondary phases. These are found in samples for S-poor or stoichiometric compositions, but with increasing sulphur excess the phase fraction of pure CZTS increases until no secondary phases are formed for an excess of 10 % (N.B. this is in the sample itself, not just the precursor material or sulphurisation environment). This is of particular relevance to the sulphurisation procedure (see Section 4.3). [463]

4.2.5. Substrate temperature

It is usual for the substrate to be at room temperature during deposition of the CZTS precursor layers, but substrate heating has been reported to have a beneficial effect on the quality of the CZTS produced.

A high substrate temperature of between 500 and 800 K during growth gives denser films and lower compressive stress, which is important for both adhesion and grain growth, [464] and improves the CZTS crystallinity, giving larger grains. [465-468]

Substrate temperature appears to affect the band gap of the resulting CZTS, although it is unclear how. Increasing temperature has been reported both to increase [469] and to decrease [467,470] the band gap.

Substrate temperature also has a significant effect on film composition, because it affects element loss due to the high vapour pressures of Zn, SnS, and S (see Section 4.3.2). As expected, higher substrate temperatures result in more loss of tin and zinc from samples, which must be accounted for in the initial stoichiometry of the precursor. [464]

4.2.6. Sputtering pressure

Low sputtering pressures have been found to lead to delamination and blistering of the final CZTS, due to high compressive stress in the films. To completely suppress blistering, a pressure of 0.65 Pa or above, preferably ~1 Pa, must be used. [135,471,472]

4.2.7. Sputtering power

For reactive DC sputtering of a single compound Cu-Zn-Sn target, a sputtering power of 30 W has been found to lead to a high concentration of V_{Cu} defects, which are largely passivated in $[V_{Cu}^{-} + Zn_{Cu}^{+}]$ defect complexes using 40 W instead. Hence, 40 W was concluded to be better for device performance, [473] although no mechanism or reasoning for this was given.

4.3. The sulphurisation annealing process and its parameters

Once the precursor layers have been deposited, they must be sulphurised to form CZTS by annealing in the presence of sulphur. This step simultaneously introduces the necessary amount of sulphur into the material and crystallises it.

Diode laser annealing has been successfully employed as an alternative to sulphurisation annealing. This heats the CZTS film to a higher temperature but for a much shorter time, and allows the substrate to remain at a much lower temperature. [336] This is a promising method to increase the crystallinity of CZTS, but has not yet been fully developed or widely adopted.

4.3.1. Formation reactions

The reaction of precursor materials to form CZTS during sulphurisation annealing has been shown to proceed in a number of ways. That of sulphide precursors is generally

relatively direct. Parallel reaction pathways for CZTS formation from binary sulphides have been reported:

$Cu_2S + ZnS + SnS_2 \rightarrow Cu_2ZnSnS_4$ [461,474]

$Cu_2S + ZnS + SnS + S \rightarrow Cu_2ZnSnS_4$ [475]

and

$2CuS + SnS \rightarrow Cu_2SnS_3$ [474]

$Cu_2S + SnS_2 \rightarrow Cu_2SnS_3$ [474]

$Cu_2SnS_3 + ZnS \rightarrow Cu_2ZnSnS_4$ [474]

When only copper of the precursor metals is not in sulphide form, the reaction has been found still to proceed by direct reaction of the sulphides: [476]

$4Cu + S_2 \rightarrow 2Cu_2S$

$Cu_2S + SnS_2 \rightarrow Cu_2SnS_3$

$ZnS + Cu_2SnS_3 \rightarrow Cu_2ZnSnS_4$

The reaction of all metallic precursors is generally more complicated; they tend to form alloys by mixing before reacting with sulphur to form preliminary binary or ternary phases that then react to form CZTS. Several different reaction pathways that fit this general pattern have been reported.

First, below around 540 K, binary alloys form:

$Cu + Zn \rightarrow CuZn$ [477]

$5Cu + 8Zn \rightarrow Cu_5Zn_8$ [128,478-480]

$3Cu + Sn \rightarrow Cu_3Sn$ [477]

$6Cu + 5Sn \rightarrow Cu_6Sn_5$ [128,477,480]

These then react with sulphur to form sulphides, between around 540 K and 770 K:

$CuZn + 2S \rightarrow CuS + ZnS$ [477]

$2Cu_5Zn_8 + 21S \rightarrow 5Cu_2S + 16ZnS$ [128,478-480]

$Cu_6Sn_5 \rightarrow 2Cu_3Sn + 3Sn$ [128,478]

$Cu_3Sn + 4S \rightarrow 3CuS + SnS$ [477]

$2Cu_3Sn + 3S \rightarrow 3Cu_2S + 2Sn$ [128,478]

$Cu_6Sn_5 + 11S \rightarrow 6CuS + 5SnS$ [477]

Some formation of binary sulphides from the elements also occurs up to around 570 K:

$2Cu + S \rightarrow Cu_2S$ [480]

$Zn + S \rightarrow ZnS$ [480]

$Sn + S \rightarrow SnS$ [480]

$Sn + 2S \rightarrow SnS_2$ [479]

Between around 570 K and 850 K, binary sulphides or an alloy can form Cu_2SnS_3:

$Cu_2S + Sn + 2S \rightarrow Cu_2SnS_3$ [478]

$Cu_2S + SnS + S \rightarrow Cu_2SnS_3$ [480]

$SnS_2 + Cu_2S \rightarrow Cu_2SnS_3$ [479]

$2Cu_5Sn_4 + 18S \rightarrow 5Cu_2SnS_3 + 3SnS$ [480]

CZTS forms from around 740 K, either from binary alloys or from Cu_2SnS_3:

$Cu_2S + ZnS + Sn + 2S \rightarrow Cu_2ZnSnS_4$ [128]

$Cu_2S + ZnS + SnS + S \rightarrow Cu_2ZnSnS_4$ [478,480]

$2CuS + ZnS + SnS \rightarrow Cu_2ZnSnS_4$ [477]

$Cu_2SnS_3 + ZnS \rightarrow Cu_2ZnSnS_4$ [478-480]

At 800 K CZTS becomes the main phase present, [477] and after 10 minutes at 850 K only fully crystallised CZTS remains, [478] or only CZTS with very small amounts of some binary sulphide phases. [477]

Too high a temperature, above around 820 K, will result in CZTS starting to decompose:

$Cu_2ZnSnS_4 \rightarrow Cu_2S + ZnS + SnS_2$ [479]

In contradiction to the reports of preliminary alloying of the metals, the direct formation of binary sulphides has been predicted using free energy calculations, [131] and this has also been supported with some experimental evidence.

According to these reports, the metals first react to form binary sulphides according to:

$Cu + S \rightarrow CuS$ [481]

$2Cu + S \leftrightarrow Cu_2S$ [132,482]

$Zn + S \leftrightarrow ZnS$ [132,481,482]

$Sn + S \leftrightarrow SnS$ [132,481]

$SnS + 2S \leftrightarrow Sn_2S_3$ [132]

$Sn_2S_3 + S \leftrightarrow 2SnS_2$ [132]

$Sn + 2S \rightarrow SnS_2$ [482]

These can form Cu_2SnS_3:

$2CuS + SnS \rightarrow Cu_2SnS_3$ [481]

$Cu_2S + SnS + S \rightarrow Cu_2SnS_3$ [132]

$Cu_2S + SnS_2 \rightarrow Cu_2SnS_3$ [482]

CZTS then forms from the binary sulphides or from Cu_2SnS_3:

$Cu_2S + ZnS + SnS_2 \rightarrow Cu_2ZnSnS_4$ [132]

$Cu_2SnS_3 + ZnS \rightarrow Cu_2ZnSnS_4$ [132,481,482]

The formation reactions of CZTS are not simple; it is still unclear exactly which reaction pathway CZTS will form via under given fabrication conditions, as the effects of several factors and parameters of the sulphurisation process are not yet fully understood. These are discussed individually in the following sections.

4.3.2. Element loss

Loss of both tin and, to a lesser extent, zinc from samples during sulphurisation annealing has been found to be quite problematic. [483-486] It significantly affects the stoichiometry of samples and can lead to composition gradients as zinc and tin diffuse to the surface. [487] The vapour pressures of some relevant materials over a range of temperatures are plotted in Figure 43.

Although pure tin has a very low vapour pressure (e.g. 2.1×10^{-4} Pa at 1070 K [488]), that of SnS is high (e.g. 250 Pa at 1070 K [492]), meaning that SnS sublimes at 620 K [493] and above this is easily lost from samples at lower pressures.

The vapour pressure of ZnS is relatively low (e.g. 0.16 Pa at 1070 K [489]), but that of elemental zinc is higher (e.g. 26 kPa at 1070 K [491]), meaning that zinc sublimes at 700 K [493] and above this is lost from samples at lower pressures.

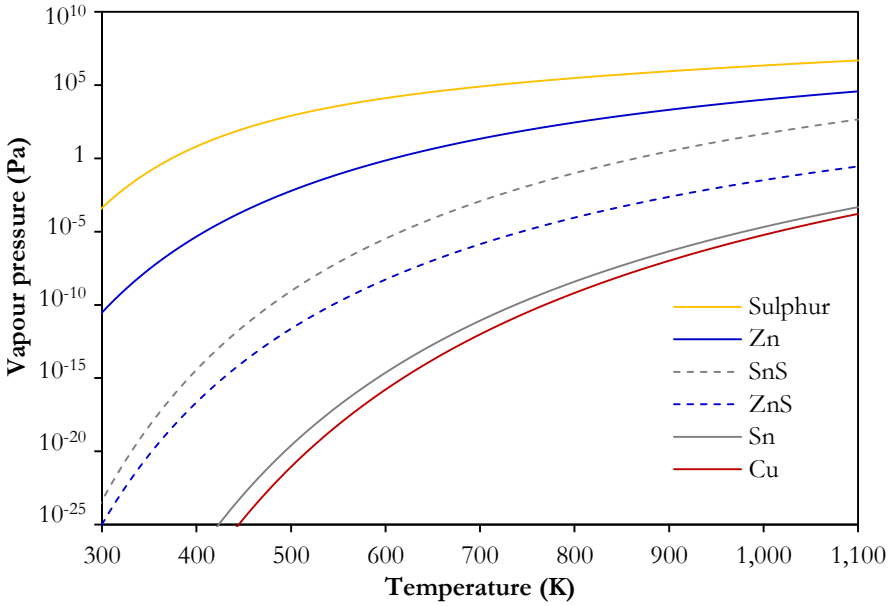

Figure 43: The vapour pressures of elements and binary phases relevant to the formation of CZTS. Data from [488-491].

CuS dissociates into copper and sulphur rather than evaporating, and elemental copper has a very low vapour pressure (e.g. 7.0×10^{-5} Pa at 1070 K [488]), so copper loss is not reported as a problem during fabricating CZTS.

For comparison, the vapour pressure of sulphur at 1070 K is 3.8 MPa. [490]

Several phases, including full CZTS, decompose according to the following reactions, which leads to evaporation of SnS: [485]

$$Cu_2ZnSnS_4 \leftrightarrow Cu_2S + ZnS + SnS + S$$

$$2Cu_2SnS_3 \leftrightarrow Cu_4SnS_4 + SnS + S$$

$$Cu_4SnS_4 \leftrightarrow 2Cu_2S + SnS + S$$

It has been shown that tin loss during annealing increases with decreasing Cu/(Zn+Sn) ratio, i.e. that tin loss is correlated with decreasing copper content, suggesting that copper in some way binds the tin and prevents its evaporation. [307,494]

For layer sputtering, element loss is significantly reduced when the top precursor layer contains copper (see Section 4.2.3). An attempt has been made to replicate this effect for a co-sputtered sample, but it was unsuccessful. The CZTS precursor was deposited by reactive sputtering using sulphide targets, and a separate CuS layer was temporarily

deposited on top of this for the annealing stage and then removed by KCN etching. However, not only did such a cap not prevent loss of SnS, it also detrimentally affected the stoichiometry of samples, making them copper-rich. [495]

Another method that successfully reduces tin loss is to use SnS_2 as a precursor and employ a two-stage sulphurisation annealing process (at 533 K and 783 K). This allows the CZTS phase to form at the lower temperature, before SnS_2 decomposes into volatile SnS, and then improve in crystal quality during the short higher-temperature stage. [417]

Simply sulphurising at a high pressure, of 105 Pa, has also been found to significantly reduce tin loss. [134]

The additional presence of SnS vapour during sulphurisation has also been found to reduce the loss of tin from the film, [496-498] as has using a static, closed sulphurisation environment rather than a dynamic one of flowing gas, [405] and using an inert gas atmosphere rather than a vacuum, i.e. the sulphurisation gas (S or H_2S, see Section 4.3.5) mixed in N_2. [485]

4.3.3. Thiourea pre-treatment

Submerging the precursor layers in thiourea for 10 minutes prior to sulphurisation has been found to enhance the crystalline structure, electrical properties, and morphology of the resulting CZTS. These improvements are due to a decrease in strain and dislocation density, although no mechanism for how thiourea effects this has been proposed. [499]

4.3.4. Pre-annealing

An annealing stage of around one hour in a vacuum prior to sulphurisation has been shown to be beneficial for device performance.

Pre-annealing ensures full inter-diffusion of the metals, promoting their alloying before the formation of sulphide phases. This can reduce the loss of tin and zinc, improve the crystallinity and compositional uniformity of the CZTS, give a more densely packed

morphology with fewer voids, and give much better adhesion to the molybdenum layer. [500-506]

A pre-annealing step also makes the surface composition more Cu-poor and Zn-rich compared to the bulk, which has led to an increase in photovoltaic efficiency (from below 3 % to 8.3 %). [507]

Pre-annealing also results in a much thinner layer of MoS_2 forming between the molybdenum and CZTS layers. [501]

Reports on the optimum pre-annealing temperature have differed. 443 K has been proposed, which gave less void formation and a smoother surface than temperatures higher than 493 K. [505] 570 K has also been reported, as CZTS crystallinity, morphology and band gap improved with increasing pre-annealing temperature up to this value, then deteriorated due to the formation of secondary phases. [508] A higher pre-annealing temperature of 723 K has also been reported to give improved performance; however, it was found that using H_2S as part of the pre-annealing atmosphere gave further significant improvement, making the process simply a two-stage sulphurisation rather than a pre-annealing step followed by sulphurisation. [509]

4.3.5. Sulphurisation gas

Both H_2S gas and elemental sulphur vapour have been used to sulphurise precursor layers. H_2S has the advantages that it is easy to introduce into the reaction chamber in a controlled way and the sputtering chamber can theoretically be used for sulphurisation in situ; however, specialist equipment is required due to its toxicity. Elemental sulphur is comparatively safe, but more difficult to control. [128]

Some studies have found that sulphurisation in elemental sulphur vapour gives better compositional uniformity than H_2S. [510,511] However, others have found that H_2S gives better crystallinity than elemental sulphur, [242] and that it gives much more uniform films with larger grains (almost 5 μm in diameter compared with 1 μm using sulphur vapour). [512]

Elemental sulphur vapour can itself be introduced in a several ways. Most common is to place a boat of sulphur powder or pellets in the furnace with the sample, usually both inside a graphite box to regulate the sulphur pressure. For this method, the sulphur is not entirely incorporated into the sample, so a 30 % excess of sulphur powder is necessary to give approximately stoichiometric sulphur content. [513] A flux of sulphur vapour introduced into the furnace as a gas has also been tested. The latter has been found to give better film morphology. [514]

If using H_2S gas, the concentration has been found to have little effect on film properties, from 5 % to 20 %. [515]

The additional presence of SnS vapour during sulphurisation reduces the loss of tin from the film (see Section 4.3.2) and leads to a more stable film surface. [496-498] However, an overpressure of SnS has been shown to guarantee the presence of deep defect states that decrease the minority carrier lifetime. [516] Using an inert gas atmosphere rather than a vacuum also reduces tin loss, so the sulphurisation gas (S or H_2S) should be mixed in N_2. [485]

A static annealing environment is better than a dynamic one, i.e. a sealed sulphurisation chamber is better than one with a constant gas flow. Grain size has been found to improve from 400-500 nm for dynamic sulphurisation to 700-800 nm for static sulphurisation, the thickness of the MoS_2 layer to reduce from 400 nm to 300 nm, and photovoltaic efficiency to increase significantly. [405] This is due to a higher sulphur and SnS partial pressure being maintained using static sulphurisation, which reduces the loss of tin (see Section 4.3.2).

4.3.6. Sulphurisation pressure

Sulphurisation pressure can affect the stoichiometry of the resulting CZTS: a sulphur vapour pressure of 1.3 MPa has been found to give near-stoichiometric samples while 0.1 & 0.7 MPa gave S-poor samples and 2.7 MPa gave S-rich samples. [517] A high sulphurisation pressure of 10^5 Pa has been found to significantly reduce tin loss (see Section 4.3.2). [134]

Morphology is also affected. A low sulphurisation pressure (0.03 MPa [518] to 1 MPa [519]) has usually been found to give large grain size, [128,518-520] although decreasing pressure has also been reported to decrease grain size. [517,521]

CZTS decomposition can be avoided by using a background pressure of inert gas above around 10 MPa. [128] However, too high a pressure can result in SnS reacting to form SnS_2, which then remains in the sample, instead of CZTS. [522]

A low sulphurisation pressure (0.03 MPa) of background nitrogen, rather than atmospheric pressure, gives higher compressive stress in the film, which results in smaller lattice parameters and a smoother film surface. It also gives a greater concentration of V_{Cu} defects, which are preferable to the competing Cu_{Zn}. These improvements gave a significantly increased photovoltaic efficiency, from 1.3 to 3.0 % for comparable cells using 0.03 and 0.1 MPa respectively. [518]

4.3.7. Sulphurisation temperature

Reported sulphurisation temperatures generally range from 820 to 870 K. The optimum temperature has been computationally calculated to be much lower, between 600 K and 750 K, [287] but it has been experimentally reported to be between 770 K and 870 K, [338] around 770 K, [137] around 790 K, [523] and around 850 K. [432]

Although formation of the CZTS phase has been found to start at around 570 K [524] or 670 K, [525] sulphurisation below 770 K has been found to give incomplete formation of CZTS, with Cu_2S, ZnS, and Cu_2SnS_3 also present, [140] which were eliminated to give pure CZTS by 10 min at 800 K [511,526] or 820 K. [448] Another study found that the formation of CZTS was incomplete for sulphurisation below 850 K. [432] The presence of sodium from soda lime glass substrates has been reported to lower the temperature required for complete CZTS formation: it was reduced from around 870 K for substrates without sodium such as quartz, to around 670 K for soda lime glass. [133]

Sulphurisation temperatures above 810 K [510] or 850 K [432] have been reported to cause the CZTS to decompose into Cu_2S, SnS, ZnS and S, which then left voids and pinholes

because of tin loss (see Section 4.3.2), which significantly reduce the photovoltaic performance of cells.

Increasing sulphurisation temperature also increases the thickness of the MoS_2 layer, which is detrimental to photovoltaic performance (see Section 3.8.2). [459]

Grain size has been found both to increase [301,390,459,527-530] and to decrease [531,532] with increasing sulphurisation temperature from 500 to 900 K, generally in the range 200-800 nm. The surface morphology of films becomes rougher with higher sulphurisation temperature. [479,519,531]

An increase in band gap has also been observed with both increasing [191,533] and decreasing [534] sulphurisation temperature, and one report has found that the sulphurisation temperature has little or no effect on the band gap value. [469]

It has been calculated that high annealing temperatures, which will give more disordered samples, will give lower open-circuit voltages. [286] However, it has been found that as sulphurisation temperature increases from 620 to 770 K [414] and from 770 to 870 K [535-538] the open-circuit voltage, short-circuit current, shunt resistance, and fill factor increase, and the series resistance decreases, all of which give higher photovoltaic efficiency.

A two-stage sulphurisation annealing process, at two different temperatures, has been found to be beneficial. This reduces secondary phase presence and tin loss, as the CZTS phase forms at the lower temperature, before SnS_2 decomposes into volatile SnS. The CZTS then improves in crystal quality during the short higher-temperature stage. Such two-stage temperature schemes include 533 K for 75 mins then 783 K for 15 mins, [417] and 723 K for 60 min then 823 for 15 min. [509]

4.3.8. Sulphurisation time

Sulphurisation annealing is usually carried out over around an hour, with heating rates of the order 10 $K \cdot min^{-1}$. This relatively long sulphurisation time will have a significant impact on the monetary cost and energy cost of producing CZTS solar cells on an industrial scale, and has been examined closely because of this.

A rapid thermal annealing approach has been found successful, in which the first stage of sulphurisation (the formation of Cu_2S, ZnS, and liquid tin) is complete after 60-150 seconds at 770 K and the formation of CZTS from these intermediaries takes only 3-5 minutes. Such a rapid thermal annealing process has been found to give better device performance due to less void formation. [128,539]

However, it has also been reported that the formation of CZTS takes longer than 30 minutes, only being complete after around an hour, and that shorter sulphurisation times leave secondary phases present. [540] Even if the formation of CZTS is complete after around 5 minutes, the photovoltaic performance of devices is improved for annealing times longer than this. Approximately 30 minutes [541] or 50 minutes [128] has been found to be the optimum annealing time. Longer sulphurisation times also result in a more compact morphology and reduced presence of secondary phases. [542]

Band gap has also been shown to change over extended sulphurisation: initially around 1.4 eV, it passes through a minimum after 10-15 minutes of sulphurisation before slowly rising towards a maximum of around 1.55 eV over around 2 hours. It was suggested that this is due to the formation of the stannite CZTS phase initially, which only over extended annealing forms the thermodynamically preferable kesterite phase, via a solid solution of both. [128]

An increase in grain size was also observed with annealing after the initial few minutes: immediately after formation of the CZTS phase, the grain diameter was found to be approximately 0.3 μm on average; further annealing gave an initial rate of grain size increase of approximately 8×10^{-5} μm·s^{-1}, up to the maximum grain size observed, 0.55 μm. [128]

Electrical conductivity, the concentration of both acceptors and donors, the density of traps at the grain boundaries, and the grain-boundary potential barrier height all increase with increasing annealing time. [304]

4.3.9. Sulphurisation heating and cooling rates

As well as the duration of the sulphurisation stage, the heating and cooling rates have an important effect.

Rapid heating can be problematic: delamination of the CZTS layer has been found to occur for heating rates above 0.5 $K \cdot s^{-1}$. [543] A rapid heating rate of 21 $K \cdot min^{-1}$ has also been found to give incomplete conversion of precursor materials to CZTS, with amorphous secondary phases remaining present, and a bubble-like morphology. [544] A slower rate of 2 $K \cdot min^{-1}$also produced some SnS and $Cu_4Sn_7S_{16}$ secondary phases, but it gave much better crystal quality. [544] Slower heating rates additionally give larger grain sizes but rougher CZTS film surfaces. [545]

Rapid cooling is often employed to avoid decomposition of the sulphurised CZTS film, but this has been found to result in a high density of Cu_{Zn} and Zn_{Cu} antisite defects, which contribute to band gap tailing and lower the open-circuit voltage (see Section 3.7.3). [293] Slow cooling has been confirmed to produce low crystalline disorder in CZTS, as the ordered structure is only energetically favourable below the order-disorder phase transition around 550 K (see Section 3.6). 1 $K \cdot min^{-1}$ has been concluded to be the maximum cooling rate that gives samples without significant tin disorder. [546]

4.3.10. Delamination and blistering

Delamination or blistering, i.e. partial and localised delamination, are problematic phenomena of the sulphurisation annealing process. They are due either to the relief of in-plane stress caused by thermal expansion/compression, or to gas formed in the material congregating at an interior layer interface rather than diffusing out of the sample. [472]

Rapid heating rates, above 0.5 $K \cdot s^{-1}$, have been found to be a particular cause of significant delamination of the CZTS layer. [543]

It has also been found that low sputtering pressures (see Section 4.2.6) give increased compressive stress in CZTS films, which leads to increased blistering. To completely suppress blistering, a pressure of 650 kPa or above must be used. [135,472]

Sputtering gas entrapment, and blister formation due to it, has been observed to decrease for higher sputtering pressures, higher substrate temperatures, and using a sputtering gas with larger atoms. [471]

4.3.11. Post-sulphurisation oxidation

Sodium atoms that diffuse into the CZTS layer from the soda lime glass substrate (see Section 3.7.6) have been found to congregate at the surface of the CZTS layer during sulphurisation as Na_xS impurities. These are harmful for the subsequent CdS buffer layer deposition as they give reduced grain growth and poorer morphology. It has been found that leaving samples in air for around 24 hours before deposition of the CdS layer is beneficial, as these Na_xS defects are oxidised first to Na_2SO_3 after around 1.5 hours (these are still harmful to the CdS deposition process) and then to Na_2SO_4 after around 24 hours. The latter compound is much less detrimental to the CdS growth, giving a much more homogeneous layer. [547]

4.3.12. Post-sulphurisation etching

Post-fabrication etching is often used to remove unwanted secondary phases (see Section 3.7.1). An aqueous KCN solution has been found to remove Cu_xS impurities, [264-266] and to enhance the energetic barrier to recombination across the CZTS/CdS interface. [267] An aqueous HCl solution has been found to remove ZnS impurities and significantly increase photovoltaic efficiency. [268] Tin-based secondary phases have proved more difficult to eliminate by etching, although Na_2S has been found to remove SnS. [269] A final soak in deionised water for 10 minutes has been found to preferentially eliminate any metal oxide impurities. [158]

Chapter 5:

Experimental techniques

5.1. Introduction

The second half of this thesis presents studies of bulk polycrystalline samples of CZTS produced by solid-state reaction of elemental powders and of thin films produced by layered magnetron sputtering followed by sulphurisation. Details of the specific fabrication procedures, experimental equipment, and analysis methods used for each batch of samples are described in in the relevant experimental chapters, 6-9.

This chapter covers the theory and basic operational procedures behind the analytical techniques used in the experimental chapters. An in-depth knowledge of the physical processes behind these techniques is generally required to enable accurate and meaningful interpretation of the results. They are presented in order from simple physical, through chemical and structural, to detailed optoelectronic characterisation. Reference spectra and values relevant to CZTS and its secondary phases are also given here where appropriate.

5.2. X-ray reflectivity (XRR)

X-ray reflectivity can be used to determine parameters of thin films such as thickness, density, and interface roughness. It entails a grazing-incidence X-ray beam specularly reflecting from the sample, i.e. with angle of reflection equal to angle of incidence.

X-rays undergo total reflection when incident at an angle less than the critical angle for total reflection, θ_C. Above θ_C reflectivity decreases rapidly with increasing angle of incidence, proportionally to θ^4. A logarithmic scale is therefore used to plot XRR intensity because of the large range of intensity covered.

Interference occurs between X-rays reflected from the surface and from interfaces lower down in the sample, which results in oscillations of the reflected intensity as a function of reflection angle, called Kiessig fringes. [548] Maxima correspond to constructive interference and minima to destructive interference.

The period and profile of these Kiessig fringes can be used to determine the thickness of each layer of the sample by computational model fitting. Similarly, the amplitude of Kiessig fringes gives information on the density of the layers and interface roughness: the bigger the amplitude, the smoother the surface. The decay rate of reflectivity with increasing angle reveals the surface roughness: the quicker the decay, the rougher the surface. [548] Example XRR patterns are shown in Figure 44.

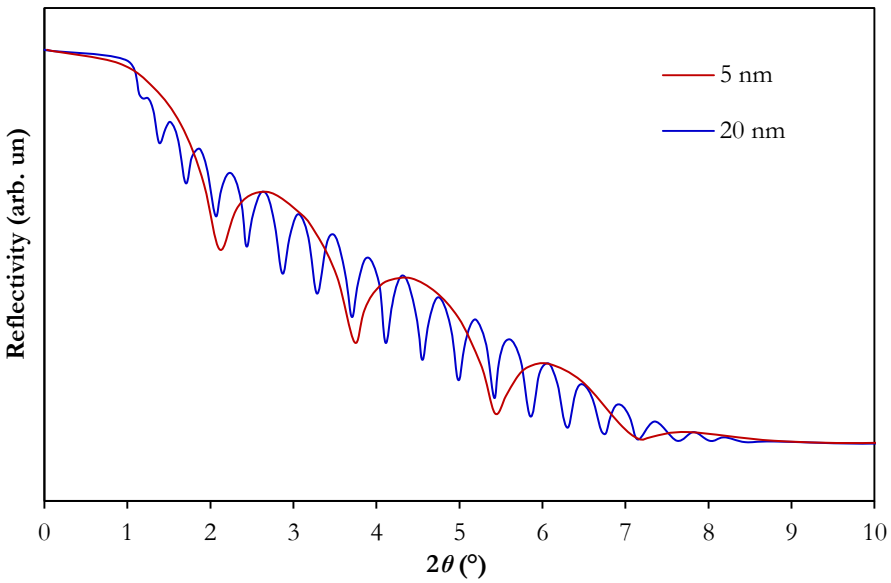

Figure 44: Example XRR patterns showing Kiessig fringes of different frequencies for films of different thicknesses. Data from [548].

The critical angle for total reflection is related to the refractive index, which is given by

$$n = 1 - \delta - i \cdot \beta \ , \qquad (21)$$

where δ and β are defined as:

$$\delta = \frac{r_e \lambda^2 N_0 \rho}{2\pi} \frac{\sum_i x_i \left(Z_i + f_i'\right)}{\sum_i x_i M_i} , \quad (22)$$

$$\beta = \frac{r_e \lambda^2 N_0 \rho}{2\pi} \frac{\sum_i x_i \left(Z_i + f_i''\right)}{\sum_i x_i M_i} , \quad (23)$$

where r_e is the classical radius of an electron (2.82×10^{-9} m), λ is the X-ray wavelength, N_0 is the Avogadro number (6.02×10^{23} mol^{-1}), ρ is the density of the film material, x_i is the atomic molar ratio of the i^{th} element in the film composition, Z_i is the atomic number of the i^{th} element in the film composition, f_i' & f_i'' are the anomalous scattering correction factors of the i^{th} element in the film composition (see Section 5.6.3), and M_i is the atomic mass of the i^{th} element in the film composition. [548]

The critical angle for total reflection is given by

$$\theta_C = \sqrt{2\delta} = \sqrt{\frac{r_e \lambda^2 N_0 \rho}{\pi} \frac{\sum_i x_i \left(Z_i + f_i'\right)}{\sum_i x_i M_i}} , \quad (24)$$

so the density of the film can be calculated from a measurement of the critical angle.

The Kiessig fringe oscillation is described by:

$$I \propto \cos\left(\frac{4\pi d}{\sqrt{\sin^2\left(\theta - 2\delta\right)}} \right) , \quad (25)$$

so the film thickness d can be calculated from the oscillation frequency. This is usually done by computationally Fourier transforming the intensity profile. If the film has more than one layer, the computation is more complicated, and is executed by non-linear least-squares fitting. Several software programs are available for the analysis of XRR curves. GenX was used for the experiments reported in this thesis. [548]

5.3. Scanning electron microscopy (SEM)

SEM is an imaging technique that can give both morphological and compositional pictures of a sample surface on the micro/nanoscale.

A beam of electrons is typically generated from a tungsten filament electron gun and accelerated to an energy of 0.2-40 keV. It is rastered over the sample using electromagnetic deflection coils and the detected signal for each point is assigned as a pixel value of the resulting image. Using electrons enables smaller wavelengths to be used than are possible with optical microscopes, so SEMs can achieve much higher resolution: better than 1 nm. [549]

When the primary-beam electrons enter the sample, they scatter from atoms within a teardrop-shaped interaction volume that extends for several hundred nanometres. There are two detector configurations, to make use of two types of scattered electrons that are emitted from the sample surface: backscattered (high-energy) and secondary (lower-energy) electrons. X-rays are also emitted, which can be used in energy-dispersive X-ray spectroscopy (see Section 5.4) [549]

5.3.1. Backscattered electron imaging

Elastic scattering of the primary electrons can occur at sufficiently high angles to return them out of the sample surface to be detected above it. The backscattered electron detector forms a ring around the primary electron beam.

The strength of this scattering is dependent on atomic mass, so backscattered electrons reveal information about the spatial variation in chemical composition of a sample, with areas containing heavier elements appearing brighter. [549] An example backscattered electron image is depicted in Figure 45.

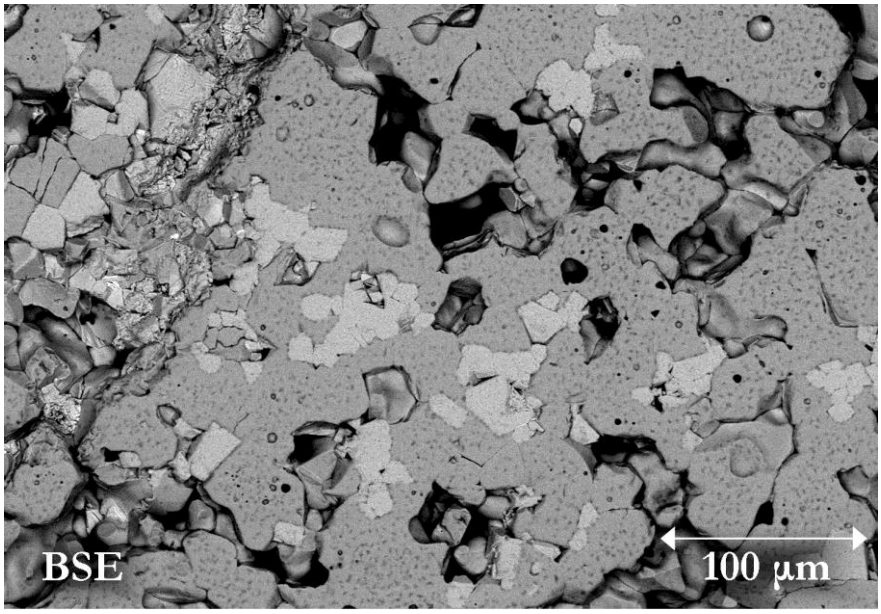

Figure 45: An example backscattered electron (BSE) image of a CZTS sample from Chapter 6.

5.3.2. Secondary electron imaging

Inelastic scattering, i.e. the transfer of energy from a primary beam electron to an electron in an atom of the sample, leads to secondary electrons being ejected from their atoms. These can also leave the sample and be detected above it by a secondary electron detector to one side of the backscattered electron detector. As secondary electrons have a lower energy, typically originating from nearer the sample surface, they are attracted to the detector by a positively charged metal grille. [549]

More secondary electrons can escape in rough or slanted regions, where the greater surface area means a greater interaction volume is close to the surface, so secondary electrons are used to image the morphology of a sample. [549] An example secondary electron image is depicted in Figure 46.

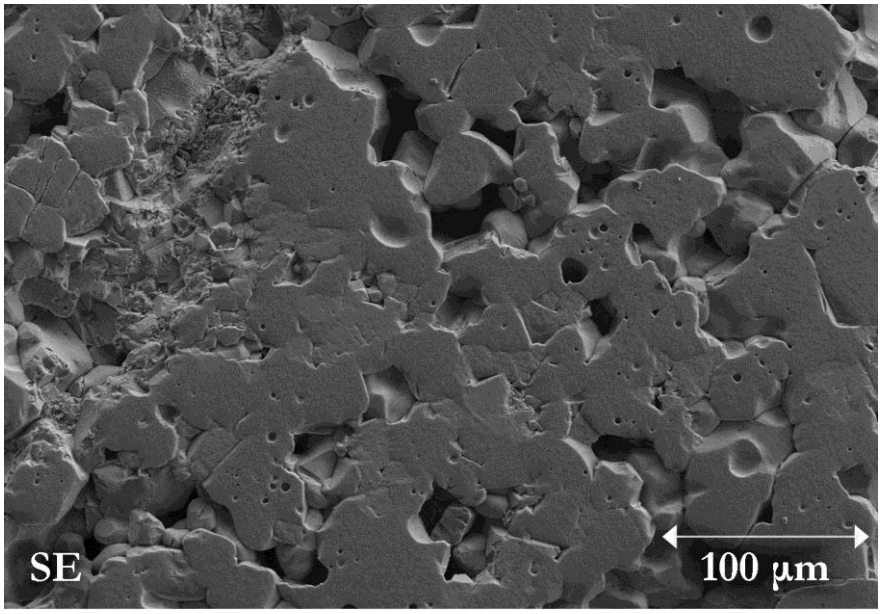

Figure 46: An example secondary electron (SE) image of a CZTS sample from Chapter 6.

5.3.3. Focused ion beam (FIB) milling

FIB systems use a finely focused, high-current beam of ions (usually gallium) to mill a small region of a sample with very high accuracy, revealing a smooth cross section. This is very useful for measuring the thickness and morphology of thin film layers. [272]

Most FIB systems use liquid metal ion sources, in which gallium coats a tungsten needle by wetting. At the tip of the needle the electric field and surface tension form the gallium into a Taylor cone, which has a very small radius of around 2 nm. The large electric field at this tip ($>10^8$ V·cm^{-1}) causes the gallium atoms to ionise and be emitted. These free ions are then accelerated to an energy of 1-50 keV and focused onto the sample by electrostatic lenses. [549]

The beam of primary ions hitting the sample surface sputters a small amount of the sample material as secondary ions. At high beam currents this sputtering can be used to mill a trench into the sample, exposing a cross section for imaging, which is usually done using an SEM in the same system. [549]

At low beam currents FIBs can also be used to image samples by detecting secondary ions or secondary electrons as the beam is rastered over the sample, with a resolution of a few

nanometres. However, most FIB systems feature an SEM, which is preferable for imaging because FIB microscopy is inherently destructive to the sample whereas electron microscopy is not. [272]

5.4. Energy-dispersive X-ray (EDX) spectroscopy

EDX is a technique used for chemical characterisation and elemental analysis. A beam of energetic particles (e.g. X-rays or electrons; EDX is often carried out in an electron microscope) is used to excite electrons from the lower energy levels of atoms in the sample. An electron from a higher level then decays into each vacant state, emitting the energy difference as an X-ray. The spectrum of this emission is determined by the atomic structure of the atoms in the sample. X-rays are referred to by the lower-energy shell the electrons fall into during their emission (K, L, M, etc.) and then by the higher-energy shell they fall from (α, β, γ, etc. in order of increasing energy from the shell just above that the electron ends in), e.g. an electron falling from the L shell to the K shell of a copper atom emits a Cu-Kα X-ray.

The emission spectrum can be measured by an energy-dispersive spectrometer and used to determine the elemental composition of a sample, with an accuracy of around ±1 %. An example spectrum for a sample of CZTS is given in Figure 47. Elemental maps of a sample can be made by recording an EDX spectrum for each point as the primary beam is rastered over the sample. The spatial resolution is determined by that of the primary beam, typically around a micrometre. [549]

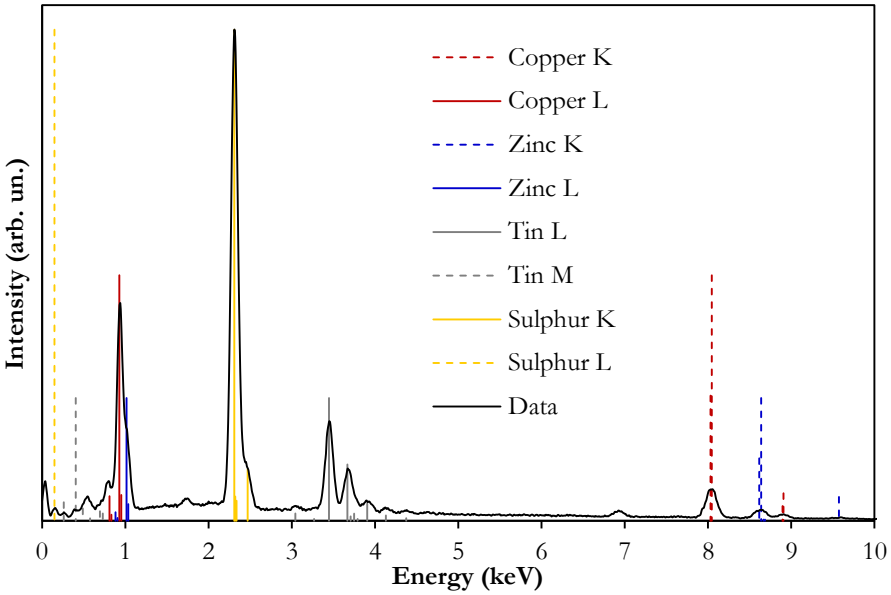

Figure 47: An example EDX spectrum for a CZTS sample from Chapter 6. The emission lines for each element are plotted for comparison, scaled by element to the ideal ratio of 2:1:1:4 for Cu:Zn:Sn:S and with each emission series (K, L, and M) normalised by its most intense line.

5.5. Inductively coupled plasma mass spectrometry (ICPMS)

ICPMS is a way to determine the average elemental composition of a sample. A small amount of the sample is dissolved in a strong acid, diluted, and ionised using an inductively coupled plasma in order to carry out mass spectrometry on it. Metals and several non-metals can be detected at concentrations as low as one part in 10^{15}. [550]

A torch consisting of three concentric quartz tubes is placed inside an induction coil carrying a radio-frequency electric current. A flow of argon is introduced between the inner and middle tubes and ignited by an electric spark to become a plasma, which is sustained by the magnetic field of the induction coil, making it an inductively coupled plasma. Its temperature is around 10,000 K. The sample, dissolved in strong acid and diluted, is introduced into the central tube as a mist of liquid using a nebuliser, with another flow of argon as a carrier gas. The sample mist evaporates and molecules break apart due to the heat from the plasma. As the sample gas emerges from the central tube, it is ionised by

contact with the argon plasma. A third flow of argon surrounds the two inner tubes as a coolant. [550]

The plasma ions then enter a mass spectrometer, which separates them using their mass-to-charge ratio. This can simply be achieved by accelerating them horizontally using an electric field while gravity accelerates them downwards. Their vertical position as they hit a vertical detector after a certain distance is then a measure of their charge-to-mass ratio. The relative intensity measured for each ratio value allows the compositional ratio of each isotope present in the sample to be measured. [550] The design of an ICPMS system is illustrated in Figure 48.

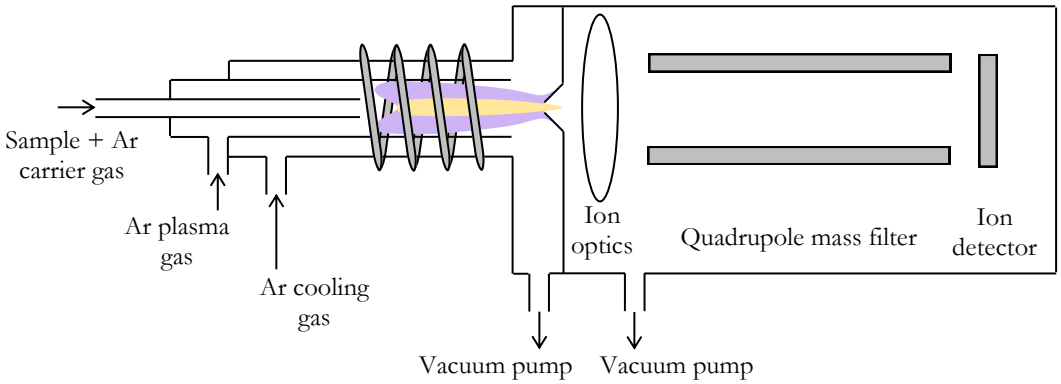

Figure 48: A schematic diagram of an ICPMS system. Not to scale.

The advantages of ICPMS are high accuracy and the measurement of an average elemental composition over the entire sample rather than a local composition at one point (assuming the small amount of material used is representative of the entire sample, i.e. the sample was powdered and mixed thoroughly). Its disadvantages are that it is destructive; the sample material must be dissolved in acid to be used and cannot be recovered. Additionally, sulphur cannot be accurately detected using ICPMS, so other methods such as EDX (see Section 5.4) must be used for sulphur content measurement. [550]

5.6. X-ray diffraction (XRD)

XRD is a powerful technique that can reveal the phase fractions and crystal structures of materials present in a sample, including associated parameters such as site occupancies and lattice parameters.

It entails a beam of X-rays being diffracted by the sample. This only occurs at angles for which X-rays scattered from any parallel atomic lattice planes in the sample interfere constructively. This occurs when the Bragg condition for diffraction,

$$\lambda = \frac{2d_{hkl}\sin(\theta)}{n}\ , \qquad (26)$$

is met, where n is the order of diffraction (an integer, assumed to be 1), λ is the wavelength of the X-rays, and d_{hkl} is the atomic planar spacing of the (hkl) planes, where h, k, & l are the Miller indices denoting the plane. [551] This is illustrated in Figure 49.

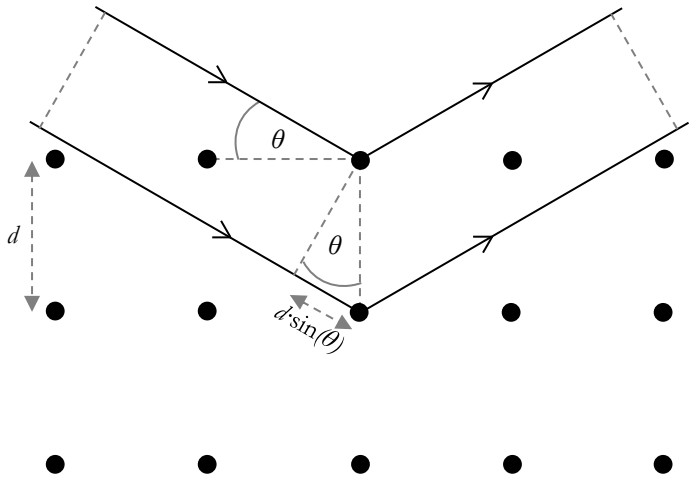

Figure 49: The geometry of X-ray diffraction. X-rays scattered from the second plane of atoms will only be in phase with those scattered from the first plane, and so interfere constructively, when the extra distance they travel, $2d\cdot\sin(\theta)$, is equal to an integer number of their wavelengths. The same holds for all deeper planes of atoms, each of which adds $2d\cdot\sin(\theta)$ to the distance travelled by the X-ray.

In the standard Bragg-Brentano experimental geometry, illustrated in Figure 50, the diffracted intensity is measured as a function of angle relative to the source, 2θ. Distinct peaks in measured intensity are observed for angles satisfying the Bragg condition for any set of parallel atomic planes. Using a powdered sample ensures that every crystal orientation is represented. [551]

The positions of diffraction peaks give information on all lattice planes present in a crystal, and so can be used to identify the structural space group and lattice parameters of the phases in a sample.

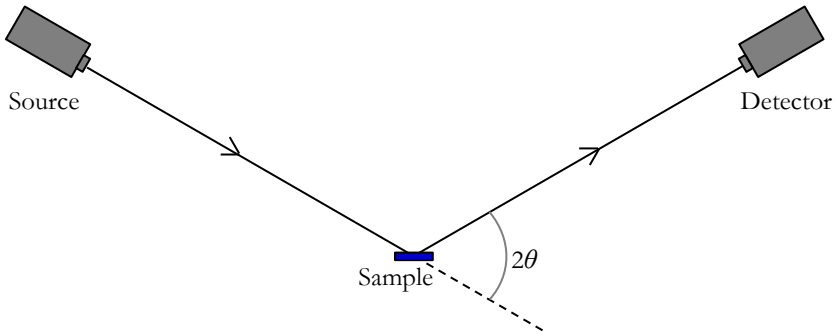

Figure 50: The Bragg-Brentano experimental geometry. The detector is moved in an arc around the sample, measuring intensity as a function of 2θ relative to the stationary X-ray source, while the sample plate is rotated to maintain an angle of θ relative to both the source and detector.

For example, the planar spacing of the tetragonal kesterite structure can be expressed as

$$\frac{1}{d_{hkl}^{\,2}} = \frac{\mathrm{h}^2 + \mathrm{k}^2}{a^2} + \frac{\mathrm{l}^2}{c^2} \ , \tag{27}$$

where h, k, & l are Miller indices and a & c are the lattice parameters. Combining this with Equation (26) gives

$$\sin^2(\theta) = \frac{\lambda^2}{4a^2} \cdot \left(\mathrm{h}^2 + \mathrm{k}^2\right) + \frac{\lambda^2}{4c^2} \cdot \mathrm{l}^2 \ , \tag{28}$$

which can be used with the 2θ values of the XRD peaks to refine the values of a and c for a sample of CZTS.

The intensity of each peak is determined both by instrumental factors and the square modulus of the X-ray structure factor, $|F_{hkl}|^2$, which is given by

$$F_{hkl} = \sum_j f_j \exp\left(-2\pi \mathrm{i}\left(\mathrm{h}x_j + \mathrm{k}y_j + \mathrm{l}z_j\right)\right) \ , \tag{29}$$

where the sum is over all atoms in the unit cell, f_j is the scattering form factor of the j^{th} atom, and x_j, y_j, and z_j are the position coordinates of the j^{th} atom within the unit cell. X-rays interact with the electron cloud during scattering, so the form factors are dependent on the number of electrons associated with the respective atoms. This can be used to identify the specific elements at each point within a crystal structure. For some values of h, k, and l, the contributions from each atom cancel, meaning that some peaks do not appear in the diffraction pattern. Each crystalline material therefore has a characteristic pattern of peaks and peak intensities, which can be used to identify all the phases present in a sample. [551]

The width of diffraction peaks is determined by several factors, the most significant of which are instrument parameters, inhomogeneous strain, crystal defects, and grain size (decreasing grain size increases peak width, converging on an amorphous material giving no distinct peaks at all). A lower limit for the grain size, *L*, can thus be calculated from the width of diffraction peaks by assuming all broadening is due to their finite size, using the Scherer formula:

$$L = \frac{K\lambda}{W\cos(\theta)}\ , \tag{30}$$

where K is a dimensionless shape factor (0.94 for spherical grains), λ is the X-ray wavelength and W is the peak width (full width at half maximum, in radians) of the peak at diffraction angle θ. [551]

5.6.1. Rietveld refinement

Computational fitting of an XRD pattern, called Rietveld refinement, is used to arrive at an accurate crystallographic model of a sample including phase types and fractions and all the numerous instrumental and structural parameters involved. Several dedicated software programs exist to carry out Rietveld refinement. TOPAS was used for the experiments reported in this thesis.

Rietveld refinement uses a least-squares approach to refine input values describing the phases present until a calculated diffraction pattern generated from these matches the experimentally measured pattern as closely as possible. The inputs used include instrumental parameters describing the X-ray beam and detector (wavelength, beam size, zero error, absorption, background, and geometric correction factors), descriptions of peak shape (peak type, peak width, and other peak-type-specific parameters), and structural descriptions of the phases present (phase fraction, elemental composition, space group, lattice parameters, atom positions, atom site occupancy values, and thermal parameters describing atom vibration). These phase structure descriptions can be found in published CIF files. [552,553] An example XRD Rietveld-refinement input file for TOPAS, featuring instrument parameters for the I11 beamline of the Diamond Light Source, is given in Appendix 1.

The Rietveld algorithm minimises the sum of weighted squared differences between the observed and computed intensity, i.e.

$$M = \sum_i \frac{\left(y_{calc,i} - y_{obs,i}\right)^2}{\sigma_i^{\,2}} \quad , \tag{31}$$

where $y_{calc,i}$ is the i^{th} intensity in the calculated pattern, $y_{obs,i}$ is the i^{th} observed intensity in the experimental pattern, and σ_i^{-2} is the statistical weight of the i^{th} intensity, defined by σ_i, the uncertainty on the i^{th} observed intensity. [552,553] The software that carries out Rietveld refinement iteratively makes an incremental change to all the parameters set to be refined and calculates a simulated pattern, for which it calculates *M*. If this is greater than the original value of *M*, the changed parameter values are discarded, but if it is smaller than the original *M*, they are kept and the refinement progresses until changing any parameter does not result in a decrease in the value of *M* above a certain threshold, i.e. until the refinement converges on the lowest possible *M*.

As with all such minimisation algorithms, care must be taken, by selecting realistic starting values and a sensible order of sequential parameter refinement, that the final model describes the global minimum rather than merely a local minimum that does not describe the physical reality.

Several values can be used to describe how well the refined model fits the data. These include the standard χ^2:

$$\chi^2 = \frac{1}{N} \sum_i \frac{\left(y_{calc,i} - y_{obs,i}\right)^2}{\sigma_i^{\,2}} \quad ; \tag{32}$$

the 'goodness of fit':

$$G = \chi = \sqrt{\frac{1}{N} \sum_i \frac{\left(y_{calc,i} - y_{obs,i}\right)^2}{\sigma_i^{\,2}}} \quad ; \tag{33}$$

the profile *R* factor, R_p:

$$R_p = \frac{\sum_i \left| y_{calc,i} - y_{obs,i} \right|}{\sum_i y_{obs,i}} \quad ; \tag{34}$$

and the weighted profile *R* factor, R_{wp}, which gives more emphasis to higher-intensity data points (i.e. the peaks rather than the background): [552,553]

$$R_{wp} = \sqrt{\frac{\sum_i \frac{\left(y_{calc,i} - y_{obs,i}\right)^2}{\sigma_i^2}}{\sum_i \frac{y_{obs,i}^2}{\sigma_i^2}}} \quad . \tag{35}$$

5.6.2. X-ray sources

X-rays are generally provided for diffraction experiments by a simple cathode ray tube. A filament is heated to produce electrons, which are accelerated by an applied voltage towards a target. The bombardment of the target by these electrons dislodges inner-shell electrons from the target-material atoms. X-rays are then emitted by outer-shell electrons falling to the vacant inner-shell levels. The X-rays have distinct energies characteristic of the target material. Copper is the most commonly used in standard laboratory XRD, giving Cu-Kα X-rays at E = 8.04 keV, λ = 1.5406 Å. Foils or crystal monochromators are used to filter the X-rays to ensure a monochromatic beam.

A synchrotron X-ray source is used instead of this simple setup when tuneable X-ray energies (e.g. for anomalous scattering), very high intensities, or other specialised X-ray beam properties are required. The Diamond Light Source was used for the anomalous X-ray diffraction experiments reported in this thesis (see Chapter 8). It is described here as an example.

X-rays are generated as synchrotron radiation from a beam of electrons travelling around a ring at very high energy. The electrons are generated by a 90 keV electron gun, linearly accelerated to 100 MeV, and then injected to a booster synchrotron (158 m in circumference), which accelerates them up to 3 GeV. The energetic electrons are then transferred to a storage ring (562 m in circumference). This is a forty-eight-sided polygon with powerful magnets at each vertex to bend the electron beam. This change of direction causes the electrons to emit an exceptionally bright beam of X-rays. Third generation synchrotrons like Diamond also use insertion devices at the vertices, which are a series of alternating magnetic dipoles that induce oscillations in the electron beam, resulting in a greater X-ray intensity. The beam of X-rays produced at each vertex can be focused and filtered through various optical instruments and used for experiments in an experimental beamline hutch placed there. [554,555]

5.6.3. Anomalous scattering

Standard laboratory XRD is unable to distinguish between copper and zinc atoms in CZTS because they are isoelectronic. Anomalous scattering is a powerful XRD tool that can overcome this. It involves a correction to the atomic scattering factor for energies close to an elemental absorption edge. The correction takes the form

$$f = f_0 + f' + i \cdot f'' \,, \tag{36}$$

where f_0 is the uncorrected scattering factor, f' is the change in scattering factor magnitude and f'' is a phase shift. Figure 51 shows these at the copper, zinc, and tin absorption edges.

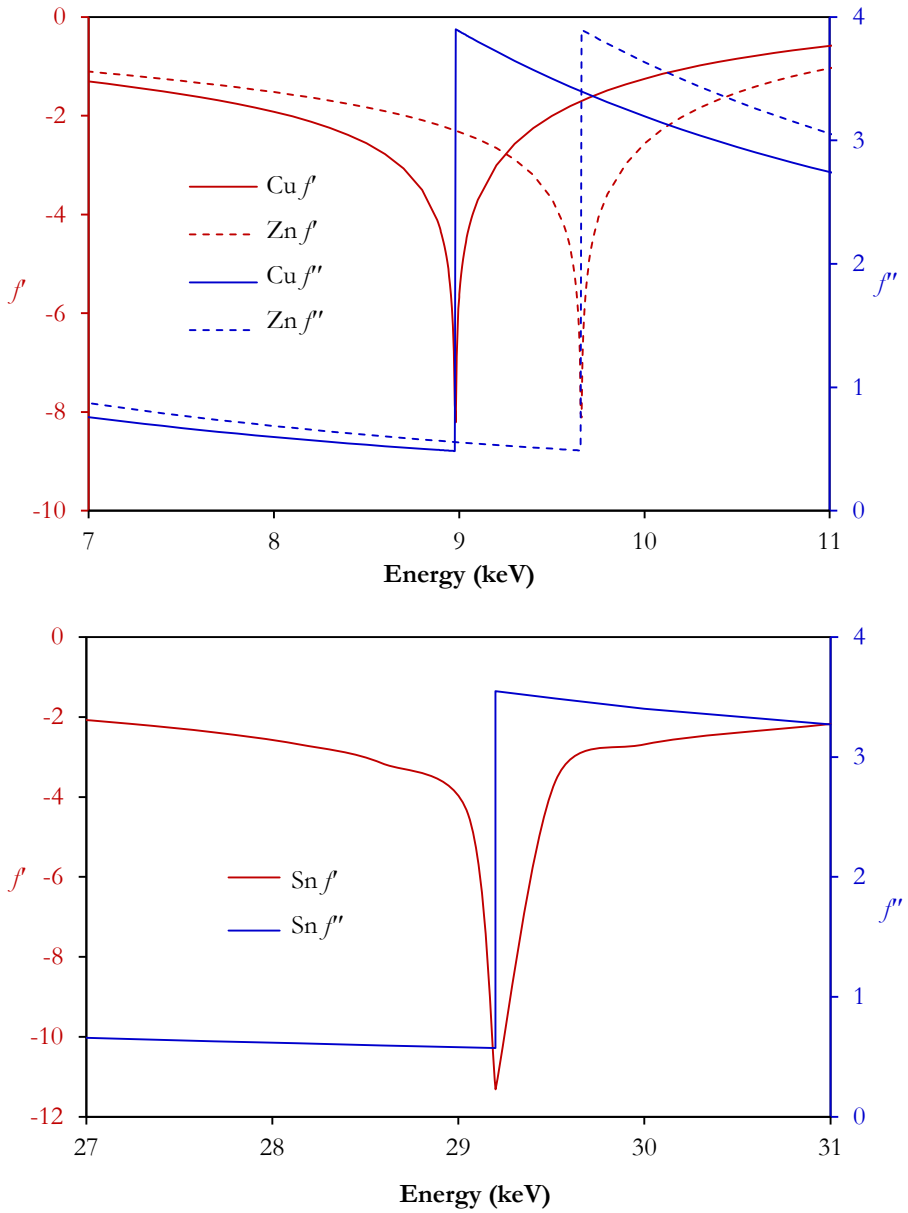

Figure 51: The X-ray anomalous scattering correction factors near absorption edges: top, copper and zinc; and bottom, tin. Data from [556].

By comparing a non-resonant spectrum with one just below the absorption edge of one of the elements in the material, where *f'* is large, scattering due to that element can be highlighted. [556] Anomalous scattering can therefore only be utilised with synchrotron radiation, as it requires the X-ray wavelength used to be tuned to desired values.

5.6.4. CZTS and related materials

Simulated XRD patterns for CZTS and its major secondary phases are shown in Figure 52. Even with Rietveld refinement, standard laboratory XRD is not particularly useful for identifying the secondary phases ZnS, Cu_2SnS_3, or Cu_3SnS_4 in CZTS, as many of the diffraction peaks they exhibit are indistinguishable from those of CZTS itself within the resolution of standard detectors. However, it has been reported that three diffraction lines from CZTS at 37 °, 37.9 °, and 44.9 ° (using Cu-Kα X-rays, corresponding to the (202), (211), and both (105) & (213) planes respectively) can confirm the presence of CZTS, as they are absent in ZnS and very weak in Cu_2SnS_3. [557] Using Rietveld refinement, ZnS can be identified at a concentration above 7 %, and Cu_2SnS_3 above 28 %. [558]

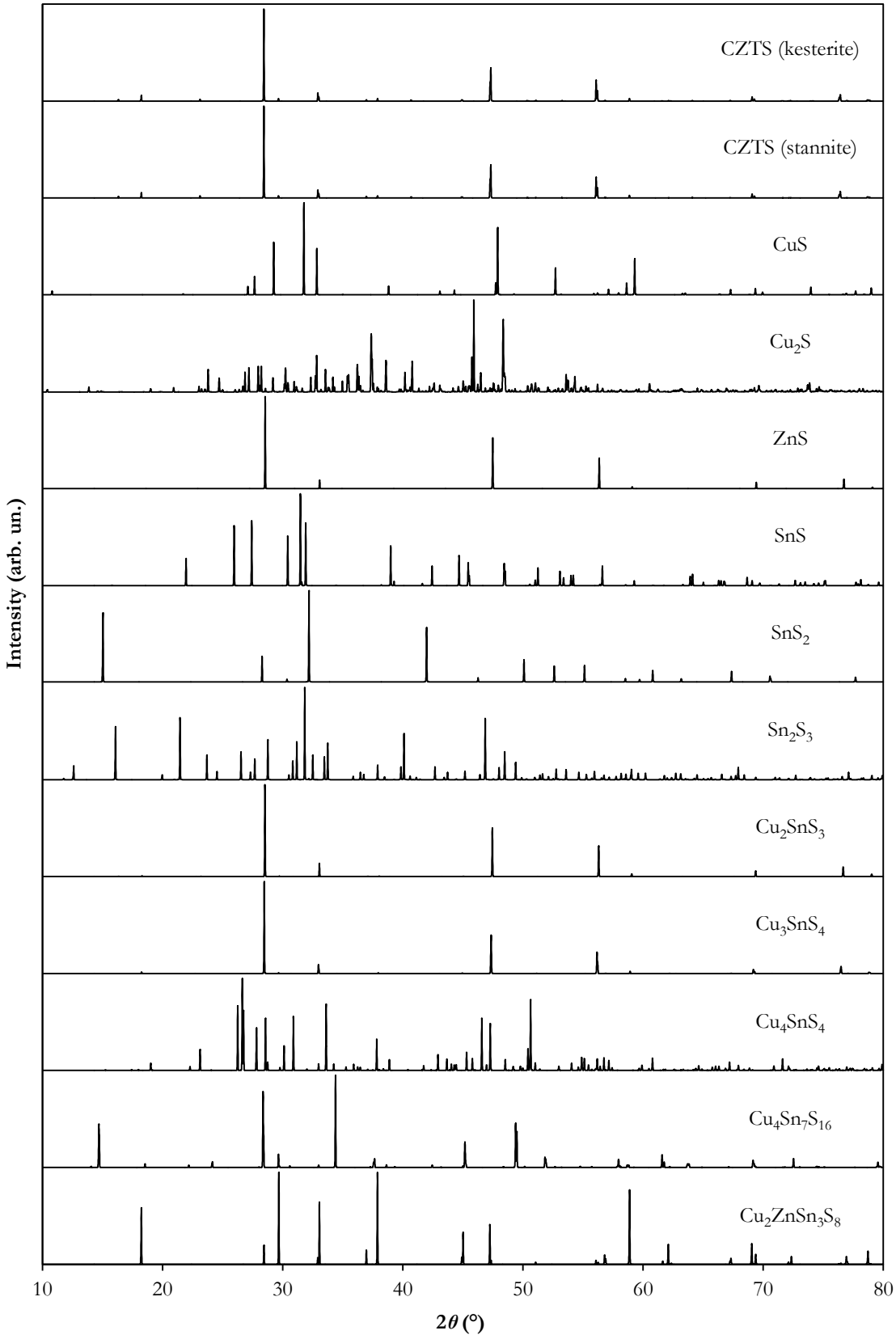

Figure 52: Simulated XRD patterns for CZTS and its major secondary phases using Cu-Kα X-rays and typical laboratory diffractometer parameters.

5.7. Neutron diffraction

Neutron diffraction operates on the same principles as X-ray diffraction (see Section 5.6). However, whereas X-rays interact with the electron cloud of atoms and so show contrast based on differences in electron presence, neutrons interact directly with the nucleus and so show contrast based on atomic mass. Neutron diffraction can therefore provide complementary structural information to XRD.

This is particularly true for CZTS: as copper and zinc are isoelectronic in CZTS it is not possible to use conventional XRD to identify the structure. However, the different neutron scattering lengths for copper and zinc (7.7 and 5.7 fm respectively [559]) overcome this difficulty, so neutron powder diffraction is a useful technique for identifying the crystal structure of CZTS samples.

Neutron diffraction is almost universally used for powder rather than single-crystal experiments, as a large sample volume (several cm^3) is required due to the relatively low scattering factors of neutrons.

Rietveld refinement (see Section 5.6.1) is used for neutron diffraction, as for XRD, to quantitatively fit a model to the data including the fraction of all phases present, their lattice parameters, and their atom site occupancies. An example neutron-diffraction Rietveld-refinement input file for TOPAS, featuring instrument parameters for the HRPD beamline of the ISIS Pulsed Neutron and Muon Source, is given in Appendix 1.

5.7.1. Neutron sources

Neutrons are generally provided for diffraction experiments by synchrotron spallation sources. The ISIS Pulsed Neutron and Muon Source was used for the neutron diffraction experiments reported in this thesis (see Chapter 7). It is described here as an example.

A beam of protons is first produced, which is used to bombard a spallation target to produce neutrons. These protons start as H^- ions produced from an electric discharge. The hydrogen ions are accelerated and separated into bunches by a radio-frequency quadrupole

accelerator, then linearly accelerated up to 37 % of the speed of light. They are then passed through a thin alumina foil that removes their electrons, leaving a beam of protons, and injected into an 800 MeV synchrotron, a 163 m circumference ring of powerful magnets that bend and focus the beam into a circle. In the synchrotron, the protons are accelerated by radio-frequency electric fields up to 84 % of the speed of light before they are extracted by fast kicker magnets. The proton bunches then collide with a tungsten spallation target, where they eject neutrons from the tungsten nuclei, giving extremely intense neutron pulses. The pulses are generated at 50 Hz with duration of 400 ns, and are directed to several beamline experiment stations, each set up for a particular kind of diffraction or spectroscopy experiment. The neutrons pass through an array of liquid water, methane, and liquid hydrogen moderators around the spallation target to select the desired wavelengths for each beamline. The beams then pass through a beam chopper to maintain the pulse separation. They then travel through a long insulated neutron guide, of around 10-100 m, to arrive at the beamlines with a pulse duration suitable for time-of-flight diffraction. [560]

5.7.2. Time-of-flight experimental geometry

Neutron diffraction experiments are often carried out in the time-of-flight (TOF) geometry, rather than the Bragg-Brentano geometry standard for XRD. For TOF measurements, the detector angle, θ, is fixed relative to the neutron beam, and a range of neutron energies are used, making θ a constant and λ the variable in the Bragg condition for diffraction, Equation (26), rather than vice versa as in the Bragg-Brentano geometry.

The range of neutron energies is selected and measured based on their speed, v. This is calculated from their time of flight, t, over the distance, L, from their source (the spallation target) to the sample. The de Broglie equation can thus be expressed for such neutrons as

$$\lambda = \frac{\mathrm{h}}{\mathrm{m_n} v} = \frac{\mathrm{h} t}{\mathrm{m_n} L} \ , \tag{37}$$

where h is the Planck constant and $\mathrm{m_n}$ is the mass of a neutron. For TOF measurements, the Bragg condition for diffraction, Equation (26), thus becomes

$$t = \frac{2\mathrm{m_n} L d_{hkl} \sin(\theta)}{n\mathrm{h}} \ , \tag{38}$$

where n is the order of diffraction (an integer, assumed to be 1), and d_{hkl} is the atomic planar spacing of the (hkl) planes, where h, k, & l are the Miller indices denoting the plane. Diffraction peaks are observed at the detector at times since the neutron pulse generation that satisfy this relation. [560]

5.7.3. CZTS and related materials

Neutron diffraction patterns are essentially the same as those from XRD, although often reported over a different variable and inverted. Simulated neutron patterns for CZTS and its major secondary phases are shown in Figure 53.

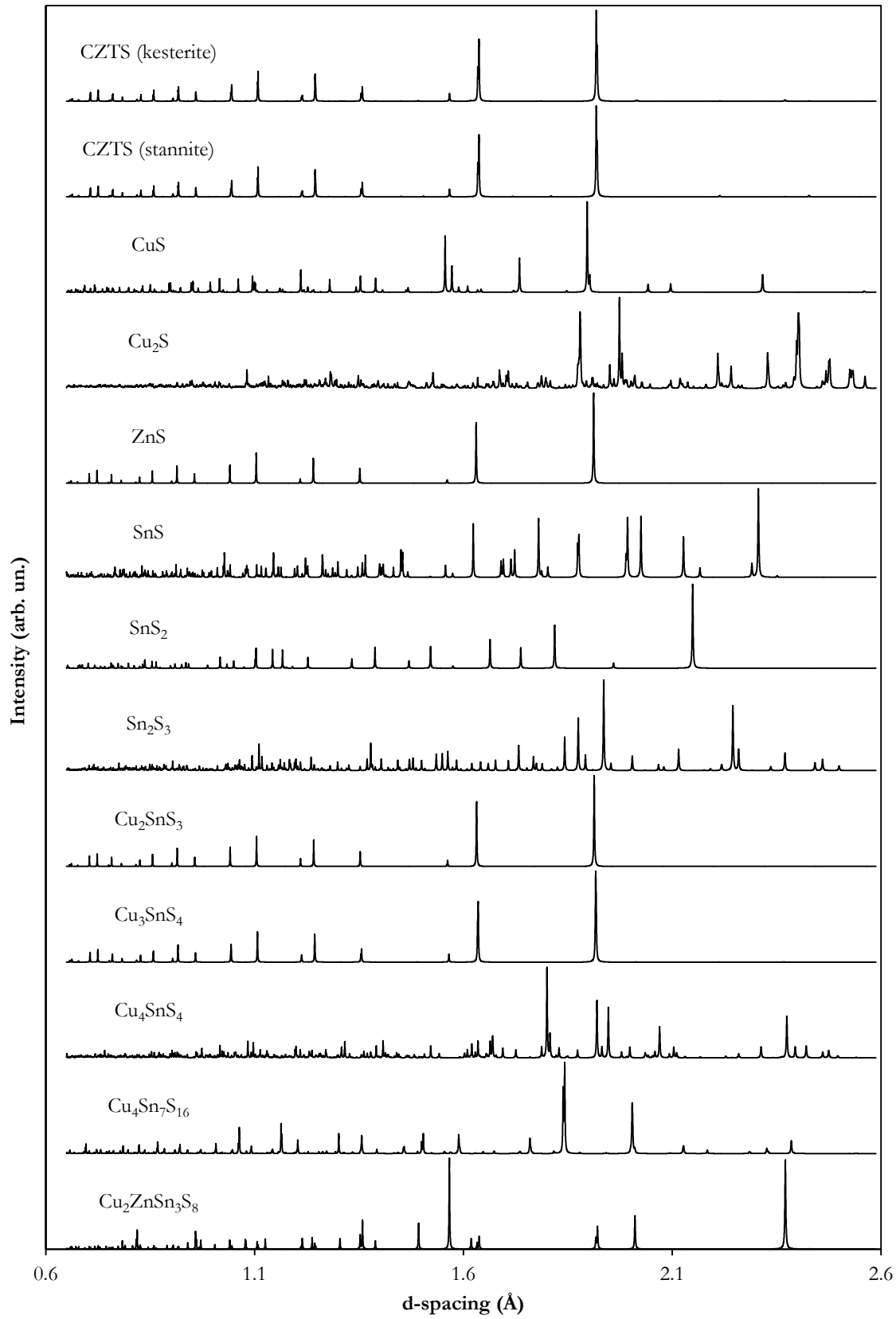

Figure 53: Simulated neutron diffraction patterns for CZTS and its major secondary phases using typical instrumental parameters of the HRPD beamline of the ISIS Pulsed Neutron and Muon Source. The units are d-spacing rather than time of flight to be instrument-independent.

5.8. Solid-state nuclear magnetic resonance (SSNMR) spectroscopy

Nuclear magnetic resonance spectroscopy uses the magnetic properties of atomic nuclei to determine their chemical environments, i.e. the atoms they are spatially surrounded by, which allows the phases present in a sample to be identified.

The sample is placed in a strong magnetic field, which splits nuclear energy levels due to the Zeeman effect, i.e. spin states parallel and antiparallel to the field have slightly different energy levels. The change in energy level is given by

$$E_Z = \mu B_0 = \gamma m_s \hbar B_0 \ , \qquad (39)$$

where $\mu = \gamma m_s \hbar$ is the nuclear magnetic moment, γ is the gyromagnetic ratio (the proportionality constant between magnetic moment and angular momentum), m_s is the spin quantum number (the different values of which define the different Zeeman energies), $\hbar$ is the reduced Planck constant, and B_0 is the magnitude of the applied magnetic field. The splitting is dependent on the magnetic field strength, so higher fields give better spectroscopic resolution. [561]

The local chemical environment (i.e. the atoms by which the nuclei are surrounded) perturbs these energy levels further through shielding and spin-coupling interactions, which are dependent on the orientation of the local chemical environment with respect to the applied field. These perturbations to the Zeeman splitting, known as the chemical shift, are typically on the parts per million scale, i.e. around 0.0001 % of the Zeeman splitting, which is already very small at the order of 10^{-7}-10^{-6} eV. [561]

The effect of the chemical shift on the Zeeman splitting can be observed by measuring the resonant energy of the transition between the spin states. This is done by illuminating the sample in the magnetic field with electromagnetic radiation at the resonant energy for a particular isotope of a particular element, which is dependent on the magnetic field strength used. This is in the radio-frequency range (60-1000 MHz) for typical magnetic field strengths. The resonant energy can be observed by simply measuring absorption as a function of incident radiation frequency for a constant magnetic field B_0, or as a function of magnetic field for a constant incident-radiation frequency, however both of these

methods give very weak signals. A more modern detection method uses the change in magnetisation that accompanies the excitation of the nuclei to the higher-energy spin state. [561]

In the applied magnetic field the spin magnetic moments of the nuclei precess around the field direction because of the torque

$$\vec{\tau} = \vec{\mu} \times \vec{B}_0 \ . \tag{40}$$

This is called Larmor precession, and occurs with frequency equal to the resonant frequency of the Zeeman splitting, which is referred to in this context as the Larmor frequency and given by

$$\omega_0 = \gamma B_0 \ . \tag{41}$$

The total net spin magnetic moment of all nuclei has no component in the plane orthogonal to the applied magnetic field, because those of the individual nuclei average to zero (i.e. they are not in phase). However, because there are more nuclei in the lower energy state, parallel to the field rather than antiparallel, there is non-zero net magnetisation along the direction of the applied field B_0. [561]

The resonant excitation of the nuclei is by a pulse of a second magnetic field B_1 rotating in the plane orthogonal to B_0 at the resonant frequency, i.e. for

$$\vec{B}_0 = B_0 \hat{\mathbf{z}} \ , \tag{42}$$

$$\vec{B}_1 = B_1 \left(\cos(\omega_0 t) \hat{\mathbf{x}} + \sin(\omega_0 t) \hat{\mathbf{y}} \right) . \tag{43}$$

The nuclear spin magnetic moments precess around B_1 just as around B_0, but at a much lower frequency, ω_1, because the amplitude of B_1 is much lower than that of B_0 (see Equation (41)). Because a net component of the magnetic moments is in phase with respect to B_1, having started along the z direction because of B_0, the effect of the precession around B_1 is that the magnetisation vector rotates from the z direction into the x-y plane, through the -z direction, back through the x-y plane and to the z direction again, spiralling around the z direction as it does so because it is simultaneously precessing around B_0 with a higher frequency. This phenomenon only occurs when B_1 rotates with the same frequency as that at which the magnetic moments precess around B_0, i.e. when B_1 is resonant. If the frequency of B_1 is not equal to the resonant Larmor frequency, the precession of the magnetic moments around it has no net effect because the relative directions of B_1 and the magnetic moments are not constantly orthogonal. [561]

The duration or amplitude of the applied resonant excitation is calculated to rotate the magnetisation vector by 90 °, and so the burst of excitation radiation is known as a 90 ° pulse. This means that when the pulse ends and B_0 is the only field present, the populations of the parallel and antiparallel spin states are exactly balanced, making their contributions to the component of the magnetisation in the direction of B_0 cancel exactly. However, the newly-excited nuclei precess in phase, giving a non-zero magnetisation in the plane orthogonal to B_0, which precesses around B_0 at the resonant Larmor frequency. This means that exciting the nuclei using a 90 ° pulse of resonant radiation (specifically a rotating magnetic field) makes the sample magnetisation precess at the resonant frequency. [561]

The precession of the magnetisation is measured by a pickup coil surrounding the sample, in which it induces a current. A burst of electromagnetic radiation over a range of frequencies is used to excite nuclei regardless of their chemical shifts, rather than using a single, well-defined frequency as for the method of measuring absorption. The electrical signal induced in the pickup coil then contains the range of frequencies due to the chemical shifts of all chemical environments of the relevant isotope in the sample. The signal is Fourier transformed to become a function of frequency rather than time, so these different chemical environments then correspond to particular peaks in the signal. [561]

The induced signal decays quite rapidly because once the excitation pulse ends, spatial inhomogeneity in the B_0 magnetic field and interactions between the individual nuclei mean that the nominally in-phase precession of the magnetic moments of the excited nuclei loses coherency as some emerge in front and some lag behind the average position. This can be reversed by applying a resonant excitation pulse with twice the duration or amplitude of the initial 90 ° pulse, giving a 180 ° pulse that flips the positions of the magnetic moments by 180 °, meaning the faster magnetic moments are now behind the average position and the slower ones in front of it, and so they converge again, coinciding after the same time as between the 90 ° pulse and the 180 ° pulse. At this convergence the induced signal strength reaches a maximum again, known as a spin echo or Hahn echo.

Whether the NMR spectrum as a function of frequency is of absorption or signal intensity induced by magnetisation rotation, the peaks correspond to the chemical shifts of particular chemical environments. These chemical shift perturbation values are reported in parts per million relative to the unperturbed Zeeman splitting to make them independent

of the applied magnetic field strength. The chemical shifts of the peaks are then characteristic of particular chemical environments, meaning they can be used to identify particular phases containing the element in question. [561]

In solution NMR, the random motion of molecules averages the orientationally dependent effects. In solid-state NMR, however, anisotropic perturbations of the nuclear energy levels can be observed. In polycrystalline samples, a distribution of orientations will exist, leading to broad NMR peaks. The spectral resolution can be increased significantly by using magic-angle spinning (MAS). This entails rotating the sample at a frequency of 1 to 100 kHz at the 'magic angle', θ_m, of approximately 54.74 ° with respect to the magnetic field (defined by $\cos^2(\theta_m) = ⅓$). This significantly reduces the line widths by removing the first-order anisotropic causes of broadening: the nuclear dipole-dipole interaction between nuclear magnetic moments, the chemical shift anisotropy (a nuclear-electron interaction), and the quadrupolar interaction. However, magic-angle spinning introduces scaled replicas of the spectrum (spinning sidebands) shifted by integer multiples of the spinning frequency. [561]

5.8.1. CZTS and related materials

Example ^{65}Cu, ^{67}Zn, and ^{119}Sn SSNMR spectra for CZTS and its major secondary phases are shown in Figure 54, Figure 55, and Figure 56 respectively. ^{65}Cu NMR is particularly useful for identifying the crystal structure of CZTS, as the kesterite structure features two copper environments, the 2*a* and 2*c* lattice sites (see Section 3.5), while the stannite only features one. The kesterite NMR shift, illustrated in Figure 54, has a central peak due to the 2*c* site and smaller peaks to either side of this due to the 2*a* site. [295]

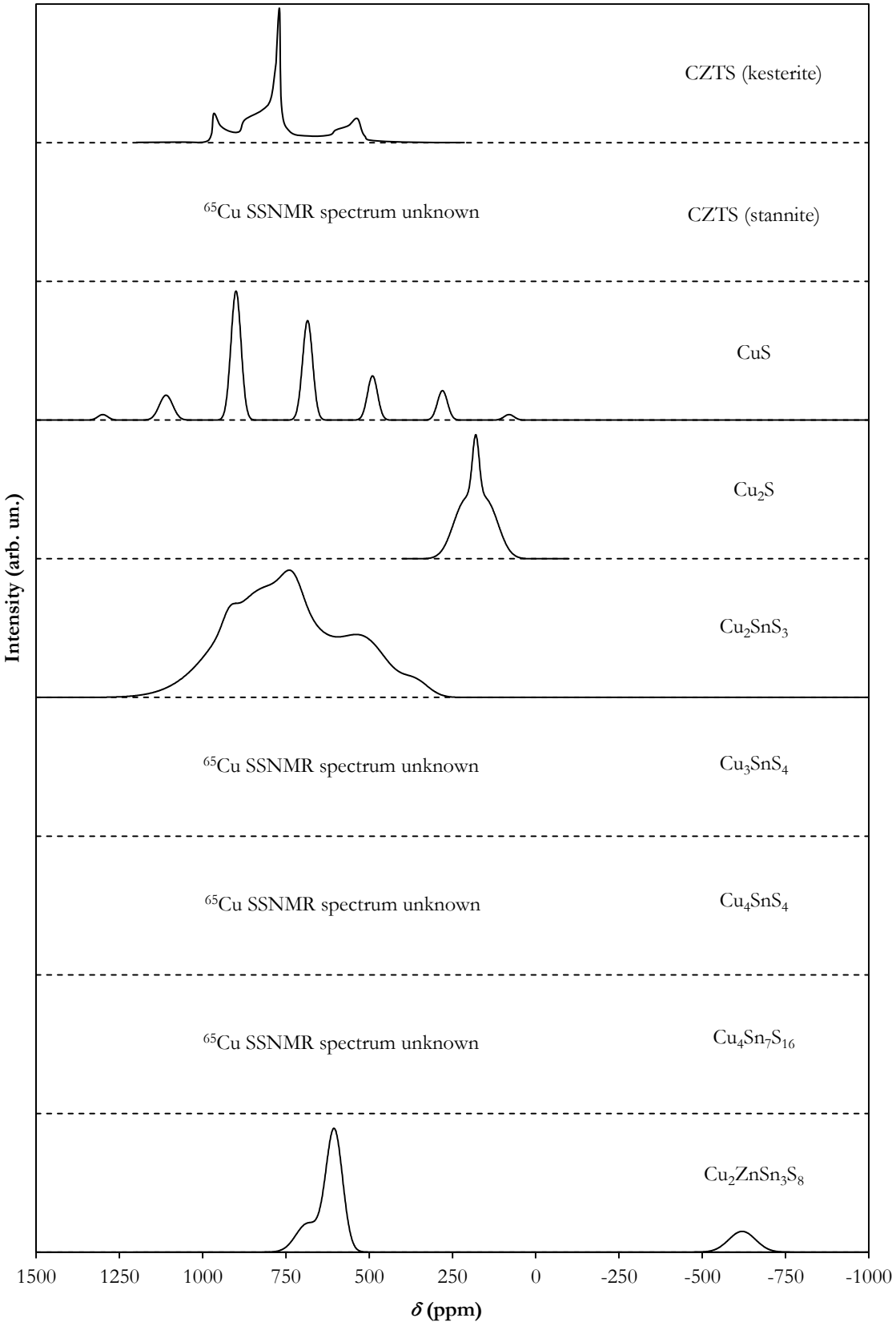

Figure 54: Example ^{65}Cu SSNMR spectra for CZTS and its major copper-containing secondary phases. Data from [241,562-564], collected under different conditions, so not necessarily directly comparable.

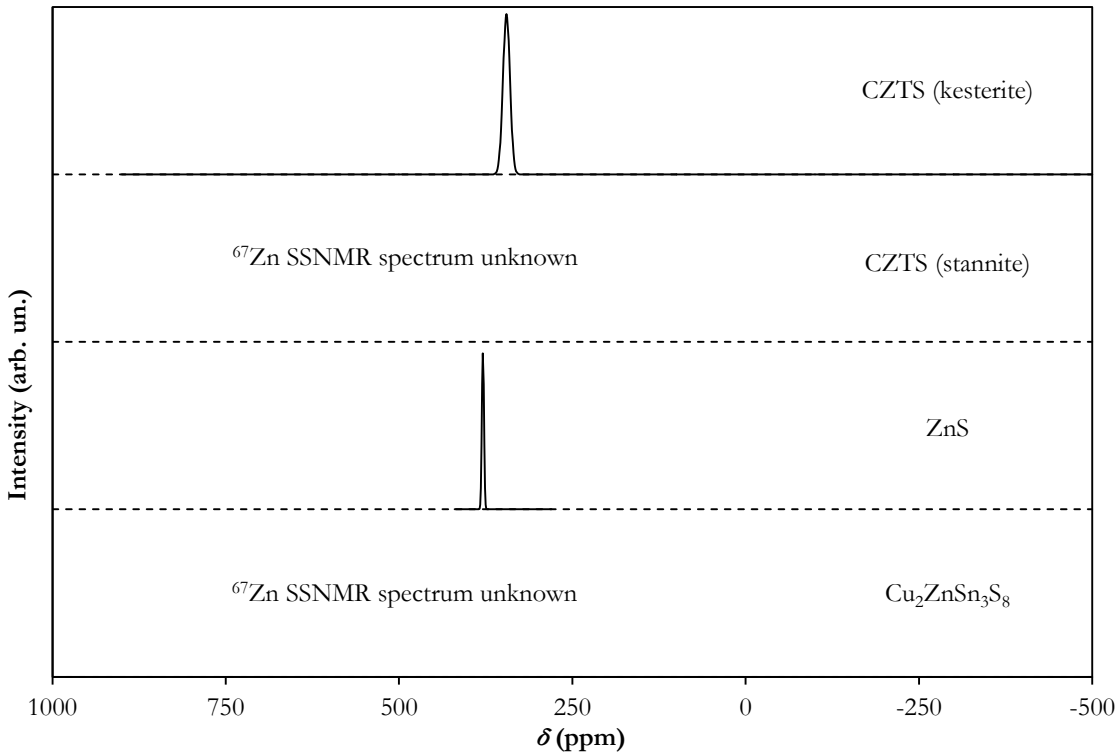

Figure 55: Example ^{67}Zn SSNMR spectra for CZTS and its major zinc-containing secondary phases. Data from [295,564], collected under different conditions, so not necessarily directly comparable.

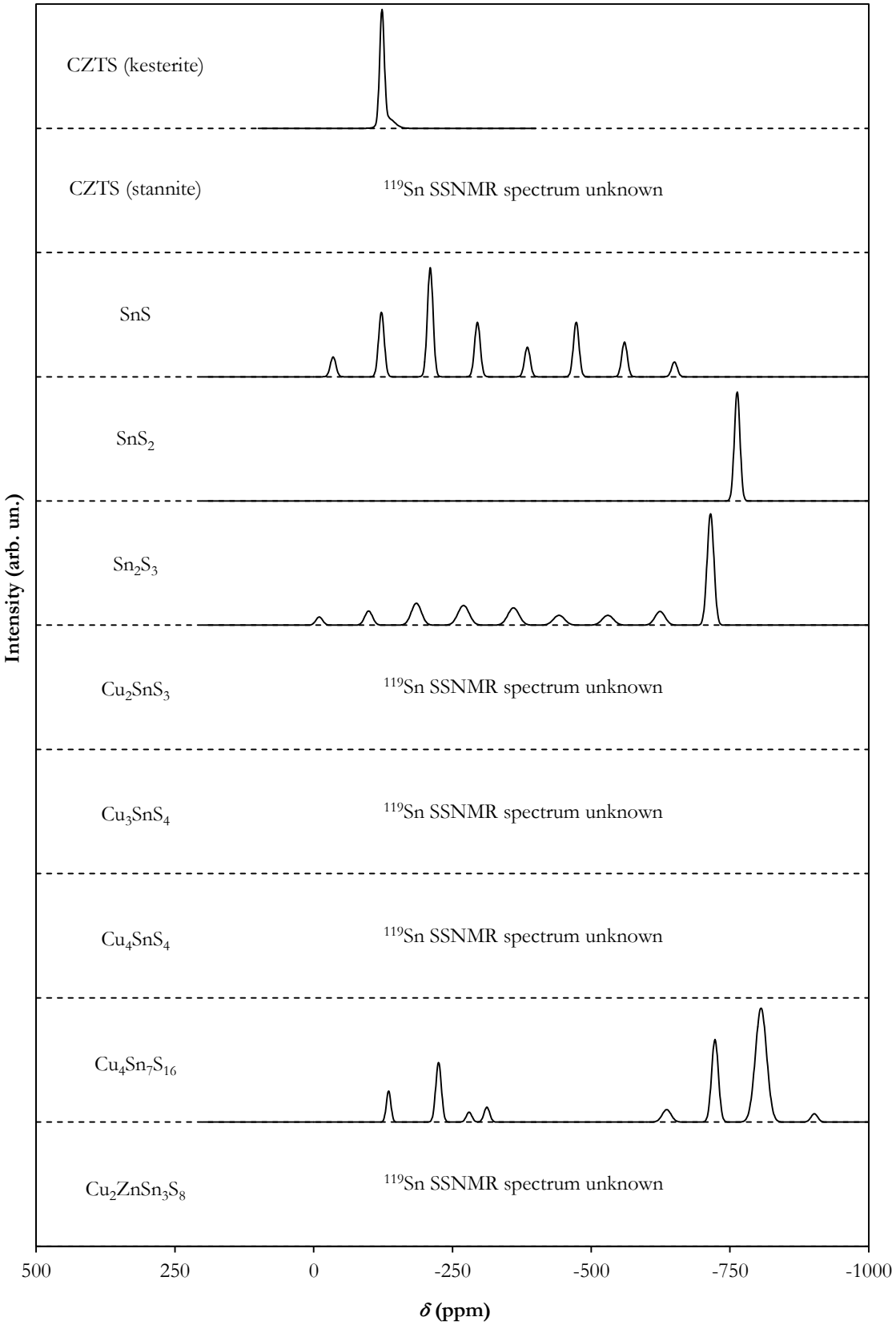

Figure 56: Example ^{119}Sn SSNMR spectra for CZTS and its major tin-containing secondary phases. Data from [241,564,565], collected under different conditions, so not necessarily directly comparable.

5.9. Raman spectroscopy

Raman spectroscopy is an optical technique that can be used to identify materials using their vibrational, rotational, and other low-frequency modes. It entails the sample being illuminated by monochromatic laser light, which undergoes inelastic Raman scattering.

This scattering can be thought of as absorption and immediate reemission, with an electron being promoted to and falling from a virtual energy state in the process. In Rayleigh scattering, which is elastic, the starting and final energy state is the same, as the electron has neither gained nor lost energy. However, in Raman scattering, the final energy state is a slightly different vibrational or other low-frequency mode to the starting one; either higher, meaning the scattered light has lost energy, which is called Stokes Raman scattering, or lower, meaning the scattered light has gained energy, which is called Anti-Stokes Raman scattering. [566] These processes are illustrated in Figure 57.

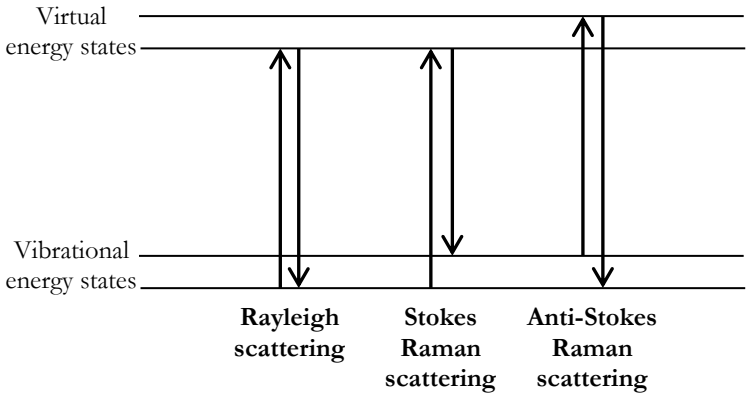

Figure 57: Rayleigh and Raman scattering.

The shift in energy of the scattered light is measured, and gives information on the vibrational phonon modes in the material. Each material has a characteristic spectrum of Raman peaks, so these can be used to identify the phases present in the sample.

The intensity of a Raman peak is given by the expression [567]

$$I(\omega) = I_b(\omega) + \frac{A\Gamma^2\omega_p\omega(n+1)}{\left(\omega_p{}^2 - \omega^2\right) + \Gamma^2\omega^2}\ , \tag{44}$$

where $I_b(\omega)$ is the background, ω_p is the peak wave number, Γ is the width of the peak, A is its amplitude, and n is the phonon occupation number, which tends to zero at 0 K and is given by

$$n = \frac{1}{\exp\left(\frac{\hbar\omega}{k_B T}\right) - 1} \quad . \tag{45}$$

Raman peaks and the phonon modes they are associated with are commonly referred to using Mulliken notation. This is summarised in Table 12.

Symbol	Meaning
A	Singly degenerate state, symmetric with rotation about the principal C_n axis
B	Singly degenerate state, antisymmetric with rotation about the principal C_n axis
E	Doubly degenerate
T	Triply degenerate
Subscript g	'Gerade' (symmetric): the wavefunction sign is the same on inversion through the atom centre
Subscript u	'Ungerade' (antisymmetric): the wavefunction sign changes on inversion through the atom centre
Subscript 1	The wavefunction sign does not change upon rotation about the atom centre
Subscript 2	The wavefunction sign changes upon rotation about the atom centre
'	Symmetric with respect to a horizontal symmetry plane σ_h
"	Antisymmetric with respect to a horizontal symmetry plane σ_h

Table 12: Mulliken notation symbols and their meaning. [566]

Raman scattering is very weak compared to Rayleigh scattering, so great care must be taken to separate the low-intensity, inelastically scattered light from the dominating, un-shifted laser light. Notch or edge filters are therefore used to reject the latter and pass only the Raman scattered light to the detector. [566]

5.9.1. CZTS and related materials

As non-resonant excitation gives a very low Raman efficiency, resonant conditions must be used to achieve reliable detection of secondary phases in CZTS. [258] For this reason, multiple wavelength Raman analysis is required to give accurate results. [558] CZTS itself has optimal Raman scattering efficiency for excitation at around 532.5 nm, [258] and ZnS, which has a larger band gap, is often identified using 325 nm. [346]

Raman peak values of CZTS and its major secondary phases are given in Table 13, and these are depicted graphically in Figure 58. Although these are quite precise (quoted to 1 cm^{-1}), small deviations in the peak positions are likely. [166]

Material		Peaks (cm^{-1})	Reference
CZTS	A mode:	286, 300, 337	[222,258,412,517,568-578]
	B mode:	82, 84, 97, 98, 247, 248, 252, 264, 313, 319, 352, 373	
	E mode:	67, 83, 141, 147, 160, 165, 255, 272, 293, 300, 347, 365	
	Disorder:	331	
MoS_2		288, 384, 410	[579,580]
CuS		137, 265, 472	[246,581]
Cu_2S		475	[580]
ZnS		273, 276, 290, 352, 352, 386, 422	[248,582]
SnS		96, 160, 190, 219, 288	[580,583]
SnS_2		215, 314	[583]
Sn_2S_3		52, 60, 71, 87, 183, 234, 251, 306	[583]
Cu_2SnS_3		290, 352	[584]
Cu_3SnS_4		318	[580]
Cu_4SnS_4		317	[254]
$Cu_4Sn_7S_{16}$		78, 94, 182, 192, 274, 305, 311, 350, 365, 466	[241,585]
$Cu_2ZnSn_3S_8$		?	-

Table 13: The Raman peaks of CZTS and its major secondary phases.

CZTS has 8 atoms per unit cell, which means it has 27 vibrational modes (3 A modes, 12 B modes, and 12 E modes). Of these, 15 (the A, B, E_1, and E_2 modes) are Raman active for the kesterite structure and 14 (the A_1, B_1, B_2, and E modes) for the stannite. The main difference between the Raman spectra of the kesterite and stannite structures of CZTS is therefore the nonexistence of the B_1 modes for kesterite, due to the absence of individual layers of copper atoms. [567,586] The Raman spectra of eskebornite and PMCA structures of CZTS have also been calculated, [206] but only the kesterite has been observed experimentally.

The A modes of kesterite and A_1 modes of stannite result from symmetric vibration of only the anions and give the strongest Raman peaks. The B and E modes include both anion and cation vibration. The B_1 modes of stannite involve only copper cations: half are displaced positively in the *c* direction and half negatively, and the sulphur anions move only in the *a*-*b* plane. The B modes of kesterite and B_2 modes of stannite involve all the cations,

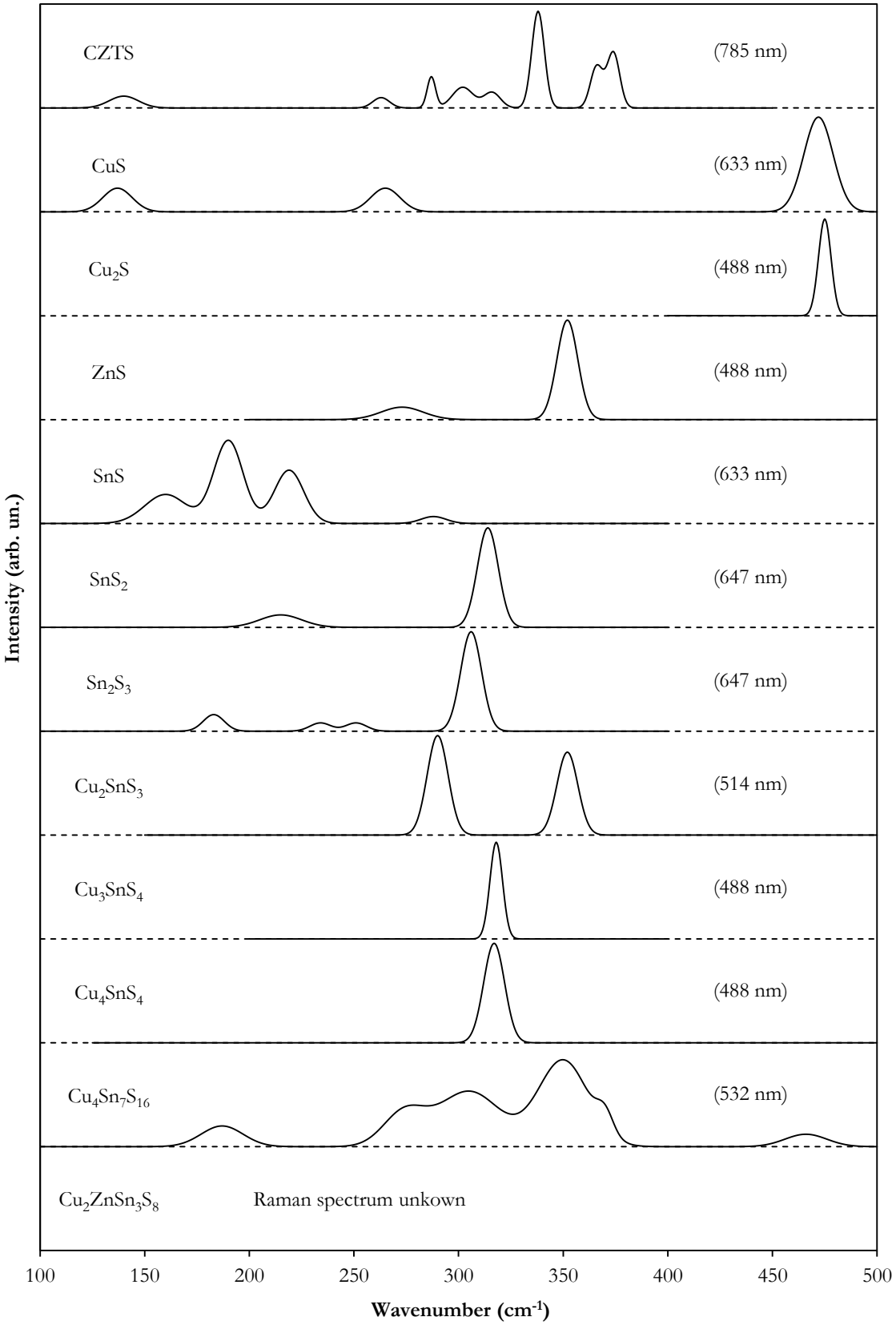

Figure 58: Example room-temperature Raman spectra of CZTS and its major secondary phases. Data from [254,575,580,581,583-585], collected under different conditions, so not necessarily directly comparable. The incident laser wavelengths used are given in brackets.

but they still move only in the *c* direction. The E modes of both structures involve the cations moving only within the *a-b* plane. [569,571,587]

Significant low-frequency asymmetry has been observed in CZTS Raman peaks, and has been attributed to lower crystalline quality leading to phonon confinement effects. [574]

Raman peaks vary with temperature; for example, the CZTS A mode peak generally quoted as 337cm^{-1} has been observed to shift from 337 cm^{-1} at 80 K to 329 cm^{-1} at 450 K and the peak at 288 cm^{-1} could not be distinguished at 450 K. [588,589] This variance with temperature is due to thermal expansion and interaction of the relevant phonon with other phonons that arise at higher temperatures.

The cation disorder of CZTS can be determined by its effect on the Raman spectrum. The ratio of the two A mode peaks at 286 cm^{-1} and 300 cm^{-1},

$$Q = I_{286} / I_{300} , \quad (46)$$

has been shown to have a linear relation to cation order in CZTS. [233] The parameter used to quantify cation disorder is conventionally defined as

$$S = 2Cu_{2c} - 1 , \quad (15)$$

which ranges from 1 for full copper occupancy of the 2*c* site and assumed full zinc occupancy of the 2*d* site, to 0 for a full and equal occupancy by copper and zinc of both sites. This is an incomplete description as it does not account for disorder on the 2*a* site (see Section 3.5), but is useful for considering order in relation to annealing and the order-disorder phase transition. This has been found to be related to Q according to

$$S = (0.18 \pm 0.02)Q , \quad (47)$$

for $1.0 < Q < 3.5$, [233] or in general according to [234]

$$S = 0.40Q - 0.23 . \quad (48)$$

Additionally, the main peak at 337 cm^{-1} is redshifted with increasing disorder to 331 cm^{-1}. [570-575,578].

5.10. Photoluminescence spectroscopy

Photoluminescence analysis is an optical technique that can reveal important information about radiative recombination methods and defect levels in a material. It entails the sample being optically excited by absorbing a beam of monochromatic light from a laser. The

excited material then undergoes spontaneous emission, or photoluminescence. Between absorption and reemission, the excited carriers thermalise to the band edges or near-band-edge states of the material, or to a trap state in the band gap, and so emission is over a spectrum of energies, which reveals information about the energy structure of the phases present.

Photoluminescence is extremely sensitive to discrete electronic states, including surface, interface, and impurity levels. It can also give temporal information: under pulsed excitation, transient photoluminescence shows the lifetime of non-equilibrium states. Crucially, photoluminescence analysis is non-destructive, and it requires little sample preparation. [590]

5.10.1. Laser power dependence

Using a model of coupled rate equations that considers all possible radiative and non-radiative transitions in a direct-band-gap semiconductor, [591] the intensity of emission at each peak can be related to the power of the incident laser light by a simple power law,

$$I = I_0 L^{k} \ , \tag{49}$$

where L is the incident laser power and k is determined experimentally as the gradient of ln(I) as a function of ln(L),

$$\ln(I) = k \cdot \ln(L) + \ln(I_0) \ . \tag{50}$$

This can give useful information about the transition mechanism that gives rise to the peak in question. $0.2 < k < 0.6$ suggests a donor-acceptor pair transition, $0.6 < k < 1.0$ suggests non-excitonic band-to-band recombination, and $1 < k < 2$ suggests exciton-like transitions (k = 1.6 for band-to-tail recombination and 1.65 for band-to-band recombination [592]). It is possible that in logarithmic form, as in Equation (50), the relationship is not linear, meaning that the model given by Equation (49) is not valid. This has been shown to be the case for decays that can occur non-radiatively. [322,591]

Debye screening, i.e. the Coulomb screening of electric fields by free charge carriers, leads to a blue shift of photoluminescence peaks with increasing laser power. The Debye screening length is the scale over which free carriers exert this screening effect, and is given by

$$\lambda_D = \sqrt{\frac{\varepsilon k_B T}{n e^2}} \ , \tag{51}$$

where ε is the dielectric permittivity of the material, k_B is the Boltzmann constant, T is temperature, n is the carrier concentration, and e is the charge of an electron. [62] With increasing laser power, the concentration of excited free carriers increases, so the Debye length decreases and carriers must be closer in order to interact electrostatically, leading to a smaller potential, and so greater recombination energy. This blue shift is a few meV per order of magnitude of intensity for donor-acceptor pair transitions and significantly larger for recombination due to potential fluctuations. [319]

5.10.2. Temperature dependence

Photoluminescence peaks are often quenched at high temperatures, i.e. their intensity decreases with increasing temperature, due to non-radiative recombination becoming thermally activated. The intensity, I, of each peak as a function of sample temperature, T, can be described by several closely related models. The first, non-radiative recombination involving a discrete defect level, involves a simple exponential,

$$I = \frac{I_0}{1 + \alpha_1 \cdot \exp\left(\frac{-E_1}{k_B T}\right)} \ , \tag{52}$$

where I_0 is the intensity at 0 K, E_1 is a thermal activation energy associated with the quenching method, a_1 is a measure of the degeneracy of the state corresponding to E_1 relative to that of the radiative state of the photoluminescence peak in question, and k_B is the Boltzmann constant. A factor of $T^{3/2}$ is added if a band is involved in the non-radiative recombination rather than a discrete defect, to account for the effective density of states, giving

$$I = \frac{I_0}{1 + \alpha_1 T^{3/2} \cdot \exp\left(\frac{-E_1}{k_B T}\right)} \ . \tag{53}$$

A single-exponential model usually does not fit the data well over a large temperature range, so a bi-exponential function is often required, in which the two exponential terms correspond to two quenching channels dominant in different temperature ranges. This can involve two discrete defects,

$$I = \frac{I_0}{1 + \alpha_1 \cdot \exp\left(\frac{-E_1}{k_B T}\right) + \alpha_2 \cdot \exp\left(\frac{-E_2}{k_B T}\right)} , \quad (54)$$

one discrete defect and one band,

$$I = \frac{I_0}{1 + \alpha_1 \cdot \exp\left(\frac{-E_1}{k_B T}\right) + \alpha_2 T^{3/2} \cdot \exp\left(\frac{-E_2}{k_B T}\right)} , \quad (55)$$

or two bands

$$I = \frac{I_0}{1 + \alpha_1 T^{3/2} \cdot \exp\left(\frac{-E_1}{k_B T}\right) + \alpha_2 T^{3/2} \cdot \exp\left(\frac{-E_2}{k_B T}\right)} , \quad (56)$$

with the factors of $T^{3/2}$ again accounting for the effective density of states in the bands. These models are usually shown in plots of $\ln(I)$ as a function of $1/T$, known as Arrhenius plots. [322,593-596]

5.10.3. Phonon replicas

Phonon replicas are peaks in a photoluminescence spectrum that accompany the characteristic emission peak (in this context known as the zero-phonon line) at lower energies when phonons are involved in the recombination. They occur when the electron and hole together have a net momentum. The energy of the n^{th} phonon replica is simply given by

$$E_n = E_0 - n\hbar\omega , \quad (57)$$

where E_0 is the zero phonon energy, n is a positive integer (the number of phonons involved in the n^{th} replica), ħ is the reduced Planck constant, and ω is the phonon frequency. The intensity of the n^{th} phonon assisted peak is proportional to the population of carriers with the necessary excess energy, given by the Boltzmann distribution and the density of states. The replica intensity is characterised by the Huang-Rhys parameter, S, the average number of phonons involved in the transition. The intensities of each peak follow a Poisson distribution such that [590]

$$I_n \propto \frac{S^n \cdot \exp(-S)}{n!} . \quad (58)$$

5.10.4. CZTS and related materials

The photoluminescence peaks reported for CZTS and its major secondary phases are given in Table 14 and example photoluminescence spectra using these are shown in Figure 59. Photoluminescence has been found to be a useful tool for identifying Cu_2SnS_3, which cannot easily be identified using XRD, the standard technique for phase identification (see Section 5.6). [130]

Material	Band gap (eV)	Peaks (eV)	Reference
Cu_2ZnSnS_4	1.5	0.66, 1.23, 1.35, 1.48	[595,597]
CuS	1.0	2.38, 2.50, 2.56, 2.71	[246]
Cu_2S	1.2	1.22	[247]
ZnS	3.8	1.80, 1.94, 2.09, 2.34, 3.02	[598,599]
SnS	1.3	0.75, 1.12, 1.23, 1.47	[249,600]
SnS_2	2.2	1.77, 2.25	[250]
Sn_2S_3	2.1	2.08, 2.38, 2.50, 2.64, 2.82, 3.03	[601]
Cu_2SnS_3	1.4	0.95	[252]
Cu_3SnS_4	1.2	3.38	[602]
Cu_4SnS_4	1.2	?	-
$Cu_4Sn_7S_{16}$	0.8	?	-
$Cu_2ZnSn_3S_8$	?	?	-

Table 14: The photoluminescence peaks of CZTS and its major secondary phases at room temperature. N.B. some peaks undergo significant energy shift of up to several hundred meV with changing temperature.

Two photoluminescence bands are attributed to CZTS: one around 0.66 eV, caused by donor-to-band recombination at $[Cu_{Zn}^{-} + Sn_{Zn}^{2+}]^{+}$ defect-complex donor levels, [595] and one around 1.35 eV, the dominating radiative recombination band.

The individual peaks of the 1.35 eV band and their mechanisms have been contested in academic literature. The band was initially considered as a single peak assigned to donor-acceptor pair recombination with an activation energy of 48 meV. [603] It was then reported as two peaks at 1.48 and 1.51 eV due to donor-acceptor pair recombination and excitonic recombination respectively, [604] then as a single peak again, attributed to a band-to-band transition at 1.29 eV with a thermal activation energy of 140 meV. [318,605] Following that, it was again considered to consist of two peaks, at 1.27 and 1.35 eV, due this time to band-to-acceptor recombination at a deep defect in different phases of CZTS

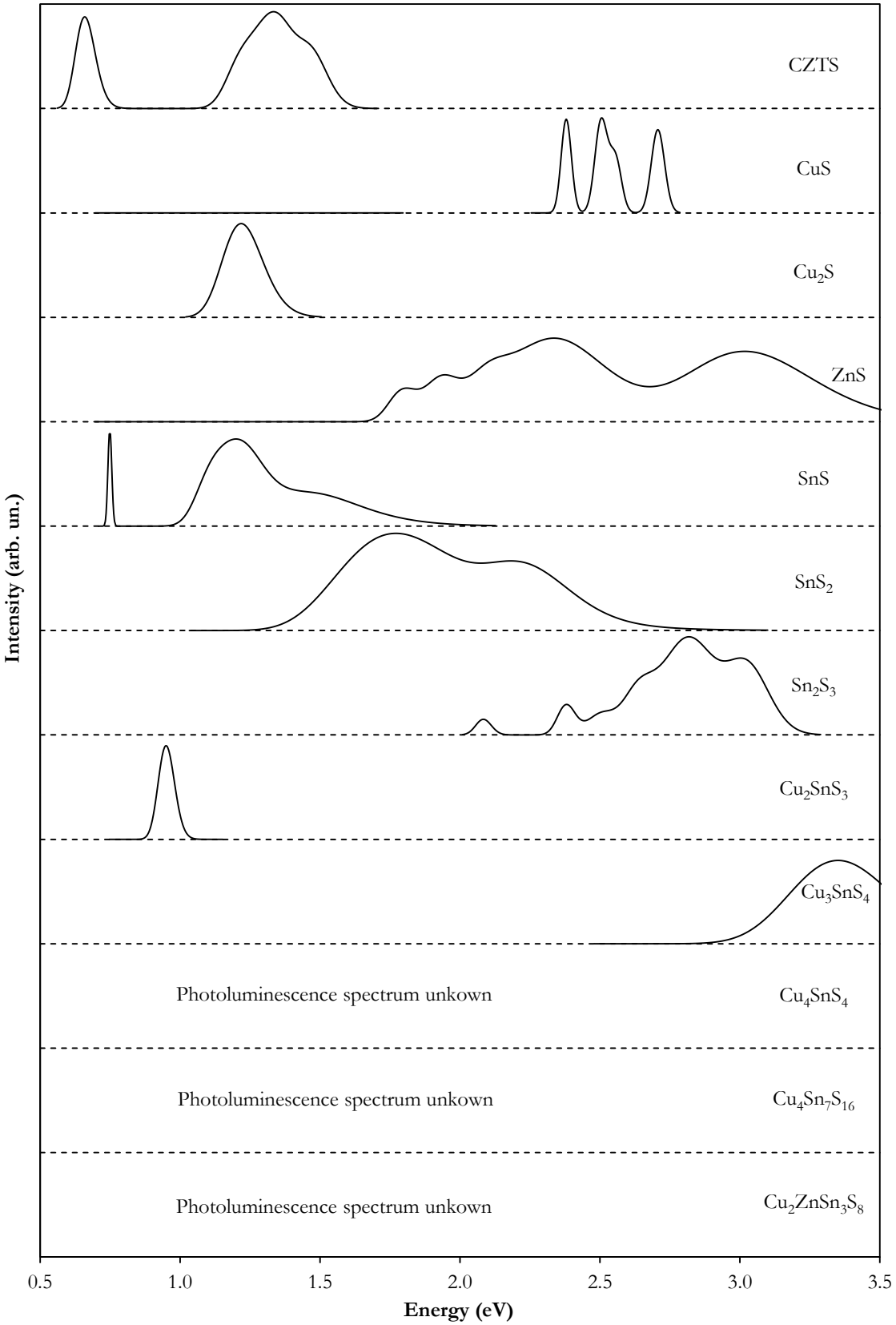

Figure 59: Example room-temperature photoluminescence spectra for CZTS and its major secondary phases. Data from [246,247,249,250,252,598-601], collected under different conditions, so not necessarily directly comparable.

(disordered kesterite and ordered kesterite), with ionisation energy of around 280 meV. [332,606] Then its two components were reported at 1.39 and 1.53 eV and attributed to band-to-tail and band-to-band recombination respectively. [592] The main peak was then identified at 1.2 eV and attributed to donor-acceptor pair recombination, [607,608] then it was assigned at 1.35 eV due to recombination in potential wells at [$2Cu_{Zn}^{-} + Sn_{Zn}^{2+}$] defect clusters. [595] The emission band has most recently been reported to consist of three peaks, attributed to band-to-acceptor, band-to-tail, and band-to-band emission, at around 1.23, 1.35, and 1.48 eV respectively. [597] These peaks have also been reported at lower energies: 1.02, 1.10, and 1.17 eV. [609]

The position of this CZTS photoluminescence band has been found to depend on the ordering of the crystal structure: its largest peak was observed to shift from 1.21 to 1.35 eV with increasing cation order. [110]

The characteristic CZTS peaks have been observed to undergo a blue shift with increasing laser power due to Debye screening (see Section 5.10.1). [607,610]

It has also previously been observed that the characteristic CZTS band-to-band peak is blue-shifted with increasing temperature, [610] due to the thermal excitation of free electrons in the conduction band. However, for recombination due to potential fluctuations, the peak is red-shifted with increasing temperature instead. [319]

Chapter 6:

A structural and optoelectronic study of bulk CZTS

6.1. Introduction

Some material properties of CZTS cannot be examined fully or easily in thin-film form, so bulk samples are occasionally used instead. This chapter presents a study of such bulk polycrystalline samples produced by solid-state reaction.

Elemental composition is one of the major factors that affect CZTS photovoltaic performance, as it largely determines the secondary phases present and the defects formed within the CZTS crystal lattice itself. A range of sample compositions around the stoichiometric point were therefore selected for study. The secondary phases present were identified as a function of sample composition using several analysis techniques, and the effects of these secondary phases on the material and optoelectronic properties relevant to the photovoltaic performance of CZTS were then identified.

6.2. Experimental method

Bulk polycrystalline samples were fabricated by solid-state reaction. Finely ground copper, zinc, and tin powders were mixed together and placed in one alumina boat and sulphur powder was placed in another, with a 30 % excess to encourage full sulphurisation. The powders had manufacturer-certified purities of Cu 99.9 %, Zn 98.0 %, Sn 99.85 %, and S

99.5 %, which are typical for the fabrication of CZTS for solar cells. Both boats were sealed together in an evacuated quartz ampoule, depicted in Figure 60. The ampoules were heated in a small tube furnace with a ramping rate of 5 $K \cdot min^{-1}$ to 1073 K, at which they were kept for 24 hours and then left in the furnace to cool naturally back to room temperature (over around 24 hours, at a rate of around 0.5 $K \cdot min^{-1}$).

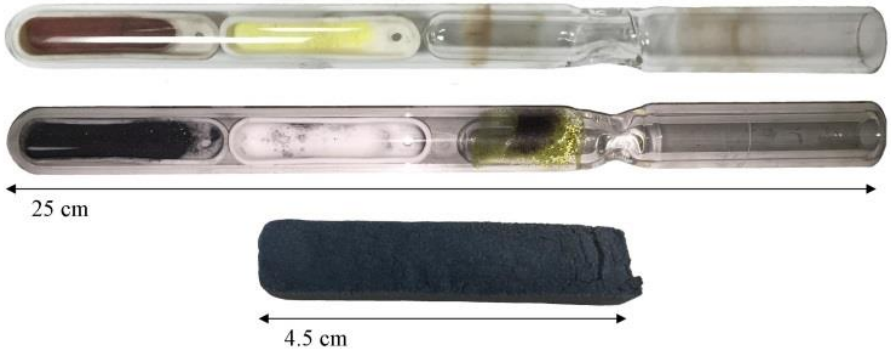

Figure 60: Top to bottom: the elemental powders sealed in an ampoule pre-heat treatment, the ampoule post-heat treatment, and a final ingot of CZTS produced (sample B23).

Seven samples were prepared with a range of starting compositions, given in Table 15 and plotted in Figure 61. Each sample yielded around 5.5 g of material, approximately half of which was ground to a fine powder using an agate mortar and half of which was kept bulk.

Sample	Starting atomic fraction (%)				Starting composition
	Cu	Zn	Sn	S	
B21	25.0	12.5	12.5	50.0	Stoichiometric
B22	22.5	15.0	12.5	50.0	Cu-poor, Zn-rich
B23	25.0	15.0	10.0	50.0	Sn-poor, Zn-rich
B24	27.5	12.5	10.0	50.0	Sn-poor, Cu-rich
B25	27.5	10.0	12.5	50.0	Zn-poor, Cu-rich
B26	25.0	10.0	15.0	50.0	Zn-poor, Sn-rich
B27	22.5	12.5	15.0	50.0	Cu-poor, Sn-rich

Table 15: The initial compositions of samples B21-B27, determined from the masses of copper, zinc, and tin powders used and assuming complete sulphurisation.

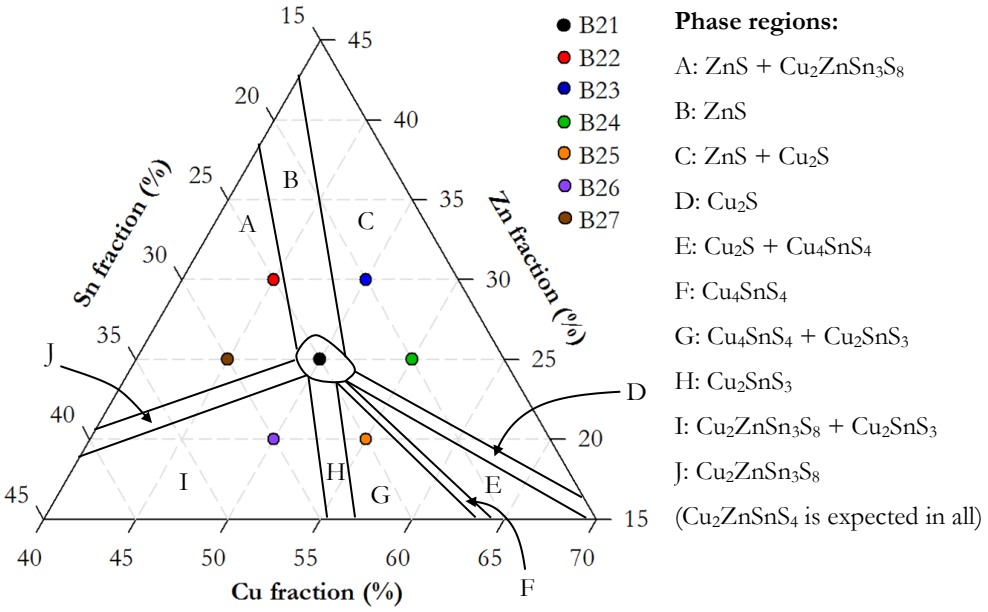

Figure 61: A quasi-ternary composition plot of CZTS showing the starting compositions of samples B21-B27 (black dots). The regions of expected secondary phases from [128] are shown for reference; no secondary phases are expected in the central region.

Inductively coupled plasma mass spectrometry (ICPMS) was carried out using an Elan 6000 Perkin Elmer Sciex ICPMS to quantify the overall elemental composition of the samples. This technique is not sensitive to sulphur, so only the copper, zinc, and tin ratios could be determined.

Each sample was viewed extensively using an Hitachi SU-70 FEG scanning electron microscope (SEM), in both backscattered and secondary-electron configurations. Representative images were taken at two scales to illustrate their morphological structures.

Energy-dispersive X-ray (EDX) spectroscopy was carried out to identify the phases visible in the backscattered SEM images, using an INCA x-act LN2-free analytical silicon drift detector and INCA software. For each phase identified in each sample, measurements were taken at six different points on the sample and averaged, with the uncertainty on these average values given by the standard deviation between the six measurements.

Powder X-ray diffraction (XRD) patterns were taken for each sample in the Bragg-Brentano geometry using Cu-Kα X-rays in a Bruker d7 diffractometer. Additional XRD patterns were taken at high resolution using 15 keV X-rays at the I11 beamline of the

Diamond Light Source. Rietveld refinement of the crystal structures for both sets of diffraction patterns was performed using TOPAS v.6 software.

^{65}Cu SSNMR measurements were taken using a Bruker Avance III HD spectrometer and ^{119}Sn measurements using a Varian VNMRS spectrometer. Spectra were referenced to external samples of $[Cu(CH_3CN]_4][PF_6]$ saturated in MeCN, and $Sn(CH_3)_4$ via $Sn(C_6H_{12})_4$ respectively. A Hahn echo was used to record the bandshapes for the copper measurements. Magic-angle spinning was used for the tin measurements.

Raman spectra were obtained using a Horiba JY LabRAM-HR Raman microscope system in the backscattering configuration. A solid-state laser was used to provide resonant excitation for CZTS at 785 nm and an Ar^+ ion laser was used to provide non-resonant excitation at 488 nm. The Raman signal was detected after dispersion through a 1,800 mm^{-1} (for 785 nm excitation) or 600 mm^{-1} (for 488 nm) diffraction grating. Spectra were taken at 17 locations across the sample surface and cross-section and averaged to give a single representative spectrum for each sample using each wavelength.

Photoluminescence spectroscopy was carried out using the 458 nm line of an Ar^+ ion laser as the excitation source. The incident power was calibrated using a Molectron laser power meter. The samples were mounted under vacuum in a closed-cycle helium cryostat (Cryomech ST405), using copper tape, and cooled to 3 K for low-temperature measurements. The sample luminescence was passed through long-pass filters (GG435 and GG455) to remove laser light, dispersed by a grating monochromator (Bentham, TM300), and then collected by a silicon photodiode array cooled to 253 K. Spectra were obtained for a range of sample temperatures.

6.3. Inductively coupled plasma mass spectrometry

The elemental cation compositions of the seven samples, determined by ICPMS, are given in Table 16 and plotted in Figure 62. They show significant and systematic tin loss and some zinc loss, leaving a greater increase in the copper fraction than zinc.

Sample	Atomic cation fraction (%)			Final composition
	Cu	Zn	Sn	
B21	55(4)	28(2)	18(2)	Sn-poor, Cu-rich
B22	49(3)	32(2)	19(2)	Sn-poor, Zn-rich
B23	53(3)	32(2)	16(1)	Very Sn-poor, Cu-rich, Zn-rich
B24	59(4)	27(2)	14(1)	Very Sn-poor, very Cu-rich
B25	60(4)	21(1)	19(2)	Zn-poor, Sn-poor, very Cu-rich
B26	54(4)	21(1)	25(2)	Zn-poor, Cu-rich
B27	48(3)	27(2)	26(2)	Cu-poor, Zn-rich

Table 16: The metal ratios of samples B21-27, determined by ICPMS. The numbers in brackets are the uncertainties on the last significant figures.

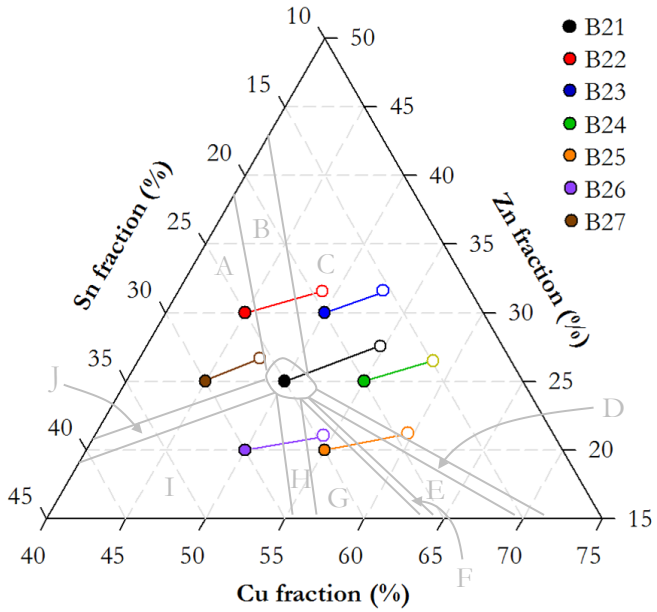

Figure 62: The starting (solid circles) and final (determined by ICPMS, hollow circles) cation fractions of samples B21-27. The grey labelled areas show the regions of expected secondary phases from Figure 61.

Tin loss, by SnS evaporation, is a common problem with CZTS fabrication (see Section 4.3.2). It has been reported that tin loss during annealing is inversely correlated with copper content, suggesting that copper in some way binds the tin and prevents its evaporation, [494] but this trend is not observed here; in fact, tin loss appears to be completely independent of starting composition.

The rate of tin loss per area from thin films during sulphurisation under a constant gas supply has previously been quantified, [485] but tin loss from bulk samples in a closed sulphurisation container, as in this study, has not. In this case, an average of 28(2) % of the

initial tin and 1.1(6) % of the initial zinc was lost from the samples, assuming that no copper was. If all the tin and zinc lost remained gaseous as SnS and Zn (which have higher vapour pressures than Sn and ZnS respectively) throughout the reaction, only condensing once the ampoules cooled, the ideal gas law would give average partial pressures during sulphurisation of 1.4 MPa for SnS and 65 kPa for ZnS (and 3.8 MPa for excess sulphur). However, the vapour pressures of SnS and Zn at the sulphurisation temperature are 250 Pa [492] and 26 kPa [491] respectively (and that of sulphur is 3.8 MPa [490]). This suggests that significant amounts of solid SnS and Zn(S) were present in the samples during sulphurisation and that the tin and zinc loss from the sample occurred more slowly, as SnS and Zn(S) condensed on the ampoule wall.

While the exact loss will depend on the volume of the sulphurisation container and the amount of material, these values can be used to approximately determine the starting compositions required to give an intended final sample composition for fabrication of CZTS by solid-state reaction.

6.4. Scanning electron microscopy

The SEM images shown in Figure 63-Figure 69 demonstrate a high degree of porosity in the samples, which is probably a result of the significant tin loss discussed in Section 6.3. B21 in particular was very brittle; it was not possible to achieve a polished surface as grains were very easily ripped away. Several phases are distinguishable in the backscattered electron images, which were identified using EDX as described in Section 6.5.

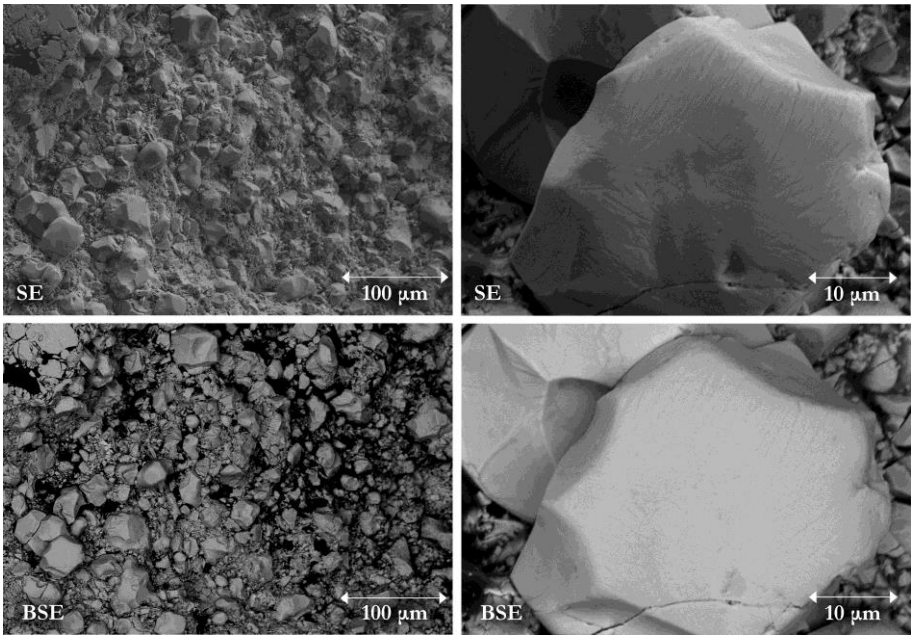

Figure 63: SEM images of B21. The backscattered images reveal only one phase is present, identified as CZTS.

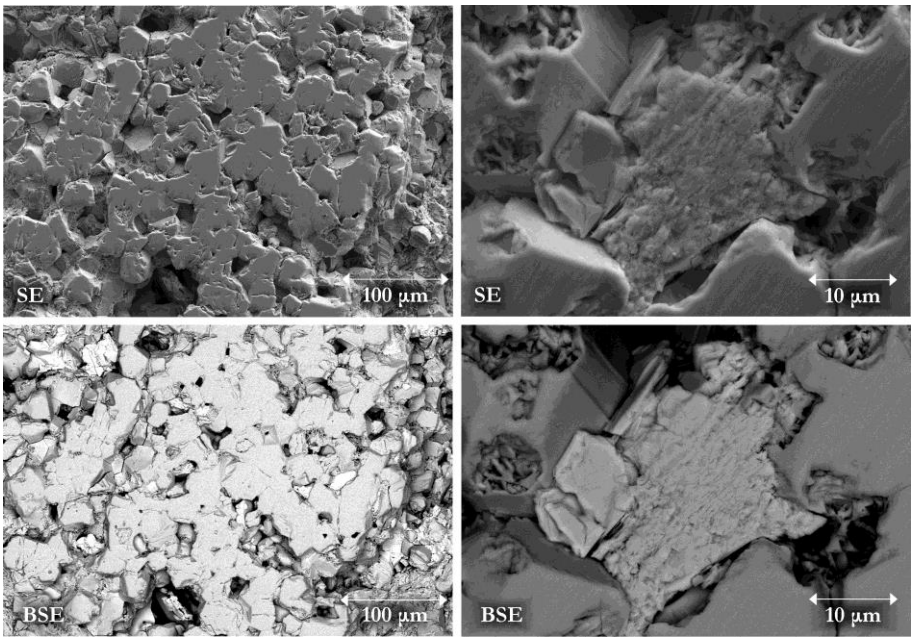

Figure 64: SEM images of B22. The backscattered images reveal a main phase, CZTS, with small grains of ZnS and SnS_2.

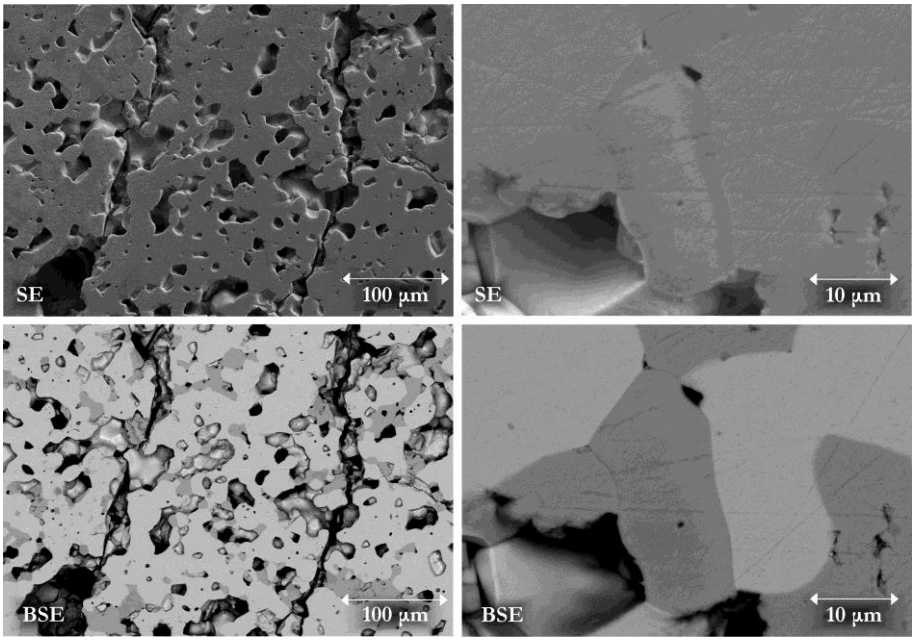

Figure 65: SEM images of B23. The backscattered images show a main phase, CZTS, with darker regions of ZnS and of CuS.

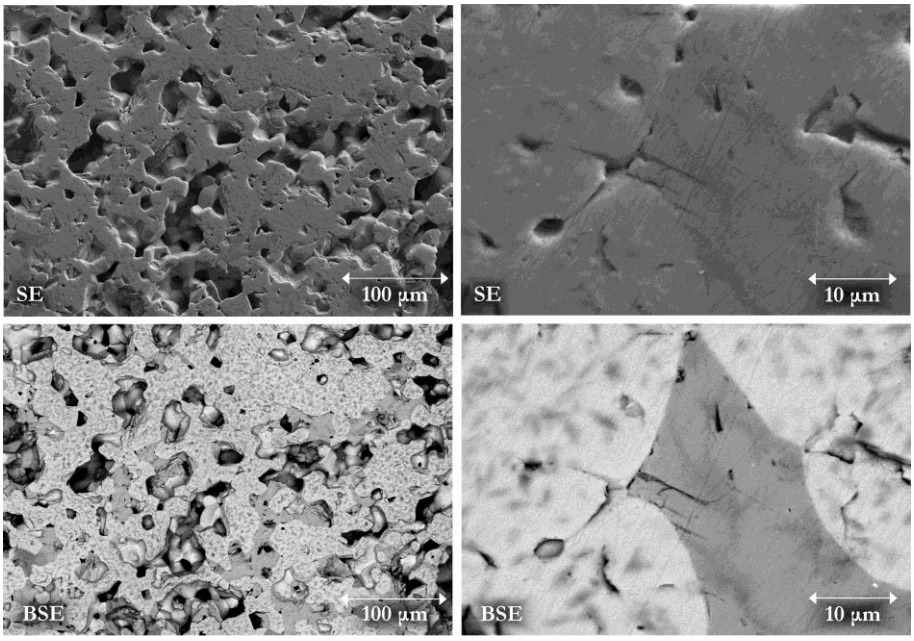

Figure 66: SEM images of B24. The backscattered images show a CZTS phase, containing unidentified darker specks, and darker grains of CuS and ZnS.

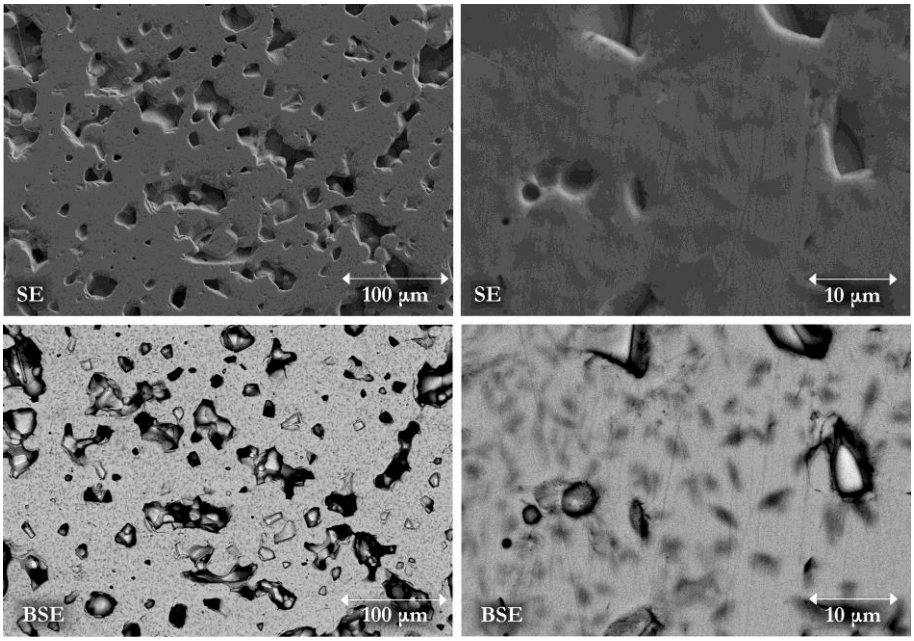

Figure 67: SEM images of B25. The backscattered images show only a CZTS phase, containing unidentified darker specks.

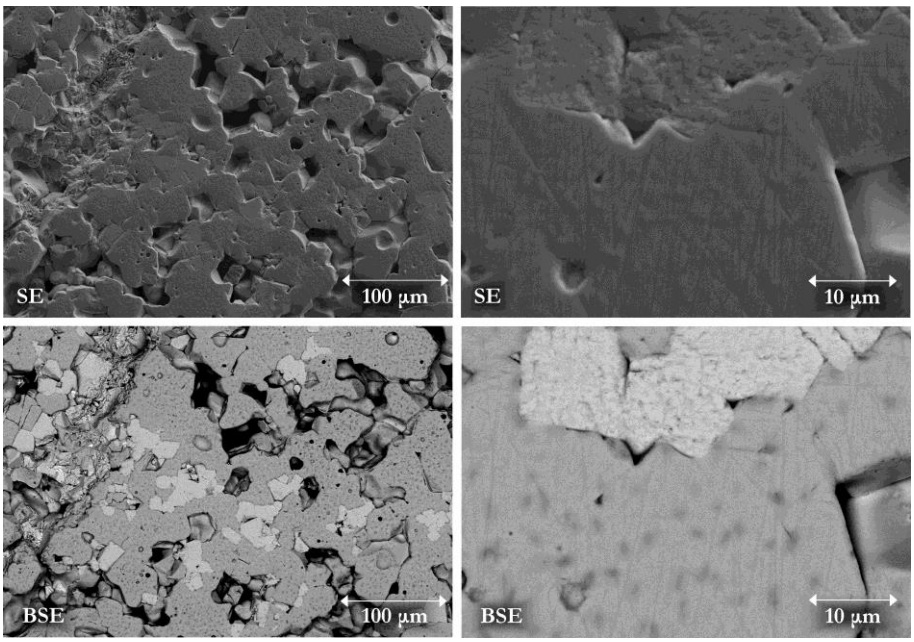

Figure 68: SEM images of B26. The backscattered images reveal a main CZTS phase, containing unidentified darker specks, and lighter regions thought to be $Cu_4Sn_7S_{16}$.

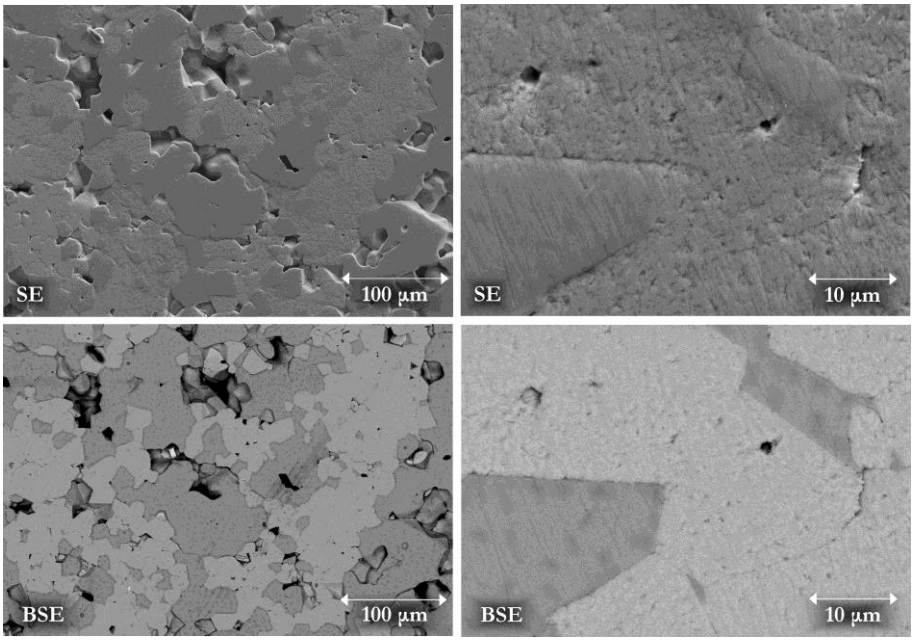

Figure 69: SEM images of B27. The backscattered images reveal a main CZTS phase, containing unidentified darker specks, and lighter regions thought to be $Cu_4Sn_7S_{16}$.

6.5. Energy-dispersive X-ray spectroscopy

EDX was used to identify the phases visible in the backscattered SEM images, and to quantify the stoichiometry of the CZTS phases. The results are given in Table 17.

Sample	CZTS atomic percentages				Secondary phases
	Cu	Zn	Sn	S	
B21	28(2)	13(2)	11(1)	48(2)	None
B22	25.5(9)	16(1)	11(1)	48(1)	ZnS, SnS_2
B23	27.7(6)	14.3(8)	10.4(4)	48(1)	CuS, ZnS
B24	28.0(5)	14(1)	11.0(9)	47.2(8)	CuS, ZnS
B25	30(1)	11(2)	11.4(3)	48(1)	None
B26	28(1)	11.8(6)	12.2(5)	48(2)	$Cu_4Sn_7S_{16}$
B27	28.3(9)	12.4(9)	11.7(3)	48(1)	$Cu_4Sn_7S_{16}$

Table 17: The compositions of the CZTS phases and the secondary phases identified by EDX in samples B21-27. The numbers in brackets are the uncertainties on the last significant figures.

The CZTS compositions are all Sn-poor, implying that some of the tin deficit, due to the evaporation of SnS during fabrication, is accounted for by the CZTS phase incorporating

defects, such as Cu_{Sn} and Zn_{Sn} antisites, rather than or as well as by the formation of secondary phases such as ZnS and CuS. This is confirmed in Chapters 7 and 8.

The CZTS compositions are also S-poor, despite the sulphur excess in the sulphurisation ampoule. This incomplete sulphurisation means that the secondary phases predicted in each region of the quasi-ternary phase diagram in Figure 61 are likely to be incorrect, which is indeed the case. Any future CZTS growth by solid-state reaction under the same conditions should therefore include a sulphur excess greater than 30 %.

In all samples, the binary secondary phases were found to be exactly stoichiometric within the experimental uncertainty. The ternary/quaternary secondary phases found in B26 and B27, however, are more difficult to identify, and are described in Table 18. The atomic percentages found for these phases are within the experimental uncertainty of each other, so it is assumed that the same phase is present in both samples. $CuSn_2S_5$ is a likely ratio, but not a physically observed structure, so is discarded as a possibility for the identity of this phase. $CuSnS_3$, $Cu_2ZnSn_3S_8$, and $Cu_4Sn_7S_{16}$ could all fit the data too, and as the latter gives the best fit and has recently been reported as a secondary phase, [241] this is taken to be the structure. This identification is confirmed by XRD in Section 6.6. From the atomic ratios given in Table 18, it is clear that this $Cu_4Sn_7S_{16}$ features significant atomic disorder.

Sample	Atomic percentages				Atomic ratio
	Cu	Zn	Sn	S	
B26	16(4)	3(2)	23(3)	57(3)	$Cu_{0.8}Zn_{0.2}Sn_{1.2}S_{2.9}$ $Cu_{1.3}Zn_{0.2}Sn_{1.8}S_{4.6}$ $Cu_{2.3}Zn_{0.4}Sn_{3.2}S_{8.0}$ $Cu_{4.5}Zn_{0.8}Sn_{6.2}S_{15.5}$
B27	12(1)	3(1)	25(1)	60(1)	$Cu_{0.6}Zn_{0.2}Sn_{1.3}S_{3.0}$ $Cu_{0.9}Zn_{0.2}Sn_{2.0}S_{4.8}$ $Cu_{1.6}Zn_{0.4}Sn_{3.6}S_{8.4}$ $Cu_{3.2}Zn_{0.8}Sn_{3.9}S_{16.1}$

Table 18: The composition of the seemingly ternary secondary phase in samples B26 and B27, determined by EDX. The numbers in brackets are the uncertainties on the last significant figures.

It should be noted that the ICPMS and EDX composition results are fundamentally different: ICPMS gives a sample-average composition, while EDX gives the composition

of each phase; but it is interesting to compare them (using the EDX CZTS composition). This is shown graphically in Figure 70. As CZTS is the significant-majority phase in all samples, the two results are largely in agreement within uncertainty. As expected, the differences are due to the inclusion of the secondary phases in the ICPMS measurements to skew the values. For example, ICPMS gives a higher zinc content for B23 than EDX (of just the CZTS phase) because it includes the significant amount of ZnS present in the sample; the same occurs for copper in B24 because of CuS. Both B23 and B24 also contain smaller amounts of CuS and ZnS respectively, giving a net effect of ICPMS showing a lower tin fraction than EDX. The broad agreement between the two methods demonstrates that the secondary phases occur with relatively small phase fractions.

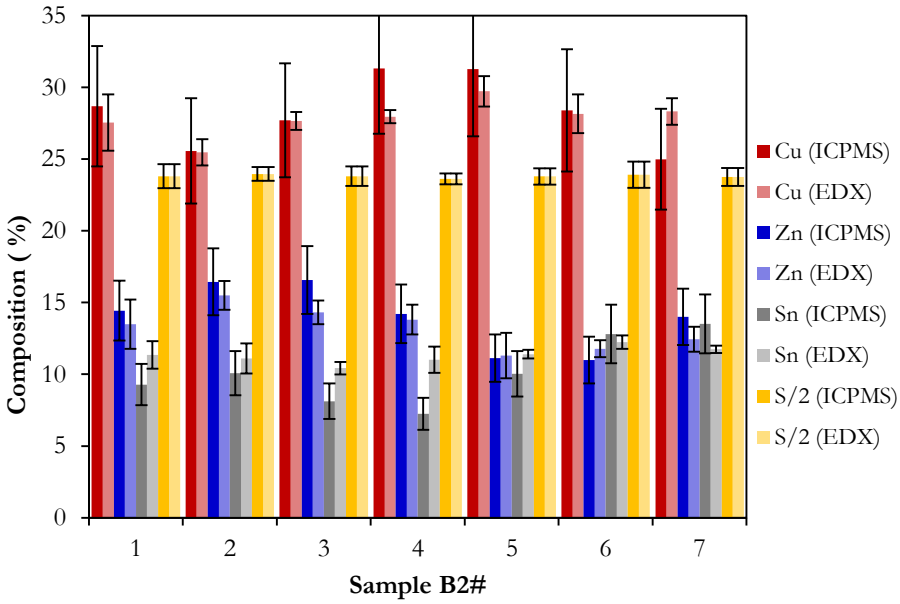

Figure 70: Comparison of the composition of samples B21-27 determined by ICPMS (with S fraction from EDX) and the composition of the CZTS phases thereof determined by EDX.

6.6. X-ray diffraction

Cu-Kα XRD patterns are plotted in Figure 71, and the phase fractions found from Rietveld refinement are given in Table 19, along with the lattice parameters of the CZTS phase. These results largely agree with the phases identified using EDX, with the exception of Cu_2SnS_3 in B21 and B25, and Cu_3SnS_4 in B26. The latter is also clearly identified by Raman spectroscopy in Section 6.8, so is considered genuine. The Cu_2SnS_3 in B21 and B25,

however, is not found using any other method, and as XRD is notoriously unable to properly distinguish Cu_2SnS_3, Cu_3SnS_4, and CZTS, these are concluded to be spurious.

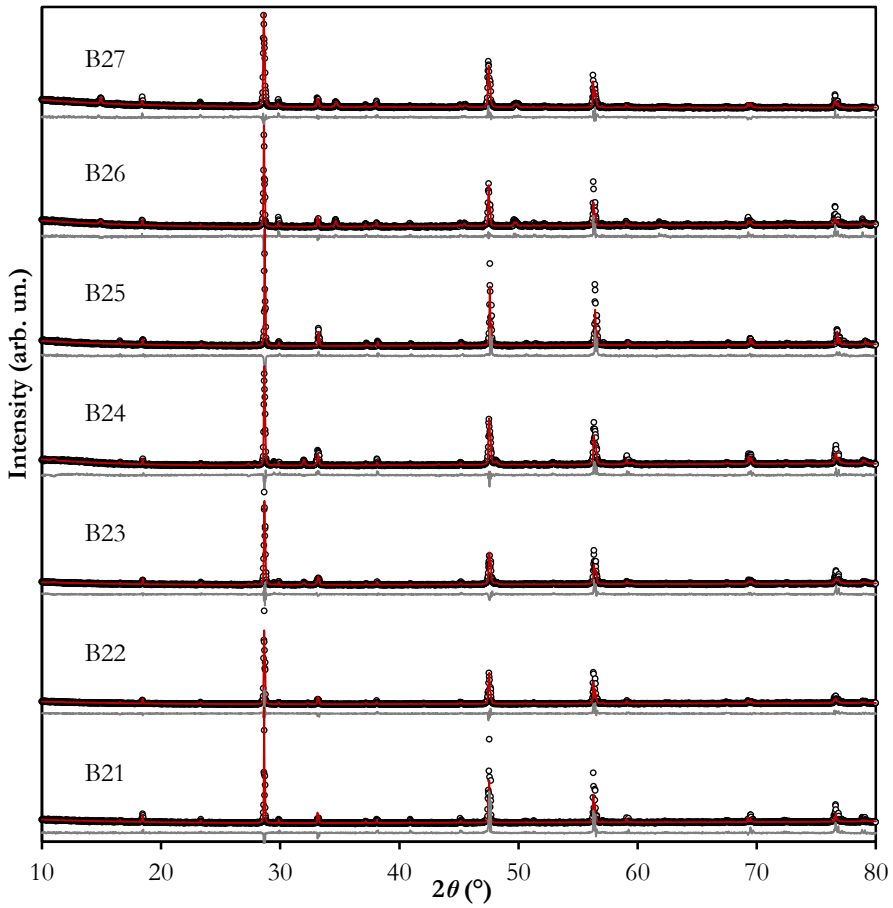

Figure 71: Cu-Kα XRD patterns of samples B21-27 (black circles) with calculated patterns for best-fit models overlaid (red lines), and residuals underneath each one (grey lines); all displaced vertically for clarity.

Sample	Phases			*a* (Å)	*c* (Å)
B21	CZTS 76 %	Cu_2SnS_3 24 %		5.4370(1)	10.840(1)
B22	CZTS 74 %	ZnS 25 %	SnS_2 1 %	5.4376(6)	10.839(1)
B23	CZTS 63 %	ZnS 33 %	CuS 4 %	5.4329(9)	10.839(3)
B24	CZTS 63 %	ZnS 29 %	CuS 8 %	5.4335(9)	10.844(2)
B25	CZTS 77 %	Cu_2SnS_3 23 %		5.4219(8)	10.834(2)
B26	CZTS 63 %	$Cu_4Sn_7S_{16}$ 19 %	Cu_3SnS_4 17 %	5.4356(9)	10.852(2)
B27	CZTS 52 %	$Cu_4Sn_7S_{16}$ 14 %	ZnS 34 %	5.4348(3)	10.842(6)

Table 19: The phase compositions of samples B21-27, and room-temperature lattice parameters of their CZTS phases, found from Rietveld refinement using standard laboratory Cu-Kα XRD. The numbers in brackets are the uncertainties on the last significant figures.

15 keV XRD patterns taken at the I11 beamline of the Diamond Light Source are plotted in Figure 72 and the phase fractions found from Rietveld refinement are given in Table 20, along with the lattice parameters of the CZTS phase. These patterns have a much higher resolution than the standard Cu-Kα ones, meaning the peaks due to different phases that overlap in standard XRD are individually resolved, allowing much more accurate determination of phase fractions. These results agree entirely with the phases identified using EDX, with the exception of the Cu_3SnS_4 in B26. Its identification here further confirms its genuine presence, just as the absence of Cu_2SnS_3 confirms that its identification in B21 and B25 using Cu-Kα X-rays is indeed spurious.

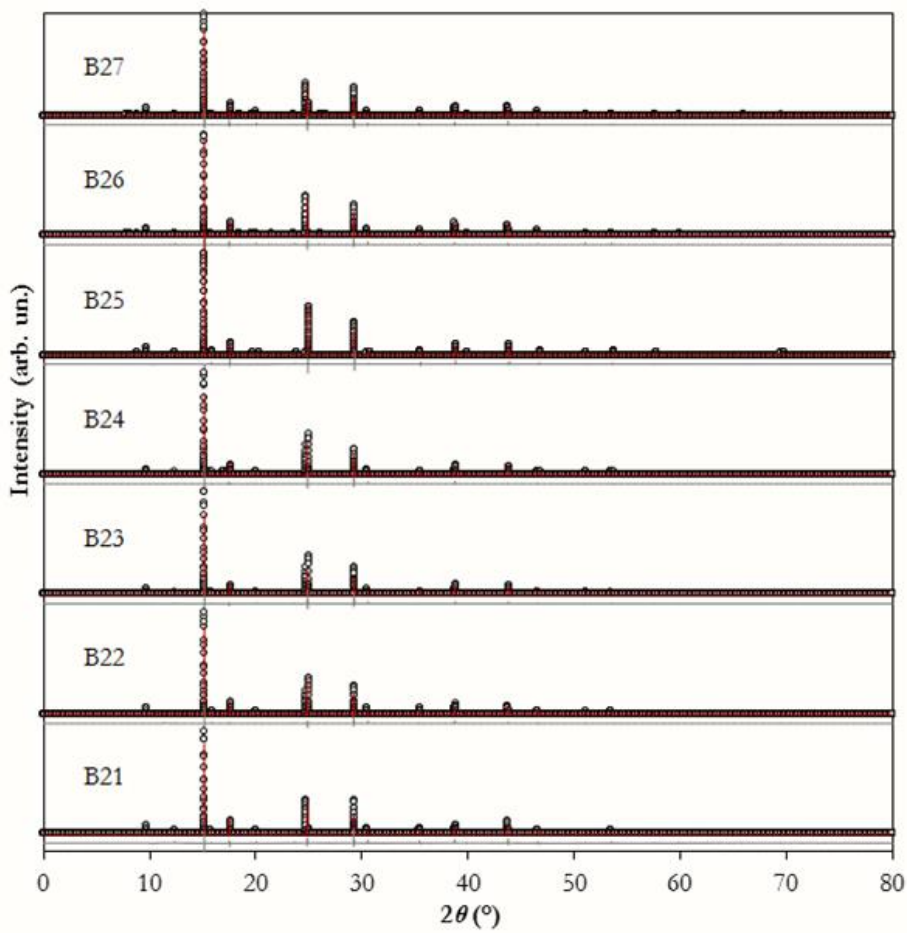

Figure 72: 15 keV XRD patterns taken at the I11 beamline of the Diamond Light Source of samples B21-27(black circles) with calculated patterns for best-fit models overlaid (red lines), and residuals underneath each one (grey lines); all displaced vertically for clarity.

Sample	Phases			*a* (Å)	*c* (Å)
B21	CZTS 100 %			5.43396(1)	10.83593(2)
B22	CZTS 89 %	ZnS 10 %	SnS_2 1 %	5.43294(1)	10.82806(2)
B23	CZTS 80 %	ZnS 12 %	CuS 8 %	5.42940(3)	10.83600(5)
B24	CZTS 79 %	CuS 16 %	ZnS 5 %	5.42917(2)	10.83555(3)
B25	CZTS 100 %			5.41930(2)	10.83047(5)
B26	CZTS 73 %	$Cu_4Sn_7S_{16}$ 17 %	Cu_3SnS_4 10 %	5.43240(1)	10.84586(3)
B27	CZTS 71 %	$Cu_4Sn_7S_{16}$ 21 %	ZnS 8 %	5.43296(4)	10.84356(7)

Table 20: The phase compositions of samples B21-27, and room-temperature lattice parameters of their CZTS phases, found from Rietveld refinement using 15 keV XRD at the I11 beamline of the Diamond Light Source. The numbers in brackets are the uncertainties on the last significant figures.

The lattice parameter values found using the 15 keV patterns are smaller than those found using the Cu-Kα ones. This could be due to the 15 keV patterns being measured while the samples were at a lower temperature, having thermally contracted slightly, or it could simply represent a systematic error in the Cu-Kα measurements. The lattice parameter values from the 15 keV patterns are more precise than those from standard laboratory XRD measurements because of the high resolution possible at the I11 beamline of the Diamond Light Source. Even using the lattice parameter values from the 15 keV patterns, no dependence of either lattice parameter on the compositional fraction of any of the three cation elements is discernible. It is therefore unclear from these measurements what causes the differences in lattice parameters between the samples, although they are likely to be related to point defects in some way.

6.7. Solid-state nuclear magnetic resonance

The ^{65}Cu SSNMR spectra are plotted in Figure 73.

These spectra confirm that the majority of all samples is kesterite CZTS. The bandshapes of samples B21 and B22 both exactly match that reported in academic literature for pure CZTS, [564] showing two copper environments with similar isotropic chemical shifts but quite different quadrupole coupling. The central peak corresponds to the 2*c* site of the kesterite structure and the smaller peaks to either side of this (really a single very broad shift) to the 2*a* site. [295] Sample B27 shows a very similar main structure corresponding to these two environments. B23 and B24 also show the same main pattern, but broader,

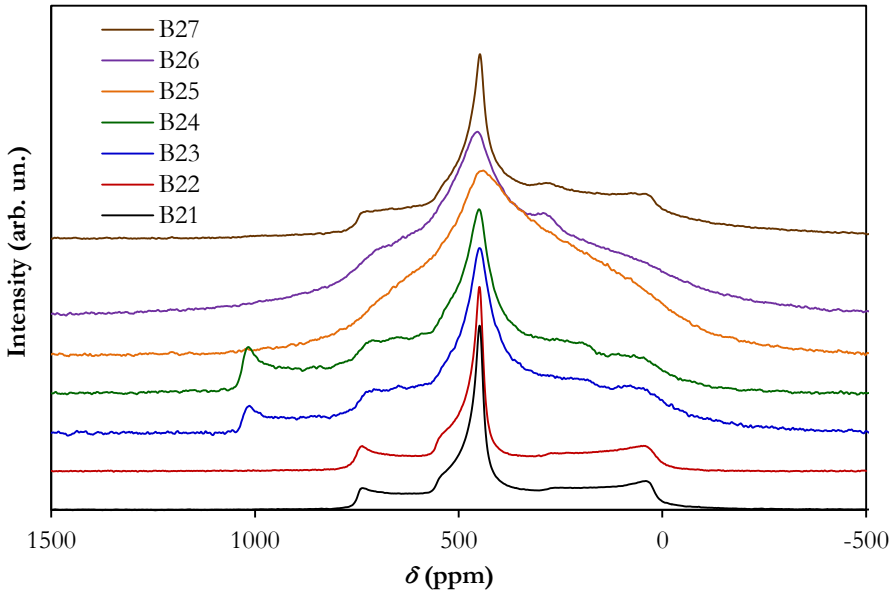

Figure 73: Normalised ^{65}Cu SSNMR spectra of samples B21-27.

suggesting more disorder within the CZTS phases of each sample. The main CZTS peaks of B25 and B26 are much broader still; so much so that the distinct shifts due to the 2*a* and 2*c* lattice sites cannot be distinguished, suggesting either extreme disorder within the kesterite structure or a secondary phase with copper in similar chemical environments, such as Cu_3SnS_4. In Section 6.8, Raman spectroscopy reveals a significant amount of Cu_3SnS_4 in B26, and a particularly large amount of disorder within the CZTS phase in B25, so the broadening of the Cu SSNMR spectra for the two samples is concluded to be due to these two different causes: disorder in the CZTS structure for B25 and Cu_3SnS_4 for B26.

B21 and B22 show only the two CZTS copper environments, consistent with no significant amounts of copper-containing secondary phases being identified in these samples by SEM, EDX, or XRD.

B23 and B24 have at least one additional copper environment, shown by the edge at 1000 ppm, which suggests the presence of a copper-containing secondary phase in these samples. B23 and B24 are the only samples to have been found from EDX and XRD measurements to contain CuS, which is therefore likely to correspond with the peak at 1000 ppm.

B26 and B27 show a different additional weaker peak at approximately 280 ppm, which corresponds to a different third environment, probably a different secondary phase.

$Cu_4Sn_7S_{16}$ was found by EDX and XRD in both B26 and B27, suggesting it could be responsible for the peak at 280 ppm in the Cu NMR spectra. A Cu NMR peak at the same position relative to the CZTS spectrum (although both were reported at different δ values) has previously been reported for Cu_4SnS_{16}, [241] confirming this identification.

The ^{119}Sn SSNMR spectra are plotted in Figure 74. There is no spectrum for sample B25, as this showed signs of conducting and so, for technical reasons, being difficult to spin (magic-angle spinning was necessary to achieve a reasonable signal for ^{119}Sn SSNMR; see Section 5.8),. A 10 s recycle delay was used to record the tin spectra; static work also performed suggests that the relaxation, at least in part, might have been slower than this, so the 10 s delay might be underrepresenting one of the components in the spectra (probably the one with the narrower line).

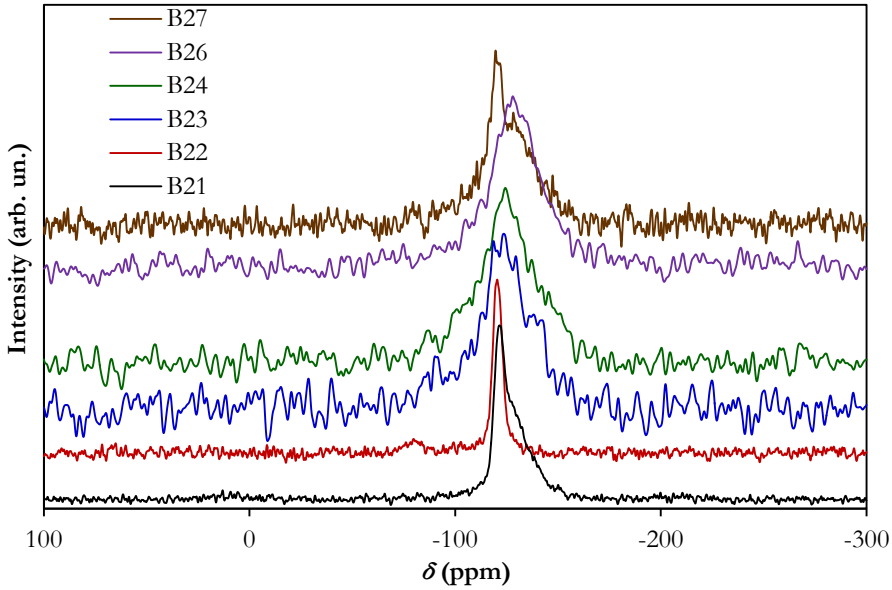

Figure 74: Normalised ^{119}Sn SSNMR spectra of samples B21-27.

The tin spectra do show differences between them, although these are obscured by the significant noise. The main CZTS peak, a symmetric line at -120 ppm, is evident in all samples. B22 is the only one in which it is relatively narrow, which is consistent with a single, well defined tin environment as expected. In other samples it is either significantly broadened or accompanied by a shoulder peak.

B21 and B27 both show the main -120 ppm peak, but with a broad low-frequency shoulder at a more negative shift, suggesting a slightly different disordered environment. B26

appears only to show this broad, more negative component, suggesting a single, very disordered environment. This cannot be the $Cu_4Sn_7S_{16}$ phase identified using EDX, XRD, and Cu NMR, as it is present in B21, which none of the other analysis methods show $Cu_4Sn_7S_{16}$ to be. Similarly, it cannot be Cu_3SnS_4 because this is present only in B26. It cannot be Cu_2SnS_3 or Cu_4SnS_4, as the other analysis methods show this phase is not present in any of the samples. This tin environment must therefore be related to a specific defect rather than a secondary phase.

Both elements of the peak are much broader in samples B23 and B24, suggesting much greater disorder.

B22 shows a second peak, with very low intensity, at -80 ppm, which is not evident in the spectra for any other sample. This has previously been assigned to tin nuclei at the 2*b* site influenced by copper vacancies in their second coordination shells. [295] However, the peak could represent a tin-containing secondary phase instead: B22 is the only sample in which SnS_2 is found, suggesting that this phase could give rise to the -80 ppm peak.

6.8. Raman spectroscopy

For each sample, the Raman spectra taken across the surface and cross-section were all of approximately the same shape, showing a reasonable degree of compositional uniformity throughout the sample. The spectra were averaged to give a single representative spectrum for each sample using each excitation wavelength. Each spectrum, with background removed and normalised, was fitted using up to 13 peaks, which are listed in Table 21. These were identified using previous literature reports (CZTS, [222,258,412,517,568-578] CuS, [581] and Cu_3SnS_4; [580] see Section 5.9.1). The fitted spectra are shown in Figure 75 for 785 nm excitation and Figure 76 for 488 nm.

For 785 nm excitation, samples B21, B22, and B27 show strong signals with clear CZTS peaks, while B23, B24, B25, and B26 show much smaller signals relative to the background, with broader peaks and greater noise, which makes fitting the smaller peaks less certain. For example, the three peaks at 250, 262, and 273 cm^{-1} are indistinguishable by sight for these four samples and therefore their fitted amplitudes may have significant error. For 488 nm all samples show a strong Raman signal relative to the background, but the smaller

Peak value (cm^{-1})	Phase	Symmetry
250	CZTS	B
262	CZTS	B
273	CZTS	E
286	CZTS	A
300	CZTS	A
312	CZTS	B
317	Cu_3SnS_4	-
332	CZTS Cu-Zn disorder	A_1
337	CZTS	A
351	CZTS	B
362	CZTS	E
371	CZTS	B
472	CuS	-

Table 21: The peaks identified in the Raman spectra of B21-27.

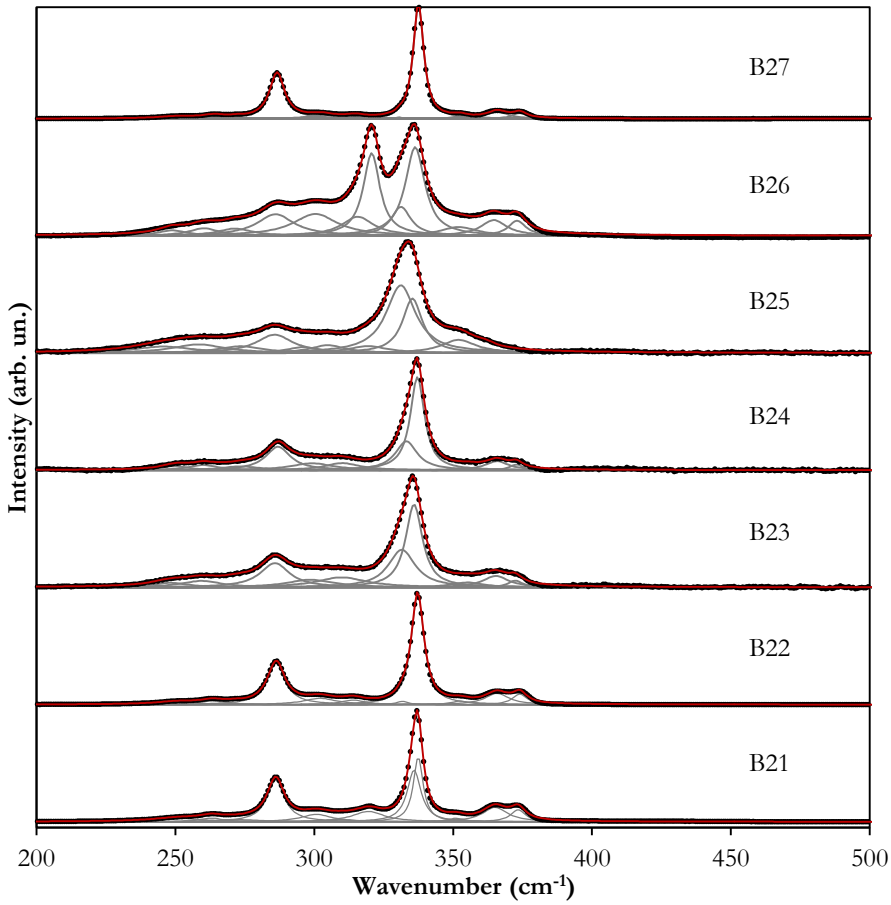

Figure 75: The Raman spectra for samples B21-27 using 785 nm excitation, with background removed and normalised, displaced vertically for clarity.

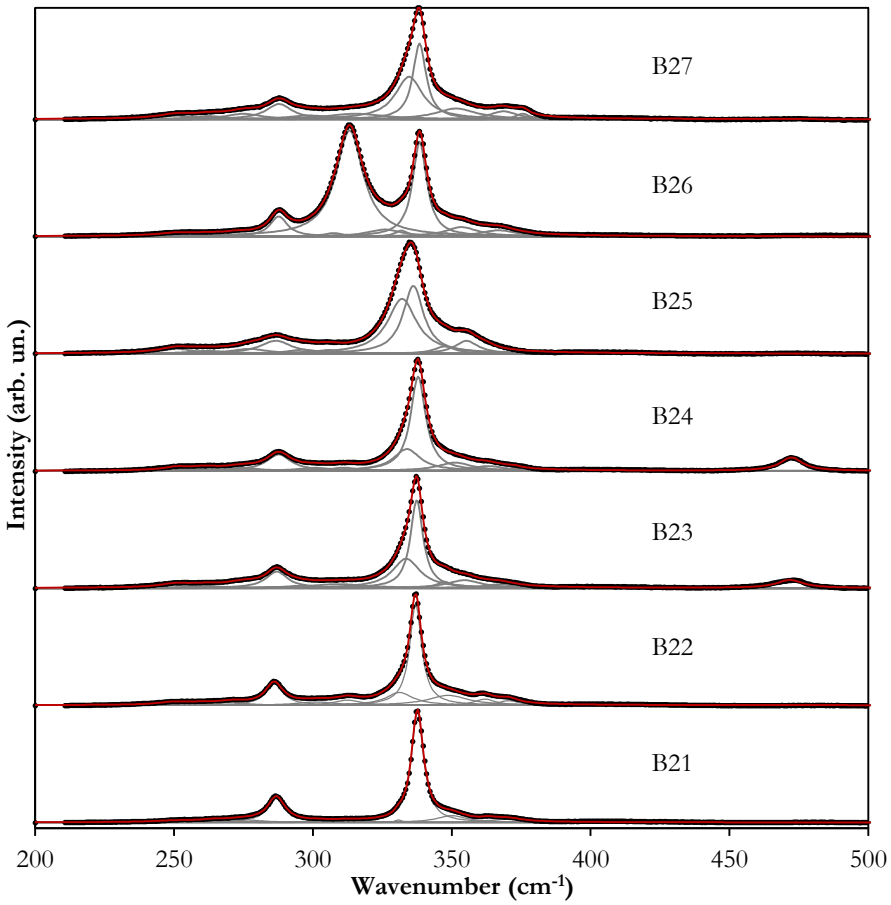

Figure 76: The Raman spectra for samples B21-27 using 488 nm excitation, with background removed and normalised, displaced vertically for clarity.

peaks are less well defined than their 785 nm equivalents as is to be expected for non-resonant excitation.

The Raman spectra confirm that the majority of all samples is CZTS, with the possible exception of B26, which has a very strong Cu_3SnS_4 peak. This peak is also present with much lower intensity in the 785 nm spectra for samples B21 and B25. Interestingly, this peak occurs at lower wavenumber for 488 nm excitation, for which no explanation has yet been found.

The 488 nm spectra confirm the presence of CuS in B23 and B24. The corresponding 785 nm spectra do not show these peaks at all, demonstrating the usefulness of multi-wavelength Raman analysis.

Almost all of the samples have significant peaks at 332 cm^{-1}, reported to represent the Cu-Zn disorder within a sample, as it is the main peak of the disordered kesterite phase. [570-575,578] The ratio of the two A mode peaks at 286 cm^{-1} and 300 cm^{-1},

$$Q = I_{286} / I_{300} , \quad (46)$$

has also been shown to be a measure of cation order in CZTS (see Section 5.9.1). [233,234] However, there is no correlation between these two supposed measures of disorder for the data presented here, and also no correlation between the two measurements of each parameter per sample, from the two excitation wavelengths used, as shown in Figure 77. This suggests either that they are both poor measures of disorder, or that there is significant uncertainty in the peak fitting.

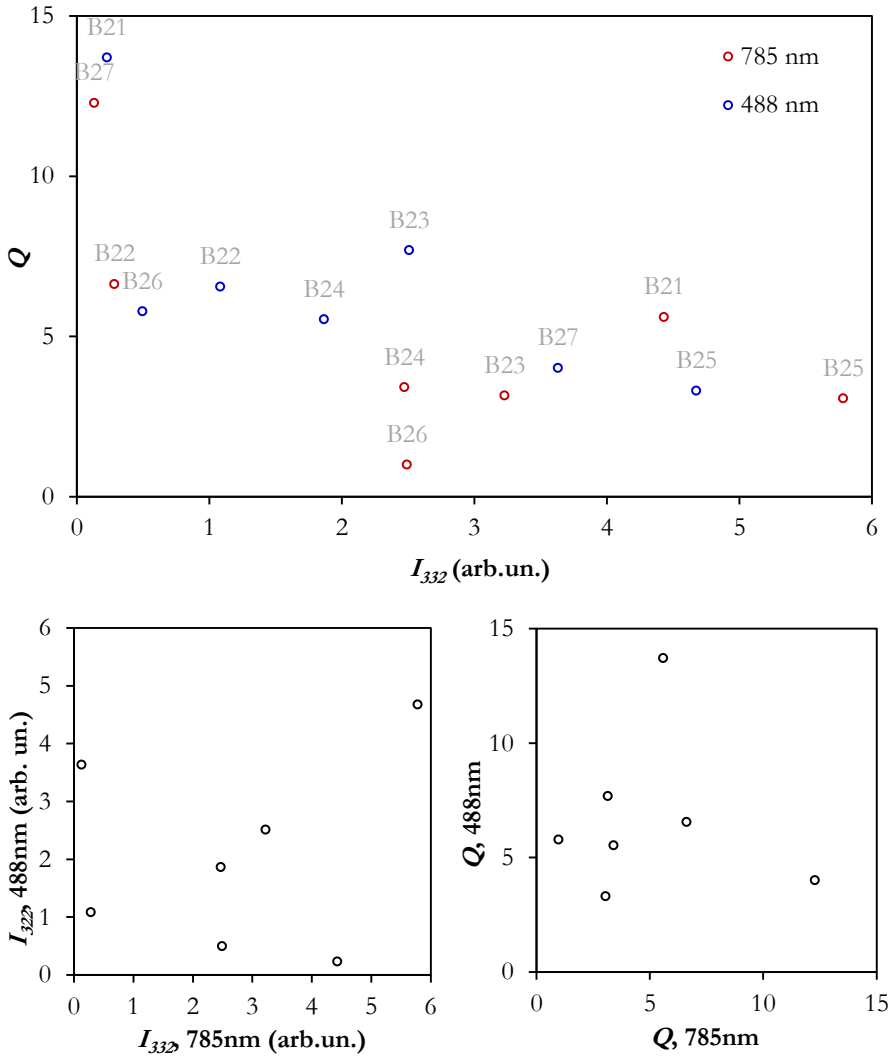

Figure 77: The lack of correlation between (top) the two measures of cation disorder from Raman spectra of B21-27: the intensity of the 'disordered kesterite' peak at 332 cm^{-1} and the Q ratio of the CZTS A modes at 286 and 300 cm^{-1}; and between the two measurements of each parameter from the two different wavelengths used: (bottom left) the intensity of the peak at 332 cm^{-1} and (bottom right) the Q ratio.

6.9. Photoluminescence spectroscopy

The photoluminescence spectra taken over a range of temperatures for each sample are plotted in Figure 78-Figure 84.

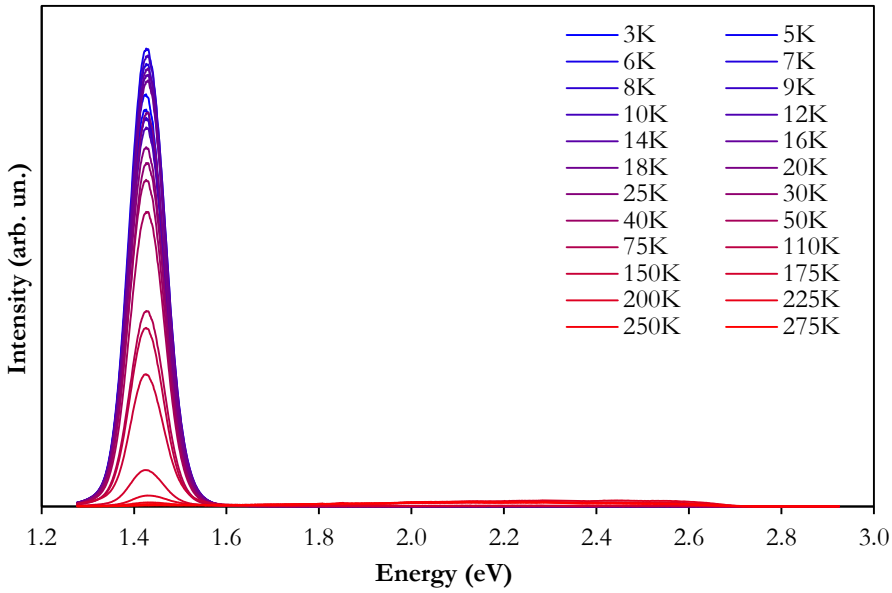

Figure 78: Photoluminescence spectra over a range of temperatures for B21.

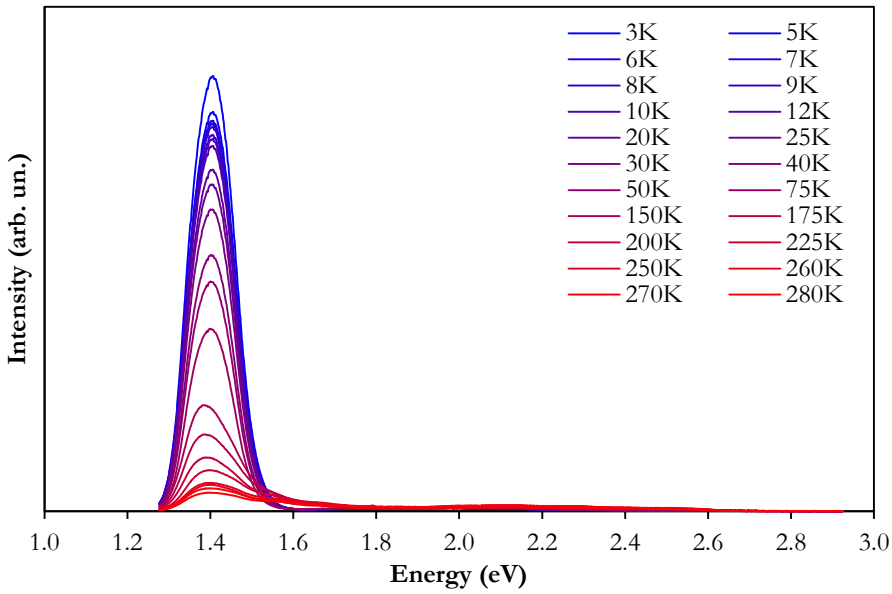

Figure 79: Photoluminescence spectra over a range of temperatures for B22.

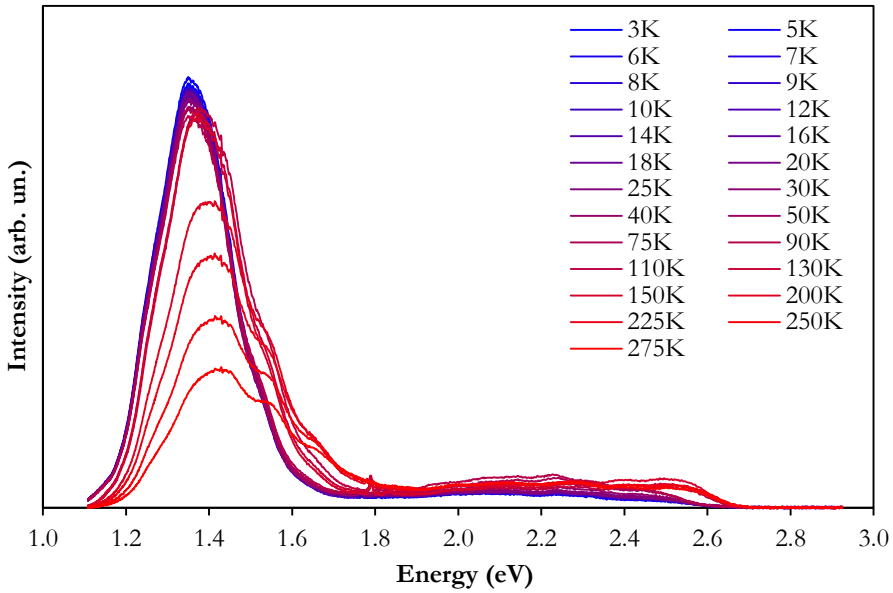

Figure 80: Photoluminescence spectra over a range of temperatures for B23.

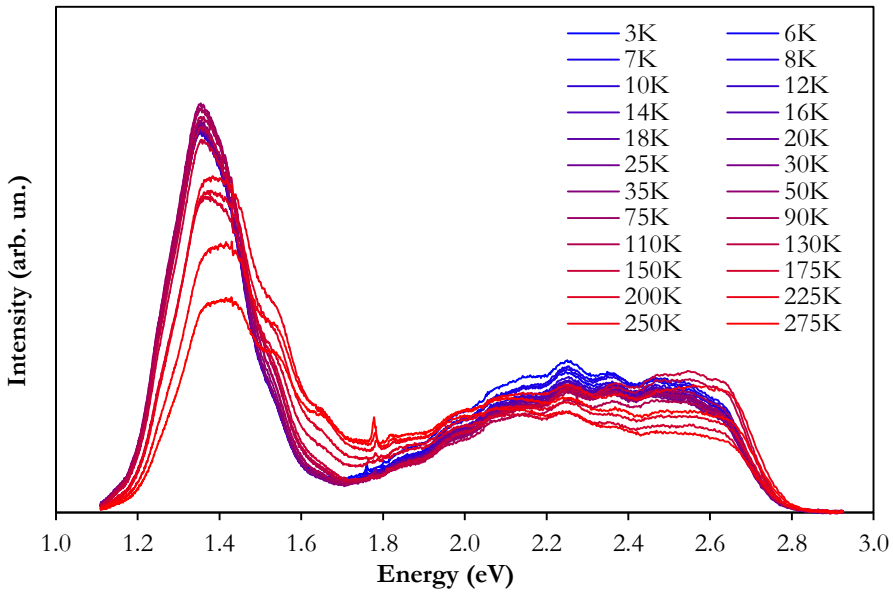

Figure 81: Photoluminescence spectra over a range of temperatures for B24.

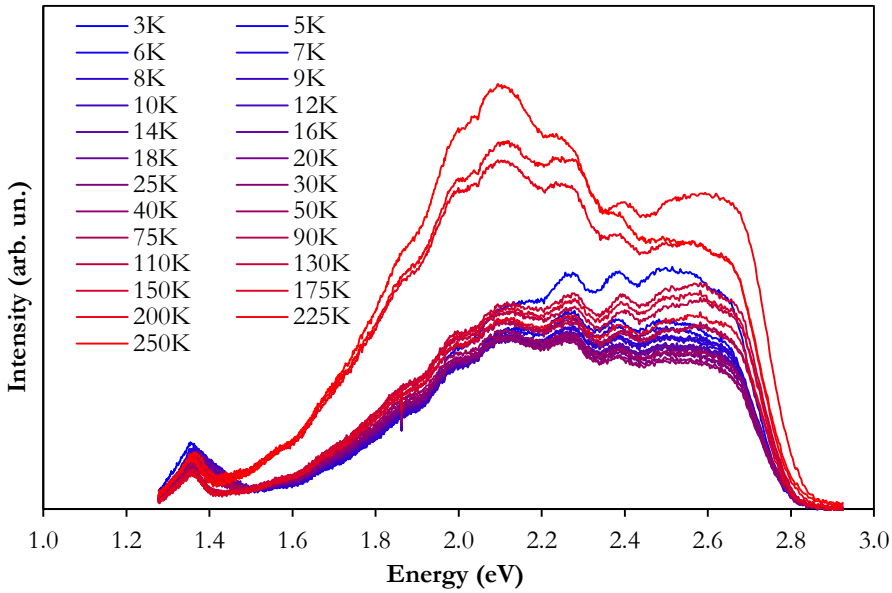

Figure 82: Photoluminescence spectra over a range of temperatures for B25.

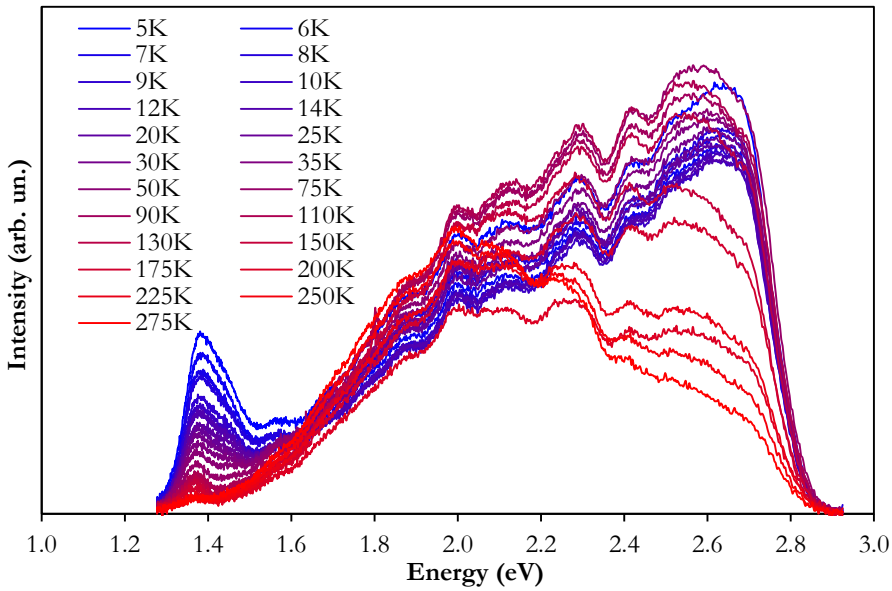

Figure 83: Photoluminescence spectra over a range of temperatures for B26.

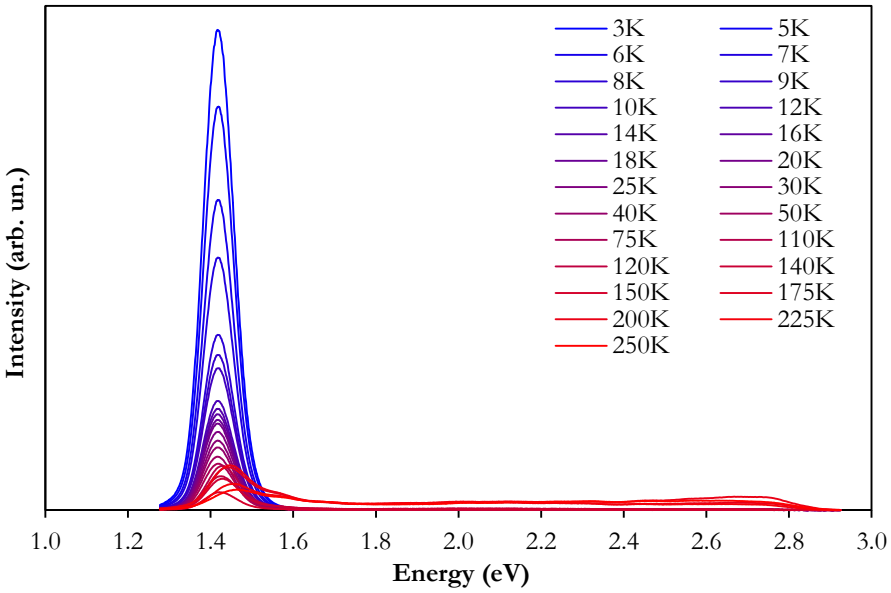

Figure 84: Photoluminescence spectra over a range of temperatures for B27.

The spectra for all samples were accurately fitted using Gaussian peaks at the energy values listed in Table 22. Fitted low-temperature spectra are shown in Figure 85.

Literature peak value (eV)	Material	Experimental peak value (eV)	Energy shift (meV·K^{-1})
1.23	SnS	1.16	0.1
1.27	Cu_2ZnSnS_4	1.27	0.04
1.35	Cu_2ZnSnS_4	1.34	0.04
1.48	Cu_2ZnSnS_4	1.42	0.1
1.53	Cu_2ZnSnS_4	1.52	0.08
1.77	SnS_2	1.69	0.03
1.80	ZnS	1.73	0.05
1.94	ZnS	1.89	-0.01
2.06	ZnS	1.98	-0.01
2.13	ZnS	2.12	-0.09
2.26	SnS_2	2.26	-0.06
2.38	CuS	2.34	-0.02
2.50	CuS	2.45	0.02
2.56	CuS	2.56	0.03
2.71	CuS	2.68	0.07

Table 22: The photoluminescence peaks used to fit the observed spectra. The two lowest-energy peaks were only used for samples B23 and B24, which required measurement at lower energy to capture the full CZTS peak. The experimental peak values have been linearly extrapolated to 3 K and averaged; the energy shift is the gradient of this extrapolation.

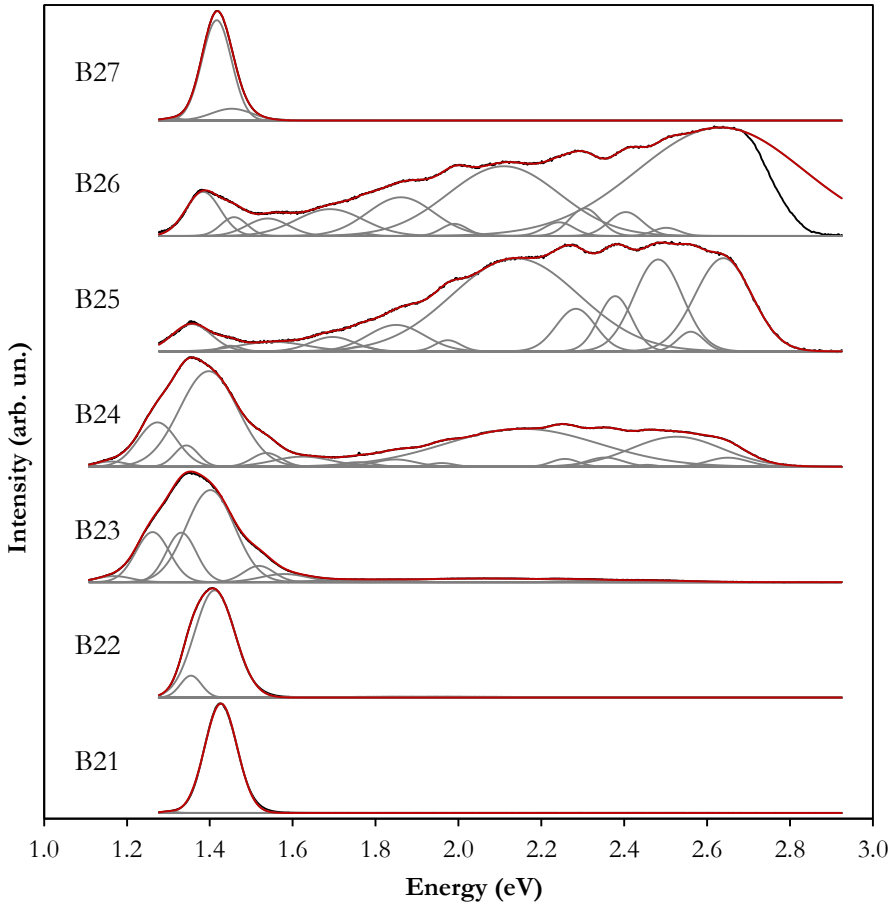

Figure 85: Low-temperature (3 or 5 K) photoluminescence spectra for samples B21-27 with the peaks used to fit them.

It should be noted that some of the peak values are doubtful. The significant overlap of secondary-phase peaks is perhaps the greatest source of uncertainty, and makes consistent intensity fitting difficult. The photoluminescence signal was observed to be highly location sensitive on the sample surface; this means that the observed luminescence might not be representative of the entire sample, and also that small random shifts in alignment, e.g. due to thermal contraction/expansion of the cryostat finger the samples were mounted on, sometimes meant a qualitatively different signal was measured over a temperature range: see for example the jump to the hottest three spectra for sample B25 in Figure 82. Additionally, it is possible that some peak assignations are significantly affected by the cut-off filters or detector range at either end of the spectral range, and that the joining together of two spectra for samples B22 and B23 (in order to cover a sufficiently low energy range to capture the whole CZTS peak) may have altered the position of the fitted peaks near the join.

The temperature dependence of the peak positions was fitted using a simple linear gradient. The values of these fits at 3 K are given as the experimental peak values in Table 22, and the gradients as the energy shift, averaged over all samples for which the peaks were sufficiently discernible. The peak energies are in good agreement between samples, with the standard deviation being ~10 meV for all peaks. However, there is significant variation in the temperature-dependent energy shifts, with the standard deviation between samples often comparable to the average value itself.

The amplitudes of the secondary phase peaks are negligible for B21, B22, and B27; they are present for B23 and, at higher temperatures, B24; and dominant for B25 and B26. While peak intensities cannot be taken as quantitative representations of phase fractions, some qualitative comparison between samples is interesting. The 3 K spectra are used for this, with the intensities of all peaks attributed to a phase added together. The B21, B22, and B27 spectra are 100 % CZTS, with negligible secondary phase photoluminescence. 90 % of the luminescence from B23 and approximately 50 % of that from B24 is due to CZTS, with the remainder mostly being equally from ZnS and CuS. The luminescence from both the B25 and B26 is around 50 % CuS, 30 % ZnS, and some CZTS and SnS_2. A small amount of SnS_2 is identified in B23-26, but as this has not been identified using any other experimental technique, it is concluded to be negligible, with the measured values erroneously shifted towards higher intensities by inaccurate peak fitting.

These secondary phase results do not agree with those of the other experimental techniques, particularly in the identification of such large amounts of CuS and ZnS in B25 and B26. This implies that the identification of the photoluminescence in the range 1.5 to 3 eV using peak values reported in academic literature is incorrect. Qualitative comparison of the spectra for each sample using the secondary phase information from other techniques suggests that the dominance of this higher-energy photoluminescence might be linked to the presence of Cu_3SnS_4 and the significant disorder (or possibly other ternary secondary phase) that is also particularly evident in the Cu SSNMR spectra (Figure 73 in Section 6.7). Photoluminescence is concluded not to be an appropriate tool to identify the presence of specific secondary phases, even qualitatively.

Despite this failure to identify secondary phases, the CZTS photoluminescence peaks can be studied to determine information on recombination in the samples.

The 1.27 eV and 1.34 eV CZTS peaks have previously been attributed to band-to-acceptor recombination in disordered and ordered kesterite CZTS respectively, the 1.42 eV peak to band-to-tail recombination involving fluctuating-potential tail states on the valence band edge, and the 1.52 eV peak to band-to-band recombination. [332,592] These peaks are all observed to blueshift with increasing temperature due to thermal excitation of free electrons in the conduction band. [610] The acceptor involved in the 1.27 and 1.34 eV emission, indicated by the experimental peak values here to have a defect level of 180 meV for ordered kesterite CZTS, seems likely to be Cu_{Zn} as the CZTS phases of all samples are Cu-rich and Cu_{Zn} has previously been theoretically calculated to have a defect level between 120 meV [190] and 217 meV [611] above the valence band. The amplitude of the fluctuations in potential, calculated as the difference between the band-to-band and band-to-tail peak energies, is 100 meV; this value has previously been reported as from 11 meV [332] to 172 meV. [318] The band-to-tail recombination is dominant in all samples except B25 and B26, for which the band-ro-impurity recomination is found to be dominant, although the latter could be incorrect due to inaccurate fitting of the very low intensity of the peaks for those samples.

All the CZTS peaks gave lower intensity at higher temperature. This thermal quenching is due to non-radiative recombination channels becoming activated at higher temperatures. The intensity variation with temperature was fitted for the four CZTS peaks using the exponential models described in Section 5.10.2. All four were best fitted in almost all samples by a bi-exponential model involving two discrete defects, of the form

$$I = \frac{I_0}{1+\alpha_1 \cdot \exp\left(\frac{-E_1}{k_B T}\right)+\alpha_2 \cdot \exp\left(\frac{-E_2}{k_B T}\right)}, \qquad (54)$$

where E_1 and E_2 are the thermal activation energies associated with the two non-radiative recombination channels responsible for the thermal quenching of the photoluminescence at high temperatures ($E_1 < E_2$), a_1 and a_2 are measures of the concentration (i.e. relative degeneracy) of the states corresponding to E_1 and E_2., I_0 is the intensity at 0 K, k_B is the Boltzmann constant, and T is temperature. All bi-exponential models gave significantly better fits than single exponential models, but the difference between the three bi-exponential models (corresponding to two discrete defects, one defect and one band-related channel, and two band-related channels) was much smaller, meaning these cannot be conclusively ruled out as the true thermal quenching mechanisms. For the secondary phase peaks, the noise due to inaccurate intensity fitting because of the significant peak

overlap was too large to give meaningful model parameters. The parameters for the CZTS peaks are given in Table 23, except for B23, B24, and B25 because the low intensity of the CZTS peaks for these samples also led to the uncertainty on the model values being too large for them to be meaningful. The corresponding fits are plotted in Figure 86-Figure 89.

Sample	1.27 eV peak		1.34 eV peak		1.42 eV peak		1.52 eV peak	
	E_1	E_2	E_1	E_2	E_1	E_2	E_1	E_2
B21	-	-	85	8	90	8	-	-
B22	-	-	52	5	63	5	-	-
B23	85	46	-	-	223	27	-	-
B24	-	-	-	-	-	-	-	-
B25	-	-	-	-	-	-	-	-
B26	-	-	16	0	16	1	749	11
B27	-	-	36	1	48	1	24	1

Table 23: The activation energies for the CZTS photoluminescence peaks of B21-27, found by fitting Equation **Error! Reference source not found.** to the data. Several values are not shown because their uncertainty was too great for them to be meaningful.

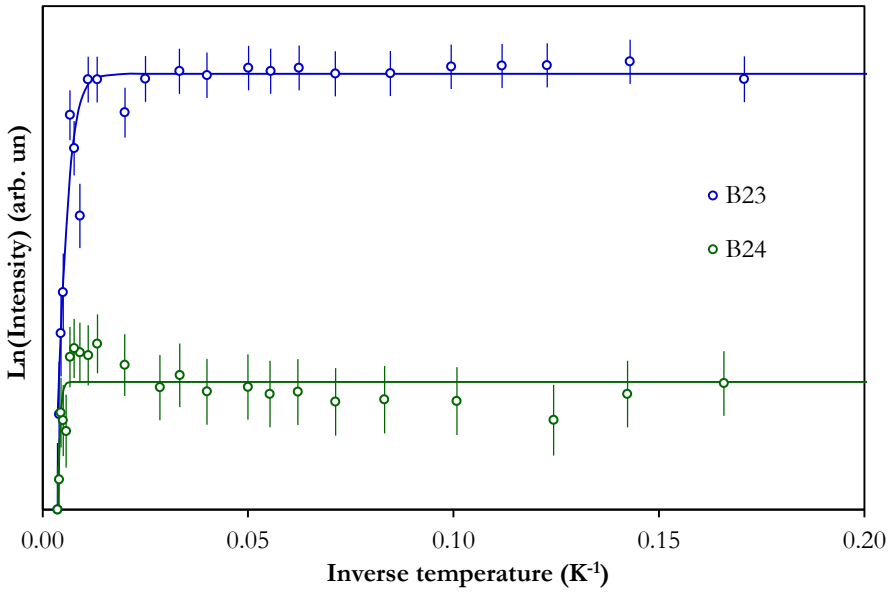

Figure 86: Intensity as a function of temperature for the CZTS photoluminescence peak at 1.27 eV of B23 and B24, with fitted models described by Equation (54).

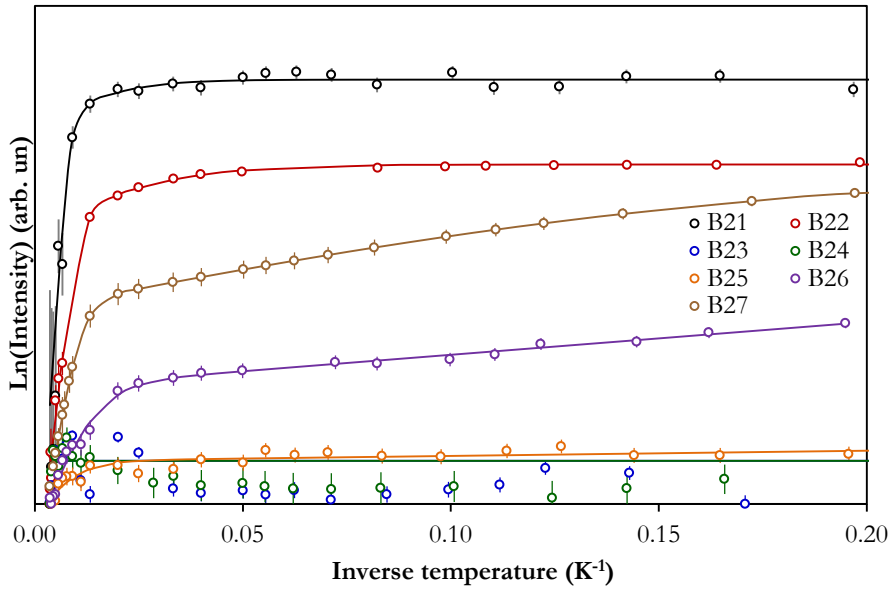

Figure 87: Intensity as a function of temperature for the CZTS photoluminescence peak at 1.34 eV of samples B21-27, with fitted models described by Equation (54).

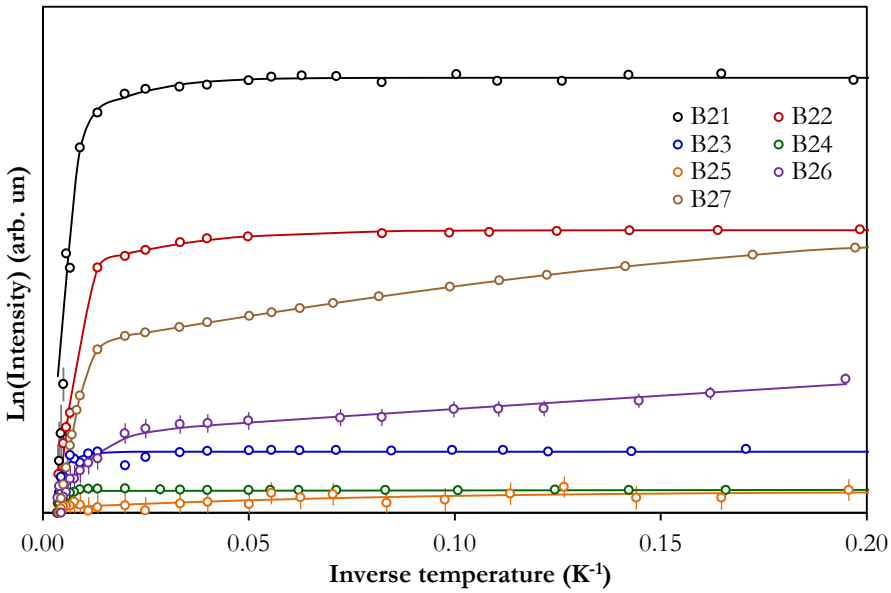

Figure 88: Intensity as a function of temperature for the CZTS photoluminescence peak at 1.42 eV of samples B21-27, with fitted models described by Equation (54).

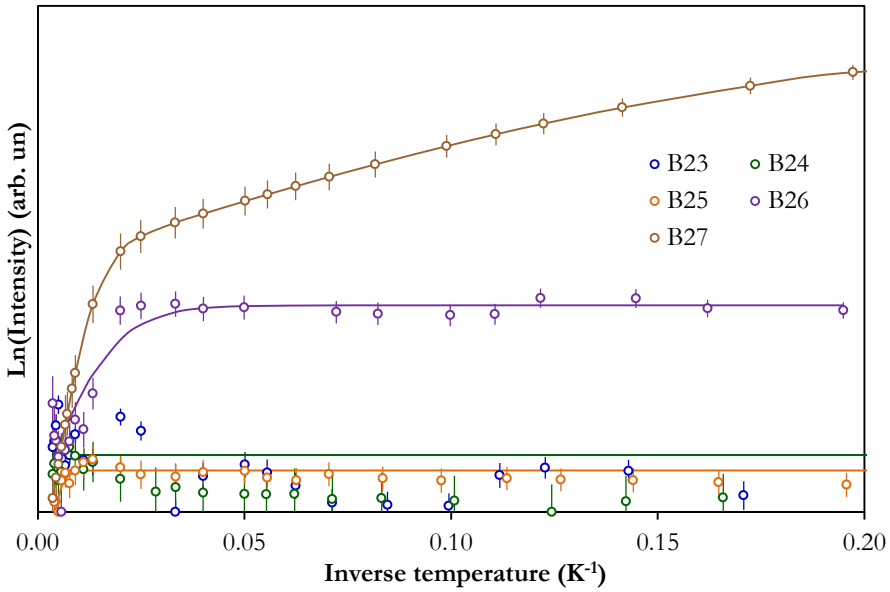

Figure 89: Intensity as a function of temperature for the CZTS photoluminescence peak at 1.53 eV of samples B21-27, with fitted models described by Equation (54).

6.10. Conclusions

The effect of elemental composition was studied by fabricating seven samples with different compositions in the region around the stoichiometric point. Several optoelectronic and structural analysis techniques were used to successfully identify the secondary phases in the samples and to study their effects on some properties and behaviour of the CZTS phase itself.

6.10.1. Element loss

Element loss from the samples during fabrication was quantified: 28(2) % of tin and 1.1(6) % of zinc was lost. These values allow future bulk samples to be manufactured with desired final compositions. It was also concluded that significant amounts of solid SnS and Zn(S) were present in the samples during sulphurisation and that the tin and zinc loss from the sample occurred slowly, as SnS and Zn(S) condensed on the ampoule wall.

The main assumption behind the quasi-ternary phase diagram, that complete stoichiometric sulphurisation always occurs, was shown to be incorrect, meaning that it does not correctly predict the secondary phases that will be formed for a given elemental composition.

6.10.2. Secondary phases

The secondary phases found in the samples using each method are compared in Table 24.

Sample	EDX	XRD	^{65}Cu NMR	^{119}Sn NMR	Raman	Photolum-inescence	Total
B21	-	~~Cu_2SnS_3~~	-	-	-	-	-
B22	ZnS SnS_2	ZnS SnS_2	-	SnS_2	-	-	ZnS SnS_2
B23	CuS ZnS	CuS ZnS	CuS	-	CuS	~~CuS~~ ~~ZnS~~	CuS ZnS
B24	'Specks' CuS ZnS	CuS ZnS	CuS	-	CuS	~~CuS~~ ~~ZnS~~	'Specks' CuS ZnS
B25	'Specks'	~~Cu_2SnS_3~~	-		-	~~CuS~~ ~~ZnS~~	'Specks'
B26	'Specks' $Cu_4Sn_7S_{16}$	Cu_3SnS_4 $Cu_4Sn_7S_{16}$	Cu_3SnS_4 $Cu_4Sn_7S_{16}$	-	Cu_3SnS_4	~~CuS~~ ~~ZnS~~	'Specks' Cu_3SnS_4 $Cu_4Sn_7S_{16}$
B27	'Specks' $Cu_4Sn_7S_{16}$	ZnS $Cu_4Sn_7S_{16}$	$Cu_4Sn_7S_{16}$	-	-	-	'Specks' ZnS $Cu_4Sn_7S_{16}$

Table 24: The secondary phases found in samples B21-27 by each analysis technique. Struck-though text indicates phases that were concluded to have been incorrectly identified. The greyed-out entry represents a measurement it was not possible to take.

None of the analysis techniques used identified the 'specks' visible in the SEM images of samples B24-B27, or the tin defect identified by Sn SSNMR.

The Cu_3SnS_4 clearly identified in B26 by XRD and Raman was not observed in the SEM images because, as copper and zinc have such similar masses, Cu_3SnS_4 and CZTS appear indistinguishable to backscattered electrons. Similarly, the copper and tin environments of Cu_3SnS_4 do not appear separately in the NMR spectra, because the difference in chemical environments between CZTS and Cu_3SnS_4 may be negligible due to copper and zinc being isoelectronic in CZTS.

The $Cu_4Sn_7S_{16}$ in B26 and B27, observed using EDX, XRD, and Cu SSNMR, was not detected using Raman spectroscopy, despite its Raman peaks occurring within the measurement range. This may be because a resonant excitation wavelength for $Cu_4Sn_7S_{16}$ was not used. The tin environments of $Cu_4Sn_7S_{16}$ do not appear in the Sn NMR spectra because their peaks are outside the range of δ values over which this data was taken.

Some trends in the dependence of secondary phases on composition are evident. ZnS is the most prevalent secondary phase, being found in four of the seven samples: all those Zn-rich except B21 (B22, B23, B24, and B27). The very Sn-poor samples (B23 and B24) were the only ones to form CuS; this implies that ternary or quaternary phases are energetically favourable to CuS, and so only when these cannot form due to a lack of tin does CuS form. However, the only ternary phase found, Cu_3SnS_4, was only found in one sample, which is both one of the richest in tin (approximately stoichiometric) and Zn-poor. $Cu_4Sn_7S_{16}$ was found in both of the only samples not Sn-poor.

It is clear that only a combination of several analysis techniques can identify all the secondary phases found in CZTS. XRD remains the most successful, and has the advantage that it provides quantitative phase fractions. It is particularly notable that XRD was the most successful at identifying ZnS here, despite being widely accepted as unable to differentiate between this and CZTS with the resolution of standard diffractometers. However, other techniques are needed to confirm or rule out the presence of Cu_2SnS_3 and Cu_3SnS_4. Raman accomplishes this well, although multi-wavelength Raman analysis is required to identify many secondary phases (such as CuS, and $Cu_4Sn_7S_{16}$).

6.10.3. CZTS properties

The CZTS phase in all samples was confirmed to form the kesterite crystal structure by the Cu SSNMR spectra showing the two distinct copper environments corresponding to the 2*a* and 2*c* lattice positions.

While Cu-Zn disorder is likely to be present in the CZTS in all samples, it was found to be drastically so for B25 in particular, as evidenced by the significantly broadened Cu SSNMR and Raman spectra. B25 is identified by being both very Cu-rich and Zn-poor, which makes sense for the CZTS composition featuring the most Cu-Zn disorder.

However, while Raman is effective at qualitatively identifying Cu-Zn disorder, it was not found able to quantify it, as has been done in previous academic literature. Both the peak associated with the disordered kesterite phase and the Q factor (the ratio of intensities of two of the A mode peaks) have previously been found to be linearly related to an order parameter, but here they were found to correlate neither with each other nor even with themselves when found using different excitation wavelengths.

Photoluminescence showed four separate peaks for CZTS, corresponding to three different recombination methods: band-to-impurity recombination (which shows separate peaks for recombination in disordered and ordered CZTS; in reality this emission probably occurs over the range between these two extremes), band-to-tail recombination involving fluctuating-potential tail states on the valence band edge, and band-to-band recombination. The impurity involved in the first of these was found to have a defect level of 180 meV for ordered CZTS and was identified as the Cu_{Zn} antisite. Band-to-tail was found to be the dominant recombination method. The amplitude of the fluctuations in potential was calculated to be 100 meV. If such CZTS is used in solar cells, this is large enough to be responsible for a significant deficit in open-circuit voltage, which is known to severely limit the photovoltaic performance of CZTS.

In summary, while XRD and multi-wavelength Raman spectroscopy were confirmed to be the most useful analysis techniques for the identification of secondary phases, allowing several conclusions to be drawn about the effect of composition on their formation, no standard analysis technique was found able to quantify Cu-Zn disorder, which was confirmed to be a significant issue and thus to require more focused investigation.

Chapter 7:

A neutron diffraction study of CZTS phase transitions

7.1. Introduction

CZTS thin films for photovoltaic devices typically undergo a high-temperature sulphurisation annealing stage after the initial deposition of precursor layers. It is therefore important to understand the impact of the temperature history of CZTS on the properties that in turn have a significant impact on its photovoltaic performance, such as the presence of point defects.

The kesterite order-disorder phase transition at around 550 K in CZTS is known to have a significant effect on the defects remaining once it is cooled to room temperature after fabrication (see Section 3.6). These defects, and the fluctuations in electrostatic potential they lead to (see Section 3.7.7), are a significant source of the deficit in open-circuit voltage commonly observed in CZTS solar cells, which is one of the main problems hindering their best photovoltaic performance. Prior to this work, the half-disordered kesterite model of CZTS was favoured over the fully disordered model (see Section 3.5), and so the order-disorder transition had not been correctly characterised. It was also unknown whether chemical composition affected the transition in any way. The work reported in this chapter therefore aimed to comprehensively investigate the order-disorder transition to inform the growth of better-performing CZTS for photovoltaic devices.

X-ray diffraction is the usual technique for studying crystal structure, but conventional XRD cannot distinguish copper from zinc in CZTS, because their ions are isoelectronic (see Section 5.6). Neutron diffraction, for which this is not a problem, was therefore used in this study, allowing the cation disorder to be studied directly.

Despite not being particularly relevant for photovoltaic application, the high-temperature phase transition around 1150 K was also investigated during this study for completeness.

The work reported in this chapter was primarily published in [2].

7.2. Experimental method

Bulk polycrystalline samples were fabricated by solid-state reaction as described in Section 6.2. Finely ground copper, zinc, and tin powders (Cu 99.9 %, Zn 97.5 %, and Sn 99.85 %) were mixed together and placed in one alumina boat, sulphur powder (99.5 % pure, with a 30 % excess to encourage full sulphurisation) was placed in another, and both boats were sealed together in a quartz ampoule under vacuum. The ampoules were heated with a ramping rate of 5 $K \cdot min^{-1}$ to 1073 K in a small tube furnace, and kept at that temperature for 24 hours before being left to cool naturally back to room temperature in the furnace (over around 24 hours, at a rate of around 0.5 $K \cdot min^{-1}$).

Two samples were produced with different compositions: the same as B21 and B22 from Chapter 6, i.e. Sn-poor, Cu-rich and Sn-poor, Zn-rich respectively. Because neutron diffraction requires relatively large sample volumes of several cm^3 of powder, six batches of each sample (i.e. six ingots of CZTS all having the same composition) were grown. They were ground to a fine powder using an agate mortar, and standard laboratory XRD using Cu-Kα X-rays in a Bruker d7 diffractometer was used to confirm that all six batches of each sample were consistent with each other. They were then mixed together thoroughly to give a large enough volume of sample powder for neutron diffraction with consistent chemical and phase composition.

Inductively coupled plasma mass spectroscopy (ICPMS) was carried out using an Elan 6000 Perkin Elmer Sciex ICPMS to determine the post-fabrication elemental compositions of the samples. As ICPMS cannot accurately detect sulphur, EDX spectroscopy was

carried out on cross-sections of small amounts of the CZTS ingots not ground to a powder, in order to measure the sulphur content. An Hitachi SU-70 FEG SEM with an INCA x-act LN2-free analytical silicon drift detector and INCA software were used for this.

The phase compositions of the samples were identified using EDX, ^{65}Cu and ^{119}Sn SSNMR, and Raman spectroscopy using resonant and non-resonant excitation at 785 nm and 488 nm respectively, as described in Chapter 6.

High-resolution powder neutron diffraction measurements were carried out at the HRPD beamline of the ISIS Pulsed Neutron and Muon Source. The samples were each held in an aluminium slab can in a cryostat and patterns were taken at regular 10 K intervals from 4 to 480 K. The samples were then each sealed in a quartz ampoule under vacuum and held in a vanadium can in a furnace to record patterns at higher temperatures: in 25 K intervals from 300 to 1275 K for sample B21, and in 20 K intervals from 460 to 640 K for B22. Patterns were taken using both setups at several temperatures in the overlapping range to ensure that the data sets were consistent with each other.

Rietveld refinement was carried out using TOPAS v6. An example input file is included in Appendix 1. Batch-processing was used to successively refine the models for the many patterns over the temperature range.

7.3. Composition

The post-fabrication compositions, measured by ICPMS for copper, zinc, and tin, and EDX for sulphur, are given in Table 25 and plotted in Figure 90.

Sample	Composition	Cu	Zn	Sn	S
B21	Sn-poor, Cu-rich	28.7 %	14.4 %	9.3 %	47.6 %
B22	Sn-poor, Zn-rich	25.6 %	16.4 %	10.1 %	47.9 %

Table 25: The post-fabrication compositions of samples B21 and B22, measured by ICPMS (Cu, Zn, & Sn) and EDX (S).

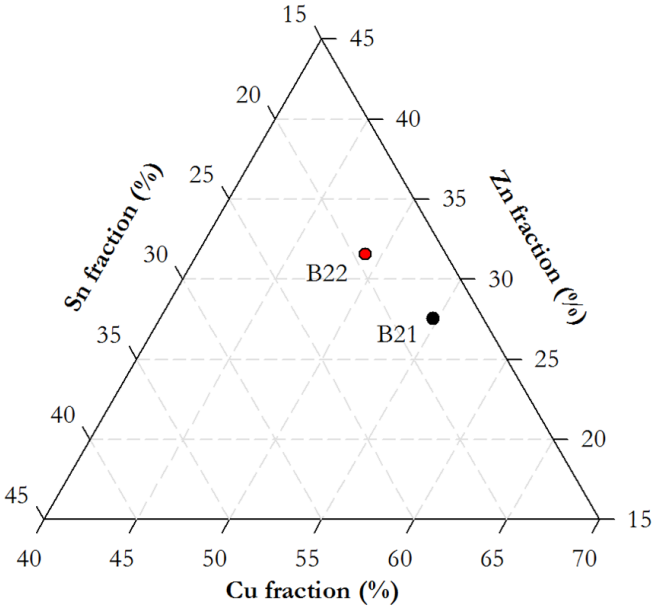

Figure 90: The post-fabrication cation compositions of samples B21 and B22 measured by ICPMS.

The phase characterisation described in Chapter 6 revealed no secondary phases in B21 and only negligible amounts of ZnS and SnS_2 in B22.

7.4. Diffraction results

7.4.1. Crystal structure

Figure 91 depicts a typical neutron diffraction pattern as an example. Rietveld refinement revealed no secondary phases to be present in sufficient quantity to affect the diffraction pattern for either sample.

Rietveld refinement also revealed that both samples are purely kesterite, with no stannite, eskebornite, or PMCA phase presence. Both eskebornite and PMCA give a poor fit to the data and, despite it giving a reasonable fit to the stronger peaks, the weaker peaks rule out stannite because they are much better fit by kesterite.

The best models of the structures of B21 and B22 are described in Table 26 and Table 27 respectively.

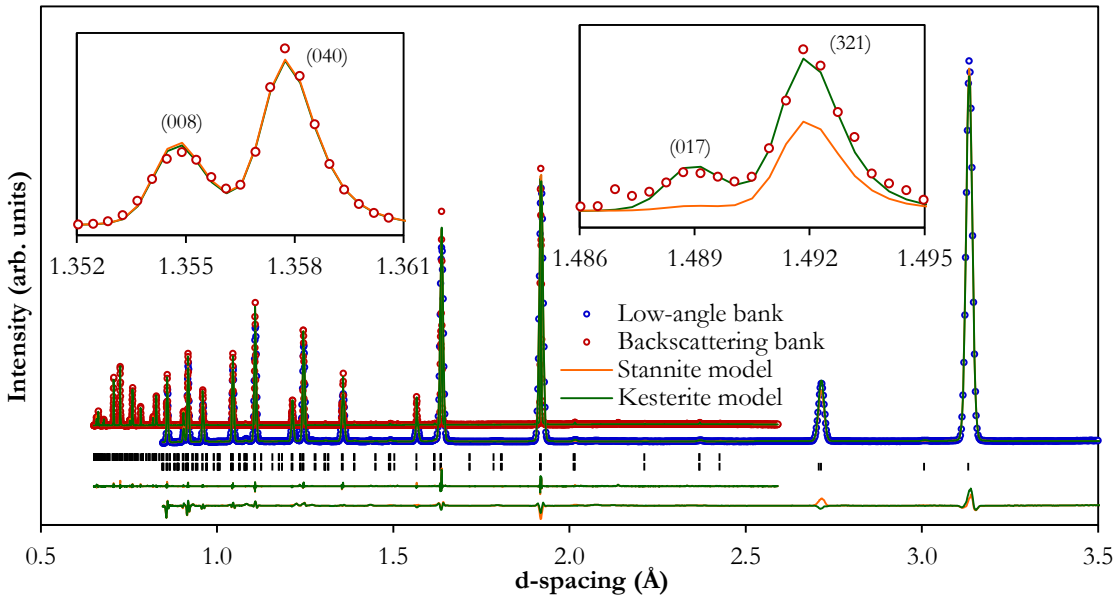

Figure 91: A neutron diffraction pattern for B21 taken at 4 K, showing data from two detector banks at HRPD, with calculated patterns for both kesterite and stannite models plotted over the data, the peak positions marked below the patterns, and the residuals for each model for each bank at the bottom. Inset are sections of the backscattering bank pattern as examples of the tetragonal peak splitting; the (017) and (321) peaks also demonstrate the kesterite model fitting better than stannite.

Temperature	Lattice parameters	Occupancies					Sulphur positions
		2*a* site	2*c* site	2*d* site	2*b* site	8*g* site	
4 K	***a***: 5.42321(3) Å ***c***: 10.82246(1) Å	***Cu***: 0.93(1) ***Zn***: 0.07(1)	***Cu***: 0.93(1) ***Zn***: 0.07(1)	***Cu***: 0.32(7) ***Zn***: 0.68(7)	***Cu***: 0.00(7) ***Zn***: 0.29(7) ***Sn***: 0.71(3)	***S***: 0.91(3) ***V*S**: 0.09(3)	S_x: 0.241(2) S_y: 0.245(4) S_z: 0.128(1)
300 K	***a***: 5.43300(1) Å ***c***: 10.83527(3) Å	***Cu***: 0.96(9) ***Zn***: 0.04(9)	***Cu***: 0.86(8) ***Zn***: 0.14(8)	***Cu***: 0.37(9) ***Zn***: 0.63(9)	***Cu***: 0.00(4) ***Zn***: 0.29(4) ***Sn***: 0.71(3)	***S***: 0.91(3) ***V*S**: 0.09(3)	S_x: 0.241(2) S_y: 0.245(4) S_z: 0.128(1)

Table 26: The best model of B21, the Sn-poor, Cu-rich sample, at 4 K and 300 K. The numbers in brackets are the uncertainties on the last significant figures.

The dominant defect in B21 is Cu_{Zn}, as expected because of its Cu-rich composition, and in B22 Zn_{Cu}, likewise as expected because of its Zn-rich composition. This supports the hypothesis that Cu-poor CZTS gives the best photovoltaic performance because it has a lower concentration of Cu_{Zn} defects. Contrary to expectations, the Cu-rich B21 contains more Zn_{Sn} defects than Cu_{Sn} and the Zn-rich B22 contains more Cu_{Sn} than Zn_{Sn}; both of these defects give deep trap levels and so are detrimental to photovoltaic performance.

Temperature	Lattice parameters	Occupancies					Sulphur positions
		2*a* site	2*c* site	2*d* site	2*b* site	8*g* site	
4 K	***a***: 5.42365(3) Å ***c***: 10.81813(7) Å	***Cu***: 0.74(8) ***Zn***: 0.26(8)	***Cu***: 0.90(7) ***Zn***: 0.10(7)	***Cu***: 0.10(7) ***Zn***: 0.90(7)	***Cu***: 0.22(8) ***Zn***: 0.01(8) ***Sn***: 0.77(1)	***S***: 0.92(1) ***V_S***: 0.08(1)	***S_x***: 0.240(3) ***S_y***: 0.242(5) ***S_z***: 0.123(1)
300 K	***a***: 5.43360(1) Å ***c***: 10.83093(4) Å	***Cu***: 0.67(8) ***Zn***: 0.33(8)	***Cu***: 0.90(5) ***Zn***: 0.10(5)	***Cu***: 0.17(9) ***Zn***: 0.83(9)	***Cu***: 0.23(8) ***Zn***: 0.00(8) ***Sn***: 0.77(1)	***S***: 0.92(1) ***V_S***: 0.08(1)	***S_x***: 0.240(3) ***S_y***: 0.242(5) ***S_z***: 0.123(1)

Table 27: The best model of B22, the Sn-poor, Zn-rich sample, at 4 K and 300 K. The numbers in brakets are the uncertainties on the last significant figures.

7.4.2. Temperature variation

The diffraction patterns are plotted as a function of temperature in Figure 92.

At high temperatures, the samples might be expected to lose sulphur and tin because of the decomposition of CZTS into several secondary phases followed by SnS subliming. However, this was not observed to occur sufficiently to affect the results. The diffraction patterns indicate that purely kesterite CZTS is present up to 1275 K, and neither SnS itself nor the phase(s) composed of the elements it would have left are evident.

The variation of the lattice parameters with temperature is plotted in Figure 93 for both samples. The *a* values are approximately the same for both samples, but $c/2$ is slightly smaller below 500 K for B22, the Sn-poor, Zn-rich sample. Figure 94 shows the ratio $c/2a$ as a function of temperature, which is a useful metric for highlighting the difference between the lattice parameters of the two compositions, and shows minima around the points of the two phase transitions. These can be seen in a previous report, [218] but have not yet been explained.

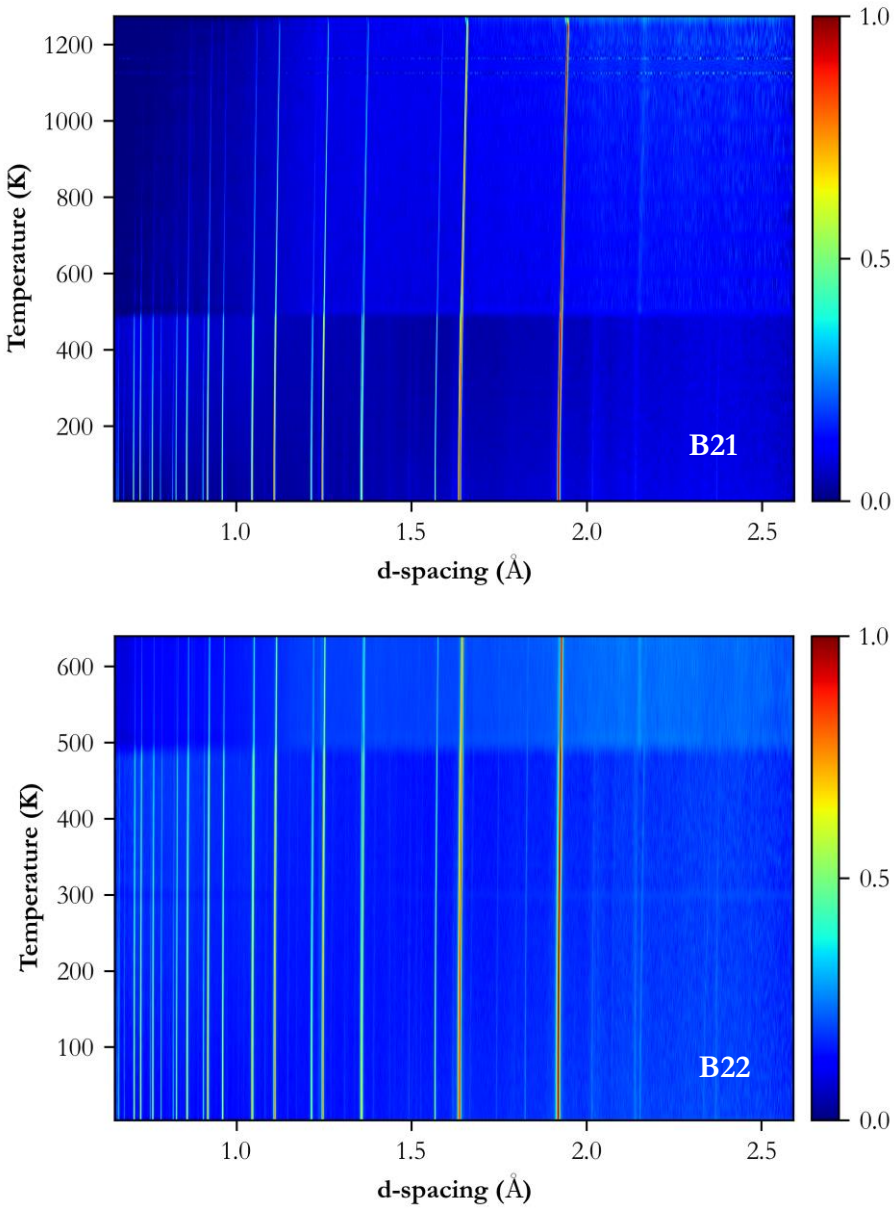

Figure 92: The variation in diffraction pattern with temperature for (top) B21 and (bottom) B22. The data is in logarithmic form to make more peaks visible. The change in background shape at 500 K is due to the change between cryostat and furnace. The order-disorder phase transition cannot be distinguished, but the kesterite-sphalerite transition in B21 can just be seen in the small discontinuity to the highest-temperature pattern. The general thermal expansion is evident in the trend of all peaks to slightly larger d-spacing with increasing temperature.

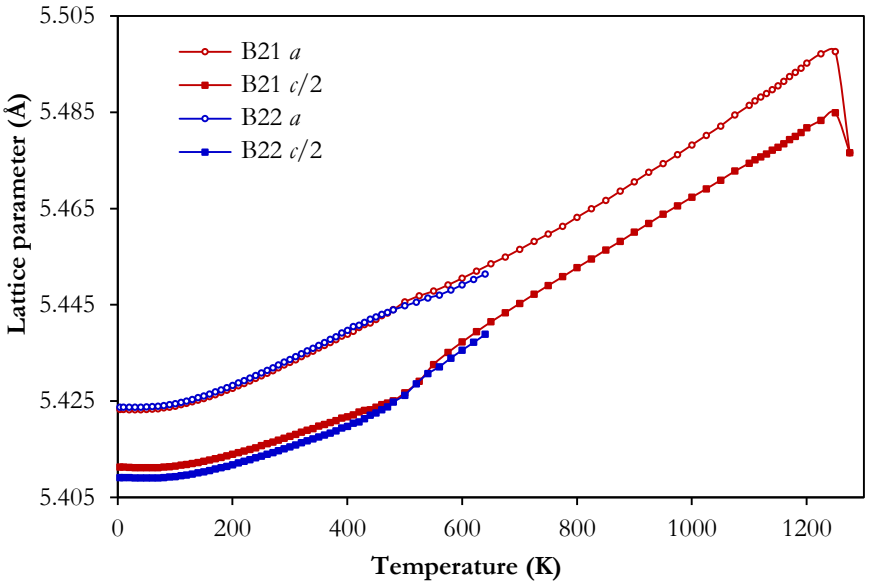

Figure 93: The variation with temperature of the lattice parameters for B21 (red), the Sn-poor, Cu-rich sample, and B22 (blue), the Sn-poor, Zn-rich sample, from 4 to 1275 K.

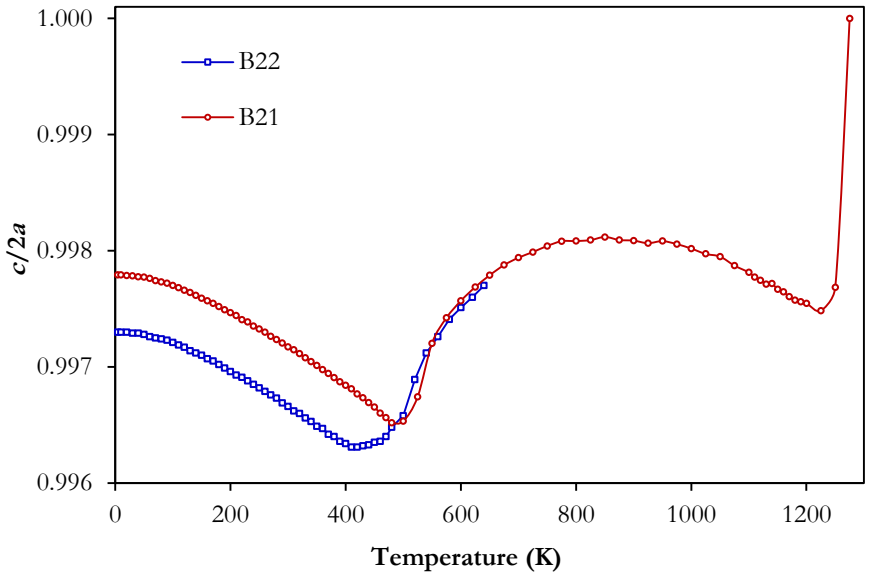

Figure 94: The variation with temperature of the ratio $c/2a$ for samples B21 and B22, showing minima between 400 and 500 K and at 1250 K.

7.4.3. Low-temperature thermal expansion

Neither sample exhibited thermal expansion with increasing temperature below 50 K, and the c lattice parameter of B21 even showed slight negative thermal expansion, as illustrated in Figure 95. Many other adamantine (i.e. tetrahedrally structured) materials also exhibit

negative thermal expansion below 100 K, including several other chalcopyrite materials. [612]

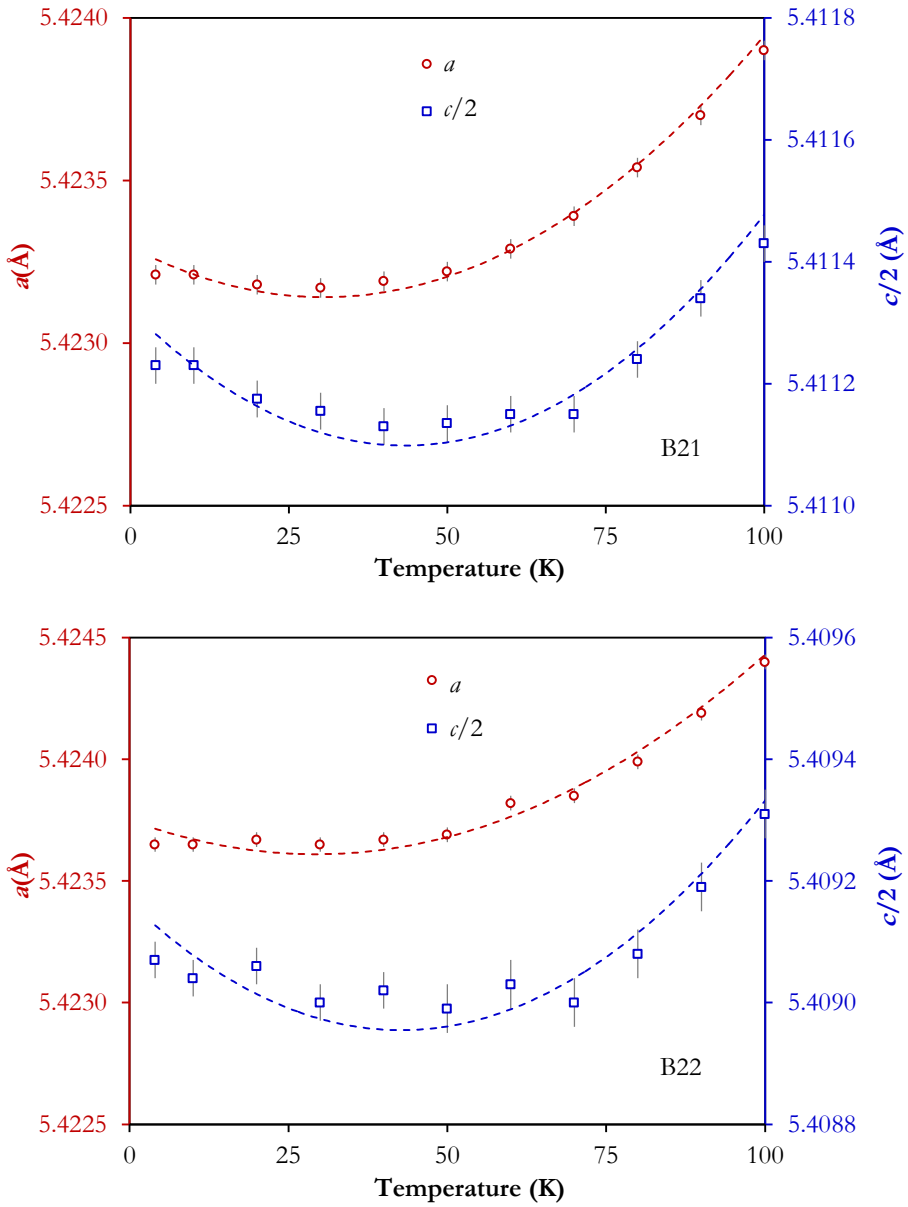

Figure 95: The low-temperature thermal expansion of the lattice parameters of (top) B21 the Sn-poor, Cu-rich sample; and (bottom) B22 the Sn-poor, Zn-rich sample. The dashed lines are second order polynomials.

7.4.4. Order-disorder phase transition

The copper occupancies of the 2*a*, 2*c*, and 2*d* sites are used here as a metric of cation order; their evolution with temperature is depicted for both samples in Figure 96. The order-disorder transition is easily discernible despite the large error bars: the occupancy values are

significantly different below around 500 K and converge to the same value, within experimental uncertainty, above this.

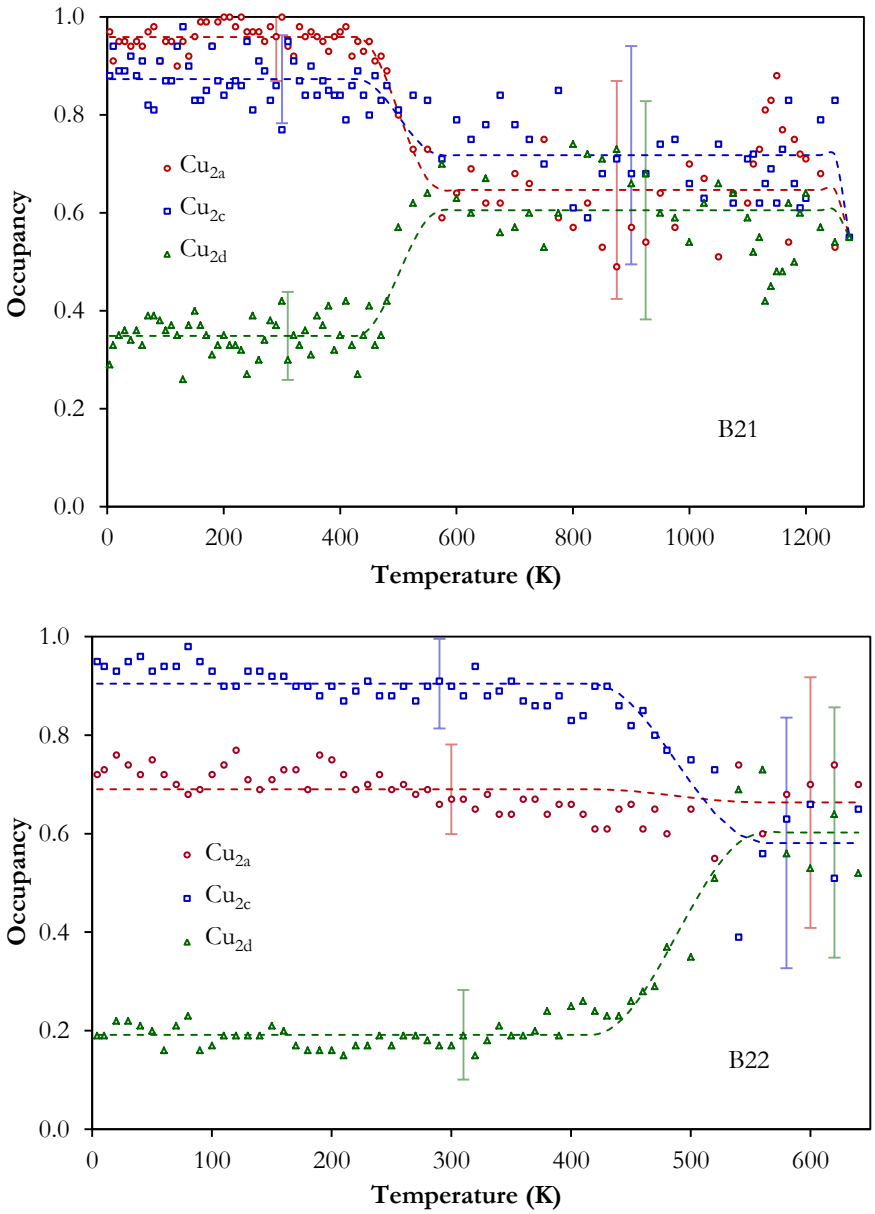

Figure 96: The evolution with temperature of the copper occupancy of the 2*a*, 2*c*, and 2*d* sites for, top, B21 the Sn-poor, Cu-rich sample; and bottom, B22 the Sn-poor, Zn-rich sample. The dashed lines are a simple fit to find the transition temperature and range, and the error bars are representative of the regions of data (≤ 480 K & ≥ 500 K).

A simple fit was used to find the transition temperature, T_C, and a value for the temperature range over which the transition occurs, w. Constant occupancy values below and above the transition were also used as parameters. The fit is described by

$$Cu_X = \begin{cases} Cu_{X,low} & \text{for } T \le \left(T_C - w/2\right) \\ Cu_{X,low} + \left(Cu_{X,high} - Cu_{X,low}\right)\left(\frac{1}{2} + \frac{1}{2}\sin\left(\frac{\pi\left(T - T_C\right)}{w}\right)\right) & \text{for } \left(T_C - w/2\right) < T < \left(T_C + w/2\right) \\ Cu_{X,high} & \text{for } T \ge \left(T_C + w/2\right) \end{cases}, \quad (59)$$

where $Cu_{X,low}$ and $Cu_{X,high}$, (X is replaced by notation of the specific atom site) represent the constant copper occupancies below and above the transition, and the sinusoidal term describes the gradual change in occupancies between these two values. T_C = 501 K and w = 148 K for B21 and, T_C = 489 K and w = 146 K for B22. The transition temperature is 12 K lower for the Sn-poor, Zn-rich composition of B22 than for the Sn-poor, Cu-rich composition of B21. The temperature range over which the transition takes place is approximately the same for both samples, and is quite large. This might be due to the time spent at each temperature (15 minutes equilibration and 90 minutes measurement in the region of the transition) being insufficient for the samples to fully equilibrate, which would artificially extend the transition to higher temperatures. It should additionally be noted that the values are full-widths rather than half-widths of the transition.

A minimum in $c/2a$ occurs at around the transition temperature for both samples, as shown in Figure 94, which suggests that $c/2a$ is a useful parameter to indicate the transition. The minima are at or just below the beginning of the occupancy value transition, which suggests that the change in lattice parameters causes the increase in disorder, rather than disorder causing the change in lattice parameters. It may be that the additional strain energy associated with unequal thermal expansion of the two lattice parameters becomes larger than the defect formation energies at the transition point and so the lattice parameters begin to return to their preferred ratio by accommodating disorder in the crystal lattice.

It is still unclear why the a lattice parameter increases at a greater rate than c below the transition to create this extra strain. Cation disorder is clearly involved in this somehow, but the details remain to be explained.

7.4.5. Kesterite-sphalerite phase transition

The peaks that were split to slightly different d-spacings by the tetragonal rather than cubic nature of the kesterite structure converge between the 1250 and 1275 K patterns, as

depicted in Figure 97. This indicates the cubic sphalerite structure being adopted from the tetragonal kesterite.

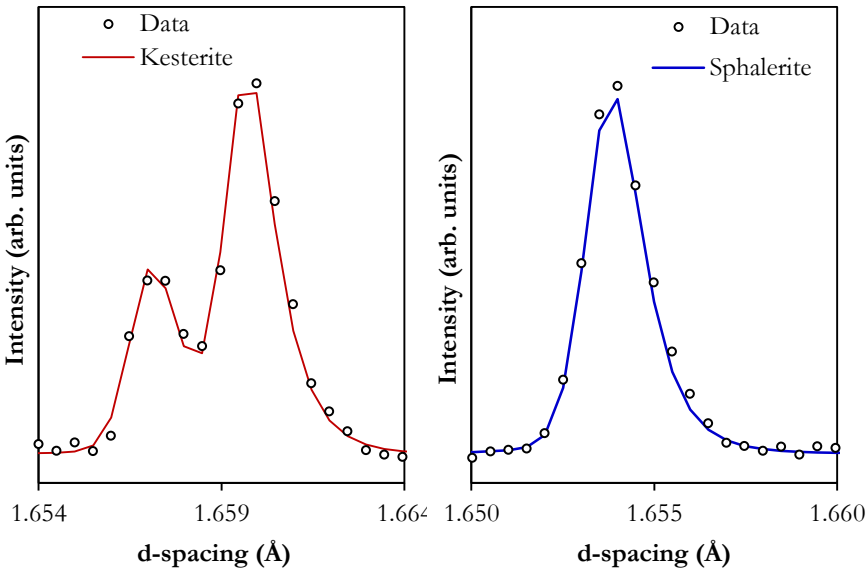

Figure 97: The (116) and (132)/(312) peaks for B21 at 1250 K (left), demonstrating tetragonal splitting, and at 1275 K (right), demonstrating only a single peak position, suggesting the formation of a cubic structure.

Figure 94 shows the disappearance of the tetragonal distortion directly in $c/2a$ going steeply to 1 for the 1275 K pattern. Another local minimum in $c/2a$ occurs just before this at 1225 K. When forming the cubic structure, the lattice parameters not only converge, but also decrease, as depicted in the plot of the lattice parameters themselves, Figure 93.

In addition to the lack of tetragonal distortion, the sphalerite structure also differs from the disordered kesterite in the complete mixing of all cations, including tin, equally on every cation site. This was found in the 1275 K pattern, which was indeed more accurately fitted by a sphalerite structure than by simply the disordered kesterite structure with $c/2a = 1$.

The temperature found here for the transition, between 1250 and 1275 K, is significantly higher than the previously reported value of between 1139 and 1156 K, [218] which suggests that the temperature and mechanism of this transition are also very sensitive to elemental composition.

7.5. Conclusions

Samples of CZTS with two compositions, Sn-poor, Cu-rich (B21) and Sn-poor, Zn-rich (B22), were fabricated by solid-state reaction and their cation compositions were measured using inductively coupled plasma mass spectrometry.

The crystal structures of the samples were investigated using high-resolution neutron diffraction. The kesterite crystal structure was found to be adopted by both, with significant cation disorder. Contrary to almost all previous literature reports, which described complete order on the 2*a* site, these results demonstrate Zn_{Cu} occupancy of the 2*a* site equal to the 2*c* site for a Sn-poor, Cu-rich composition, and higher than the 2*c* site for a Sn-poor, Zn-rich composition. The high resolution of this data means the *a* and *c* lattice parameters can to be reported to 6 and 7 significant figures respectively, which makes them the highest-resolution values reported for CZTS.

The dominant defect in B21 is Cu_{Zn}, as expected because of its Cu-rich composition, and in B22 it is Zn_{Cu}, likewise as expected because of its Zn-rich composition. This supports the hypothesis that Cu-poor CZTS gives the best photovoltaic performance because it has a lower concentration of Cu_{Zn} defects. Contrary to expectations, the Cu-rich B21 contains more Zn_{Sn} defects than Cu_{Sn} and the Zn-rich B22 contains more Cu_{Sn} than Zn_{Sn}; both of these defects give trap levels deep in the band gap and so are detrimental to photovoltaic device performance.

Neither sample exhibits thermal expansion with increasing temperature below 50 K, and the *c* lattice parameter of B21 even shows slight negative thermal expansion

An order-disorder phase transition took place in B21 at 501 K and in B22 at 489 K, which are both lower than the previously reported temperatures. The transition occurred in both samples over a range of approximately 150 K. This is quite a large range, but could be artificially so because of insufficient equilibration time during the experiments. The transition occurred at a different temperature in each sample, which suggests that the transition mechanism is affected by elemental composition. This is important for the procedure of CZTS production for photovoltaic cells.

Another phase transition, from the tetragonal kesterite to the cubic sphalerite structure, was measured between 1250 and 1275 K in B21. This transition temperature is significantly higher than the value previously reported, which suggests that this transition is also affected by elemental composition.

The work presented here will aid the development of fabrication approaches for CZTS devices to achieve higher photovoltaic efficiency by encouraging cation disorder to be investigated correctly, including all cation lattice sites, rather than just the 2*c* and 2*d* sites, and by revealing that composition affects the order-disorder transition.

Chapter 8:

An anomalous XRD study of off-stoichiometric CZTS types

8.1. Introduction

Point defects, and the fluctuations in electrostatic potential they lead to (see Section 3.7.3 and Section 3.7.7), are a significant source of the deficit in open-circuit voltage commonly observed in CZTS solar cells, which is one of the main problems hindering their best photovoltaic performance. These defects preferentially form charge-neutral defect complexes, which have a lower formation energy than the individual point defects (see Section 3.7.4). These complexes have been observed to congregate to produce long-range order to the extent of individual grains within a sample having different compositions due to the prevalence of different defect complexes.

Clearly the existence of these distinct types of CZTS will have a significant effect on photovoltaic performance, but prior to this work the formation mechanisms behind them were unknown. The order-disorder phase transition at around 550 K is likely to be responsible, as it has a significant effect on the defects remaining in CZTS once cooled to room temperature after fabrication (see Section 3.6), but how this is affected by elemental composition had not been investigated thoroughly either. The work presented in this chapter therefore aimed to investigate the formation of the various composition types of CZTS by fully characterising the atomic disorder within the CZTS crystal structures of

samples over a range of compositions, both above and below the order-disorder transition, in order to inform the growth of better-performing CZTS for photovoltaic devices.

X-ray diffraction is the usual technique for studying crystal structures, but conventional XRD cannot distinguish copper from zinc in CZTS, because their ions are isoelectronic. Anomalous diffraction using synchrotron radiation was therefore used in this study, allowing the cation disorder present to be investigated directly, with a sufficiently high resolution to distinguish the different composition types within the same sample (see Section 5.6).

The work reported in this chapter was primarily published in [4].

8.2. Experimental method

Bulk polycrystalline samples were fabricated by solid-state reaction as described in Section 6.2. Finely ground copper, zinc, and tin powders (Cu 99.9 %, Zn 97.5 %, and Sn 99.85 %) were mixed together and placed in one alumina boat, sulphur powder (99.5 % pure, with a 30 % excess to encourage full sulphurisation) was placed in another, and both boats were sealed together in a quartz ampoule under vacuum. The ampoules were heated with a ramping rate of 5 $K \cdot min^{-1}$ to 1073 K in a small tube furnace, and kept at that temperature for 24 hours before being left to cool naturally back to room temperature in the furnace (over around 24 hours, at a rate of around 0.5 $K \cdot min^{-1}$).

Samples with five different compositions were produced: the same as B21, B22, B25, B26, and B27 from Chapter 6. These were ground to a fine powder using an agate mortar.

Inductively coupled plasma mass spectroscopy (ICPMS) was carried out using an Elan 6000 Perkin Elmer Sciex ICPMS to determine the post-fabrication elemental compositions of the samples. As ICPMS cannot accurately detect sulphur, EDX spectroscopy was carried out on cross-sections of small amounts of the CZTS ingots not ground to a powder, in order to measure the sulphur content. An Hitachi SU-70 FEG SEM with an INCA x-act LN2-free analytical silicon drift detector and INCA software were used for this.

The phase compositions of the samples were identified using EDX, ^{65}Cu and ^{119}Sn SSNMR, and Raman spectroscopy using resonant and non-resonant excitation at 785 nm and 488 nm respectively, as described in Chapter 6.

High-resolution anomalous X-ray powder diffraction experiments were carried out at the Diamond Light Source. The I11 beamline was used for the Cu and Zn K absorption edges at 8.98 and 9.66 keV respectively, and the I15 beamline for the Sn K absorption edge at 29.2 keV (samples B21 and B22 only). For the Sn edge measurements, patterns were taken using X-ray energies precisely at the absorption edge (resonant) and at 2 keV below it (non-resonant). For the Cu and Zn edges, patterns were taken both at 300 K and 600 K using X-ray energies at 10 eV below each edge (resonant) and at 15 keV (non-resonant). The fluorescence signals of the samples were used to calibrate the Cu and Zn absorption edges by scanning the monochromator.

Rietveld refinement was carried out using TOPAS v6. Patterns for resonant and non-resonant X-ray energies were fitted simultaneously using the measured sample elemental composition, and refining multiple phases, the elemental composition of CZTS phases, disorder on all CZTS cation sites, and vacancies on all CZTS cation and anion sites in addition to the standard Rietveld parameters. An example input file is given in Appendix 1.

8.3. Composition

The post-fabrication compositions, measured by ICPMS for copper, zinc, and tin, and EDX for sulphur, are given in Table 28 and plotted in Figure 98 relative to the defect-complex-defined off-stoichiometric type compositions.

Sample	Composition	Cu	Zn	Sn	S
B21	Sn-poor, Cu-rich	28.7 %	14.4 %	9.3 %	47.6 %
B22	Sn-poor, Zn-rich	25.6 %	16.4 %	10.1 %	47.9 %
B25	Sn-poor, Cu-rich	31.3 %	11.1 %	10.0 %	47.6 %
B26	Zn-poor, Cu-rich	28.4 %	11.0 %	12.8 %	47.8 %
B27	Cu-poor, Zn-rich	25.0 %	14.0 %	13.5 %	47.5 %

Table 28: The post-fabrication measured compositions of samples B21, B22, and B25-27.

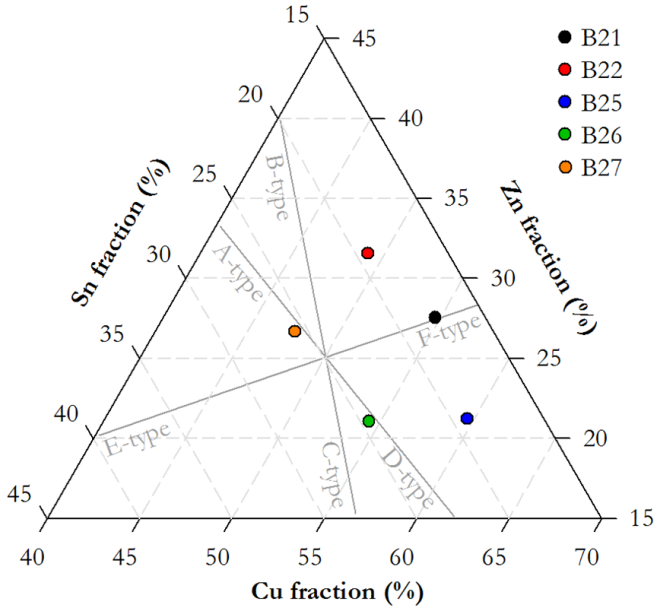

Figure 98: The cation compositions of samples B21, B22, and B25-27 measured by ICPMS, shown with the compositions of the defect-complex-defined off-stoichiometric CZTS types.

The secondary phases concluded to be present in each sample from the phase characterisation presented in Chapter 6 are given in Table 29. It is well established that CZTS has a very small region of stability around the stoichiometric composition, so the presence of secondary phases in most samples is unsurprising.

Sample	Secondary phases
B21	(negligible Cu_3SnS_4)
B22	(negligible ZnS and SnS_2)
B25	(None)
B26	Cu_3SnS_4, $Cu_4Sn_7S_{16}$
B27	$Cu_4Sn_7S_{16}$

Table 29: The secondary phases identified in samples B21, B22, and B25-27 in addition to CZTS using EDX, NMR, and Raman spectroscopy. Additionally, B25 contains very high Cu-Zn disorder in the CZTS.

8.4. Diffraction Results

Figure 99 and Figure 100 show typical non-resonant X-ray diffraction patterns from I15 and I11 respectively as examples.

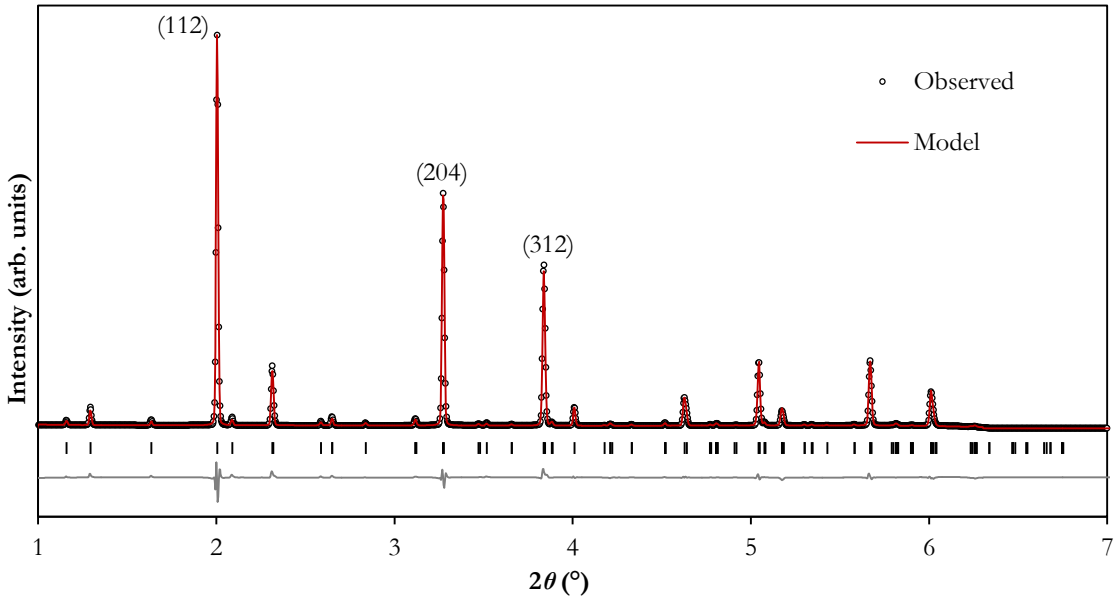

Figure 99: X-ray diffraction pattern for sample B21 taken at room temperature using 27.2 keV X-rays at the I15 beamline of the Diamond Light Source, showing the calculated pattern for a kesterite best-fit model, the peak positions marked below the pattern, and the residual at the bottom.

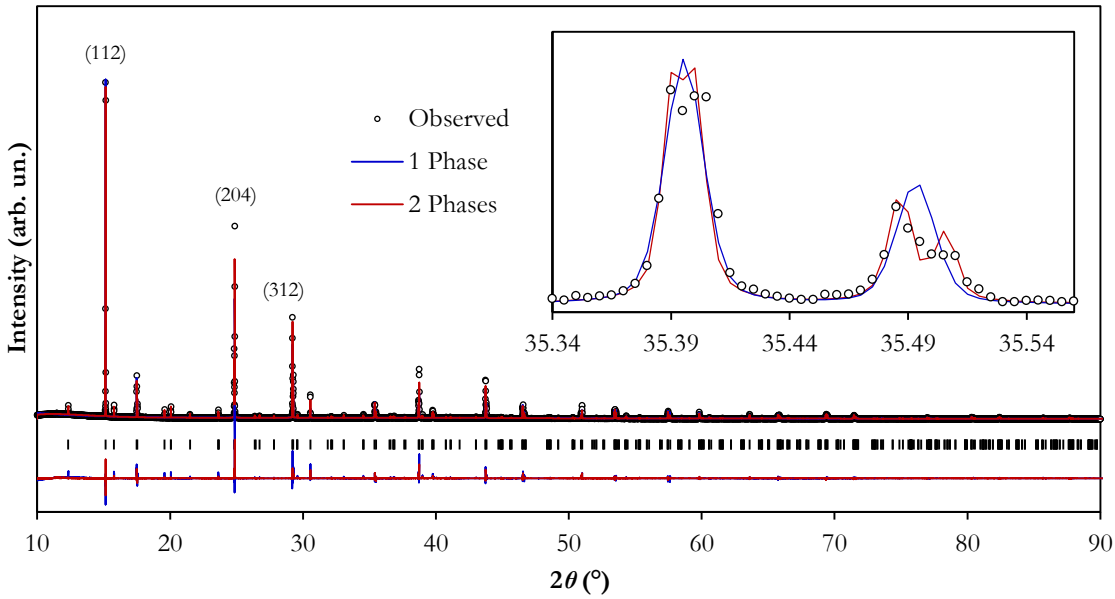

Figure 100: X-ray diffraction pattern for sample B21 taken at room temperature using 15 keV X-rays at the I11 beamline of the Diamond Light Source, showing calculated patterns for models with a single kesterite phase and with two kesterite phases plotted over the data, the peak positions marked below the patterns, and the residuals for each model at the bottom. The (400) and (008) peaks are shown in the inset, demonstrating peak splitting by ~0.1 ° because the tetragonal ratio $a/2c$ is slightly less than one; each individual peak demonstrates further small splitting of ~0.02 ° due to the presence of two almost identical tetragonal phases.

The crystal structures of the samples have been determined here with the highest accuracy and precision of any CZTS to date, which was possible because of the high resolution of the I11 beamline of the Diamond Light Source.

The Sn-edge X-ray data for B21 and B22 revealed complete order of the tin atoms, as expected: they are all present on the 2*b* site within experimental uncertainty. It is more difficult to interpret the Cu and Zn edge patterns, however.

8.4.1. Phases present at 300 K

It was not straightforward to identify the phases to include in refinements for the I11 patterns. Slight splitting ($\Delta 2\theta \sim 0.02$ °) of some peaks of the CZTS pattern was observed in the 300 K patterns for B21, B25, B26, & B27, which is illustrated in the inset of Figure 100 and in Figure 101. This is the first time this miniscule splitting has been observed because this is the first report of sufficiently high-resolution diffraction on CZTS.

These phases were all identified as tetragonal by Pawley refinements, which eliminated the cubic ZnS secondary phase as a candidate. The remaining potential explanations for the multiple structures are therefore: a secondary phase with a similar tetragonal structure (Cu_2SnS_3 or Cu_3SnS_4; N.B. not Cu_4SnS_4 because it has a very different structure and so diffraction pattern), or two structures of CZTS with small differences in their lattice parameters, which could be both kesterite, both stannite, or one of each.

A model of two stannite phases and one of a kesterite phase and a stannite phase are both eliminated as possibilities for all samples because they fit the measured patterns less well than the other options. The stannite structure does not contribute any intensity in calculated patterns to several small peaks of the measured patterns, such as (123) and (231).

For B21, Cu_2SnS_3 and Cu_3SnS_4 are ruled out because they do not fit the data well, the low-intensity peaks in particular, and because the phase characterisation presented in Chapter 6 did not show any significant evidence of these materials. The best model is therefore a mixture of two phases of kesterite CZTS.

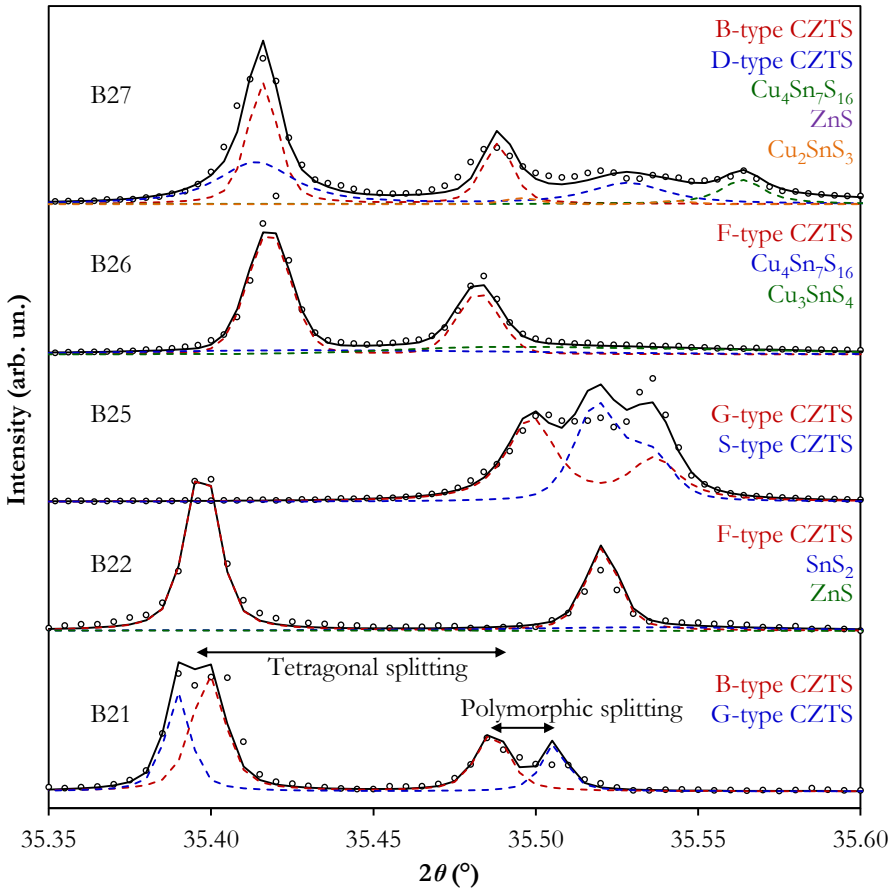

Figure 101: Peak splitting due to multiple phases in the 15 keV patterns at 300 K for samples B21, B22, and B25-27. The circles show the experimental data, the solid black line the total model intensity, and the dashed lines the contribution of each individual phase to the model.

For B22, the splitting is not exhibited by the CZTS peaks. Distinct peaks from ZnS and SnS_2 are evident, which is consistent with the identification of these phases by EDX (see Section 6.5).

For B25, the tetragonal splitting is much smaller than for the other samples, which could be because of the high level of disorder identified by NMR and Raman (see Sections 6.7 and 6.8). Cu_3SnS_4 is discounted as the second tetragonal phase because Raman spectroscopy does not show it to be present, but Cu_2SnS_3 remains a possibility. However, a model featuring two phases of kesterite CZTS with different lattice parameters fits the measured pattern slightly better, so this is taken to be the true explanation.

For B26, Cu_3SnS_4 is shown to make up a significant proportion of the sample by Raman spectroscopy (see Section 6.8), and so this rather than a second CZTS phase or Cu_2SnS_3 is

taken to be the second tetragonal structure identified by the diffraction patterns for B26. $Cu_4Sn_7S_{16}$ is also clearly identified by the diffraction patterns, as well as by EDX and NMR (see Sections 6.5 and 6.7).

For B27, the collection of peaks its diffraction patterns contain is the most complicated of all the samples. ZnS and Cu_2SnS_3 were identified in small amounts as well as the $Cu_4Sn_7S_{16}$ that EDX and NMR found (see Sections 6.5 and 6.7). The quantities of these phases present are sufficiently small for them to have been missed by the other techniques. This sample also exhibits a second CZTS phase in its diffraction pattern. Cu_3SnS_4 is discounted because Raman analysis did not identify it as present (see Section 6.8).

The assignation of phases from the diffraction patterns is subjective to some degree, particularly for B27, regardless of the high resolution of the data, because many of the peaks still overlap and several secondary phases are present. The phase structure models given here are consistent with all results, but for some samples they might not be the only possibilities. However, that anomalous XRD can successfully distinguish copper and zinc gives confidence that the differences in refinements using CZTS, Cu_2SnS_3, and Cu_3SnS_4 are accurate, which means these phases can be identified with a high level of confidence.

Table 30 gives the best-fit model of the phase composition of each sample. Significant mixing of copper and zinc on the cation sites was found in all the CZTS phases. This is discussed below.

Sample	CZTS Phases		Secondary Phases		
B21	B-type 56 %	G-type 44 %			
B22	F-type 84 %		SnS_2 9 %	ZnS 7 %	
B25	G-type 53 %	S-type 47 %			
B26	F-type 71 %		$Cu_4Sn_7S_{16}$ 17 %	Cu_3SnS_4 12 %	
B27	B-type 38 %	D-type 35 %	$Cu_4Sn_7S_{16}$ 17 %	ZnS 9 %	Cu_2SnS_3 2 %

Table 30. The phase compositions of samples B21, B22, and B25-27 at 300 K determined by Rietveld refinement of I11 data.

The two samples that contain $Cu_4Sn_7S_{16}$ (B26 and B27) are the richest in tin, both with approximately stoichiometric tin content; this is consistent with the high tin content of $Cu_4Sn_7S_{16}$ itself. Only two of the three Zn-rich samples (B22 and B27) contained any ZnS, and even those contained very little; it is unclear why B21 does not contain any. Only one

sample (B27) contained Cu_2SnS_3, and only in a very small amount, despite it being considered one of the main CZTS secondary phases. The presence of a significant amount of Cu_3SnS_4 in B26 is explained by the Cu-rich, Zn-poor composition of that sample. It appears that the formation of ternary secondary phases is prevented by a Sn-poor or significantly Zn-rich composition.

8.4.2. CZTS types at 300 K

During refinement, the elemental composition of each CZTS phase was allowed to vary, subject to the constraint that the weighted-average composition of all phases present in the sample be equal to the overall sample composition as determined using ICPMS and EDX. Figure 102 depicts the best-fit cation compositions of each phase of CZTS.

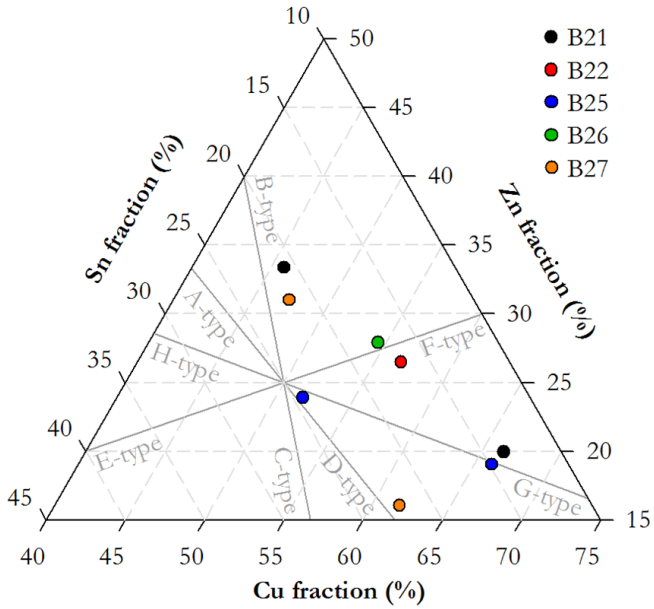

Figure 102. The cation compositions of each CZTS phase in samples B21, B22, and B25-27 at 300 K, with the defect-complex-defined off-stoichiometric type compositions, including two new types proposed here: G and H.

All the phase compositions, except one of the B21 phases and one of the B25 phases, approximately match an established defect-complex-defined CZTS type. Both of the exceptions have approximately the same composition, and so two new composition types, labelled G and H, are proposed here for this composition and its opposite through the stoichiometric point. These are given in Table 31.

CZTS type	Defects	Stoichiometry
G-type	$[2Cu_{Sn}^{3-} + Cu_{Zn}^{-} + Cu_{i}^{+} + 3V_{S}^{2+}]$	Sn-poor, Cu-rich
H-type	$[3S_{i}^{2-} + V_{Cu}^{-} + Zn_{Cu}^{+} + 2Sn_{Cu}^{3+}]$	Cu-poor, Sn-rich

Table 31. Two proposed new types of CZTS, with the prevalence of the respective defects defining the compositions.

The compositions of the two new types require a larger number of defects than those previously established. It is therefore possible that they do not exist as single defect clusters, but could instead occur as smaller clusters together in the same grains; for example the defects of the G-type composition could be grouped as $[Cu_{Sn}^{3-} + Cu_{i}^{+} + V_{S}^{2+}]$ and $[Cu_{Sn}^{3-} + Cu_{Zn}^{-} + 2V_{S}^{2+}]$ charge-neutral complexes. The larger number of point defects needed to explain the compositions of the new types might be the reason they have not previously been reported.

It is significant that sulphur-related defects are important in the new types. Incomplete sulphurisation during the production of CZTS has long been established as an issue, but this is rarely considered when explaining or predicting the presence of secondary phases in CZTS, despite the significant impact it obviously has.

These results may begin to illuminate the complex mechanism of CZTS secondary phase formation, which has seemed inexplicable for so long because the secondary phases found in experimental samples did not match those predicted by calculations. What matters is not simply which secondary phases are stable for a particular composition, but which combination of type(s) of CZTS and secondary phases is the most energetically favourable.

Even if the overall elemental composition of a sample is equal to that of a CZTS type, the most stable phase composition is not necessarily a phase-pure sample of that type. Despite the elemental composition of B21 being almost exactly that of F-type CZTS, B21 is actually a mixture of B-type and G-type. That of B25 matches G-type CZTS, but B25 split into a mixture of S-type and G-type with a greater density of defects. The elemental composition of B27 corresponds to A-type (or possibly S-type) CZTS, but the sample split into B-type and D-type. Figure 103 depicts this contrast between the elemental compositions of the samples on average and those of their various CZTS phases.

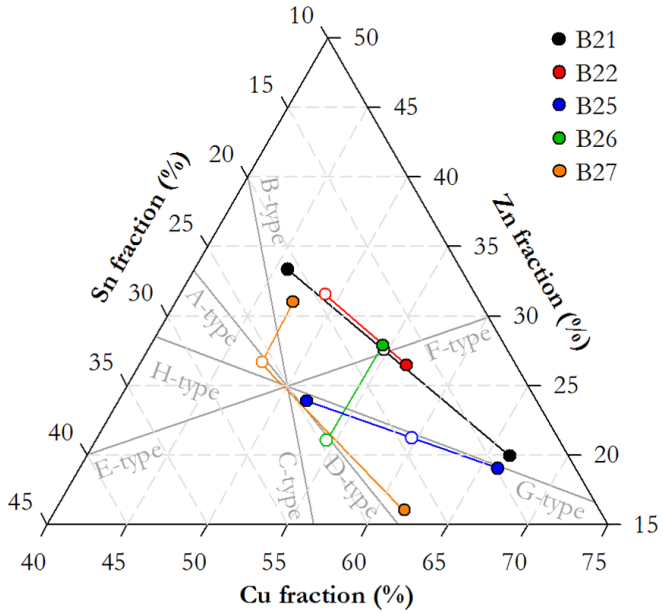

Figure 103: The cation compositions of each CZTS phase in samples B21, B22, and B25-27 at 300 K (filled circles) relative to the overall sample compositions measured by ICPMS (hollow circles).

A theoretical study not just of the formation energies of individual defect complexes, but of the formation energy of a multi-phase sample as a function of the phases present, their phase fractions, and the concentration of defects and defect complexes within the CZTS phase(s) would be illuminating, but would perhaps be prohibited by the computational demands this would entail.

Table 32 depicts the occupancies of each lattice site of each CZTS phase in the best models of each sample from simultaneous Rietveld refinement of resonant and non-resonant diffraction patterns. These can be used to confirm whether the defect complexes that define the CZTS types are in fact responsible for the phase compositions.

These results essentially match the defects of the respective CZTS type-defining complexes, where it is possible for them to do so. In most cases some other defects are additionally present in small amounts, as will always be the case in real samples rather than ideal ones; for example Cu_{Sn} and Zn_{Sn} are found in all samples to some extent.

However, because technical limitations meant that interstitials were not modelled during this work, the site occupancies given in Table 32 cannot accurately represent the types that do include interstitial defects by definition (D-type, F-type, and G-type). Because of this,

CZTS type	Sample	2*a*	2*c*	2*d*	2*b*	8*g*	Lattice parameters (Å)
S-type	B25	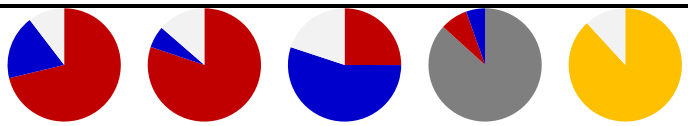					*a* = 5.417766(9) *c* = 10.83068(3)
B-type	B21	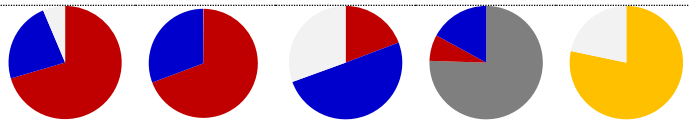					*a* = 5.433014(6) *c* = 10.84009(1)
	B27						*a* = 5.433021(7) *c* = 10.84460(2)
D-type	B27	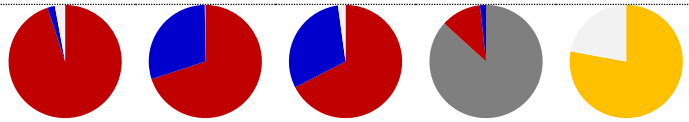					*a* = 5.433374(9) *c* = 10.83298(4)
F-type	B22	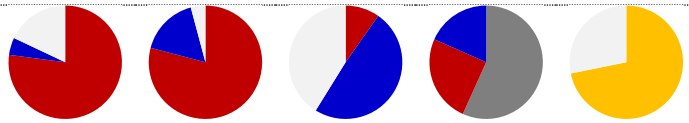					*a* = 5.433263(4) *c* = 10.83005(1)
	B26						*a* = 5.432676(3) *c* = 10.84625(8)
G-type	B21	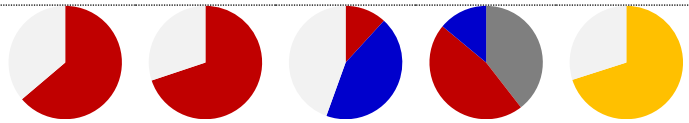					*a* = 5.434419(5) *c* = 10.83451(1)
	B25						*a* = 5.420721(9) *c* = 10.83023(6)

Table 32. The lattice site occupancies (red represents copper, blue zinc, dark grey tin, yellow sulphur, and light grey vacancies) and lattice parameters of the modelled CZTS phases in samples B21, B22, and B25-27 at 300 K, grouped by type. The numbers in brackets are the uncertainties on the last significant figures.

Zn_{Cu} and Cu_{Sn} are overrepresented in the D-type phase of B27; vacancies are overrepresented in the 'F-type' phases of B22 and B26; V_{Cu} and V_{Zn} are overrepresented in the 'G-type' phase of B21; and Zn_{Cu} and Zn_{Sn} are overrepresented and Cu_{Sn} underrepresented in the 'G-type' phase of B25. Each of these is due to the inability to model interstitials, meaning the refinement returns other results with the same elemental composition.

The mixing of copper and zinc, which does not affect elemental composition, was found in most CZTS phases to some extent in addition to the disorder due to defect complexes. The finding of Chapter 7 is confirmed, that Zn_{Cu} occupancy is present on the 2*a* site as much as the 2*c* site. The ordering process is evidently more complicated than simply a function of temperature and annealing time covered by a single order parameter for the mixing of two elements on two lattice sites, which has been used previously. The disorder of copper and zinc is found on all four cation sites. Understanding the complexities of this disorder will evidently require more investigation, but will lead to identifying the fabrication procedure necessary to promote optimum cation ordering.

It is also notable that despite sulphur vacancies rarely having been considered in previous CZTS disorder studies, they were found in all phases of CZTS in significant quantity here.

8.4.3. Phases present at 600 K

The same secondary phases were found in each sample at almost the same phase fractions for the 600 K patterns as for the 300 K ones. However, as Figure 104 shows, the peak splitting due to the presence of two phases of CZTS at 300 K is no longer present at 600 K for samples B21 and B25, but it remains for B27. B26 shows a larger peak splitting at 600 K, which is consistent with the second peaks being due to Cu_3SnS_4 rather than a second phase of CZTS for this sample, because CZTS and Cu_3SnS_4 will naturally have slightly different thermal expansion behaviour. The phase compositions of each sample at 600 K are given in Table 33.

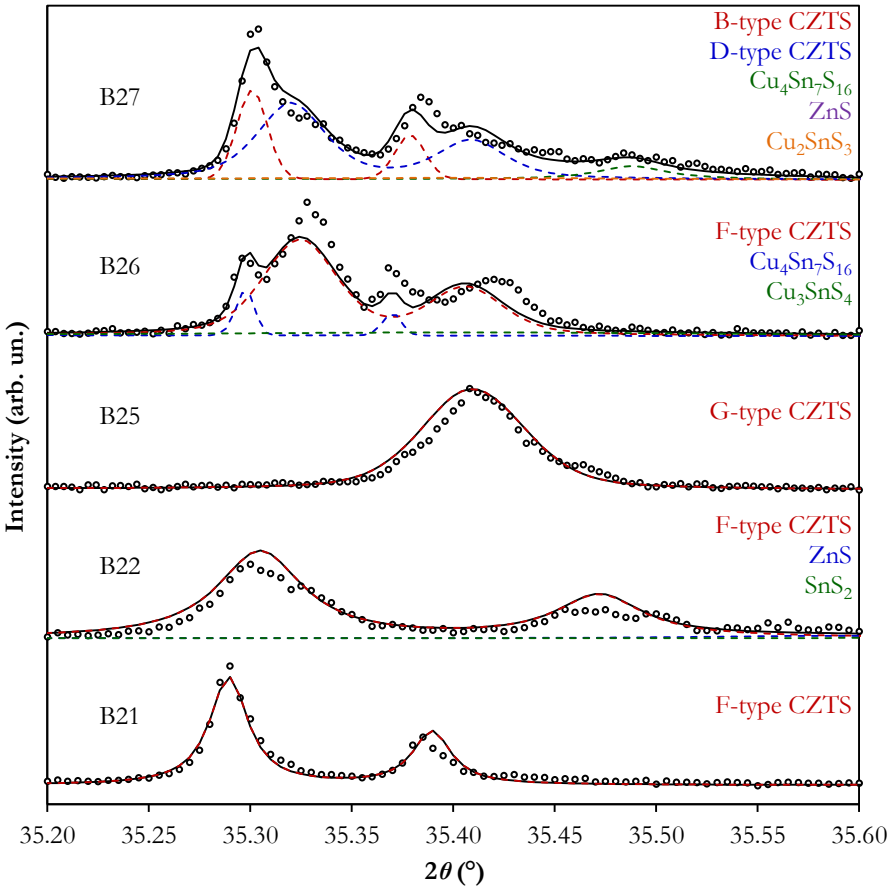

Figure 104: Peak splitting due to multiple phases in the 15 keV patterns at 600 K of samples B21, B22, and B25-27. The circles show the experimental data, the solid black line the total model intensity, and the dashed lines the contribution of each individual phase to the model.

Sample	CZTS Phases		Secondary Phases		
B21	F-type 100 %				
B22	F-type 93 %		ZnS 6 %	SnS_2 1 %	
B25	G-type 100 %				
B26	F-type 78 %		$Cu_4Sn_7S_{16}$ 13 %	Cu_3SnS_4 9 %	
B27	B-type 49 %	D-type 26 %	$Cu_4Sn_7S_{16}$ 15 %	ZnS 7 %	Cu_2SnS_3 3 %

Table 33. The phase compositions of samples B21, B22, and B25-27 at 600 K determined by Rietveld refinement of I11 data.

8.4.4. CZTS types at 600 K

Figure 105 depicts the cation compositions of the remaining CZTS phases at 600 K. Above the order-disorder phase transition, every phase of CZTS is still of a distinct type.

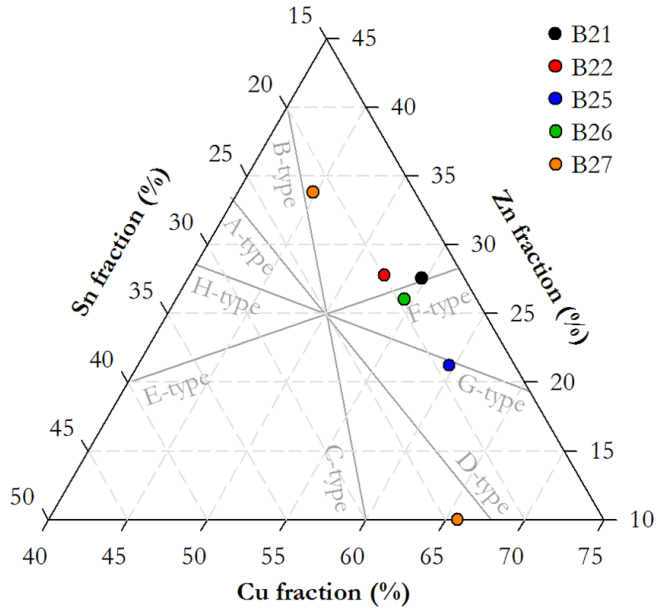

Figure 105. The cation compositions of each CZTS phase in samples B21, B22, and B25-27 at 600 K.

This convergence of two CZTS type phases below the transition to one above it, depicted in Figure 106, suggests that a single phase of CZTS is in general energetically favourable to two separate phases for temperatures higher than the order-disorder phase transition. The existence of the two CZTS phases in B27 above the transition could imply that the transition temperature is higher than 600 K for the composition of B27 or for one of the types of CZTS it contains. However, the occupancy values of the lattice sites, given in Table 34, demonstrate that the phases of CZTS are also more disordered at 600 K than at 300 K in B27, confirming that at 600 K the sample has in fact passed through the transition. It is simply the case that for the specific composition of B27 two phases of CZTS remain energetically favourable above the transition.

In the samples containing just a single CZTS phase both above and below the transition temperature (B22 and B26) the CZTS phase remains the same type on both sides of the transition. A higher temperature would be required to change the phase fractions of the secondary phases, which would be necessary to affect the elemental composition of the CZTS phase.

Both phases of CZTS in B27 retain their type, but their concentrations of the type-defining defects increases (i.e. the compositions move away from the stoichiometric point).

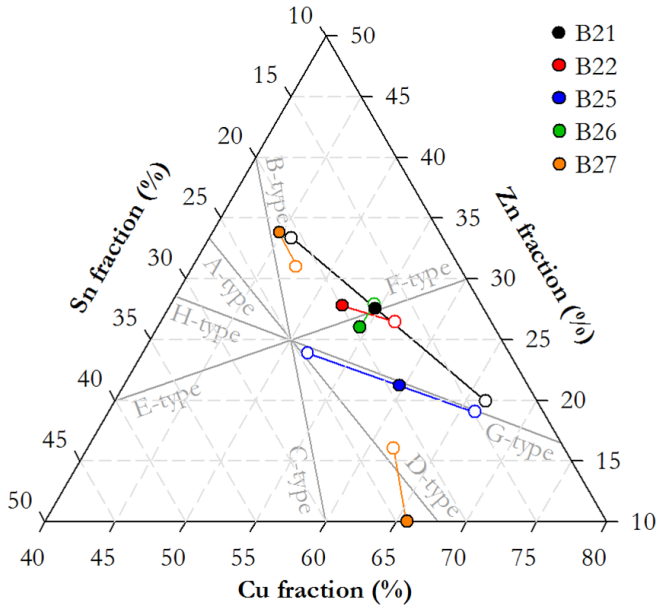

Figure 106: The cation compositions of each CZTS phase in samples B21, B22, and B25-27 at 600 K (filled circles) relative to those at 300 K (hollow circles).

CZTS type	Sample	2*a*	2*c*	2*d*	2*b*	8*g*	Lattice parameters (Å)
B-type	B27						*a* = 5.4473(6) *c* = 10.8683(1)
D-type	B27						*a* = 5.45024(4) *c* = 10.87726(9)
F-type	B21						*a* = 5.44913(4) *c* = 10.86843(8)
	B22						*a* = 5.44759(6) *c* = 10.8656(1)
	B26						*a* = 5.447386(5) *c* = 10.8704(1)
G-type	B25						*a* = 5.43468(5) *c* = 10.8641(1)

Table 34: The lattice site occupancies (red represents copper, blue zinc, dark grey tin, yellow sulphur, and light grey vacancies) and lattice parameters of the modelled CZTS phases in samples B21, B22, and B25-27 at 600 K, grouped by type. The numbers in brackets are the uncertainties on the last significant figures.

For the samples in which two phases of CZTS converge (B21 and B25), the composition of the single phase above the transition is a weighted average of the compositions of the two phases below the transition, and is also itself of a defect-complex-defined type: F-type for B21 and G-type for B25.

This sheds some light on the phase formation mechanism of CZTS. During the high-temperature step of sample production a single phase of CZTS is usually formed first, determined by the energetic stability of the combination of that CZTS composition and any secondary phases. It is also possible that a mixture of two different CZTS types and the necessary secondary phases is energetically favourable to a single CZTS phase and the different mixture of secondary phases this would necessitate, as was the case for B27. As the sample cools below the order-disorder transition, the ordering of the CZTS may cause different compositions, potentially defined by different defect complexes, to become energetically favourable. However, with the temperature too low to change the secondary phases present, the CZTS is confined by retaining a constant average composition. The result of the change in energetic favourability for a single phase of CZTS is therefore for it to separate into a mixture of separate grains of two different compositions.

It is possible that what has previously been identified as the 'order-disorder' transition is purely the convergence/splitting of phases of CZTS. However, the lattice site occupancy values of the CZTS phases at 600 K, illustrated in Table 34, demonstrate much greater disorder of copper and zinc than those for 300 K, approximating the fully disordered kesterite structure as much as possible while maintaining a composition of one of the defect-complex-defined types. Therefore, an order-disorder transition has clearly taken place in addition to the convergence of the phases of CZTS types.

The occurrence of the order-disorder transition even in single-phase CZTS suggests that the phase splitting is caused by the formation of the ordered crystal structure during the cooling stage of production, rather than the ordering being caused by the phase splitting. For some compositions, the formation of different defect complexes is made energetically favourable by the reduction in the concentration of particular defects by the ordering process, and so the ordering below the transition instigates the splitting of the single CZTS phase.

8.5. Conclusions

Five samples of CZTS with different elemental compositions were fabricated by solid-state reaction. The secondary phases in each sample were identified using EDX, ^{65}Cu & ^{119}Sn NMR, and resonant and non-resonant Raman spectroscopy using 785 nm and 488 nm respectively (described in detail in Chapter 6). Their crystal structures were investigated using high-resolution anomalous X-ray diffraction. All the CZTS phases were concluded to form the kesterite crystal structure with high levels of cation disorder.

Two distinct phases of kesterite CZTS with slightly different lattice parameters (Δ~0.004 Å) and different elemental compositions were discovered to exist simultaneously in three of the samples. These are attributed to off-stoichiometric 'types' of CZTS defined by the prevalence of charge-neutral defect complexes, which have been reported previously.

Every CZTS phase was found to be of a specific CZTS type, and two new types are proposed here. These are G-type, in which $[2Cu_{Sn}^{3-} + Cu_{Zn}^{-} + Cu_{i}^{+} + 3V_{S}^{2+}]$ defects dominate, and H-type, in which $[3S_{i}^{2-} + V_{Cu}^{-} + Zn_{Cu}^{+} + 2Sn_{Cu}^{3+}]$ defects dominate. In both types, the large number of the defects mean that they probably do not form a single complex.

In two of the three samples the two phases of CZTS converge to a single phase above the order-disorder phase transition, at 600 K. Irrespective of the number of phases and their type, all the samples feature greater disorder of copper and zinc at 600 K than at 300 K.

A mechanism of CZTS phase formation is proposed based on these results. During the high-temperature step of sample production a single phase of CZTS is usually formed first, determined by the energetic stability of the combination of that CZTS composition and any secondary phases. It is also possible that a mixture of two different CZTS types is energetically favourable to a single CZTS phase. As the sample cools through the order-disorder transition, the ordering of the CZTS may cause different compositions, potentially defined by different defect complexes, to become energetically favourable. However, with the temperature too low to change the secondary phases present, the CZTS is confined by retaining a constant average composition. The result of the change in energetic

favourability for a single phase of CZTS is therefore for it to separate into a mixture of separate grains of two different compositions.

This mechanism evidently has important implications for the design of the fabrication process of CZTS for application in solar photovoltaic cells.

This work was only possible because of the high resolution of the I11 beamline of the Diamond Light Source, the highest resolution that has been used to investigate the crystal structure of CZTS. Therefore this is the first observation of this two-phase structure using diffraction.

Further work studying the reproducibility of the phase formation through several heating and cooling cycles would be illuminating, as would a theoretical study not just of the formation energies of individual defect complexes, but of the formation energy of a multi-phase sample as a function of the phases present, their phase fractions, and the concentration of defects and defect complexes within the CZTS phase(s). It is this more complex, overall stability that is the real driving force behind CZTS disorder and phase formation, and it is therefore critically important for increasing the photovoltaic efficiency of solar cells using CZTS.

Chapter 9:

A structural and optoelectronic study of sputtered thin-film CZTS

9.1. Introduction

While studying bulk samples of CZTS can be useful in order to understand the fundamental properties and behaviour of the material, it is ultimately limited as an approach to inform the fabrication of solar cells because the thin-film CZTS used in photovoltaic devices will be different in many respects to the bulk material. Aside from the inherent dissimilarities due simply to the morphological difference between bulk samples and thin films, many of the material properties relevant to photovoltaic performance are heavily affected by the fabrication process itself. The most useful studies for informing the growth of CZTS for industrial photovoltaic application will therefore use a fabrication method suitable for that purpose. Sputtering followed by sulphurisation annealing is such a fabrication method, as it is easily scaled up to an industrial level and represents a promising compromise between low cost and high sample quality.

Prior to this project, fabricating CZTS by sputtering had not been attempted in Durham, and so the entire process had to be realised largely from scratch, following reports in academic literature (see Chapter 4). While an existing sputtering system suitable for CZTS deposition was available, it was shared with many other users, making available time limited, and it was found to be prone to breakages and other technical challenges, resulting

in many delays. All equipment for the sulphurisation process had to be acquired or designed and built entirely from scratch.

It was the initial aim of this doctoral project to focus largely on studying sputtered thin films and photovoltaic cells produced using them, but the lengthy delays and numerous setbacks that arose in the course of developing the fabrication route gradually made this impossible. It remains an achievement that a working fabrication system for sputtered CZTS films now exists in Durham, and future work will hopefully utilise this to carry out some of the in-depth study that was planned. This chapter details the characterisation carried out on the few samples sufficiently successful to have made it all the way through the nascent fabrication procedure.

9.2. Experimental method

Substrates of soda lime glass 25 mm × 25 mm × 2 mm were cut from microscope slides 75 mm × 25 mm × 2 mm. They were cleaned before deposition by submersion and manual stirring 5 times for 1 minute each in acetone to remove grease and dust, followed by 5 times for 1 minute each in isopropanol to remove acetone residue.

A layer of molybdenum approximately 800 nm thick was deposited directly on each substrate by DC magnetron sputtering. A small single-target sputtering chamber was loaded with up to four substrates on a rotating carousel above the molybdenum sputter target, behind a mask to restrict deposition to one substrate at a time. The chamber was evacuated to a base pressure of around 10^{-4} Pa and a flow of argon was introduced as the sputtering gas, giving a working pressure of 0.5-1.0 Pa. The sputtering power used was around 25 W. The system did not include a deposition rate monitor, so the deposition time was calibrated by measuring the thickness of deposited molybdenum films. This was done first by X-ray reflectivity (XRR), using a BEDE D1 XRR system, and then checked by examining a film cross section by FIB milling and SEM viewing, using an FEI Helios Nanolab 600, to directly measure the thickness. A deposition time of 2 h 15 m was found to give Mo films of the desired thickness, approximately 800 nm, and so was used for the samples reported here.

A larger, multi-target, two-chamber sputter system was used to deposit the CZTS precursor layers. For each sample, the substrate was placed on a transfer arm inside a small load-lock vacuum chamber, which was then evacuated to a pressure of around 0.5 Pa. A gate between this and the main deposition chamber was opened and the substrate was transferred into it and deposited on a sample holder above the targets. The transfer arm was then removed from the main chamber and the gate valve between the two chambers was closed. This process allows an ultra-high vacuum to be maintained in the growth chamber without long evacuation times.

The sputtering chamber was evacuated to a background pressure of 10^{-6} Pa. Argon was introduced as the sputtering gas, at a flow rate of 50-100 sccm, giving a working pressure of approximately 0.1 Pa. Layers of Cu, SnS, and ZnS were sequentially deposited using a mask to confine the area of each deposited film to a 20 mm × 20 mm square. Several layer orders were used, which will be discussed below. The power supplied to each target varied slightly between samples, but was approximately 40 W (DC), 100 W (RF), and 100 W (RF) to the Cu, ZnS, and SnS targets respectively, giving growth rates of approximately 0.59, 0.12, and 0.45 $Å \cdot s^{-1}$ respectively. The thickness of each precursor to be deposited was calculated from the desired element ratios of the samples and the densities and atomic masses of the precursor materials. Several elemental compositions were used, which will be discussed below.

Two batches of samples reached a sufficient stage of development to be worth discussing, although none of the samples were sufficiently successful to be worth developing into photovoltaic cells. The two batches underwent different sulphurisation annealing stages.

The first batch, S01-S05, was intended to investigate the effect of layer order, and so several different orders were used, which are given in Table 35. The layer thicknesses were 65 nm for Cu, 153 nm for ZnS, and 144 nm for SnS, which were calculated using the respective densities and molecular masses to give a final CZTS thickness of 500 nm with Cu/(Zn+Sn) = 0.8 and Zn/Sn = 1.2.

Sample	Precursor layer order	Notes
S01	glass/Mo/ZnS/SnS/Cu	
S02	glass/Mo/Cu/ZnS/SnS	
S03	glass/Mo/Cu/SnS/ZnS	Amount of ZnS deposited was questionable. H_2S supply possibly ran out during sulphurisation.
S04	glass/Mo/Cu/ZnS/SnS	H_2S supply ran out during sulphurisation.
S05	glass/Mo/ZnS/Cu/SnS	Held at 590 K for 1 hr then cooled before sulphurisation.

Table 35: The precursor layer orders of the first batch of sputtered thin-film samples, S01-05.

The second batch, S06-S12, was intended to investigate the effect of elemental composition, as a parallel to the bulk samples studied in Chapter 6, and so several different precursor layer thickness combinations were used, which are given in Table 36. In each case they were calculated to give a final CZTS thickness of 1,000 nm. The layer order was fixed as glass/Mo/SnS/Cu/ZnS/Cu with the two copper layers having equal thickness.

Sample	Intended composition	Intended atomic fraction (%)				Layer thicknesses (nm)		
		Cu	Zn	Sn	S	Cu (×2)	ZnS	SnS
S06	Stoichiometric	25.0	12.5	12.5	50.0	73.6	246.6	299.7
S07	Cu-poor, Zn-rich	22.5	15.0	12.5	50.0	66.2	296.0	299.7
S08	Sn-poor, Zn-rich	25.0	15.0	10.0	50.0	147.2	296.0	239.8
S09	Sn-poor, Cu-rich	27.5	12.5	10.0	50.0	81.0	246.6	239.8
S10	Zn-poor, Cu-rich	27.5	10.0	12.5	50.0	81.0	197.3	299.7
S11	Zn-poor, Sn-rich	25.0	10.0	15.0	50.0	73.6	197.3	359.7
S12	Cu-poor, Sn-rich	22.5	12.5	15.0	50.0	66.2	246.6	359.7

Table 36: The intended elemental compositions and layer thicknesses of the second batch of sputtered thin-film samples, S06-S12. N.B. each sample precursor featured two copper layers of the thickness given here.

S01-S05 were sulphurised in situ, i.e. within the sputtering chamber. A background vacuum pressure of 10^{-6} Pa was established, and then a gas mixture of H_2S at 3 % by volume in Ar was introduced. Such a low volume percentage of H_2S was used because H_2S mixed in Ar becomes extremely flammable above 3.5 %, [613] although other studies have used it at higher concentrations. [614] The gas mixture was supplied as a constant flow of 100 sccm, giving a sulphurisation pressure of around 0.1 Pa. A heating rate of 10 $K \cdot min^{-1}$ was used to reach a maximum temperature of 848 K, which was held for 1 hour, followed by natural cooling down to room temperature over approximately 24 hours. However, there was a

problem with the supply of H_2S during the sulphurisation of this batch, meaning S03 and S04 were probably under-sulphurised and S05 was annealed at 590 K for an hour before H_2S was introduced.

S06-S12 were sulphurised in a sealed quartz chamber in a tube furnace, in H_2S at 20 % by volume in N_2, which is much safer than H_2S in Ar. [615] A heating rate of 5 $K \cdot min^{-1}$ was used to reach a maximum temperature of 850 K, which was maintained for 1 hour, followed by natural cooling down to room temperature.

After the formation of the CZTS layer by sulphurising the precursor layers, the samples of the second batch were etched by submersion for 2 minutes in an aqueous KCN solution (5 % by weight) to remove copper sulphide impurities, and then rinsed in deionised water to remove any residual KCN. They were then etched by submersion for 5 minutes in an aqueous HCl solution (10 % by weight) to remove ZnS impurities, and then rinsed in deionised water again to remove any residual HCl.

For both batches of samples, each was viewed extensively using an Hitachi SU-70 FEG scanning electron microscope (SEM), in both backscattered and secondary-electron configurations.

Energy-dispersive X-ray (EDX) spectroscopy was carried out to identify the phases visible in the backscattered SEM images, using an INCA x-act LN2-free analytical silicon drift detector and INCA software. For each phase identified in each sample, measurements were taken at six different points on the sample and averaged, with the uncertainty on these average values given by the standard deviation between the six measurements.

Powder X-ray diffraction (XRD) patterns were taken for each sample in the Bragg-Brentano geometry using Cu-Kα X-rays in a Bruker d7 diffractometer. Rietveld refinement of the crystal structures was performed using TOPAS v.6 software.

Raman spectra were obtained using a Horiba JY LabRAM-HR Raman microscope system in the backscattering configuration. A solid-state laser was used to provide resonant excitation for CZTS at 785 nm and an Ar^+ ion laser was used to provide non-resonant excitation at 488 nm. The Raman signal was detected after dispersion through a 1,800 mm^{-1}

(for 785 nm excitation) or 600 mm^{-1} (for 488 nm excitation) diffraction grating. Spectra were taken at 9 locations across the sample surface and averaged to give a single representative spectrum for each sample using each wavelength.

Photoluminescence spectroscopy was carried out using a 375 nm solid-state laser as the excitation source. The samples were mounted under vacuum in a closed-cycle helium cryostat (Cryomech ST405), using copper tape, and cooled to 3 K for low-temperature measurements. The sample luminescence was passed through long-pass filters (GG400 and GG435) to remove laser light, dispersed by a grating monochromator (Bentham, TM300), and then collected by a silicon photodiode array cooled to 253 K. Spectra were obtained for a range of sample temperatures and laser powers.

9.3. The molybdenum layer

As part of setting up the thin-film CZTS sample fabrication route, the rate of deposition of molybdenum using the small, single-target sputtering system needed to be determined, as the system did not include a rate monitor in situ. To do so, layers of molybdenum were deposited on glass with four different sputtering times, and their thicknesses were measured by XRR, the patterns from which are shown in Figure 107. The thicknesses of the films were determined by fitting a model to the period of the oscillation in intensity of reflected light (see Section 5.2). An average deposition rate of 0.98 $Å \cdot s^{-1}$ was calculated.

FIB milling became available later in the project, so this was used to confirm the deposition rate measurement by directly measuring the thickness of a deposited molybdenum film. An example image is given in Figure 108. The thickness was measured at several locations over the sample film and found to be uniformly ~400 nm, which agreed with the deposition rate measurement of 0.98 $Å \cdot s^{-1}$.

The molybdenum layer was observed to exhibit a compact morphology and smooth surface on the scale of ~100 nm which is good for CZTS growth.

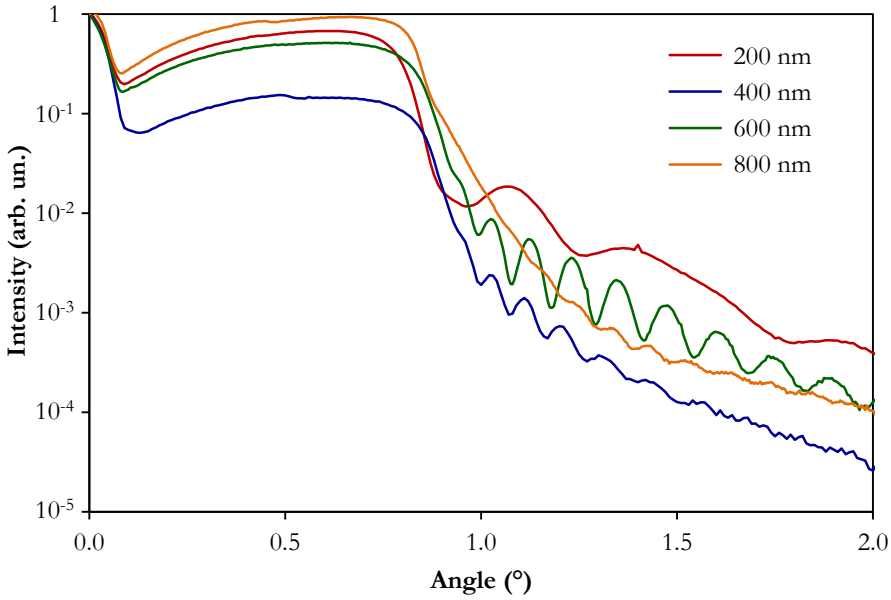

Figure 107: XRR data of molybdenum films of various thicknesses.

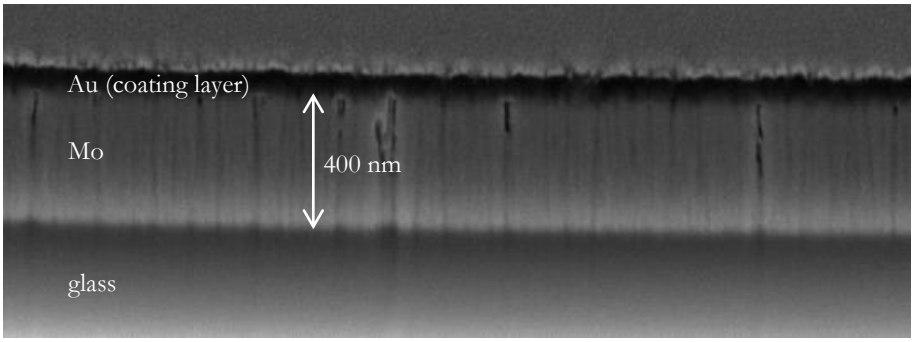

Figure 108: FIB-milled cross-sectional SEM image of a molybdenum layer, for measurement of its thickness. A thin layer of gold was deposited on top of the molybdenum to prevent unintended sputtering of it during milling.

9.4. The effects of precursor layer order

Precursor layer order is likely to have a significant effect on the growth mechanism of the CZTS phase during fabrication, due to its effect on the ability of each element to diffuse throughout the sample and/or evaporate and be lost if near the surface. Samples with different layer orders were grown to investigate this effect, as described in Table 37.

Photographs of the samples, after undergoing sulphurisation annealing inside the sputter deposition chamber, are shown in Figure 109. They show that CZTS was not the main phase in any of them, and that S03, S04, and S05 experienced severe delamination.

Sample	Precursor layer order
S01	glass/Mo/ZnS/SnS/Cu
S02	glass/Mo/Cu/ZnS/SnS
S03	glass/Mo/Cu/SnS/ZnS
S04	glass/Mo/Cu/ZnS/SnS
S05	glass/Mo/ZnS/Cu/SnS

Table 37: The layer orders of the first batch of sputtered thin-film samples, S01-S05.

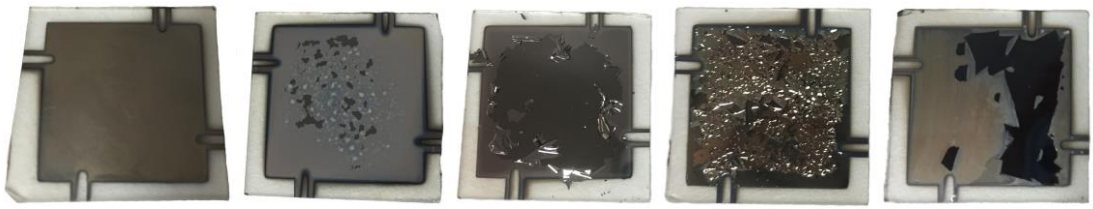

Figure 109: Photographs of, from left to right, S01, S02, S03, S04, and S05.

9.4.1. Scanning electron microscopy

SEM imaging revealed the morphology of each sample on the microscale, example images of which are given in Figure 110-Figure 114.

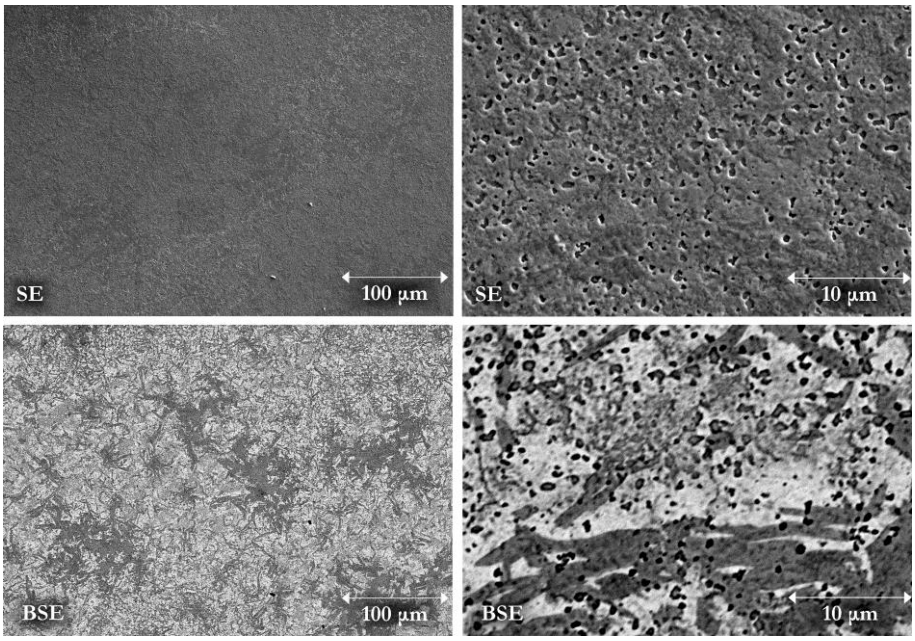

Figure 110: SEM images of S01. The film is smooth with good adhesion but is covered in pinholes. The backscattered images and EDX reveal two ternary Cu-Sn-S phases.

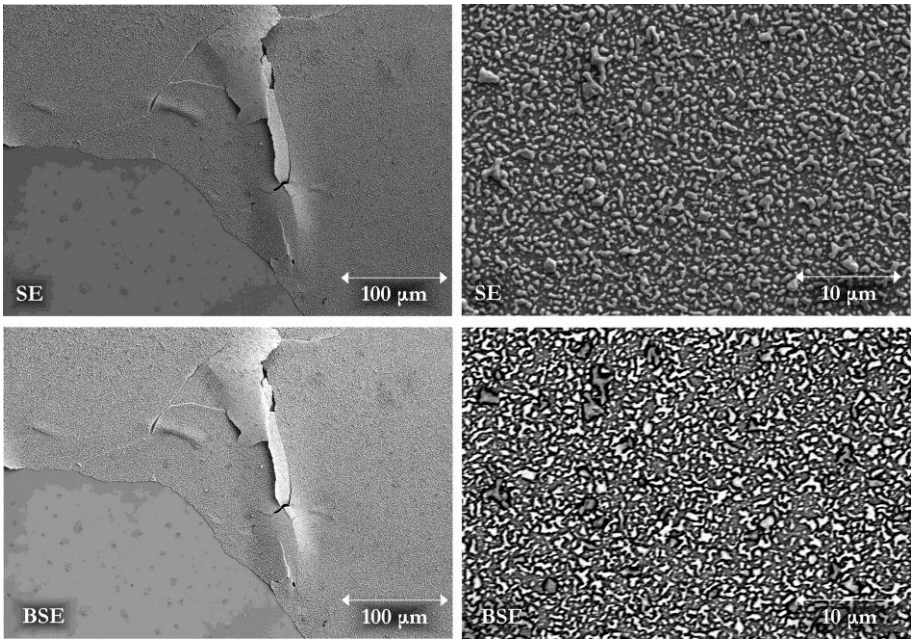

Figure 111: SEM images of S02. The film is rough because of small droplets of a secondary phase decorating its surface, and there are some areas where delamination has occurred. The backscattered images and EDX reveal that the main phase is a Cu-Zn-S ternary phase and that the droplets decorating the surface are a Cu-Sn binary alloy.

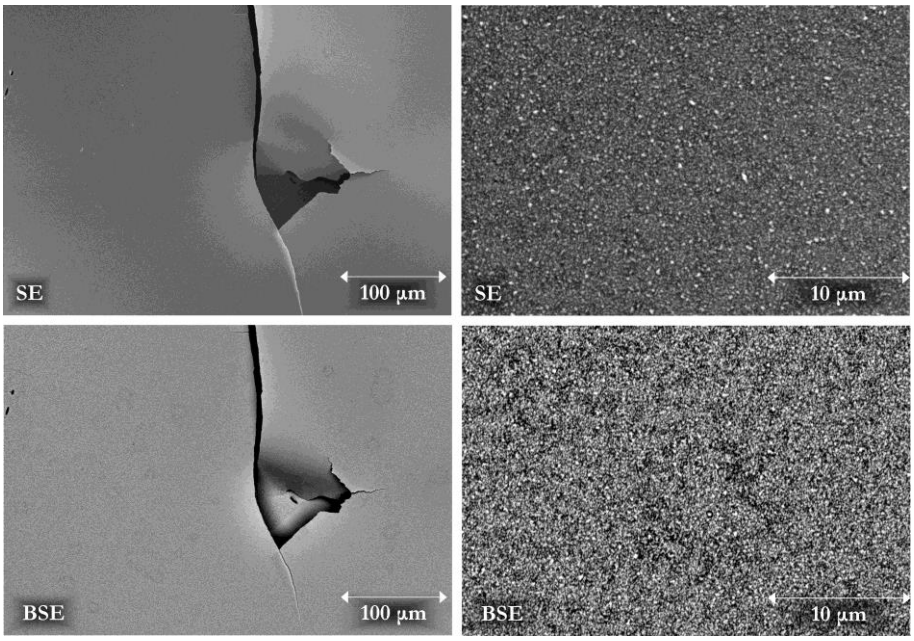

Figure 112: SEM images of S03. Most of the 'CZTS' layer has delaminated, leaving just the molybdenum layer underneath, but some remains around the edges of the sample. The backscattered images and EDX reveal that this consists of very small grains of two phases: a ternary Cu-Sn-S phase and a Cu-rich, S-poor quaternary phase.

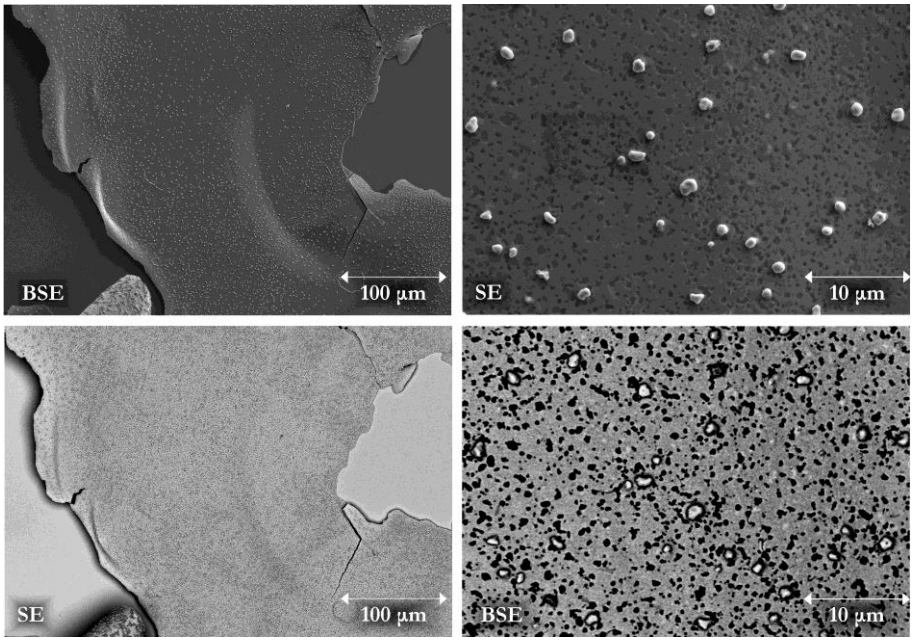

Figure 113: SEM images of S04. This sample has also undergone severe delamination. The backscattered images and EDX reveal that the remaining 'CZTS' layer is composed of a main Cu-Sn-S ternary phase containing grains of a Cu-Zn-S ternary phase and is decorated with droplets of a Cu-Sn binary alloy.

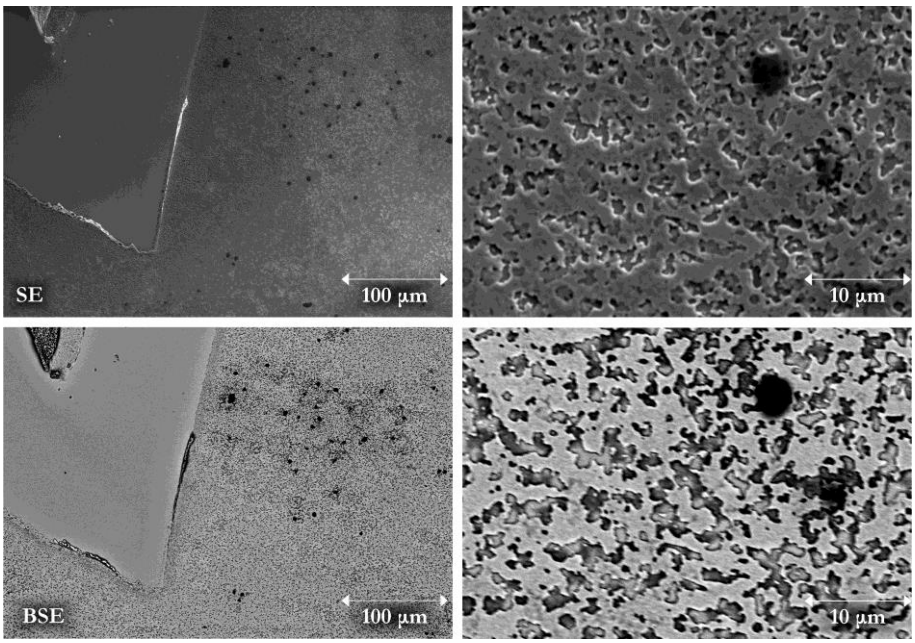

Figure 114: SEM images of S05. The backscattered images and EDX reveal that the smooth dark blue area is a ternary Cu-Zn-S alloy, and the rough area is composed of two distinct ternary Cu-Sn-S phases. The dark spots are a Cu-rich, S-poor quaternary phase.

9.4.2. Energy-dispersive X-ray spectroscopy

EDX identified the phases visible in the backscattered-electron SEM images, which are listed in Table 38. It confirmed that CZTS did not form in a significant amount in any of the samples.

Sample	Phases			
S01	Cu_4SnS_2	Cu_6SnS_2		
S02	$CuZnS_2$	Cu_3Sn		
S03	Cu_3ZnSnS_2	Cu_6SnS_3		
S04	Cu_5SnS_2	CuZnS	Cu_3Sn	
S05	Cu_2ZnS_6	Cu_5SnS_2	Cu_4SnS_5	Cu_3ZnSnS_3

Table 38: The phases identified in samples S01-05 using EDX.

The average compositions of the samples (or of the two distinct areas of the sample for S05) were measured by EDX in addition to the composition of each phase within each sample. These are given in Table 39 and plotted relative to the intended composition of the samples in Figure 115.

Sample	Cu	Zn	Sn	S
S01	56.2 %	0.0 %	9.9 %	33.8 %
S02	33.4 %	22.3 %	9.2 %	35.1 %
S03	52.9 %	7.2 %	10.0 %	30.0 %
S04	55.7 %	6.9 %	11.6 %	25.8 %
S05 (smooth blue area)	21.6 %	11.4 %	0.8 %	66.2 %
S05 (rough grey area)	51.1 %	0.0 %	12.4 %	36.4 %

Table 39: The average sample compositions of S01-05 as measured by EDX. The smooth blue and rough grey areas of S05 were measured separately.

All samples experienced tin loss during sulphurisation. This was particularly severe for the smooth blue area of S05, which lost almost all of its tin. S01, S03, S04, and the rough grey area of S05 also lost most or all of their zinc. Loss of both tin and zinc during sulphurisation is a well-known issue for CZTS (see Section 4.3.2), but rarely to the extent observed here, and loss of tin is usually more severe than of zinc.

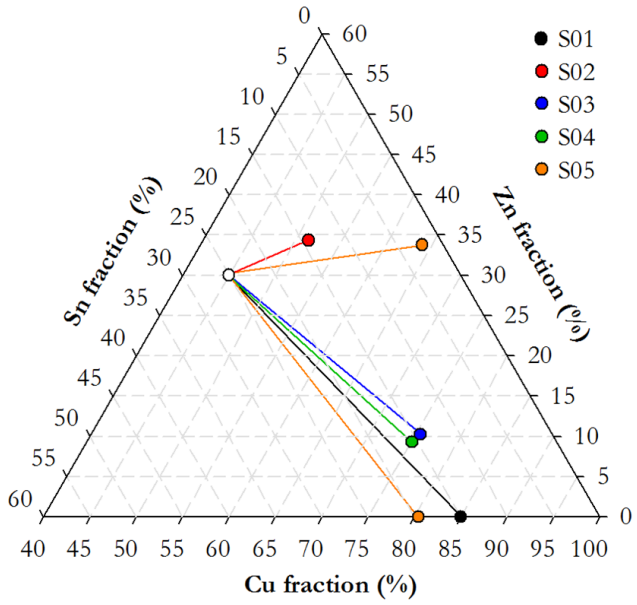

Figure 115: The average sample compositions of S01-05 measured by EDX (filled circles), relative to their intended composition (hollow circle). The smooth blue and rough grey areas of S05 were measured separately. All samples experienced tin loss (particularly the smooth blue part of S05, which lost almost all its tin), and S01, S03, S04, and the rough grey area of S05 lost most or all of their zinc.

All samples are also significantly S-poor (with the exception of the smooth blue area of S05), suggesting that the sulphurisation was incomplete. This was probably due to the low pressure of the H_2S-N_2 mixture used for this batch of samples.

9.4.3. The way forward

The first batch of samples were sulphurised in situ within the sputtering chamber, which was designed to achieve and maintain an ultra-high vacuum rather than a constant reactive atmosphere, and so it is unsurprising that the chamber did not make a successful sulphurisation vessel. It was therefore evident that this baseline sulphurisation process needed to be improved. This conclusion led to the development of the separate sulphurisation system in the tube furnace used for the second batch of samples.

9.5. The effects of elemental composition

The elemental composition of samples intended to form CZTS has a significant effect on the secondary phases that form, and on the defects formed within the CZTS crystal lattice itself. These in turn significantly affect potential photovoltaic performance. These effects of composition are still not fully understood, and so require further research. A range of compositions around the stoichiometric point were selected for study here as a parallel to the bulk-sample investigation presented in Chapter 6. These compositions are given in Table 40 and plotted in Figure 116.

Sample	Intended composition	Intended atomic fraction (%)			
		Cu	Zn	Sn	S
S06	Stoichiometric	25.0	12.5	12.5	50.0
S07	Cu-poor, Zn-rich	22.5	15.0	12.5	50.0
S08	Sn-poor, Zn-rich	25.0	15.0	10.0	50.0
S09	Sn-poor, Cu-rich	27.5	12.5	10.0	50.0
S10	Zn-poor, Cu-rich	27.5	10.0	12.5	50.0
S11	Zn-poor, Sn-rich	25.0	10.0	15.0	50.0
S12	Cu-poor, Sn-rich	22.5	12.5	15.0	50.0

Table 40: The intended elemental compositions of samples S06-12.

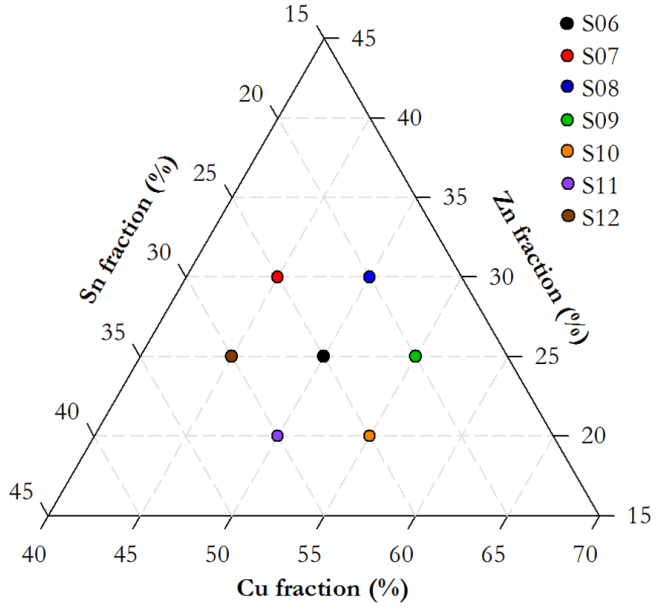

Figure 116: The intended Cu-Zn-Sn compositions of samples S06-12.

Photographs of the samples, after undergoing sulphurisation annealing in the purpose-built sulphurisation chamber, are shown in Figure 117. They show that S08 and S09, and to a lesser extent S06, experienced severe delamination. A leak developed during the sulphurisation of S11 so it was oxidised and then evaporated rather than forming CZTS. Very little of it appears to remain; even much of the molybdenum layer was removed. The remaining samples appear dull and grey, except S08, which is blue, and S10, which features yellower areas.

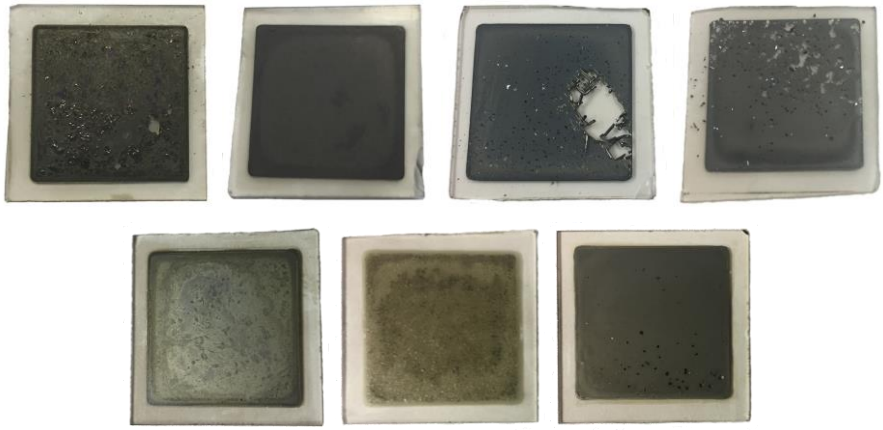

Figure 117: Photographs of, from left to right, top: S06, S07, S08, and S09; and bottom: S10, 11, and S12.

9.5.1. Scanning electron microscopy

SEM was used to examine the morphology of each sample on the microscale, example images of which are given in Figure 118-Figure 124.

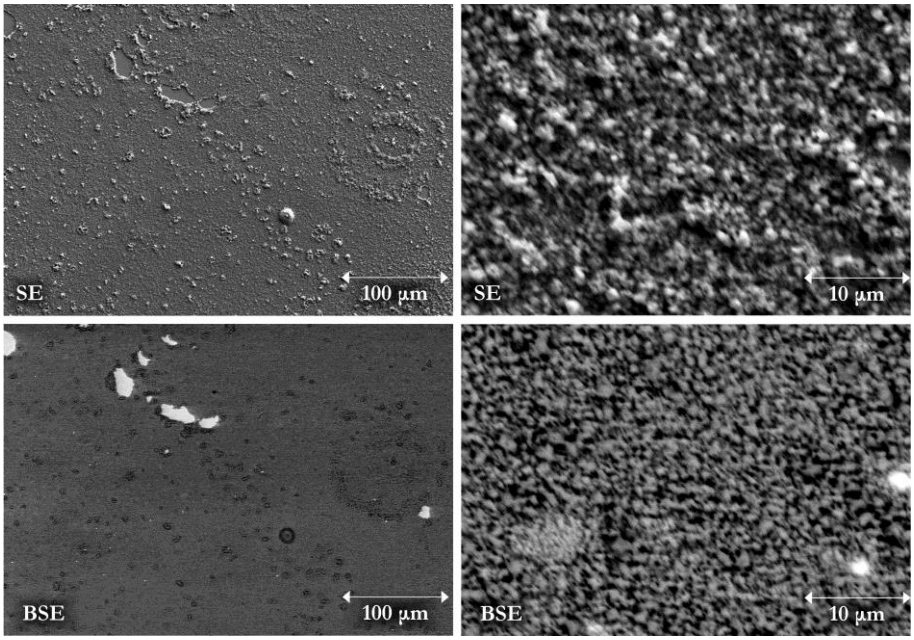

Figure 118: SEM images of S06. The backscattered images and EDX reveal apparently phase-pure CZTS, with pure molybdenum visible in areas where the precursor layers delaminated.

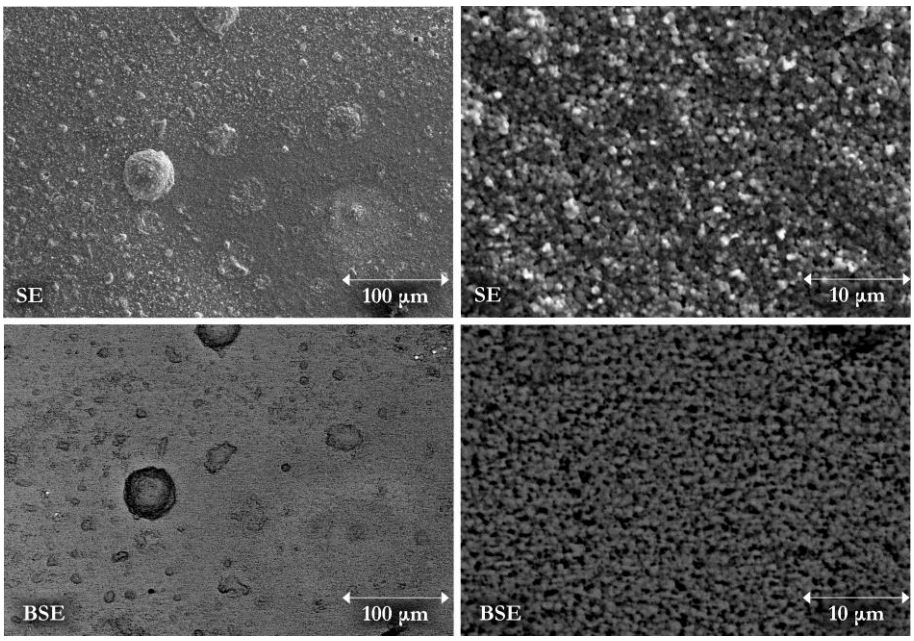

Figure 119: SEM images of S07. The backscattered images and EDX reveal apparently phase-pure CZTS.

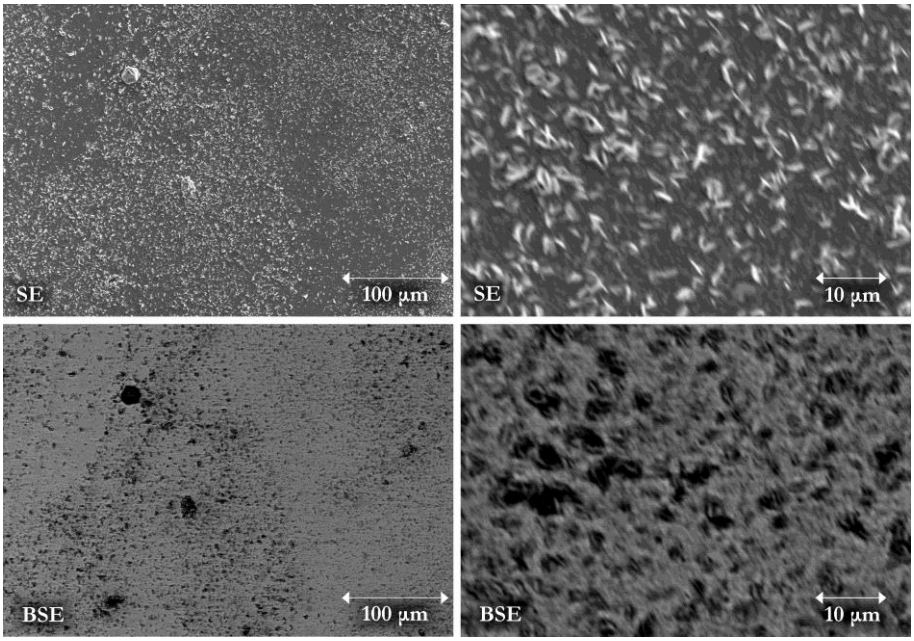

Figure 120: SEM images of S08. The backscattered images and EDX reveal a majority CZTS phase, with flakes of what appears to be CuS on the surface.

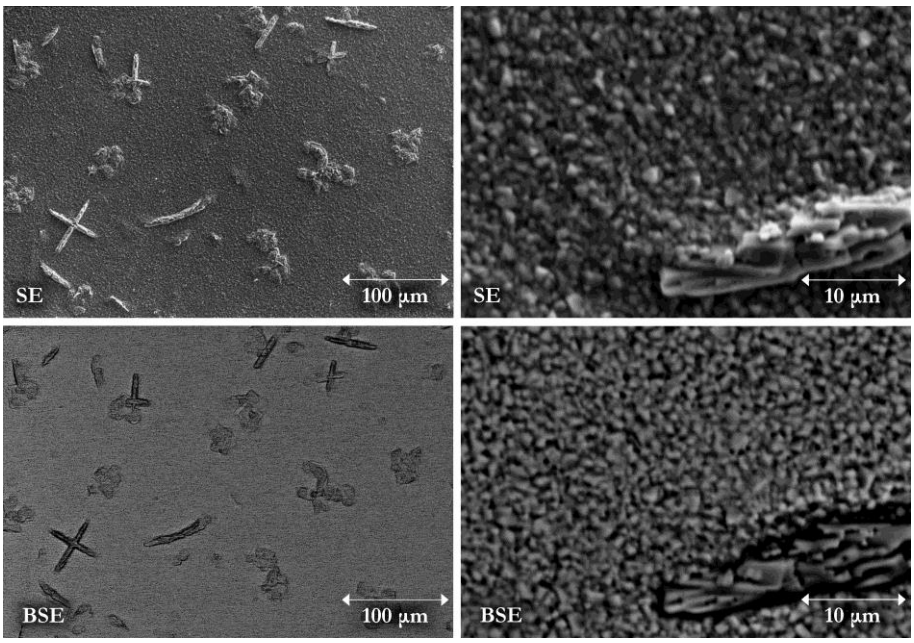

Figure 121: SEM images of S09. The backscattered images and EDX reveal apparently phase-pure CZTS, including the structures on the surface. It is unclear what causes these structures to form.

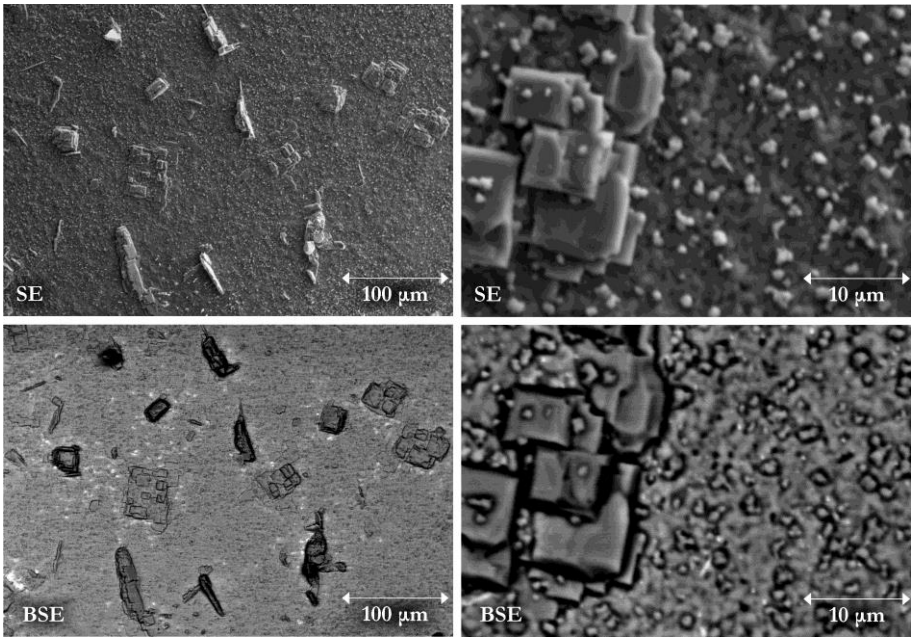

Figure 122: SEM images of S10. The backscattered images and EDX reveal a majority CZTS phase, including the large surface structures, but with very small droplets of a secondary phase, which cannot accurately be distinguished by EDX because of their small size. It is unclear what causes the surface structures to form.

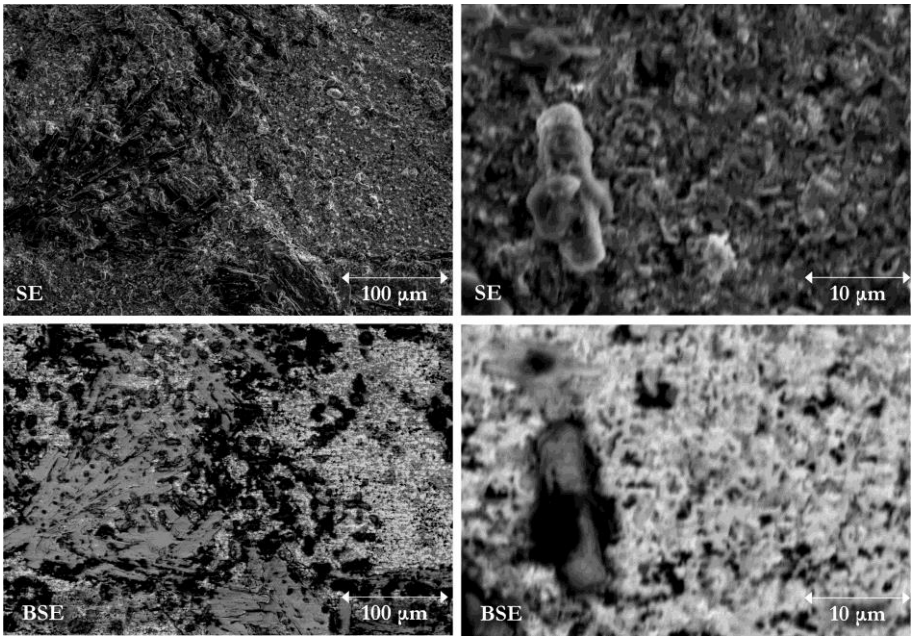

Figure 123: SEM images of S11. The backscattered images and EDX reveal a mixture of oxides with no CZTS present. The sample was spoilt by a leak during sulphurisation.

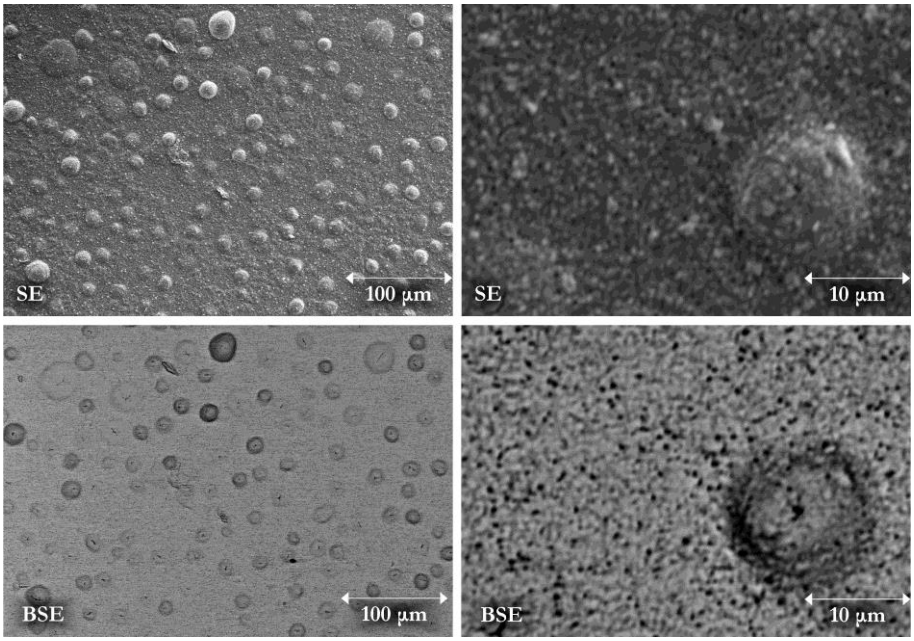

Figure 124: SEM images of S12. The sample layer has blistered significantly, but the backscattered images and EDX reveal apparently phase-pure CZTS.

9.5.2. Energy-dispersive X-ray spectroscopy

The samples were all (except S11, which was largely destroyed by a leak during sulphurisation) found to be phase-pure CZTS by EDX, with the exception of flakes of CuS on the surface of S08 and unidentified droplets on the surface of S10. It is interesting that the CuS survived etching in KCN, which has previously been reported to remove it. The elemental compositions of the CZTS phase in each sample, measured by EDX, are given in Table 41 and plotted relative to the intended composition of the samples and the off-stoichiometric defect-complex-defined types in Figure 125.

Sample	Cu	Zn	Sn	S
S06	27.2 %	10.7 %	11.8 %	50.3 %
S07	26.6 %	11.3 %	11.9 %	50.2 %
S08	27.5 %	14.6 %	7.4 %	50.5 %
S09	29.9 %	9.9 %	11.8 %	48.4 %
S10	26.0 %	7.4 %	13.2 %	53.5 %
S11	-	-	-	-
S12	26.5 %	11.3 %	13.6 %	48.7 %

Table 41: The average compositions of the CZTS in S06-S12 as measured by EDX.

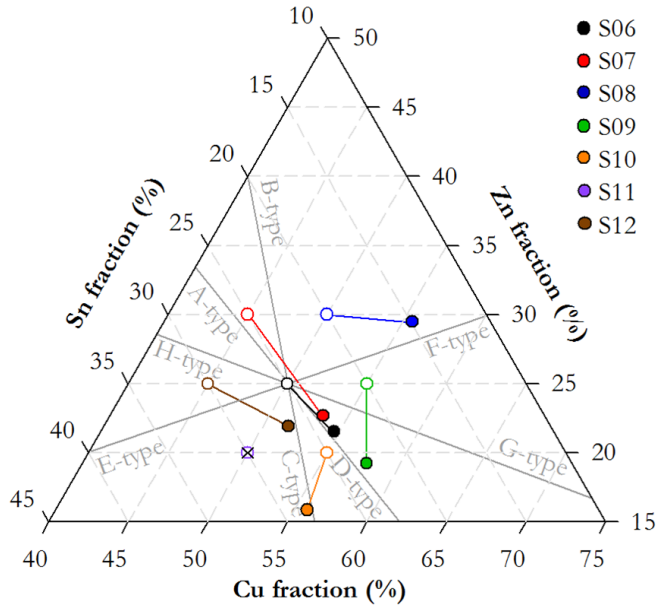

Figure 125: The Cu-Zn-Sn compositions, measured by EDX, of the CZTS in samples S06-12 (filled circles), relative to their intended compositions (hollow circles). S11 is crossed out as it was largely destroyed by a leak during sulphurisation.

It is notable that all the sample compositions migrated to a defect-complex-defined off-stoichiometric type. As no secondary phases were formed in any significant quantity, this appears to have occurred solely through the loss of zinc and tin. S06, S07, S09, S10, and S12 all lost more zinc than tin, which is unusual. Only S08 lost a significant amount of tin as expected (see Section 4.3.2).

9.5.3. X-ray diffraction

XRD patterns for all the samples are shown in Figure 126. The results of Rietveld refinement are given in Table 42. All the samples (except S11) showed molybdenum peaks at 41 and 74 °, which gave rise to significant molybdenum phase fractions in the Rietveld refinement results. These are ignored in the results given in Table 42 as the molybdenum is present as a separate layer beneath the sample material rather than within it.

Rietveld refinement of the XRD patterns confirms that S06 and S08 are phase-pure CZTS, and that the large majority of S07 is too, but reveals that S09, S10, and S12 are not. These samples and S07 all feature an additional tetragonal phase similar to CZTS. This is concluded to be Cu_3SnS_4 in S09, S10, and S12 as Raman spectroscopy also identified this in

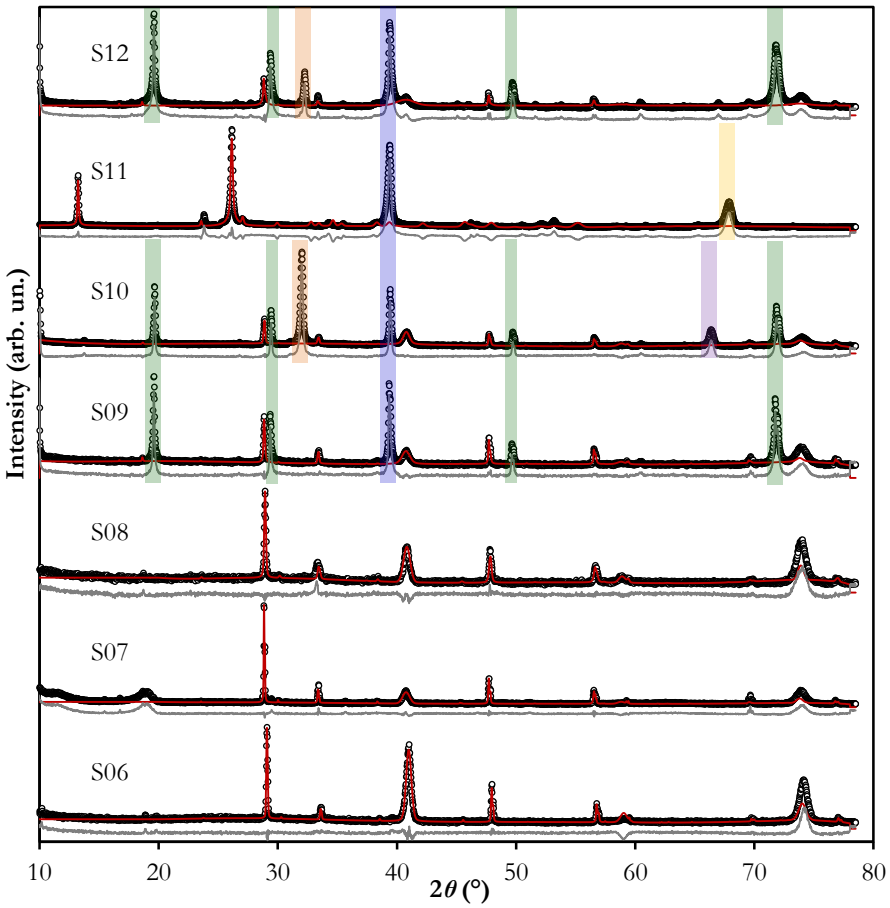

Figure 126: Cu-Kα XRD patterns of samples S06-12 (black circles) with calculated patterns for best-fit models overlaid (red lines), and residuals underneath each one (grey lines); all displaced vertically for clarity. Well-fitting models were found for S06-08, but S09-12 all featured peaks for which no material could be identified. These peaks can be ascribed to 5 different materials because of the various combinations that occur together in a sample, and are highlighted in different colours accordingly.

these samples (see Section 9.5.4), and to be Cu_2SnS_3, which does not exhibit discernible Raman peaks, in S07.

Additionally, the XRD patterns for S09-12 feature a number of high-intensity unidentified peaks. From their occurrence in various combinations in each sample they can be grouped as five separate phases, as illustrated in Figure 126. None of these match any of the usual secondary phases (CuS, Cu_2S, ZnS, SnS, SnS_2, Cu_2SnS_3, Cu_3SnS_4, Cu_4SnS_4, $Cu_4Sn_7S_{16}$, and $Cu_2ZnSn_3S_8$), common oxides (CuO, ZnO, SnO_2, and Zn_2SnO_4), Mo-containing structures (Mo, MoS_2, Mo_2S_3, and MoO_3), bronze alloys (CuSn, three crystal structures of Cu_3Sn, two structures of Cu_5Sn_4, two structures of Cu_6Sn_5, $Cu_{10}Sn_3$, and $Cu_{41}Sn_{11}$), brass alloys (CuZn,

Sample	Phases		*a* (Å)	*c* (Å)
S06	CZTS 100.0 %		5.4297(6)	10.832(2)
S07	CZTS 74.0 %	Cu_2SnS_3 26.0 %	5.4275(5)	10.868(2)
S08	CZTS 100.0 %		5.4268(9)	10.812(3)
S09	CZTS 43.7 %	Cu_3SnS_4 56.3 %	5.4286(9)	10.841(7)
S10	CZTS 26.3 %	Cu_3SnS_4 73.7 %	5.4318(9)	10.850(9)
S11	-	MoO_3 100.0 %	-	-
S12	CZTS 14.0 %	Cu_3SnS_4 86.0 %	5.4271(8)	10.834(3)

Table 42: The phase compositions of samples S06-S12, and room-temperature lattice parameters of their CZTS phases, found from Rietveld refinement using standard laboratory Cu-Kα XRD. These phase fractions exclude the contributions to the XRD patterns of the molybdenum layers underneath the sample layers, and of the unidentified phases in samples S09-12. The numbers in brackets are the uncertainties on the last significant figures.

$CuZn_3$, Cu_3Zn, Cu_4Zn, Cu_5Zn_8, Cu_7Zn_{20}, and $Cu_{13}Zn_7$), or CZTS structures (kesterite, stannite, eskebornite, PMCA, sphalerite, or wurtzite), and thus they remain a mystery.

The unidentified phases could be due to unnoticed contamination of the sputtering chamber or sulphurisation chamber, or they could in fact correspond to common secondary phases but with a heavily preferred planar direction, meaning that only some peaks of their patterns are present, which would make Rietveld refinement inaccurate. Further investigation of these mysterious phases is needed.

9.5.4. Raman spectroscopy

For each sample at each excitation wavelength, the Raman spectra taken across the surface were all of approximately the same shape, showing a high degree of compositional uniformity across the sample. The spectra were averaged to give a single representative spectrum for each sample using each excitation wavelength. With the exception of S11, each spectrum, with background removed and normalised, was fitted using up to 15 peaks identified using previous literature reports (CZTS, [222,258,412,517,568-578] CuS, [581], Cu_3SnS_4, [580] and MoS_2; [258] see Section 5.9.1). The spectra for S11 confirmed that very little, if any, CZTS is present, as expected. The fitted spectra are shown in Figure 127 for 785 nm excitation and Figure 128 for 488 nm.

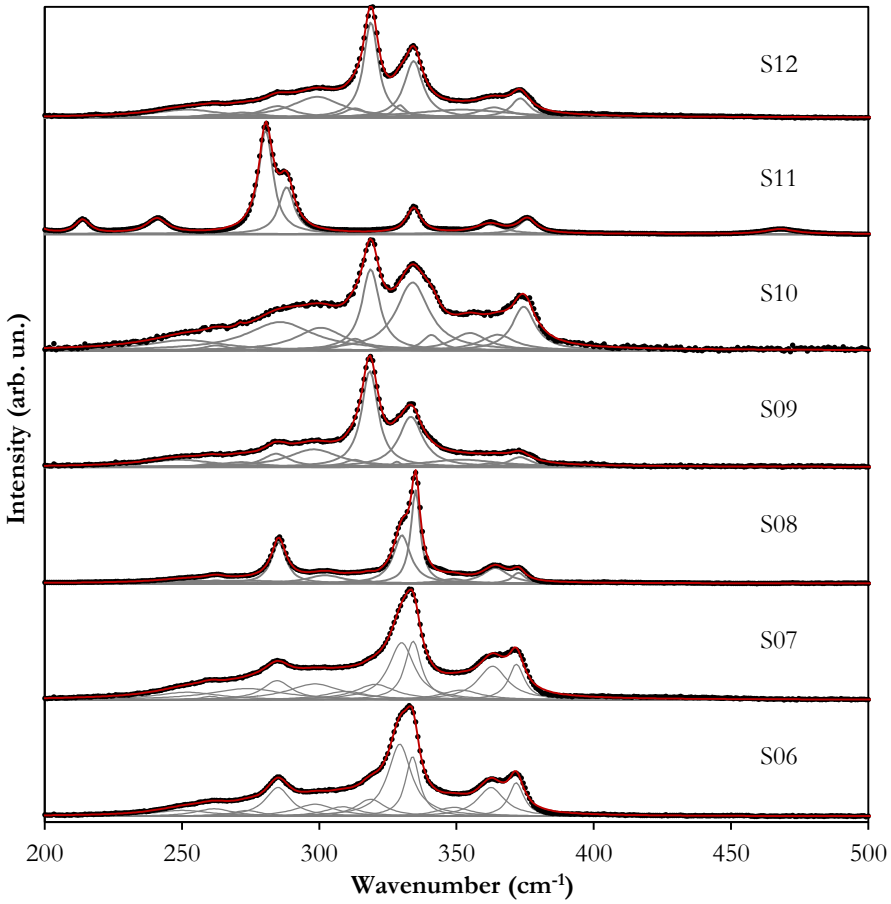

Figure 127: The Raman spectra for samples S06-12 using 785 nm excitation, with background removed and normalised, displaced vertically for clarity.

For 785 nm excitation, samples S06, S07, and S08 show clear CZTS peaks, although with large 'disordered kesterite' peaks at 331 cm^{-1} and with significant broadening. This confirms that CZTS is the majority phase in these samples, but that the crystal quality is in general quite poor, exhibiting small grain size and a high concentration of defects, which distort the crystal lattice in an unstructured and irregular way. The peaks for S08 are noticeably narrower than the other samples, however, suggesting that the quality of this sample may be better. S09, S10, and S12 also show the CZTS peaks, but the largest peak in their spectra is the Cu_3SnS_4 one at 318 cm^{-1}.

The 488 nm spectra also show that S06, S07, and S08 are primarily CZTS, with S08 having better crystalline quality than the others. CuS is evident in S08 (and S11) at 472 cm^{-1}, only visible using 488 nm excitation and not 785 because of its band gap value, as was found for the bulk samples in Section 6.8. The two peaks at 380 and 403 cm^{-1}, attributed to MoS_2, [258] are also evident only in the 488 nm spectra, for all samples except S08. It is unclear why S08 does not show MoS_2 in its Raman spectrum when all other samples do.

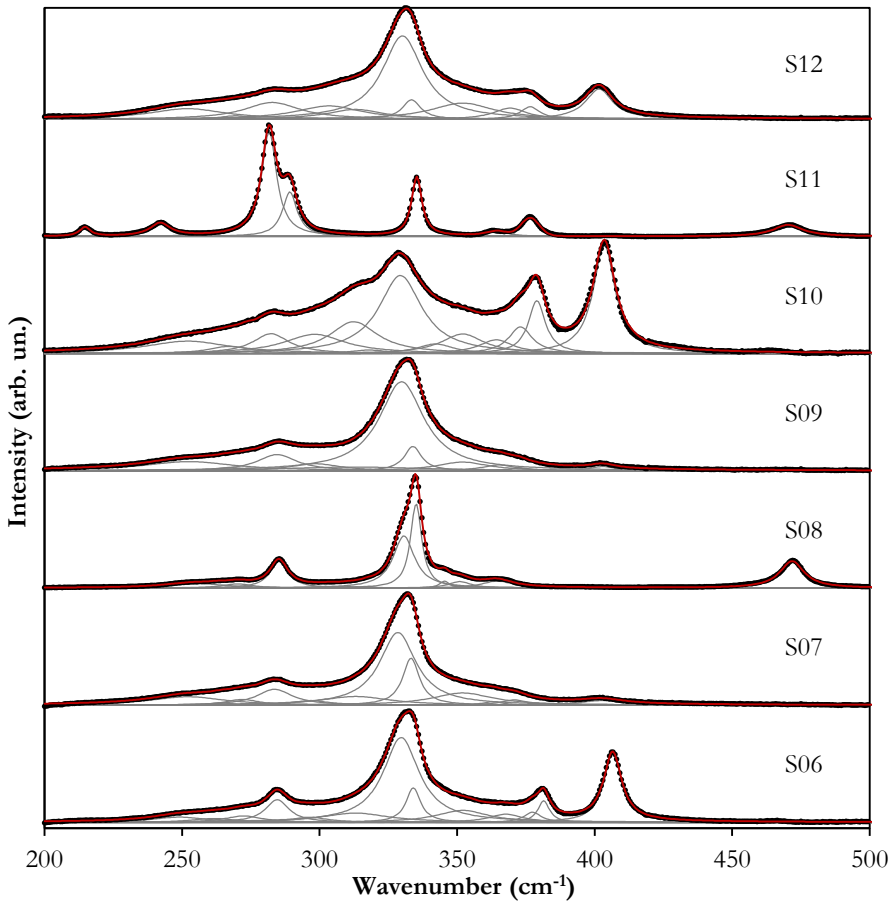

Figure 128: The Raman spectra for samples S06-12 using 488 nm excitation, with background removed and normalised, displaced vertically for clarity.

As for the bulk samples (see Section 6.8), there appears to be no correlation between the 'disordered kesterite' peak intensity at 332 cm^{-1} and the Q ratio of the two A mode peaks at 286 cm^{-1} and 300 cm^{-1},

$$Q = I_{286} / I_{300} , \tag{46}$$

and even no correlation between the two measurements of each parameter per sample, from the two excitation wavelengths used. This is shown in Figure 129 and again suggests either that they are both poor measures of disorder, or that there is significant uncertainty in the peak fitting.

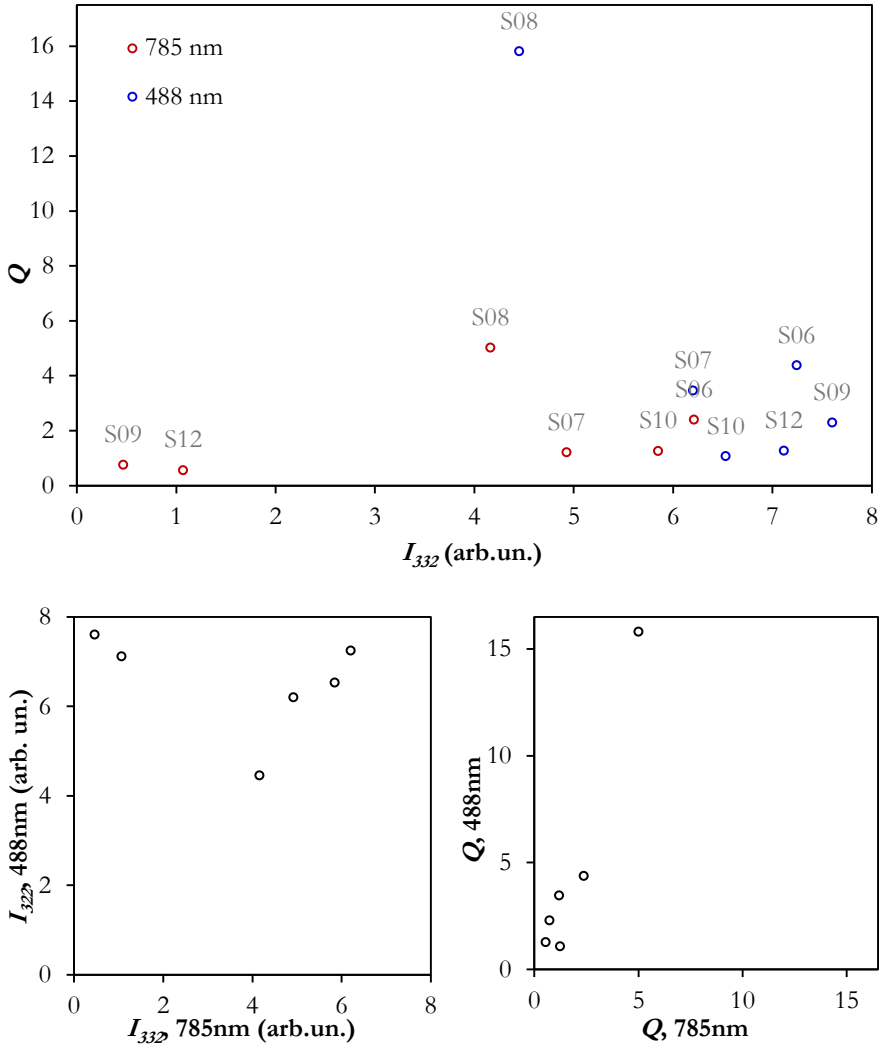

Figure 129: The lack of correlation between (top) the two measures of cation disorder from the Raman spectra for samples S06-S12: the intensity of the 'disordered kesterite' peak at 332 cm^{-1} and the Q ratio of the CZTS A modes at 286 and 300 cm^{-1}; and between the two measurements of each parameter from the two different wavelengths used: (bottom left) the intensity of the peak at 332 cm^{-1} and (bottom right) the Q ratio.

9.5.5. Photoluminescence spectroscopy

The photoluminescence spectra for the samples over a range of temperatures and laser powers are shown in Figure 130-Figure 136. The photoluminescence signal was observed to be highly consistent across the sample surfaces (except areas of delamination), suggesting good sample homogeneity.

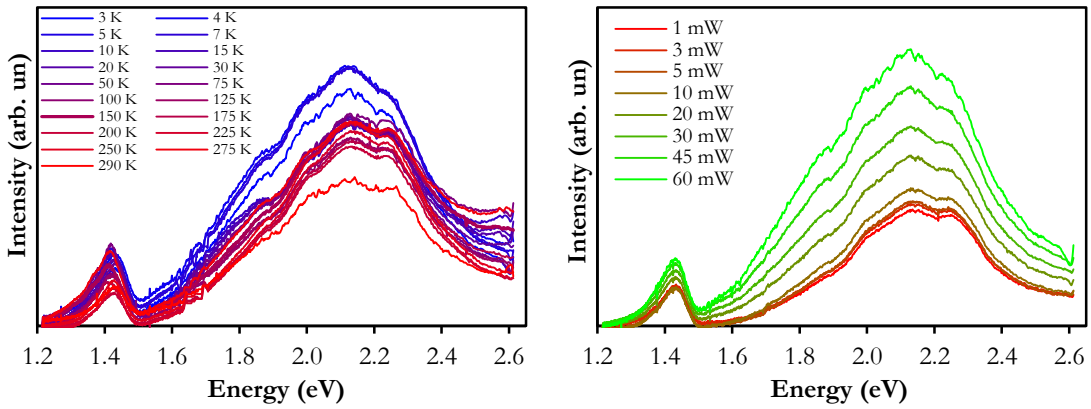

Figure 130: The photoluminescence spectra for S06 over a range of temperatures (left) and laser powers (right).

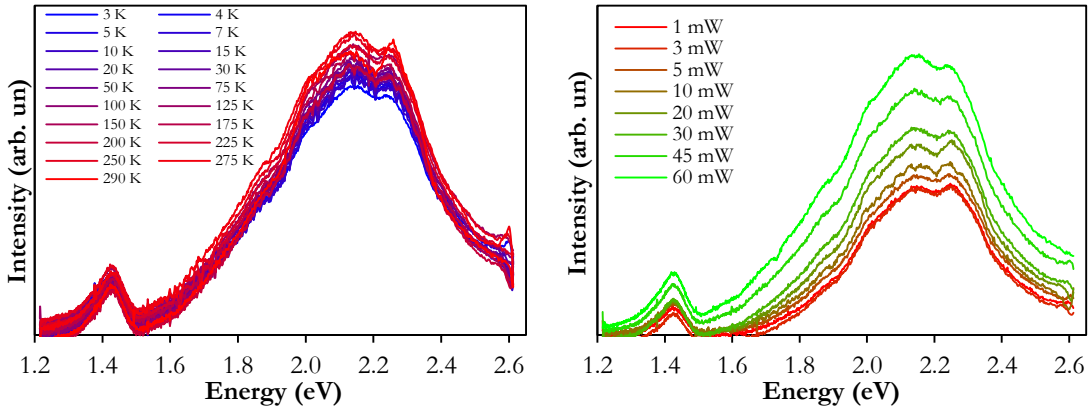

Figure 131: The photoluminescence spectra for S07 over a range of temperatures (left) and laser powers (right).

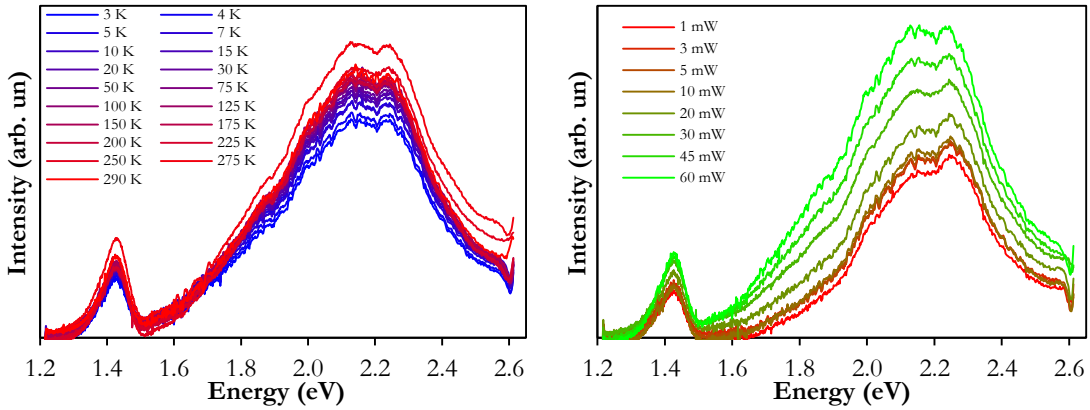

Figure 132: The photoluminescence spectra for S08 over a range of temperatures (left) and laser powers (right).

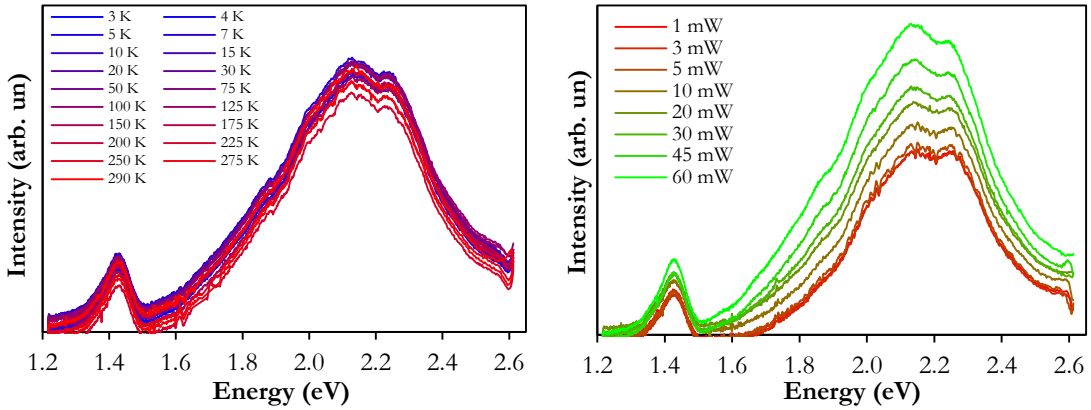

Figure 133: The photoluminescence spectra for S09 over a range of temperatures (left) and laser powers (right).

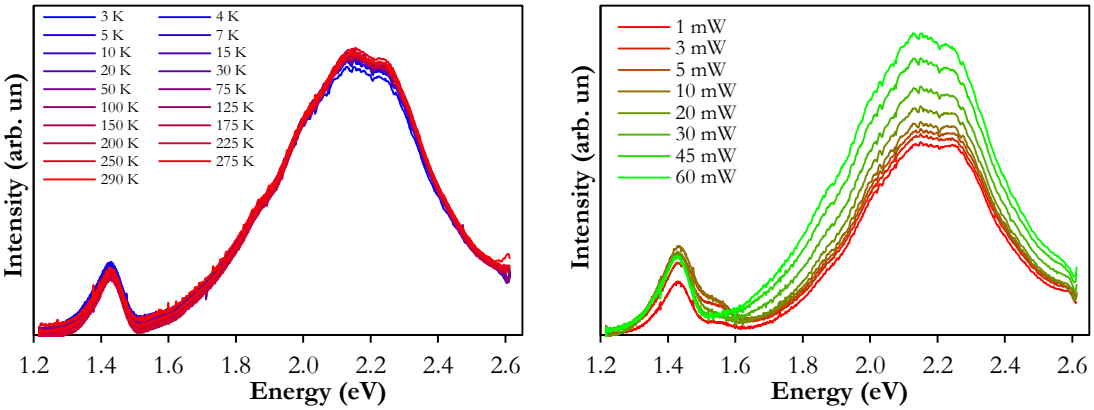

Figure 134: The photoluminescence spectra for S10 over a range of temperatures (left) and laser powers (right).

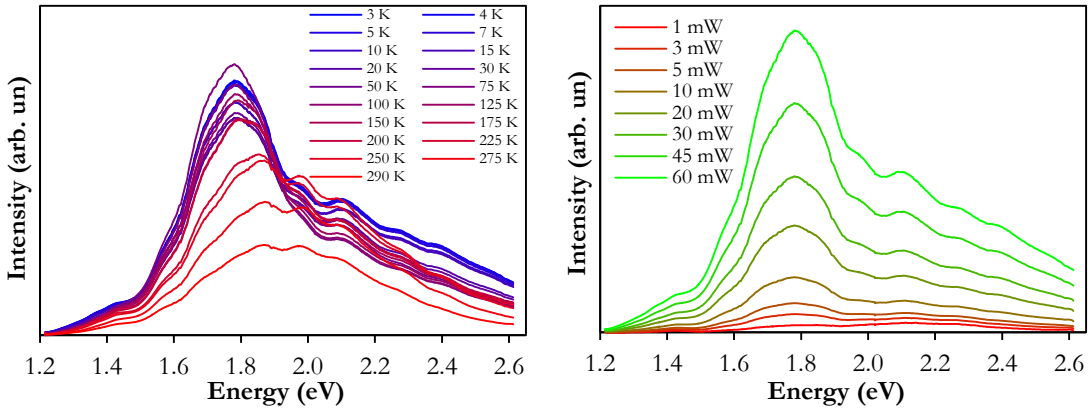

Figure 135: The photoluminescence spectra for S11 over a range of temperatures (left) and laser powers (right).

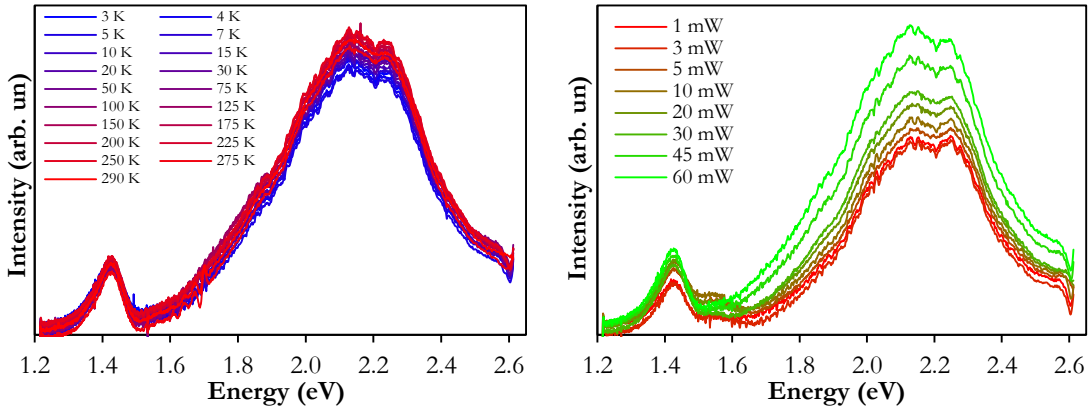

Figure 136: The photoluminescence spectra for S12 over a range of temperatures (left) and laser powers (right).

The spectra for all samples were accurately fitted using eleven Gaussian peaks, as depicted in Figure 137 for the 3 K spectra. The two lowest-energy peaks, at 1.39 and 1.43 eV, are identified with CZTS. It was concluded in Chapter 6 that the wide band of luminescence from 1.5 to 2.6 eV, which comprises the rest of the peaks, does not in fact correspond to the peaks reported for CZTS secondary phases in this range in previous academic literature. Nor is there any correlation between it and secondary phases identified in these samples by other methods here; i.e. it does not correspond to Cu_3SnS_4 nor any of the unidentified phases in S09, S10, or S12 because the luminescence band is dominant for all samples, not just those in which these phases are present. The source of this luminescence therefore remains a mystery. It may simply be an artefact of the photoluminescence system used rather than originating in the samples. This hypothesis is supported by the same peaks composing the spectra for S11, which features very little material at all and is composed almost entirely of different phases than the rest of the samples.

The temperature dependence of the intensity of the two photoluminescence peaks attributed to CZTS is plotted in Figure 138. Temperature has essentially no effect. Neither peak undergoes sufficient thermal quenching to be meaningfully fitted by any of the exponential models discussed in Section 5.10.2. This is because the luminescence signal for all samples was uniformly very weak at all temperatures (counting times up to two orders of magnitude larger than usual for the photoluminescence system were required to collect a reasonable signal-to-noise ratio). This could be because the usual radiative recombination routes in CZTS are fully quenched by dominant non-radiative recombination even at low temperature, demonstrating very poor sample quality.

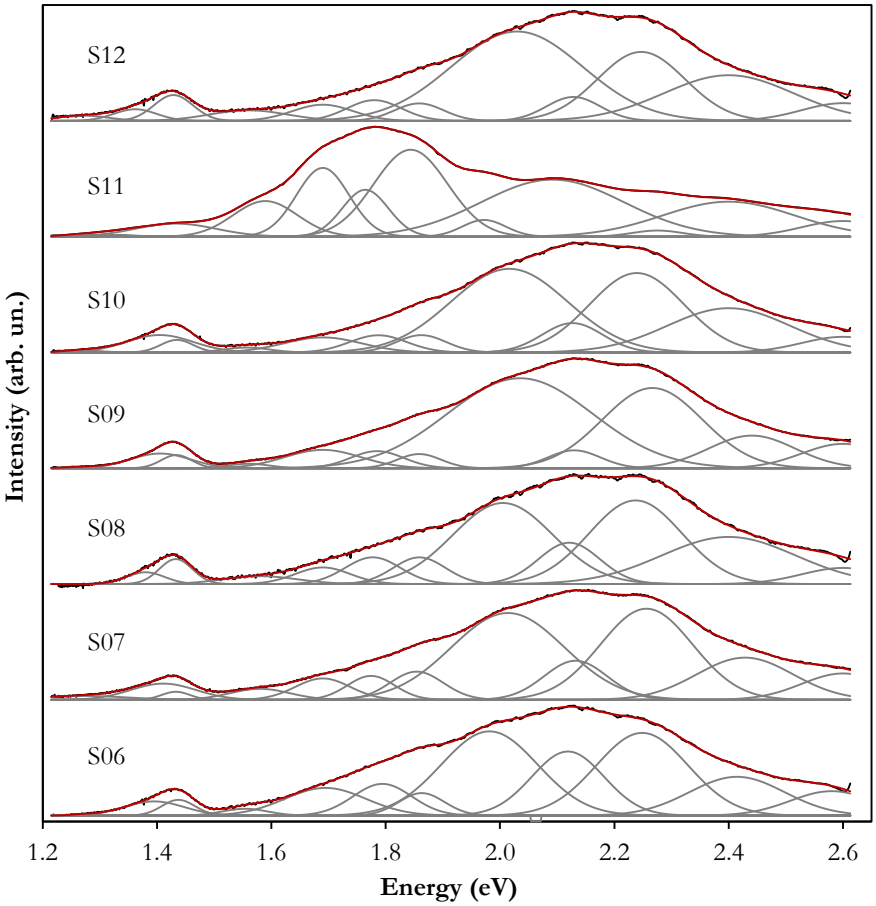

Figure 137: Fitted photoluminescence spectra for samples S06-12 at 3 K under 60 mW excitation at 375 nm.

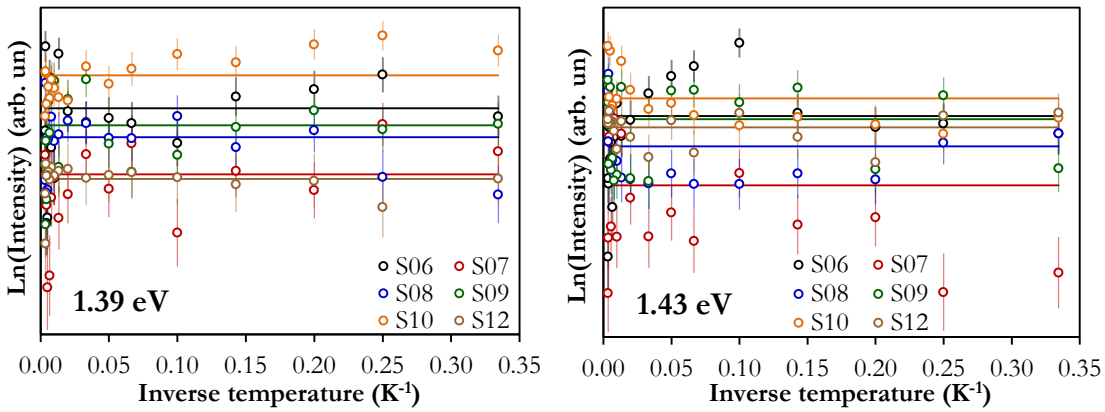

Figure 138: The temperature dependence of the intensity of the two photoluminescence peaks attributed to CZTS.

The temperature dependence of the energies of the two photoluminescence peaks attributed to CZTS is plotted in Figure 142. Again, temperature has no statistically significant effect.

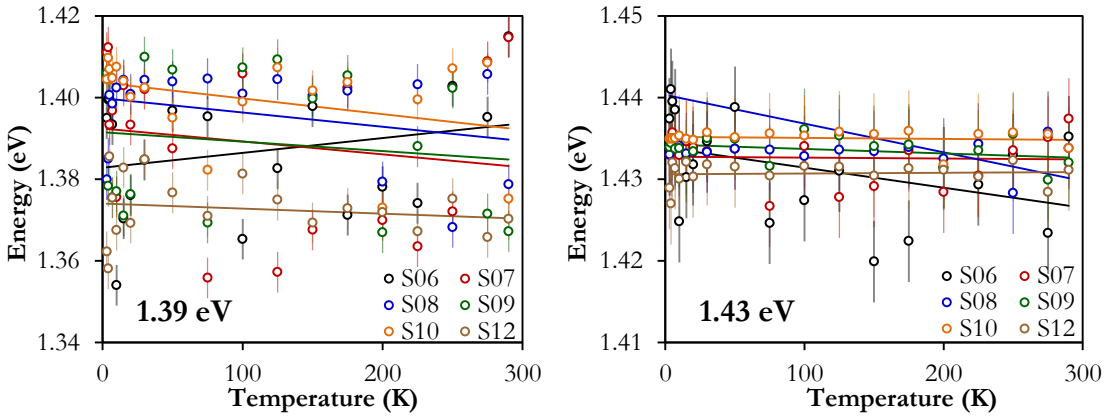

Figure 139: The temperature dependence of the energies of the two photoluminescence peaks attributed to CZTS.

The dependence on excitation laser power of the intensity of the two photoluminescence peaks attributed to CZTS is plotted in Figure 140. The *k* values (see Section 5.10.1) are 0.1 for the 1.39 eV peak and 0.2 for the 1.43 eV peak. These are lower than the typical values identified with particular radiative recombination channels, and so cannot be used to characterise the recombination routes responsible for the photoluminescence peaks. Instead, they confirm the dominance of non-radiative recombination in the samples.

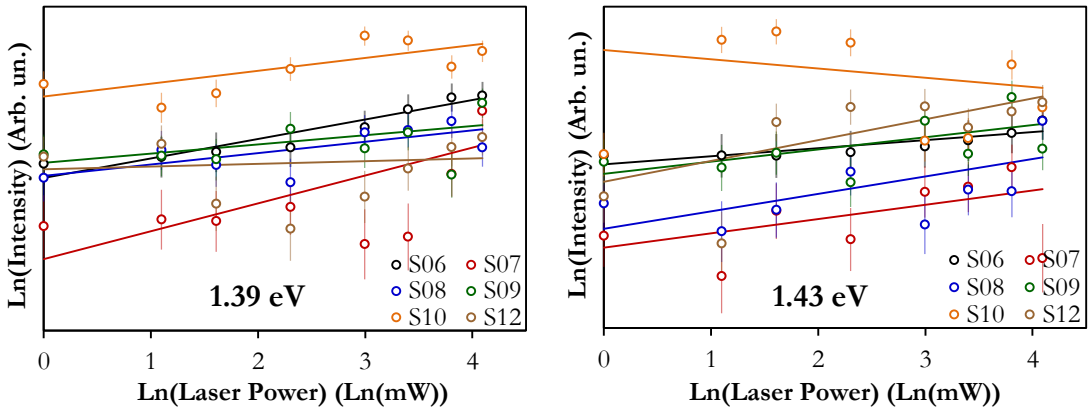

Figure 140: The dependence on excitation laser power of the intensity of the two photoluminescence peaks attributed to CZTS.

The dependence on excitation laser power of the energies of the two photoluminescence peaks attributed to CZTS is plotted in Figure 141. There is no statistically significant relationship.

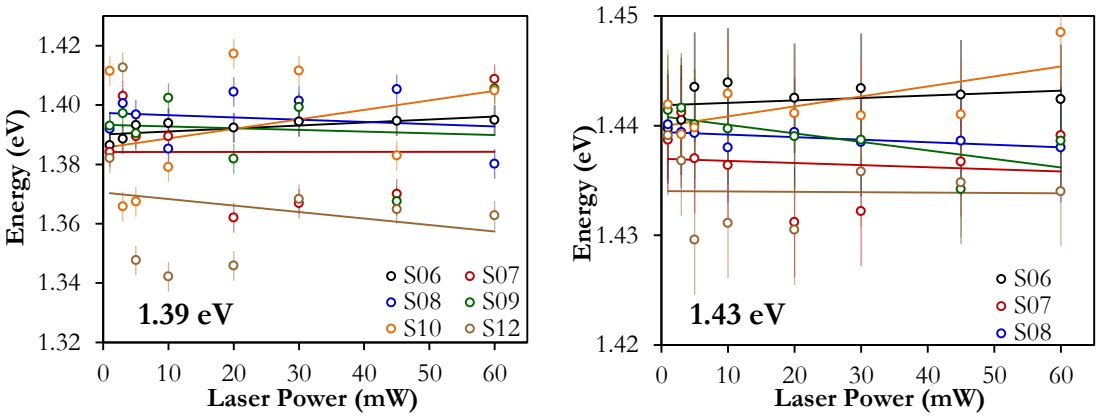

Figure 141: The dependence on excitation laser power of the energies of the two photoluminescence peaks attributed to CZTS.

9.6. Conclusions

A fabrication route for CZTS by sputtering followed by sulphurisation annealing has been established in Durham. A preliminary sulphurisation procedure, in situ in the sputtering chamber, was found to be inadequate, but a second, using a purpose-built sulphurisation chamber, was successful. Some reasonable films were produced over a range of compositions and their study has highlighted ways in which the fabrication route can now be developed.

9.6.1. The effects of precursor layer order

The main conclusion from the first batch of sputtered samples was that the initial sulphurisation route, in situ within the sputtering chamber, was ineffective, as all the samples were significantly S-poor. This is unsurprising as the sputtering chamber was designed to achieve and maintain an ultra-high vacuum rather than a constant reactive atmosphere. This led to the development of the separate sulphurisation system in the tube furnace used for the second batch of samples.

As the samples of the first batch were of such poor quality, no reliable conclusions could be drawn about the effect of precursor layer order.

9.6.2. The effects of elemental composition

The purpose-built sulphurisation system was more successful and produced samples containing the correct amount of sulphur and with significant CZTS phase presence. However, some samples experienced severe delamination and the crystallinity was very poor, so the sulphurisation process needs refining and optimising if it is to produce CZTS for high-efficiency photovoltaic cells. This will be the subject of future work.

It is notable that all the sample compositions migrated to a defect-complex-defined off-stoichiometric CZTS type. As no secondary phases were formed in any significant quantity, in samples S06, S07, and S08, this appears to have occurred solely through the loss of zinc and tin in those samples. This finding confirms the importance of these defect-complex-defined types in the formation and properties of CZTS.

XRD patterns for some of the samples feature a number of high-intensity unidentified peaks. From their occurrence in various combinations in each sample they can be grouped as five separate phases, none of which correspond to any materials that might be expected to be found in the samples. The identification of these phases could be a useful avenue of future research.

The secondary phases in these thin-film samples largely do not match those found in the bulk samples of comparable compositions reported in Chapter 6. Thin-film CZTS typically undergoes a shorter heat treatment than is required for bulk samples, and at a lower temperature, and so may not reach the equilibrium state. This emphasises that the fabrication route has a very significant effect on phase formation and that the most useful studies for informing the growth of CZTS for industrial photovoltaic application will therefore use a fabrication method suitable for that purpose.

As for the bulk samples (see Section 6.8), there appears to be no correlation between the 'disordered kesterite' Raman peak intensity at 332 cm^{-1} and the Q ratio of the two A mode peaks at 287 cm^{-1} and 300 cm^{-1}, which are commonly used as measures of crystal disorder in CZTS, nor even any correlation between the two measurements of each parameter per sample, from the two excitation wavelengths used. This again suggests either that they are

both poor measures of disorder, or that there is significant uncertainty in fitting Raman peaks that makes finding reliable values for them difficult.

Photoluminescence from the samples was very weak and was observed to be unaffected by temperature. It was therefore concluded that the usual radiative recombination routes in CZTS are fully quenched by dominant non-radiative recombination even at low temperatures in all the samples. This demonstrates very poor crystalline quality, although the specific non-radiative recombination channel that dominates could not be identified. The dependence of the luminescence on excitation laser power revealed no useful information, presumably also because of the lack of significant luminescence in general due to the dominance of non-radiative recombination.

Very little can be reliably concluded about the effect of composition from these samples, but it is notable that while no sample remained Cu-poor, the only Zn-rich one (S08) seemed to exhibit the best crystallinity, as it gave the narrowest Raman peaks, and was one of only two samples found to be phase-pure CZTS. This is consistent with the accepted empirical finding that Cu-poor, Zn-rich samples give the best photovoltaic performance.

In conclusion, a successful fabrication route for sputtered CZTS has been established, but it has not yet produced high-quality CZTS suitable for photovoltaic devices. Several avenues of research to improve the system have been identified, such as optimising the sulphurisation procedure to eliminate delamination and identifying the mysterious phases produced in some samples. This will be the subject of future work.

Chapter 10:

Conclusions

10.1. Introduction

The introductory chapters of this thesis attempted to make it very clear that the world needs solar electricity, that solar electricity is already well-established and growing exponentially, and that this growth is going to continue even without new photovoltaic technology to rival the dominance of silicon wafers. However, while most alternative photovoltaic materials such as CdTe and CIGS will ultimately have a limited impact because of problems with their raw materials, CZTS has the potential to lower the cost of solar electricity compared to silicon on a global scale, and to enable its application in a greater range of circumstances if deposited on thin, flexible substrates.

The main challenge that remains to be overcome for CZTS to be industrialised and contribute to the global move to sustainable energy is the large open-circuit voltage deficit commonly reported. The two largest contributing factors to this deficit are the CZTS-buffer interface and band gap fluctuations caused by point defects in the bulk material. Secondary phases in CZTS remain another major issue. The three key areas for current research to improve the performance of CZTS are therefore interface optimisation, defect characterisation and control, and phase stability.

This thesis aimed to contribute to the development of CZTS as a solar photovoltaic absorber by studying its material properties using the methods of experimental condensed matter physics. Sputtering followed by sulphurisation annealing was selected as the

deposition method for thin films to be used in photovoltaic cells because this has produced the best efficiency results so far, and is easily scaled to an industrial level once a fabrication route to give suitably high efficiencies has been developed.

One of the initial aims of this doctoral project was to carry out a comprehensively thorough study of all parameters involved in the sputtering and sulphurisation processes in order to find the optimum route for the fabrication of CZTS for industrial photovoltaic application. However, this became impossible due to the inability to fabricate thin-film samples for almost the entirety of the project because of equipment problems. Faults and breakdowns in the sputtering system, which was shared with many other users, and long delays in the development and installation of a sulphurisation system all extended for literally years. This caused some frustration.

Instead, most of the results presented in this thesis came from bulk samples produced by solid-state reaction, another fabrication method that was established, not without its own set of difficulties, in parallel to the sputtering route. These bulk samples were successfully studied to investigate phase and defect formation, in order to fulfil the other aim of this project: to achieve a fuller understanding of the material properties and mechanisms behind CZTS working as an absorber layer in solar cells. The results of these investigations have been reported as three chapters of this thesis, and will hopefully contribute to tackling the issue of low open-circuit voltage.

Sputtered thin films were eventually fabricated and a brief study of their properties has also been presented as a chapter of this thesis.

The main findings of each experimental chapter are summarised here.

10.2. Summary of conclusions

10.2.1. A structural and optoelectronic study of bulk CZTS

The effect of elemental composition on CZTS was studied by fabricating seven samples with different compositions in the region of the stoichiometric point. Several

optoelectronic and structural analysis techniques were used to successfully identify the secondary phases in the samples and to study their effects on some properties and behaviour of the CZTS phase itself.

Element loss from the samples during fabrication was quantified: 28 % of tin and 1.1 % of zinc was lost. These values allow future bulk samples to be manufactured with desired final compositions. It was also concluded that significant amounts of solid SnS and Zn(S) were present in the samples during sulphurisation and that the tin and zinc loss occurred slowly, as SnS and Zn(S) condensed on the ampoule wall.

The main assumption behind the quasi-ternary phase diagram, that complete stoichiometric sulphurisation always occurs, was shown to be incorrect, meaning that the currently accepted phase diagram does not correctly predict the secondary phases that will be formed for a given elemental composition.

Some trends in the dependence of secondary phases on composition were evident. ZnS is the most prevalent secondary phase, being found in four of the seven samples: all of the Zn-rich samples except one. The very Sn-poor samples were the only ones to form CuS; this implies that ternary or quaternary phases are energetically favourable to CuS, and so only when these cannot form due to a lack of tin does CuS form. However, the only ternary phase found, Cu_3SnS_4, was in only one sample, identified by being both one of the richest in tin (approximately stoichiometric) and Zn-poor. $Cu_4Sn_7S_{16}$ was found in both of the only samples not Sn-poor, suggesting it may be a more prevalent secondary phase than previously thought.

It was clearly found that multi-technique analysis is required to identify all secondary phases in CZTS. XRD remains the most successful, and has the advantage that it provides quantitative phase fractions (high-resolution anomalous XRD in particular is by far the best technique but not practical for large-scale studies of many samples). It is particularly notable that XRD was the most successful at identifying ZnS here, despite being widely accepted as unable to differentiate between this and CZTS with the resolution of standard diffractometers. However, other techniques are needed to confirm or rule out the presence of Cu_2SnS_3 and Cu_3SnS_4. Raman accomplishes this well, although multi-wavelength Raman analysis is required to identify many secondary phases (such as CuS, and $Cu_4Sn_7S_{16}$).

The CZTS phase in all samples was confirmed to form the kesterite crystal structure by ^{65}Cu SSNMR spectra showing the two distinct copper environments corresponding to the 2*a* and 2*c* lattice positions.

While Cu-Zn disorder is likely to be present in CZTS to some degree for all compositions, it was found using Raman and ^{65}Cu NMR to be drastically so for one sample in particular, with composition both very Cu-rich and Zn-poor.

However, while Raman is effective at qualitatively identifying Cu-Zn disorder, it was not found able to quantify it, as has been done in previous academic literature reports. Both the peak associated with the disordered kesterite phase and the *Q* factor (the ratio of intensities of two of the A mode peaks) have previously been presented as linearly related to an order parameter, but here they were found to correlate neither with each other, nor even with themselves when calculated using different excitation wavelengths.

Photoluminescence showed four separate peaks for CZTS, corresponding to three different recombination methods: band-to-impurity recombination (which shows separate peaks for recombination in disordered and ordered CZTS; in reality this emission probably occurs over the range between these two extremes), band-to-tail recombination involving fluctuating potential tail states on the valence band edge, and band-to-band recombination. The impurity involved in the first of these was found to have a defect level of 180 meV for ordered CZTS and was identified as the Cu_{Zn} antisite. Band-to-tail was found to be the dominant recombination method. The amplitude of the fluctuations in potential was calculated to be 100 meV. If such CZTS is used in solar cells, this is large enough to be responsible for a significant deficit in open-circuit voltage, which is known to severely limit the photovoltaic performance of CZTS.

10.2.2. A neutron diffraction study of CZTS phase transitions

Samples of CZTS with two compositions, Sn-poor, Cu-rich and Sn-poor, Zn-rich, were fabricated by solid-state reaction and their crystal structures were investigated using high-resolution neutron diffraction. The kesterite crystal structure was found to be adopted by both, with significant cation disorder. Contrary to almost all previous literature reports, which described complete order on the 2*a* site, these results demonstrate Zn_{Cu} occupancy

of the 2*a* site equal to the 2*c* site for a Sn-poor, Cu-rich composition, and higher than the 2*c* site for a Sn-poor, Zn-rich composition.

The dominant defect in the Cu-rich sample is Cu_{Zn}, and in the Zn-rich sample Zn_{Cu}, as expected. This supports the hypothesis that Cu-poor CZTS gives the best photovoltaic performance because it has a lower concentration of Cu_{Zn} defects. Contrary to expectations, the Cu-rich sample contains more Zn_{Sn} defects than Cu_{Sn} and the Zn-rich sample contains more Cu_{Sn} than Zn_{Sn}; both of these defects give trap levels deep in the band gap and so are detrimental to photovoltaic device performance.

Neither sample exhibits thermal expansion with increasing temperature below 50 K, and the *c* lattice parameter of the Cu-rich sample even shows slight negative thermal expansion

The order-disorder phase transition took place in the Cu-rich sample at 501 K and in the Zn-rich sample at 489 K, which are both lower than the previously reported temperatures. The transition occurred in both samples over a range of approximately 150 K. This is quite a large range, but could be artificially so because of insufficient equilibration time during the experiments. The transition occurred at a different temperature in each sample, which suggests that the transition mechanism is affected by elemental composition. This is important for the procedure of CZTS production for photovoltaic cells.

Another phase transition, from the tetragonal kesterite to the cubic sphalerite structure, was measured between 1250 and 1275 K in B21. This transition temperature is significantly higher than the value previously reported, which suggests that this transition is also affected by elemental composition.

10.2.3. An anomalous XRD study of off-stoichiometric CZTS types

Five samples of CZTS with different elemental compositions were fabricated by solid-state reaction. Their crystal structures were investigated using high-resolution anomalous X-ray diffraction. All the CZTS phases were concluded to form the kesterite crystal structure with high levels of cation disorder.

Two distinct phases of kesterite CZTS with slightly different lattice parameters (Δ~0.004 Å) and different elemental compositions were discovered to exist simultaneously in three of the samples. These are attributed to off-stoichiometric 'types' of CZTS defined by the prevalence of charge-neutral defect complexes, which have been reported previously.

Every CZTS phase was found to be of a specific CZTS type, and two new types are proposed here. These are G-type, in which [$2Cu_{Sn}^{3-} + Cu_{Zn}^{-} + Cu_{i}^{+} + 3V_{S}^{2+}$] defects dominate, and H-type, in which [$3S_{i}^{2-} + V_{Cu}^{-} + Zn_{Cu}^{+} + 2Sn_{Cu}^{3+}$] defects dominate. In both types, the large number of the defects mean that they probably do not form a single complex. The compositions of these types are portrayed in Figure 142.

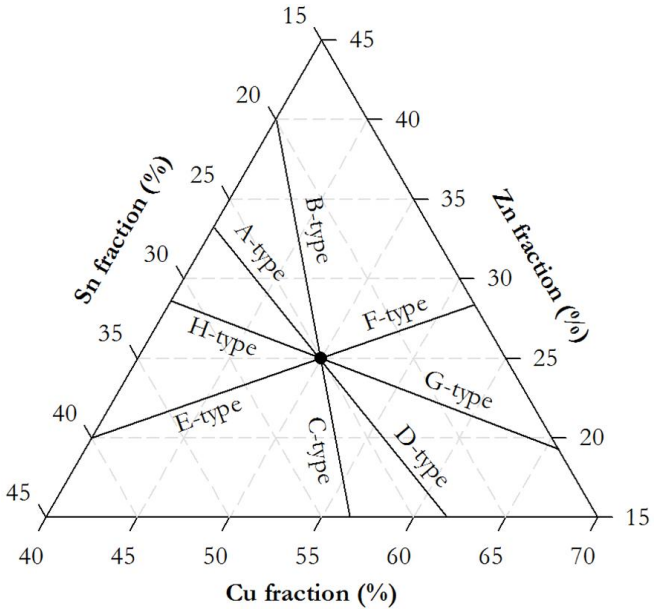

Figure 142: The off-stoichiometric CZTS types defined by the prevalence of different charge-neutral defect complexes.

In two of the three samples the two phases of CZTS converge to a single phase above the order-disorder phase transition, at 600 K. Irrespective of the number of phases and their type, all the samples feature greater disorder of copper and zinc at 600 K than at 300 K.

A mechanism of CZTS phase formation is proposed based on these results. During the high-temperature step of sample production a single phase of CZTS is usually formed first, determined by the energetic stability of the combination of that CZTS composition and any secondary phases. It is also possible that a mixture of two different CZTS types is

energetically favourable to a single CZTS phase. As the sample cools through the order-disorder transition, the ordering of the CZTS may cause different compositions, potentially defined by different defect complexes, to become energetically favourable. However, with the temperature too low to change the secondary phases present, the CZTS is confined by retaining a constant average composition. The result of the change in energetic favourability for a single phase of CZTS is therefore for it to separate into a mixture of separate grains of two different compositions.

This mechanism evidently has important implications for the design of the fabrication process of CZTS for application in solar photovoltaic cells. This work was only possible because of the high resolution of the I11 beamline of the Diamond Light Source, the highest resolution that has been used to investigate the crystal structure of CZTS. Therefore this is the first observation of this two-phase structure using diffraction.

10.2.4. A structural and optoelectronic study of sputtered thin-film CZTS

A fabrication route for sputtered CZTS has been established in Durham, and it was used to produce films over a range of composition for study as a parallel to the bulk samples studied in Chapter 6.

Some of the samples experienced severe delamination and the crystallinity was very poor, so the sulphurisation process needs refining and optimising if it is to produce CZTS for high-efficiency photovoltaic cells. This will be the subject of future work.

It is notable that all the sample compositions migrated to a defect-complex-defined off-stoichiometric CZTS type. This confirms the importance of these defect-complex-defined types in the formation and properties of CZTS. It appears that the formation of these types can occur solely through the loss of zinc and tin as well as by the formation of secondary phases.

XRD patterns for some of the samples feature a number of high-intensity unidentified peaks. From their occurrence in various combinations in each sample they can be grouped as five separate phases, none of which correspond to any materials that might be expected

to be found in the samples. The identification of these phases could be a useful avenue of future research.

The secondary phases in these thin-film samples largely do not match those found in the bulk samples of comparable compositions reported in Chapter 6. This emphasises that the fabrication route has a very significant effect on phase formation and that the most useful studies for informing the growth of CZTS for industrial photovoltaic application will therefore use a fabrication method suitable for that purpose.

As for the bulk samples (see Section 6.8), there appears to be no correlation between the 'disordered kesterite' Raman peak intensity at 332 cm^{-1} and the Q ratio of the two A mode peaks at 287 cm^{-1} and 300 cm^{-1}, which are commonly used as measures of crystal disorder in CZTS, nor even any correlation between the two measurements of each parameter per sample, from the two excitation wavelengths used. This again suggests either that they are both poor measures of disorder, or that there is significant uncertainty in fitting Raman peaks that makes finding reliable values for them difficult.

Photoluminescence from the samples was very weak and was observed to be unaffected by temperature. It was therefore concluded that the usual radiative recombination routes in CZTS are fully quenched by dominant non-radiative recombination even at low temperatures in all the samples. This demonstrates very poor crystalline quality, although the specific non-radiative recombination channel that dominates could not be identified. This presents another possible avenue of future study.

Very little can be reliably concluded about the effect of composition from these samples, but it is notable that while no sample remained Cu-poor, the only Zn-rich one seemed to exhibit the best crystallinity, as it gave the narrowest Raman peaks, and was one of only two samples found to be phase-pure CZTS. This is consistent with the accepted empirical finding that Cu-poor, Zn-rich samples give the best photovoltaic performance.

In conclusion, a successful fabrication route for sputtered CZTS has been established, but it has not yet produced high-quality CZTS suitable for photovoltaic devices. Several avenues of research to improve the system have been identified, such as optimising the

sulphurisation procedure to eliminate delamination and identifying the mysterious phases produced in some samples. This will be the subject of future work.

10.3. Future work on CZTS

There is much remaining to be understood in order to fabricate CZTS photovoltaic cells suitable for industrial deployment. The most important recommendations for future research are generally applicable, but often ignored. Experiments should ensure consistency and repeatability over a large number of results, and the effect of any parameter should be measured across the full range of relevant values, with a high sampling frequency so that the true behaviour can be determined rather than an incorrectly extrapolated or alias trend. Reporting a trend from two or three samples, or a record efficiency from an unreproducible device, is of less use. Some automation of sample production and analysis will be required to enable sufficiently detailed, high-quality experiments on a useful scale to become standard. These general recommendations for the improvement of CZTS research quality can be applied to the several concrete aspects of CZTS that require better understanding described here.

The quasi-ternary-phase diagram should be measured experimentally, for samples that have undergone a heat treatment relevant for device fabrication, with quantitative measurement of the phase fractions rather than merely an indication of their possible presence, and with a reasonably high resolution (e.g. every 1 % composition, which would require 496 distinct compositions to cover the area depicted in Figure 142, clearly requiring a degree of automation in fabrication and characterisation). Ideally, a quaternary phase diagram will be developed, which will extend the quasi-ternary diagram in a third dimension to include the sulphur fraction.

In order to aid quantitative phase identification, reliable and consistent reference spectra must be available. Spectra using multi-nuclear SSNMR (^{65}Cu, ^{67}Zn, and ^{119}Sn), multi-wavelength Raman (using e.g. 325, 488, 633, and 785 nm), and photoluminescence (at several excitation intensities) should be taken, at a consistent measurement temperature, for pure samples of all secondary phase materials possible in CZTS, with consistent measurement parameters to enable direct comparison. This amounts to producing more detailed and directly comparable versions of Figure 54-Figure 56 (SSNMR), Figure 58

(Raman), and Figure 59 (photoluminescence) in Chapter 5. This will then enable simultaneous computational fitting of phase fractions using all these techniques. Ideally, these baseline phase measurements will become standard when embarking on the use of any new equipment setup to study CZTS.

The phases and/or particular recombination mechanisms responsible for the photoluminescence observed at higher energies (~1.6-3.0 eV) should be identified. This photoluminescence is potentially a very useful tool for investigating phase presence, optical behaviour, and recombination channels in CZTS samples, but has yet to be utilised because its origin has not yet been convincingly identified.

Following the conclusions about phase formation reached in Chapter 8 of this thesis, further work investigating the reproducibility of phase formation at particular elemental compositions upon several cycles of heating and cooling would be enlightening. A theoretical study of the formation energy and energetic stability not just of individual point defect complexes, but of a multi-phase sample as a function of phases present, phase fractions, and defect complex density within the CZTS phase(s) would also be helpful. This more complex, overall stability is the real driver of phase formation and disorder in CZTS, and is therefore of critical importance in increasing the photovoltaic efficiency of CZTS solar cells.

This will also help to illuminate the effects of defects and defect complexes. Theoretical works on defects to date have largely remained quite separate from experimental works, preferring chemical potential as a variable rather than processing parameters or elemental composition, for example. Further experimental and theoretical work identifying the quantitative effects of every defect and defect complex as a function of its concentration will be required before a full understanding of their behaviour, and thus the exact optimum combination of densities of each defect type, is reached.

Once the effects of defects are more completely understood, the complete optimisation of all sputtering parameters originally planned for this doctoral project, but which remains to be undertaken because of prohibitive equipment problems, will be much easier, as it will be better informed by an understanding of the optimal CZTS state. If carried out thoroughly enough, this alone can be expected to yield significant gains in photovoltaic efficiency, as

many current recipes seem to have been developed from a mixture of approaches that worked well for other materials, often-contradictory studies of too-few samples, and chance, which is unlikely to have happened upon the global maximum in performance throughout the total parameter space. Understanding the physical mechanisms behind the effects of each parameter, rather than simply empirical trends of their effects on measurable quantities, will enable a much more intelligent and targeted approach to developing the optimum fabrication route. As mentioned previously, any such study that is to be really useful in informing an industrial growth process for CZTS solar cells needs to examine all parameters with enough samples to give a high resolution in observing trends, which are quite likely to not be linear over the possible range of values. Each parameter should also be investigated as a function of every other one, because their effects are of course highly related.

The non-CZTS layers of CZTS photovoltaic cells also require significant research attention. The CZTS-CdS interface in particular is known to be a significant contributor to the open-circuit voltage deficit, and so CdS should be either replaced by a different substance with better material properties and band alignment with CZTS, or optimised through deposition conditions, doping, or some other means. This will require a systematic and thorough search, probably theoretical at first, to select likely candidate materials or variations. A promising start would be a systematic literature or database search of all suitably abundant materials, similar to that carried out by Crovetto [142] to arrive at CeO_2 for testing. All the layers of the CZTS cell structure described in Section 3.8 should be optimised in this way.

It is of course also worth remembering that scaling up laboratory CZTS solar cell results to the industrial scale will itself require significant work. Different problems will be faced by fabrication on a continuous industrial production line than by research-scale techniques conducted on an ad hoc basis. It is difficult to predict exactly what these will be, but the equivalent processes for silicon, CdTe and CIGS can be learned from. It will undoubtedly be useful for CZTS researchers to have a reasonable knowledge of these historical scaling processes, and of industrial processing in general, to avoid research solutions being found that are unsuitable for industrial application.

Future CZTS research at Durham, which will continue with new students after this doctoral project, will involve developing the now established baseline procedure for the fabrication of sputtered CZTS to include all the device layers mentioned in Section 3.8 and create functioning solar cells. The process will also be improved by carrying out all the deposition and processing steps immediately successively, rather than with large delays in between due to equipment problems. It will remain to those who take up this work to decide on its future focus. Many of the above suggestions would provide a fruitful project in themselves.

In summary, much of the behaviour and properties of CZTS remains to be investigated. Much more rigour, in the form of more numerous samples, demonstrably repeatable results, and a more systematic approach, is needed in its study than has usually been found in published results to date (including, because of equipment problems, this thesis, much to its author's frustration). Hopefully future research will rectify this and result in the ascendance of CZTS to high photovoltaic efficiencies and a useful contribution to the global adoption of solar electricity.

10.4. The future of solar electricity

Realistically, the role of CZTS in the ultimate future of global solar power is not likely to be as a direct replacement for silicon cells. It is more likely to be in tandem cells with silicon, [616] on flexible substrates for specific uses, or in other novel applications. Silicon works very well, with a record efficiency over 26 %, and the price of silicon modules is now low enough for solar electricity to have reached grid parity in some areas of the world, and is continuing to drop. Silicon is therefore unlikely to be replaced as the dominant material for applications in which rigid modules in their current form are acceptable, such as utility-scale solar farms. The extra efficiency gained by multi-junction solar cells will make tandem silicon-CZTS cells very appealing, though, and so this synthesis of technologies, rather than competition between them, is likely to characterise the future of industrial solar electricity.

Additionally, single-junction CZTS cells will possibly find a role where aesthetic considerations will be important, such as domestic roof installations. Tesla's Solar Roof tiles, which maintain the efficiency of a more conventional module while being aesthetically

indistinguishable from a standard roof tile, represent the future direction of domestic installations, and show the domestic and industrial requirements beginning to diverge as solar electricity transitions from its infancy into a dominant force of the energy industry.

A useful analogy can be drawn to the development of computers. The first were expensive, had low capabilities, and were very unwieldy, taking up entire rooms, so were only used for very specific applications; just as the first solar panels were restricted to satellites or low-power requirements like calculators. The first revolution in computing came with the introduction of desktops, which were sufficiently convenient and cheap for individuals to own; these were impressive for their time, but ugly and not very powerful, like the rack-mounted solar panels first installed on roofs, which represent the current state of solar electricity. Desktops and laptops then developed into separate classes, catering to different needs: pure capability at the cheapest cost, or portable, robust, and easily integrated into everyday life. Both were slowly refined, increasing in power, and the latter came to be designed as desirable objects of beauty and convenience, rather than merely as functional office equipment. This represents the near future of solar electricity as photovoltaic tiles for domestic installation begin to diverge from conventional rack-mounted modules for utility-scale installations, and become fully integrated aesthetic design elements themselves.

With some imagination, the future development of solar can be extrapolated along the same lines. As laptops also gave rise to tablets and smartphones, making computing ability present in every aspect of modern life for a previously unimagined range of applications, so photovoltaic technology will become ubiquitous. Semi-transparent coatings could make every window a low-efficiency solar cell. Electric vehicles could be charged by the roads they drive on. Flexible, easily-applied technologies could mean passive charging of all electronic devices by their casings and every manmade environment. Augmented-reality technology giving real-time visual information overlays could be powered by photovoltaic clothing. The most exciting applications will no doubt be unimaginable today.

The prevention of the worst effects of climate change and making our management of the world sustainable will be important steps in the growth of humanity into a mature species completely in control of our environment and our effects on it.

However, while the possibilities for a future of unlimited, completely sustainable energy are exciting, the transition to such a futuristic world will not be direct, and certainly not quick. It will only happen over several decades, and only incrementally, in small steps such as the current transition from a central utility-dominated transmission and distribution grid to a smart grid designed for electricity prosumers, with production and some usage behaviour optimised for high-penetrations of solar and wind. The roll-out of energy storage will be the next step, and is already on the horizon with developments such as Tesla's Powerwall. The electrification of transport and heating/cooling will also be important steps in the not-too-distant future.

CZTS may well be an important part of the route to that future, and possibly even have its niche in such a world. Hopefully the work presented in this thesis has made a small contribution to such progress, and towards humanity's eventual responsible and sustainable management of our planet, and beyond.

Symbols and abbreviations

The symbols used throughout this thesis, their meanings, and their typical units are given in Table 43.

Symbol	Quantity	Typical units
a	Lattice parameter	nm
A	(1) Area	(1) cm^2
	(2) Diode ideality factor	(2) -
	(3) Constant of proportionality	(3) -
	(4) Amplitude	(4) Various
a_0	The Bohr radius, 0.529 Å	Å
B_0, B_1	Magnitude of applied magnetic fields	T
c	Lattice parameter	nm
C	Capacitance	F
C_p	Specific heat capacity	$J \cdot mol^{-1} \cdot K^{-1}$
d	Film thickness	nm
D	Diffusivity	$m^2 \cdot s^{-1}$
d_{hkl}	Atomic planar spacing of the (hkl) plane	Å
e	The elementary charge, 1.6×10^{-19} C	C
E	Energy	eV
E_0	Zero-phonon energy	eV
E_1, E_2	Thermal activation energies associated with recombination	eV
E_a	Thermal activation energy	eV
E_C	Conduction band edge	eV
E_F	Equilibrium Fermi level	eV
E_g	Band gap energy	eV
E_i	Intrinsic Fermi level	eV
E_V	Valence band edge	eV
f	(1) Frequency	(1) Hz
	(2) Scattering form factor	(2) -
f'	Anomalous scattering form factor magnitude correction	-
f''	Anomalous scattering form factor phase correction	-
f_0	Uncorrected scattering form factor	-
FF	Fill factor	%
F_{hkl}	X-ray structure factor	-
g	Radiative recombination efficiency	-

Symbol	Quantity	Typical units
G	(1) Shear modulus	(1) GPa
	(2) Goodness of fit	(2) -
h	(1) The Planck constant, 6.62×10^{-34} J·s	(1) J·s
	(2) Miller index	(2) -
ħ	The reduced Planck constant, 1.05×10^{-34} J·s	J·s
I	(1) Current	(1) A
	(2) Intensity	(2) $W \cdot m^{-2}$
I_0	(1) Saturation current	(1) A
	(2) Factor of the dependence of photoluminescence on laser power	(2) -
	(2) Intensity at 0 K	(3) -
I_L	Photocurrent	A
I_{MP}	Maximum-power current	A
I_{SC}	Short-circuit current	A
k	Miller index	-
k	Exponent of dependence of photoluminescence on laser power	-
K	(1) Bulk modulus	(1) GPa
	(2) A shape factor for determining grain size (0.94 for spherical grains)	(2) -
k_B	The Boltzmann constant, 1.38×10^{-23} $J \cdot K^{-1}$	$J \cdot K^{-1}$
l	Miller index	-
L	(1) Minority carrier diffusion length	(1) nm
	(2) Grain size	(2) nm
	(3) Distance from source	(3) m
	(4) Laser power	(4) W
LCOE	Levelised cost of electricity	$\$ \cdot kWh^{-1}$
m	Mass	kg
m_e	The mass of an electron, $9.109\ 10^{-31}$ kg	kg
m_h	Hole effective mass	kg
m_m	Molecular mass	u
m_n	The mass of a neutron, 1.675×10^{-27} kg	-
m_r	Reduced mass	kg
m_s	Spin quantum number	-
M	(1) Atomic mass	(1) u
	(2) Difference between calculated and observed diffraction patterns	(2) -
n	(1) Refractive index	(1) -
	(2) Free electron density	(2) cm^{-3}
	(3) Number density	(3) cm^{-3}
	(4) Order of diffraction	(4) -
	(5) Phonon occupation number	(5) -
N	Number of data points	-

Symbol	Quantity	Typical units
N_a	Acceptor concentration	cm^{-3}
N_A	The Avogadro number, 6.02×10^{23} mol^{-1}	mol^{-1}
N_d	Donor concentration	cm^{-3}
N_T	Total charged impurity concentration	cm^{-3}
p	Hole density	cm^{-3}
Q	(1) Charge (2) Ratio of the CZTS Raman peak intensities at 285 cm^{-1} and 301 cm^{-1}	(1) C (2) -
r_D	Debye screening radius	nm
r_e	The classical radius of an electron, 2.82×10^{-9} m	m
R	(1) Reflectance (2) Resistance	- Ω
R_p	Crystallographic profile *R* factor	-
R_S	Series resistance	$\Omega \cdot cm^2$
R_{Sh}	Shunt resistance	$\Omega \cdot cm^2$
R_{wp}	Weighted crystallographic profile *R* factor	-
S	(1) Crystalline order parameter (2) Huang-Rhys parameter: number of phonons involved in a transition	(1) - (2) -
t	(1) Time	(1) s
T	(1) Temperature (2) Transmittance	(1) K (2) -
T_C	Critical temperature of a phase transition	K
T_M	Melting temperature	K
u	The atomic mass unit, 1.66×10^{-27} kg	kg
v	Speed	$m \cdot s^{-1}$
V	Electrostatic potential (i.e. voltage)	V
v_s	Speed of sound	$m \cdot s^{-1}$
V_B	Bias voltage	V
V_{bi}	Built in potential difference of a p-n junction	V
V_{MP}	Maximum-power voltage	V
V_{OC}	Open-circuit voltage	V
w	(1) Total width of the depletion region of a p-n junction (2) Temperature range of a phase transition	(1) nm (2) -
W	Peak width (full width at half maximum intensity)	Various
W_n	Work function of the n-type region of a p-n junction	eV
W_p	Work function of the p-type region of a p-n junction	eV
x	(1) Position (2) Fractional position along the *a* lattice parameter	(1) m (2) -
x_n	Width of the n-type region of a p-n junction	nm
x_p	Width of the p-type region of a p-n junction	nm

Symbol	Quantity	Typical units
y	Fractional position along the *b* lattice parameter	-
y_{calc}	Calculated diffraction intensity	-
y_{obs}	Observed diffraction intensity	-
Y	Young modulus	GPa
z	Fractional position along the *c* lattice parameter	-
Z	Atomic number	-
a	(1) Absorption coefficient	(1) cm^{-1}
	(2) Lattice angle	(2) °
a_1, a_2	Relative degeneracies of the states corresponding to E_1 & E_2	-
β	Lattice angle	°
γ	(1) Lattice angle	(1) °
	(2) Potential fluctuation amplitude	(2) eV
	(3) Gyromagnetic ratio	(3) -
Γ	Raman peak width	cm^{-1}
δ	NMR chemical shift	ppm
ε	Dielectric permittivity	$F \cdot m^{-1}$
ε_0	The vacuum permittivity, 8.85×10^{-12} $F \cdot m^{-1}$	$F \cdot m^{-1}$
ε_n	Permittivity of the n-type region of a p-n junction	$F \cdot m^{-1}$
ε_p	Permittivity of the p-type region of a p-n junction	$F \cdot m^{-1}$
η	Efficiency	%
θ	Angle	°
θ_C	Critical angle for total reflection	°
θ_D	Debye temperature	K
θ_m	The magic angle of NMR MAS, 54.74 ° (defined by $\cos^2(\theta_m) = ⅓$)	°
κ	Thermal conductivity	$W \cdot m^{-1} \cdot K^{-1}$
λ	Wavelength	nm
λ_D	Debye screening length	nm
μ	(1) Minority carrier mobility	(1) $cm^2 \cdot V^{-1} \cdot s^{-1}$
	(2) Nuclear magnetic moment	(2) $J \cdot T^{-1}$
ρ	(1) Charge density	(1) $C \cdot m^{-3}$
	(2) Mass density	(2) $kg \cdot m^{-3}$
σ	(1) Electrical conductivity	(1) $S \cdot cm^{-1}$
	(2) Uncertainty on a measured value	(2) Same as value
τ	(1) Minority carrier lifetime	(1) s
	(2) Torque	(2) N·m

Symbol	Quantity	Typical units
$\chi 2$	Pearson chi-squared test statistic	-
ω	(1) Wave number	(1) cm^{-1}
	(2) Phonon frequency	(2) radians·s^{-1}
ω_0	Larmor frequency	radians·s^{-1}
ω_p	Wave number of a Raman peak	cm^{-1}

Table 43: The symbols used throughout this thesis, their meanings, and units.

The abbreviations used throughout this thesis are explained in Table 44.

Abbreviation	Meaning
AC	Alternating current
AFOLU	Agriculture, forestry, and other land use
AM	Air mass
BAU	Business as usual
BB	Band bending
BSE	Backscattered electron
CBO	Conduction band offset
CLZTS	Dicopper-lithium zinc tin tetrasulphide, $(Cu_{1-x}Li_x)_2ZnSnS_4$
CSZTS	Dicopper-silver zinc tin tetrasulphide, $(Cu_{1-x}Ag_x)_2ZnSnS_4$
CTS	Dicopper tin trisulphide, Cu_2SnS_3
CZCTS	Dicopper zinc-cadmium tin tetrasulphide, $Cu_2Zn_{1-x}Cd_xSnS_4$
CZITS	Dicopper zinc-iron tin tetrasulphide, $Cu_2Zn_{1-x}Fe_xSnS_4$
CZTGSSe	Dicopper zinc tin-germanium tetrasulphide-selenide, $Cu_2ZnSn_{1-y}Ge_y(S_{1-x}Se_x)_4$
CZTS	Dicopper zinc tin tetrasulphide, Cu_2ZnSnS_4
CZTSe	Dicopper zinc tin tetraselenide, $Cu_2ZnSnSe_4$
CZTSSe	Dicopper zinc tin tetrasulphide-selenide, $Cu_2ZnSn(S_{1-x}Se_x)_4$
COP	Conference of the Parties of the UNFCCC
CSP	Concentrating solar power
DC	Direct current
DSC	Dye-sensitised solar cell
CIGS	Copper indium-gallium diselenide, $CuIn_xGa_{1-x}Se_2$
CIS	Copper indium diselenide, $CuInS_2$
EDX	Energy-dispersive X-ray spectroscopy
EU	European Union
FF	Fill factor
FIB	Focused ion beam
GDP	Gross domestic product
ICPMS	Inductively coupled mass spectrometry
IEA	International Energy Agency

Abbreviation	Meaning
INDC	Intended nationally determined contribution to limiting climate change
ITO	Indium tin oxide
LCOE	Levelised cost of electricity
MAS	Magic-angle spinning
NMR	Nuclear magnetic resonance
NREL	United States of America National Renewable Energy Laboratory
PERC	Passivated emitter rear contact
PMCA	Primitive mixed CuAu-like (crystal structure)
RF	Radio frequency
SE	Secondary electron
SEM	Scanning electron microscope/microscopy
TCO	Transparent conducting oxide
TOF	Time of flight
UK	United Kingdom of Great Britain and Northern Ireland
UN	United Nations
UNFCCC	United Nations Framework Convention on Climate Change
USA	United States of America
VBO	Valence band offset
XRD	X-ray diffraction
XRR	X-ray reflectivity

Table 44: The abbreviations used throughout this thesis and their meanings.

References

1 C.J. Bosson et al. 'Crystal structure and cation disorder in bulk Cu_2ZnSnS_4 using neutron diffraction and X-ray anomalous scattering'. *Proceedings of the 43rd IEEE Photovoltaic Specialists Conference,* p.0405, (2016). DOI: 10.1109/pvsc.2016.7749621.

2 C.J. Bosson et al. 'Cation disorder and phase transitions in the structurally complex solar cell material Cu_2ZnSnS_4'. *Journal of Materials Chemistry A* **5**, p.16672, (2017). DOI: 10.1039/c7ta03603e.

3 C.J. Bosson et al. 'Using high-resolution anomalous-scattering X-ray diffraction to observe off-stoichiometric Cu_2ZnSnS_4 crystal structures'. *Proceedings of the 44th IEEE Photovoltaic Specialists Conference,* (2017).

4 C.J. Bosson et al. 'Polymorphism in Cu_2ZnSnS_4 and new off-stoichiometric crystal structure types'. *Chemistry of Materials* **29** (22), p.9829, (2017). DOI: 10.1021/acs.chemmater.7b04010.

5 'Photovoltaics Report (July 2017)'. Fraunhofer Institute for Solar Energy, (2017).

6 'Climate Change Fifth Assessment Synthesis Report 2014'. UN Intergovernmental Panel on Climate Change, (2014).

7 N. Stern et al. 'The Stern Review: The Economics of Climate Change (Executive Summary)'. (2006).

8 'Technology Roadmap for Solar Photovoltaic Energy 2014'. International Energy Agency, (2014).

9 'Global Land-Ocean Temperature Index'. NASA's Goddard Institute for Space Studies, (2017).

10 'Global Health Risks: Mortality and Burden of Disease Attributable to Selected Major Risks'. UN World Health Organisation, (2009).

11 D. MacKay. 'Sustainable Energy Without the Hot Air'. UIT Cambridge, (2008).

12 J.M. Barnola et al. 'Historical CO_2 Record From the Vostok Ice Core'. Carbon Dioxide Information Analysis Center, Oak Ridge National Laboratory, USA Department of Energy, (2003).

13 E. Monnin et al. 'EPICA Dome C Ice Core High Resolution Holocene and Transition CO_2 Data'. IGBP PAGES, World Data Center for Paleoclimatology, & NOAA NGDC Paleoclimatology Program, Data Contribution Series # 2004-055, (2004).

14 D.M. Etheridge et al. 'Law Dome Atmospheric CO_2 Data'. IGBP PAGES, World Data Center for Paleoclimatology, & NOAA NGDC Paleoclimatology Program, Data Contribution Series # 2001-083, (2001).

15 P. Tans & R. Keeling. 'Trends in Atmospheric Carbon Dioxide at Mauna Loa'. NOAA ESRL & Scripps Institution of Oceanography, (2016).

16 'Tracking Clean Energy Progress 2017'. International Energy Agency, (2017).

17 'The Emissions Gap Report 2016'. UN Environment Programme, (2016).

18 'Energy Technology Perspectives 2017 (Executive Summary)'. International Energy Agency, (2017).

19 'Global Electric Vehicles Outlook 2017'. International Energy Agency, (2017).

20 'Emission Database for Global Atmospheric Research (EDGAR) v4.3.2'. European Commission Joint Research Centre, (2016).

21 'Trends in Global CO_2 Emissions 2016'. EU Commission's Joint Research Centre, (2016).

22 'Key World Energy Statistics 2017'. International Energy Agency, (2017).

23 'Statistical Review of World Energy 2017'. BP, (2017).

24 K. Zweibel. 'The Terawatt Challenge for Thin Film Photovoltaics'. USA National Renewable Energy Laboratory, (2005).

25 'Snapshot of Global Photovoltaic Markets 2016'. International Energy Agency, (2016).

26 S. Shafiee & E. Topal. 'When will fossil fuel reserves be diminished?'. *Energy Policy* **37** (1), p.181, (2009). DOI: 10.1016/j.enpol.2008.08.016.

27 B. Kruyt et al. 'Indicators for energy security'. *Energy Policy* **37** (6), p.2166, (2009). DOI: 10.1016/j.enpol.2009.02.006.

28 'Kyoto Protocol'. UN Framework Convention on Climate Change, (1997).

29 'Copenhagen Accord'. UN Framework Convention on Climate Change, (2009).

30 'Paris Agreement'. UN Framework Convention on Climate Change, (2015).

31 'Energy Matters'. International Energy Agency, (2015).

32 'Track the Energy Transition'. International Energy Agency, (2015).

33 'World Energy Outlook 2016 (Executive Summary)'. International Energy Agency, (2016).

34 'Annual Energy Outlook 2017'. USA Energy Information Administration, (2017).

35 'A Strategic Research Agenda for Photovoltaic Solar Energy Technology'. EU Photovoltaic Technology Platform, (2007).

36 'Energy Barometer 2017'. Energy Institute, (2017).

37 L.M. Peter. 'Towards sustainable photovoltaics: the search for new materials'. *Philosophical Transactions of the Royal Society A: Mathematical, Physical and Engineering Sciences* **369** (1942), p.1840, (2011). DOI: 10.1098/rsta.2010.0348.

38 'Global Market Outlook for Solar Power 2017-2021'. SolarPower Europe, (2017).

39 'English Housing Survey Headline Report 2015-16'. UK Department for Communities and Local Government, (2016).

40 'A Buyer's Guide to Solar Electricity Panels'. Energy Saving Trust, (2012).

41 'National Electricity and Gas Consumption Statistics 2016'. UK Department for Business, Energy, and Industrial Strategy, (2016).

42 'Energy from the Desert (Executive Summary)'. International Energy Agency, (2015).

43 'Trends in Photovoltaic Applications 2016'. International Energy Agency, (2016).

44 'Unlocking the Sunbelt Potential of Photovoltaics'. European Photovoltaic Industry Association, (2011).

45 D. Faiman. 'Concerning the global-scale introduction of renewable energies: Technical and economic challenges'. *MRS Energy & Sustainability* **1**, p.1, (2014). DOI: 10.1557/mre.2014.8.

46 'Building-Integrated Photovoltaics (BIPV) in the Residential Sector: An Analysis of Installed Rooftop System Prices'. USA National Renewable Energy Laboratory, (2011).

47 'Levelised Cost and Levelised Avoided Cost of New Generation Resources 2017'. USA Energy Information Administration, (2017).

48 'Solar Photovoltaics Competing in the Energy Sector: On the Road to Competitiveness'. European Photovoltaic Inductry Association, (2011).

49 'US Solar Photovoltaic System Cost Benchmark: Q1 2017'. USA National Renewable Enerby Laboratory, (2017).

50 C. Candelise, M. Winskel, & R.J.K. Gross. 'The dynamics of solar photovoltaic costs and prices as a challenge for technology forecasting'. *Renewable and Sustainable Energy Reviews* **26**, p.96, (2013). DOI: 10.1016/j.rser.2013.05.012.

51 'Connecting the Sun: Solar Photovoltaics on the Road to Large-Scale Grid Integration'. European Photovoltaic Industry Association, (2012).

52 'Renewables Global Status Report 2017'. Ren21, (2017).

53 'SunShot Vision Study'. USA Department of Energy, (2012).

54 'Next Generation Wind and Solar Power'. International Energy Agency, (2016).

55 'Status of Power System Transformation 2017 (Summary for Policy Makers)'. International Energy Agency, (2017).

56 D.K. Schroder. 'Semiconductor Material and Device Characterisation', 3rd Edn. Wiley, (2006).

57 F. Urbach. 'The long-wavelength edge of photographic sensitivity and of the electronic absorption of solids'. *Physical Review* **92** (5), p.1324, (1953). DOI: 10.1103/physrev.92.1324.

58 A.E. Becquerel. 'Mémoire sur les effets électriques produits sous l'influence des rayons solaires'. *Les Comptes Rendu de l'Academie des Sciences* **9**, p.561, (1839).

59 W. Smith. 'Effect of light on selenium during the passage of an electric current'. *Nature* **7** (173), p.303, (1873). DOI: 10.1038/007303e0.

60 E. Weston. Patent: 'Art of utilising solar radiant energy'. Patent No. US389125 A, USA, (1888).

61 R.L. Anderson. 'Experiments on Ge-GaAs heterojunctions'. *Solid-State Electronics* **5** (5), p.341, (1962). DOI: 10.1016/0038-1101(62)90115-6.

62 J.R. Hook & H.E. Hall. 'Solid State Physics'. Wiley, (2003).

63 J. Nelson. 'The Physics of Solar Cells'. Imperial College Press, (2004).

64 A. Luque & S. Hegedus. 'Handbook of Photovoltaic Science and Engineering'. Wiley, (2006).

65 P. Würfel. 'Physics of Solar Cells From Basic Principles to Advanced Concepts'. Wiley, (2009).

66 'ASTM Standard Extraterrestrial Reference Spectrum E-490-00'. American Society for Testing and Materials, (2000).

67 'ASTM Standard Extraterrestrial Reference Spectrum ASTM G173-03'. American Society for Testing and Materials, (2003).

68 W. Shockley & H.J. Queisser. 'Detailed balance limit of efficiency of p-n junction solar cells'. *Journal of Applied Physics* **32** (3), p.510, (1961). DOI: 10.1063/1.1736034.

69 R.E. Treharne. 'RF Magnetron Sputtering of Transparent Conducting Oxides and CdTe/CdS Solar Cells'. PhD thesis, University of Durham, Department of Physics, (2011).

70 C.A. Nelson, N.R. Monahan, & X.Y. Zhu. 'Exceeding the Shockley-Queisser limit in solar energy conversion'. *Energy & Environmental Science* **6** (12), p.3508, (2013). DOI: 10.1039/c3ee42098a.

71 W. Ki & H.W. Hillhouse. 'Earth-abundant element photovoltaics directly from soluble precursors with high yield using a non-toxic solvent'. *Advanced Energy Materials* **1** (5), p.732, (2011). DOI: 10.1002/aenm.201100140.

72 X. Sheng, L.Z. Broderick, & L.C. Kimerling. 'Photonic crystal structures for light trapping in thin film Si solar cells: Modeling, process and optimisations'. *Optics Communications* **314**, p.41, (2014). DOI: 10.1016/j.optcom.2013.07.085.

73 R.R. King et al. '40 % efficient metamorphic GaInP/GaInAs/Ge multijunction solar cells'. *Applied Physics Letters* **90** (18), p.183516.1, (2007). DOI: 10.1063/1.2734507.

74 M.A. Green. 'Third generation photovoltaics: Ultra-high conversion efficiency at low cost'. *Progress in Photovoltaics: Research and Applications* **9** (2), p.123, (2001). DOI: 10.1002/pip.360.

75 M.C. Hanna & A.J. Nozik. 'Solar conversion efficiency of photovoltaic and photoelectrolysis cells with carrier multiplication absorbers'. *Journal of Applied Physics* **100** (7), p.074510.1, (2006). DOI: 10.1063/1.2356795.

76 K. Tanabe. 'A review of ultrahigh efficiency III-V semiconductor compound solar cells: Multijunction tandem, lower dimensional, photonic up/down conversion and plasmonic nanometallic structures'. *Energies* **2** (3), p.504, (2009). DOI: 10.3390/en20300504.

77 H.J. Queisser. 'Multiple carrier generation in solar cells'. *Solar Energy Materials and Solar Cells* **94** (11), p.1927, (2010). DOI: 10.1016/j.solmat.2010.08.006.

78 A.J. Nozik et al. 'Semiconductor quantum dots and quantum dot arrays and applications of multiple exciton generation to third-generation photovoltaic solar cells'. *Chemical Reviews* **110** (11), p.6873, (2010). DOI: 10.1021/cr900289f.

79 M.B. Smith & J. Michl. 'Singlet fission'. *Chemical Reviews* **110** (11), p.6891, (2010). DOI: 10.1021/cr1002613.

80 B.J. Walker et al. 'Singlet exciton fission in solution'. *Nature Chemistry* **5** (12), p.1019, (2013). DOI: 10.1038/nchem.1801.

81 S.V. Boriskina & G. Chen. 'Exceeding the solar cell Shockley-Queisser limit via thermal up-conversion of low-energy photons'. *Optics Communications* **314**, p.71, (2014). DOI: 10.1016/j.optcom.2013.10.042.

82 J.A.R. Dimmock et al. 'Demonstration of a hot-carrier photovoltaic cell'. *Progress in Photovoltaics: Research and Applications* **22** (2), p.151, (2014). DOI: 10.1002/pip.2444.

83 Z. Yu, S. Sandhu, & S. Fan. 'Efficiency above the Shockley-Queisser limit by using nanophotonic effects to create multiple effective bandgaps with a single semiconductor'. *Nano Letters* **14** (1), p.66, (2013). DOI: 10.1021/nl403653j.

84 T. Chung et al. 'Evaluation of the spatial distribution of series and shunt resistance of a solar cell using dark lock-in thermography'. *Journal of Applied Physics* **115** (3), p.034901.1, (2014). DOI: 10.1063/1.4862297.

85 A. Polman et al. 'Photovoltaic materials: Present efficiencies and future challenges'. *Science* **352** (6283), p.aad4424.1, (2016). DOI: 10.1126/science.aad4424.

86 E. Yablonovitch, O.D. Miller, & S.R. Kurtz. 'The optoelectronic physics that broke the efficiency limit in solar cells'. *Proceedings of the 38th IEEE Photovoltaic Specialists Conference,* p.001556, (2012). DOI: 10.1109/pvsc.2012.6317891.

87 K. Yoshikawa et al. 'Silicon heterojunction solar cell with interdigitated back contacts for a photoconversion efficiency over 26 %'. *Nature Energy* **2**, p.17032.1, (2017). DOI: 10.1038/nenergy.2017.32.

88 M.A. Green et al. 'Solar cell efficiency tables (version 51)'. *Progress in Photovoltaics: Research and Applications* **26** (1), p.3, (2017). DOI: 10.1002/pip.2978.

89 P. Jackson et al. 'Effects of heavy alkali elements in Cu(In,Ga)Se_2 solar cells with efficiencies up to 22.6 %'. *Physica Status Solidi: Rapid Research Letters* **10** (8), p.583, (2016). DOI: 10.1002/pssr.201600199.

90 J. Benick et al. 'High-efficiency n-type HP mc silicon solar cells'. *IEEE Journal of Photovoltaics*, p.1, (2017). DOI: 10.1109/jphotov.2017.2714139.

91 S. Mathew et al. 'Dye-sensitised solar cells with 13 % efficiency achieved through the molecular engineering of porphyrin sensitisers'. *Nature Chemistry* **6** (3), p.242, (2014). DOI: 10.1038/nchem.1861.

92 W. Wang et al. 'Device characteristics of CZTSSe thin film solar cells with 12.6 % efficiency'. *Advanced Energy Materials* **4** (7), p.1301465.1, (2013). DOI: 10.1002/aenm.201301465.

93 C. Yan et al. 'Beyond 11 % efficient sulphide kesterite $Cu_2Zn_xCd_{1-x}SnS_4$ solar cell: Effects of cadmium alloying'. *ACS Energy Letters* **2** (4), p.930, (2017). DOI: 10.1021/acsenergylett.7b00129.

94 X. Lan et al. '10.6 % certified colloidal quantum dot solar cells via solvent-polarity-engineered halide passivation'. *Nano Letters* **16** (7), p.4630, (2016). DOI: 10.1021/acs.nanolett.6b01957.

95 T. Matsui et al. 'Development of highly stable and efficient amorphous silicon based solar cells'. *Proceedings of the 28th European Photovoltaic Solar Energy Conference and Exhibition,* p.2213, (2013). DOI: 10.4229/28theupvsec2013-3DO.7.2.

96 C.J. Hages et al. 'Improved performance of Ge-alloyed CZTGeSSe thin-film solar cells through control of elemental losses'. *Progress in Photovoltaics: Research and Applications* **23** (3), p.376, (2015). DOI: 10.1002/pip.2442.

97 M. Nakashima et al. 'Cu_2SnS_3 thin film solar cells fabricated by sulphurisation from NaF/Cu/Sn stacked precursor'. *Applied Physics Express* **8** (4), p.042303.1, (2015).

98 'Best Research Cell Efficiencies (April 2017)'. USA National Renewable Energy Laboratory (NREL), (2017).

99 A. Jager-Waldau. 'Progress in chalcopyrite compound semiconductor research for photovoltaic applications and transfer of results into actual solar cell production'. *Solar Energy Materials and Solar Cells* **95** (6), p.1509, (2011). DOI: 10.1016/j.solmat.2010.12.033.

100 M. Saliba et al. 'Cesium-containing triple cation perovskite solar cells: improved stability, reproducibility and high efficiency'. *Energy & Environmental Science* **9** (6), p.1989, (2016). DOI: 10.1039/c5ee03874j.

101 M.M. Furchi et al. 'Photovoltaic effect in an electrically tunable van der Waals heterojunction'. *Nano Letters*, p.4785, (2014). DOI: 10.1021/nl501962c.

102 C. Wadia, A.P. Alivisatos, & D.M. Kammen. 'Materials availability expands the opportunity for large-scale photovoltaics deployment'. *Environmental Science & Technology* **43** (6), p.2072, (2009). DOI: 10.1021/es8019534.

103 A. Zuser & H. Rechberger. 'Considerations of resource availability in technology development strategies: The case study of photovoltaics'. *Resources, Conservation and Recycling* **56** (1), p.56, (2011). DOI: 10.1016/j.resconrec.2011.09.004.

104 J.J. Scragg et al. 'New routes to sustainable photovoltaics: evaluation of Cu_2ZnSnS_4 as an alternative absorber material'. *Physica Status Solidi B* **245** (9), p.1772, (2008). DOI: 10.1002/pssb.200879539.

105 B.A. Andersson. 'Materials availability for large-scale thin film photovoltaics'. *Progress in Photovoltaics: Research and Applications* **8** (1), p.61, (2000). DOI: 10.1002/(sici)1099-159X(200001/02)8:1<61::aid-pip301>3.0.co;2-6.

106 J. Emsley. 'Nature's Building Blocks: An A-Z Guide to the Elements'. Oxford University Press, (2011).

107 'Mineral Commodity Summaries (January 2017)'. USA Geological Survey, (2017).

108 G.Q. Yang et al. 'Endemic selenium intoxication of humans in China'. *American Journal of Clinical Nutrition* **37** (5), p.872, (1983).

109 T. Todorov & D.B. Mitzi. 'Direct liquid coating of chalcopyrite light-absorbing layers for photovoltaic devices'. *European Journal of Inorganic Chemistry* **2010** (1), p.17, (2010). DOI: 10.1002/ejic.200900837.

110 K. Timmo et al. 'Influence of order-disorder in Cu_2ZnSnS_4 powders on the performance of monograin layer solar cells'. *Thin Solid Films* **633**, p.122, (2017). DOI: 10.1016/j.tsf.2016.10.017.

111 A. Pu et al. 'Sentaurus modelling of 6.9 % Cu_2ZnSnS_4 device based on comprehensive electrical & optical characterisation'. *Solar Energy Materials and Solar Cells* **160**, p.372, (2017). DOI: 10.1016/j.solmat.2016.10.053.

112 A. Polizzotti et al. 'The state and future prospects of kesterite photovoltaics'. *Energy & Environmental Science* **6** (11), p.3171, (2013). DOI: 10.1039/c3ee41781f.

113 H. Wang. 'Progress in thin film solar cells based on Cu_2ZnSnS_4'. *International Journal of Photoenergy* **2011**, p.801292.1, (2011). DOI: 10.1155/2011/801292.

114 S. Delbos. 'Kesterite thin films for photovoltaics: A review'. *EPJ Photovoltaics* **3**, p.35004.1, (2012). DOI: 10.1051/epjpv/2012008.

115 K. Ramasamy, M.A. Malik, & P. O'Brien. 'Routes to copper zinc tin sulphide Cu_2ZnSnS_4 a potential material for solar cells'. *Chemical Communications* **48** (46), p.5703, (2012). DOI: 10.1039/c2cc30792h.

116 I.L. Repins et al. 'Kesterite successes, ongoing work, and challenges: A perspective from vacuum deposition'. *Proceedings of the 38th IEEE Photovoltaic Specialists Conference,* p.1, (2012). DOI: 10.1109/pvsc-vol2.2012.6656774.

117 S. Siebentritt & S. Schorr. 'Kesterites: A challenging material for solar cells'. *Progress in Photovoltaics: Research and Applications* **20** (5), p.512, (2012). DOI: 10.1002/pip.2156.

118 C.M. Fella, Y.E. Romanyuk, & A.N. Tiwari. 'Technological status of $Cu_2ZnSn(S,Se)_4$ thin film solar cells'. *Solar Energy Materials and Solar Cells* **119**, p.276, (2013). DOI: 10.1016/j.solmat.2013.08.027.

119 S. Siebentritt. 'Why are kesterite solar cells not 20 % efficient?'. *Thin Solid Films* **535**, p.1, (2013). DOI: 10.1016/j.tsf.2012.12.089.

120 X. Song et al. 'A review on development prospect of CZTS-based thin film solar cells'. *International Journal of Photoenergy* **2014**, p.1, (2014). DOI: 10.1155/2014/613173.

121 T.J. Huang et al. 'CZTS-based materials and interfaces and their effects on the performance of thin film solar cells'. *Physica Status Solidi: Rapid Research Letters* **8** (9), p.735, (2014). DOI: 10.1002/pssr.201409219.

122 M. Kumar et al. 'Strategic review of secondary phases, defects and defect-complexes in kesterite CZTS-Se solar cells'. *Energy & Environmental Science* **8** (11), p.3134, (2015). DOI: 10.1039/c5ee02153g.

123 S. Bourdais et al. 'Is the Cu/Zn disorder the main culprit for the voltage deficit in kesterite solar cells?'. *Advanced Energy Materials* **6** (12), p.1502276.1, (2016). DOI: 10.1002/aenm.201502276.

124 X. Liu et al. 'The current status and future prospects of kesterite solar cells: A brief review'. *Progress in Photovoltaics: Research and Applications* **24** (6), p.879, (2016). DOI: 10.1002/pip.2741.

125 Z. Shi, D. Attygalle, & A.H. Jayatissa. 'Kesterite-based next generation high performance thin film solar cell: Current progress and future prospects'. *Journal of Materials Science: Materials in Electronics* **28** (2), p.2290, (2017). DOI: 10.1007/s10854-016-5753-1.

126 S.K. Wallace, D.B. Mitzi, & A. Walsh. 'The steady rise of kesterite solar cells'. *ACS Energy Letters* **2** (4), p.776, (2017). DOI: 10.1021/acsenergylett.7b00131.

127 S. Zhuk et al. 'Critical review on sputter-deposited Cu_2ZnSnS_4 (CZTS) based thin film photovoltaic technology focusing on device architecture and absorber quality on the solar cells performance'. *Solar Energy Materials and Solar Cells* **171**, p.239, (2017). DOI: 10.1016/j.solmat.2017.05.064.

128 J. Scragg. 'Studies of Cu_2ZnSnS_4 Films Prepared by Sulphurisation of Electrodeposited Precursors'. PhD thesis, University of Bath, Department of Cemistry, (2010).

129 V. Chawla. 'A Study of CZTS Thin Films for Solar Cell Applications'. PhD thesis, Stanford University, Department of Materials Science and Engineering, (2011).

130 K.M. Hönes. 'Photoluminescence Measurements on Solar Cell Materials: Chalcopyrites and Kesterites'. PhD thesis, Université du Luxembourg, Department of Physics, (2011).

131 D.M. Berg. 'Kesterite Equilibrium Reaction and the Discrimination of Secondary Phases from Cu_2ZnSnS_4'. PhD thesis, Université du Luxembourg, Department of Physics, (2012).

132 K.J. Hutchings. 'High Throughput Combinatorial Screening of Cu-Zn-Sn-S Thin Film Libraries for the Application of Cu_2ZnSnS_4 Photovoltaic Cells'. PhD thesis, Cranfield University, Department of Engineering and Applied Science, (2012).

133 M.C. Johnson. 'The Synthesis and Characterisation of Thin Film Copper Zinc Tin Sulphide for Solar Cell Applications'. PhD thesis, University of Minnesota, Department of Chemical Engineering and Materials Science, (2014).

134 X. Yin. 'On the Formation of CZTS Based Films for Photovoltaic Applications'. PhD thesis, National University of Singapore, Department of Materials Science and Engineering, (2014).

135 C. Malerba. 'Cu_2ZnSnS_4 Thin Fims and Solar Cells: Material and Device Characterisation'. PhD thesis, University of Trento, Department of Industrial Engineering, (2014).

136 X. Liu. 'Molybdenum Back Contact Treatment for Cu_2ZnSnS_4 Solar Cells'. PhD thesis, The University of New South Wales, School of Photovoltaic and Renewable Energy Engineering, (2015).

137 A. Nandur. 'Experimental Study of Pulsed Laser Deposited Cu_2ZnSnS_4 (CZTS) Thin Films For Photovoltaic Applications'. PhD thesis, Binghampton University, Department of Materials Science and Engineering, (2015).

138 E.R.S. Tay. 'Electrochemical Deposition of Cu-Zn-Sn-S Films'. PhD thesis, Imperial College, London, Department of Materials, (2015).

139 W.-C.D. Yang. 'Kesterite Thin Film Solar Cell Absorbers Derived Using Inhomogeneous CZTS Nanoparticles'. PhD thesis, Purdue University, School of Materials Engineering, (2015).

140 M.M.A. Abusnina. 'Synthesis and Characterisation of Kesterite Cu_2ZnSnS_4 (CZTS) Thin Films for Solar Cell Application'. PhD thesis, University of Denver, School of Engineering and Computer Science, (2016).

141 A. Cazzaniga. 'Fabrication of Thin Film CZTS Solar Cells With Pulsed Laser Deposition'. PhD thesis, Technical University of Denmark, Department of Micro and Nanotechnology, (2016).

142 A. Crovetto. 'Cu_2ZnSnS_4 Solar Cells: Physics and Technology by Alternative Tracks'. PhD thesis, Technical University of Denmark, Department of Micro and Nanotechnology, (2016).

143 S.L.J. Engberg. 'Cu_2ZnSnS_4 Nanoparticle Absorber Layers for Thin Film Solar Cells'. PhD thesis, Technical University of Denmark, Department of Photonics Engineering, (2016).

144 A. Ritscher. 'Synthesis and Structural Characterisation of Semiconductors Based on Kesterites'. PhD thesis, Technichal University of Berlin, Faculty of Mathematics and Natural Sciences, (2016).

145 Y. Ren. 'Annealing of CZTS Thin Films: A Study of Secondary Compounds and Their Effects on Solar Cells'. PhD thesis, Uppsala Unversitet, Department of Engineering Sciences, (2017).

146 S.R. Kodigala. 'Thin Film Solar Cells from Earth Abundant Materials: Growth and Characterisation of $Cu_2ZnSn(S,Se)_4$ Thin Films and Their Solar Cells'. Elsevier, (2014).

147 S. Adachi. 'Earth-Abundant Mateials for Solar Cells: Cu_2-II-IV-VI_4 Semiconductors'. Wiley, (2015).

148 K. Ito. 'Copper Zinc Tin Sulphide-Based Thin Film Solar Cells'. Wiley, (2015).

149 B.K. Durant & B.A. Parkinson. 'Photovoltaic response of natural Kesterite crystals'. *Solar Energy Materials and Solar Cells* **144**, p.586, (2016). DOI: 10.1016/j.solmat.2015.09.055.

150 R. Nitsche, D.F. Sargent, & P. Wild. 'Crystal growth of quaternary 1(2)246(4) chalcogenides by iodine vapour transport'. *Journal of Crystal Growth* **1** (1), p.52, (1967). DOI: 10.1016/0022-0248(67)90009-7.

151 K. Ito & T. Nakazawa. 'Electrical and optical properties of stannite-type quaternary semiconductor thin films'. *Japanese Journal of Applied Physics* **27** (Part 1, 11), p.2094, (1988). DOI: 10.1143/jjap.27.2094.

152 H. Katagiri et al. 'Preparation and evaluation of Cu_2ZnSnS_4 thin films by sulphurisation of E-B evaporated precursors'. *Proceedings of the 9th International Photovoltaic Science and Engineering Conference,* p.745, (1996).

153 H. Katagiri et al. 'Development of CZTS-based thin film solar cells'. *Thin Solid Films* **517** (7), p.2455, (2009). DOI: 10.1016/j.tsf.2008.11.002.

154 T.M. Friedlmeier et al. 'Heterojunctions based on Cu_2ZnSnS_4 and $Cu_2ZnSnSe_4$ thin films. '. *Proceedings of the 14th European Photovoltaic Solar Energy Conference,* p.1242, (1997).

155 H. Katagiri et al. 'Development of thin film solar cell based on Cu_2ZnSnS_4 thin films'. *Solar Energy Materials and Solar Cells* **65** (1-4), p.141, (2001). DOI: 10.1016/S0927-0248(00)00088-x.

156 H. Katagiri et al. 'Solar cell without environmental pollution by using CZTS thin film'. *Proceedings of the 3rd Photovoltaic Energy Conversion Conference,* p.2874, (2003).

157 K. Jimbo et al. 'Cu_2ZnSnS_4-type thin film solar cells using abundant materials'. *Thin Solid Films* **515** (15), p.5997, (2007). DOI: 10.1016/j.tsf.2006.12.103.

158 H. Katagiri et al. 'Enhanced conversion efficiencies of Cu_2ZnSnS_4-based thin film solar cells by using preferential etching technique'. *Applied Physics Express* **1** (4), p.041201.1, (2008). DOI: 10.1143/apex.1.041201.

159 B. Shin et al. 'Thin film solar cell with 8.4 % power conversion efficiency using an earth-abundant Cu_2ZnSnS_4 absorber'. *Progress in Photovoltaics: Research and Applications* **21** (1), p.72, (2013). DOI: 10.1002/pip.1174.

160 H. Sugimoto et al. 'Over 8 % efficiency Cu_2ZnSnS_4 submodules with ultra-thin absorber'. *Proceedings of the 38th IEEE Photovoltaic Specialists Conference,* p.002997, (2012). DOI: 10.1109/pvsc.2012.6318214.

161 T. Kato et al. 'Characterisation of front and back interfaces on Cu_2ZnSnS_4 thin film solar cells'. *Proceedings of the 27th European Photovoltaic Solar Energy Conference,* p.2236, (2012). DOI: 10.4229/27theupvsec2012-3co.4.2.

162 K. Sun et al. 'Towards 10 % state-of-the-art pure sulphide Cu_2ZnSnS_4 solar cell by modifying the interface chemistry '. *Proceedings of the 44th IEEE Photovoltaic Specialists Conference,* (2017).

163 D.A.R. Barkhouse et al. 'Device characteristics of a 10.1 % hydrazine-processed $Cu_2ZnSn(Se,S)_4$ solar cell'. *Progress in Photovoltaics: Research and Applications* **20** (1), p.6, (2012). DOI: 10.1002/pip.1160.

164 T.K. Todorov et al. 'Beyond 11 % efficiency: Characteristics of state-of-the-art $Cu_2ZnSn(S,Se)_4$ solar cells'. *Advanced Energy Materials* **3** (1), p.34, (2013). DOI: 10.1002/aenm.201200348.

165 B.T. Gershon et al. 'The impact of sodium on the sub-band gap states in CZTSe and CZTS'. *Applied Physics Letters* **106** (12), p.123905.1, (2015). DOI: 10.1063/1.4916635.

166 M. Grossberg et al. 'Photoluminescence and Raman study of $Cu_2ZnSn(Se_xS_{1-x})_4$ monograins for photovoltaic applications'. *Thin Solid Films* **519** (21), p.7403, (2011). DOI: 10.1016/j.tsf.2010.12.099.

167 S. Bag et al. 'Hydrazine-processed Ge-substituted CZTSe solar cells'. *Chemistry of Materials* **24** (23), p.4588, (2012). DOI: 10.1021/cm302881g.

168 F.J.C. Roe, G.A. Grant, & D.M. Millican. 'Carcinogenicity of hydrazine and 1,1-dimethylhydrazine for mouse lung'. *Nature* **216** (5113), p.375, (1967). DOI: 10.1038/216375a0.

169 G. Choudhary & H. Hansen. 'Human health perspective of environmental exposure to hydrazines: A review'. *Chemosphere* **37** (5), p.801, (1998). DOI: 10.1016/S0045-6535(98)00088-5.

170 Z.-Y. Xiao et al. 'Bandgap engineering of $Cu_2(Zn_xCd_{1-x})SnS_4$ alloy for photovoltaic applications: A complementary experimental and first principles study'. *Journal of Applied Physics* **114** (18), p.183506.1, (2013). DOI: 10.1063/1.4829457.

171 M. Pilvet et al. 'Compositionally tunable structure and optical properties of $Cu_{1.85}(Cd_xZn_{1-x})_{1.1}SnS_{4.1}$ ($0 \leq x \leq 1$) monograin powders'. *Thin Solid Films* **582**, p.180, (2015). DOI: 10.1016/j.tsf.2014.10.091.

172 Z. Su et al. 'Cation substitution of solution-processed Cu_2ZnSnS_4 thin film solar cell with over 9 % efficiency'. *Advanced Energy Materials* **5** (19), p.1500682.1, (2015). DOI: 10.1002/aenm.201500682.

173 Z. Su et al. 'Cation substitution of CZTS solar cell with >10 % efficiency'. *Proceedings of the 43rd IEEE Photovoltaic Specialists Conference,* p.0534, (2016). DOI: 10.1109/pvsc.2016.7749651.

174 Q. Zhang et al. 'Cation substitution induced structural transition, band gap engineering and grain growth of $Cu_2Cd_xZn_{1-x}SnS_4$ thin films'. *Journal of Alloys and Compounds* **695**, p.482, (2017). DOI: 10.1016/j.jallcom.2016.11.121.

175 A. Lafond et al. 'Substitution of Li for Cu in Cu_2ZnSnS_4: Toward wide band gap absorbers with low cation disorder for thin film solar cells'. *Inorganic Chemistry* **56** (5), p.2712, (2017). DOI: 10.1021/acs.inorgchem.6b02865.

176 A.C. Lokhande et al. 'Development of Cu_2SnS_3 (CTS) thin film solar cells by physical techniques: A status review'. *Solar Energy Materials and Solar Cells* **153**, p.84, (2016). DOI: 10.1016/j.solmat.2016.04.003.

177 C. Persson. 'Electronic and optical properties of Cu_2ZnSnS_4 and $Cu_2ZnSnSe_4$'. *Journal of Applied Physics* **107** (5), p.053710.1, (2010). DOI: 10.1063/1.3318468.

178 S. Kahraman et al. 'Facile synthesis of Cu_2ZnSnS_4 photovoltaic absorber thin films via sulphurisation of Cu_2SnS_3/ZnS layers'. *Metallurgical and Materials Transactions A* **45** (4), p.2326, (2014). DOI: 10.1007/s11661-013-2164-2.

179 J. He et al. 'Effect of post-sulphurisation on the composition, structure and optical properties of Cu_2ZnSnS_4 thin films deposited by sputtering from a single quaternary target'. *Applied Surface Science* **264**, p.133, (2013). DOI: 10.1016/j.apsusc.2012.09.140.

180 E.M. Mkawi et al. 'Dependence of the properties of copper zinc tin sulphide thin films prepared by electrochemical deposition on sulphurisation temperature'. *Journal of Materials Science: Materials in Electronics* **25** (2), p.857, (2014). DOI: 10.1007/s10854-013-1657-5.

181 C. Malerba et al. 'CZTS stoichiometry effects on the band gap energy'. *Journal of Alloys and Compounds* **582**, p.528, (2014). DOI: 10.1016/j.jallcom.2013.07.199.

182 P.K. Sarswat & M.L. Free. 'A study of energy band gap versus temperature for Cu_2ZnSnS_4 thin films'. *Physica B: Condensed Matter* **407** (1), p.108, (2012). DOI: 10.1016/j.physb.2011.09.134.

183 S. Chen et al. 'Crystal and electronic band structure of Cu_2ZnSnX_4 (X=S and Se) photovoltaic absorbers: First-principles insights'. *Applied Physics Letters* **94** (4), p.041903.1, (2009). DOI: 10.1063/1.3074499.

184 J. Paier et al. 'Cu_2ZnSnS_4 as a potential photovoltaic material: A hybrid Hartree-Fock density functional theory study'. *Physical Review B* **79** (11), p.115126.1, (2009). DOI: 10.1103/physrevb.79.115126.

185 S. Botti, D. Kammerlander, & M.A.L. Marques. 'Band structures of Cu_2ZnSnS_4 and $Cu_2ZnSnSe_4$ from many-body methods'. *Applied Physics Letters* **98** (24), p.241915.1, (2011). DOI: 10.1063/1.3600060.

186 W. Li et al. 'Temperature dependence of phonon modes, dielectric functions, and interband electronic transitions in Cu_2ZnSnS_4 semiconductor films'. *Physical Chemistry Chemical Physics* **14** (28), p.9936, (2012). DOI: 10.1039/c2cp41209h.

187 S. Schorr et al. 'The complex material properties of chalcopyrite and kesterite thin film solar cell absorbers tackled by synchrotron-based analytics'. *Progress in Photovoltaics: Research and Applications* **20** (5), p.557, (2012). DOI: 10.1002/pip.1256.

188 A.H. Reshak et al. 'Structural, electronic and optical properties in Earth-abundant photovoltaic absorber of Cu_2ZnSnS_4 and $Cu_2ZnSnSe_4$ from density functional theory calculations '. *International Journal of Electrochemical Science* **9** (2), p.955, (2014).

189 Y. Zhao, D. Li, & Z. Liu. 'Phase transitions and electronic properties for zincblende-derived and wurtzite-derived stannite Cu_2ZnSnS_4 under pressure'. *Journal of Electronic Materials* **46** (5), p.2812, (2017). DOI: 10.1007/s11664-016-4985-4.

190 S. Chen et al. 'Intrinsic point defects and complexes in the quaternary kesterite semiconductor Cu_2ZnSnS_4'. *Physical Review B* **81** (24), p.245204.1, (2010). DOI: 10.1103/physrevb.81.245204.

191 J. Feng et al. 'Fabrication and characterisation of Cu_2ZnSnS_4 thin films for photovoltaic application by low-cost single target sputtering process'. *Vacuum* **126**, p.84, (2016). DOI: 10.1016/j.vacuum.2016.01.023.

192 P.-A. Cormier & R. Snyders. 'Phase transformation during Cu_2ZnSnS_4 synthesis by reactive magnetron co-sputtering'. *Acta Materialia* **110**, p.53, (2016). DOI: 10.1016/j.actamat.2016.03.009.

193 A. Nagaoka et al. 'Correlation between intrinsic defects and electrical properties in the high-quality Cu_2ZnSnS_4 single crystal'. *Applied Physics Letters* **103** (11), p.112107.1, (2013). DOI: 10.1063/1.4821279.

194 J. Xu. 'Investigation of Cu_2ZnSnS_4 thin film solar cells with carrier concentration gradient'. *Journal of Physics and Chemistry of Solids* **98**, p.32, (2016). DOI: 10.1016/j.jpcs.2016.06.007.

195 L. Guen & W.S. Glaunsinger. 'Electrical, magnetic, and EPR studies of the quaternary chalcogenides $Cu_2A^{II}B^{IV}X_4$ prepared by iodine transport'. *Journal of Solid State Chemistry* **35** (1), p.10, (1980). DOI: 10.1016/0022-4596(80)90457-0.

196 M. Courel et al. 'Determination of minority carrier diffusion length of sprayed-Cu_2ZnSnS_4 thin films'. *Solid-State Electronics* **118**, p.1, (2016). DOI: 10.1016/j.sse.2015.12.003.

197 P.K. Sarswat & M.L. Free. 'An evaluation of depletion layer photoactivity in Cu_2ZnSnS_4 thin films'. *Thin Solid Films* **520** (13), p.4422, (2012). DOI: 10.1016/j.tsf.2012.02.066.

198 M. Courel, J.A. Andrade-Arvizu, & O. Vigil-Galán. 'The role of buffer/kesterite interface recombination and minority carrier lifetime on kesterite thin film solar cells'. *Materials Research Express* **3** (9), p.095501.1, (2016). DOI: 10.1088/2053-1591/3/9/095501.

199 H. Hazama et al. 'Transport properties of the Cu_2ZnSnS_4 bulk systems: Effects of nonstoichiometry and defect formation'. *Journal of Alloys and Compounds* **657**, p.179, (2016). DOI: 10.1016/j.jallcom.2015.10.032.

200 D. Tiwari et al. 'Cu_2ZnSnS_4 thin films by simple replacement reaction route for solar photovoltaic application'. *Thin Solid Films* **551**, p.42, (2014). DOI: 10.1016/j.tsf.2013.11.095.

201 W.D. Thompson, A. Nandur, & B.E. White. 'Thermal transport in Cu_2ZnSnS_4 thin films'. *Journal of Applied Physics* **119** (9), p.095108.1, (2016). DOI: 10.1063/1.4942661.

202 S. Bensalem et al. 'Theoretical study of structural, elastic and thermodynamic properties of CZTX (X=S and Se) alloys'. *Journal of Alloys and Compounds* **589**, p.137, (2014). DOI: 10.1016/j.jallcom.2013.11.113.

203 Y. Zhao, D. Li, & Z. Liu. 'Structural and elastic DFT study of four structures for Cu_2ZnSnS_4 under high pressure'. *Journal of Alloys and Compounds* **696**, p.86, (2017). DOI: 10.1016/j.jallcom.2016.11.091.

204 A. Nagaoka et al. 'Thermophysical properties of Cu_2ZnSnS_4 single crystal'. *Journal of Crystal Growth* **393**, p.167, (2014). DOI: 10.1016/j.jcrysgro.2013.11.077.

205 T. Maeda, S. Nakamura, & T. Wada. 'Phase stability and electronic structure of In-free photovoltaic semiconductors, $Cu_2ZnSnSe_4$ and Cu_2ZnSnS_4 by first-principles calculation'. *MRS Proceedings* **1165**, p.137, (2009). DOI: 10.1557/proc-1165-m04-03.

206 M. Dimitrievska et al. 'Structural polymorphism in "kesterite" Cu_2ZnSnS_4: Raman spectroscopy and first-principles calculations analysis'. *Inorganic Chemistry* **56** (6), p.3467, (2017). DOI: 10.1021/acs.inorgchem.6b03008.

207 H. Katagiri et al. 'Preparation and evaluation of Cu_2ZnSnS_4 thin films by sulphurisation of EB evaporated precursors'. *Solar Energy Materials and Solar Cells* **49** (1-4), p.407, (1997). DOI: 10.1016/S0927-0248(97)00119-0.

208 V.S. Zakhvalinskii et al. 'Structural, optical, and electrical conductivity properties of stannite Cu_2ZnSnS_4'. *Journal of Electronic Materials* **46** (6), p.3523, (2017). DOI: 10.1007/s11664-017-5297-z.

209 S. Schorr, H.-J. Hoebler, & M. Tovar. 'A neutron diffraction study of the stannite-kesterite solid solution series'. *European Journal of Mineralogy* **19** (1), p.65, (2007). DOI: 10.1127/0935-1221/2007/0019-0065.

210 S. Schorr. 'The crystal structure of kesterite type compounds: A neutron and X-ray diffraction study'. *Solar Energy Materials and Solar Cells* **95** (6), p.1482, (2011). DOI: 10.1016/j.solmat.2011.01.002.

211 S. Schorr et al. 'Neutrons and photons in materials research for thin film solar cells'. *Advanced Engineering Materials* **13** (8), p.737, (2011). DOI: 10.1002/adem.201000290.

212 T. Washio et al. 'Analysis of lattice site occupancy in kesterite structure of Cu_2ZnSnS_4 films using synchrotron radiation X-ray diffraction'. *Journal of Applied Physics* **110** (7), p.074511.1, (2011). DOI: 10.1063/1.3642993.

213 A. Lafond et al. 'Crystal structures of photovoltaic chalcogenides, an intricate puzzle to solve: The cases of CIGSe and CZTS materials'. *Zeitschrift für anorganische und allgemeine Chemie* **638** (15), p.2571, (2012). DOI: 10.1002/zaac.201200279.

214 H. Nozaki et al. 'Crystal structure determination of solar cell materials: Cu_2ZnSnS_4 thin films using X-ray anomalous dispersion'. *Journal of Alloys and Compounds* **524**, p.22, (2012). DOI: 10.1016/j.jallcom.2012.01.134.

215 F.J. Espinosa-Faller et al. 'Neutron diffraction and X-ray absorption fine structure evidence for local lattice distortions and aperiodic antisite substitution in Cu_2ZnSnS_4 nanoparticles'. *The Journal of Physical Chemistry C* **118** (45), p.26292, (2014). DOI: 10.1021/jp502150s.

216 A. Lafond et al. 'X-ray resonant single-crystal diffraction technique, a powerful tool to investigate the kesterite structure of the photovoltaic Cu_2ZnSnS_4 compound'. *Acta Crystallographica B* **70** (2), p.390, (2014). DOI: 10.1107/s2052520614003138.

217 A. Ritscher et al. 'A mechanochemical route to single phase Cu_2ZnSnS_4 powder'. *Journal of Alloys and Compounds* **670**, p.289, (2016). DOI: 10.1016/j.jallcom.2016.02.058.

218 S. Schorr & G. Gonzalez-Aviles. 'In-situ investigation of the structural phase transition in kesterite'. *Physica Status Solidi A* **206** (5), p.1054, (2009). DOI: 10.1002/pssa.200881214.

219 H. Guan et al. 'Synthesis of wurtzite Cu_2ZnSnS_4 thin films directly on glass substrates by the solvothermal method'. *Materials Letters* **159**, p.200, (2015). DOI: 10.1016/j.matlet.2015.06.049.

220 S.R. Hall, J.T. Szymanski, & J.M. Stewart. 'Kesterite $Cu_2(Zn,Fe)SnS_4$, and stannite $Cu_2(Fe,Zn)SnS_4$, structurally similar but distinct minerals'. *The Canadian Mineralogist* **16** (2), p.131, (1978).

221 L. Choubrac et al. 'Structure flexibility of the Cu_2ZnSnS_4 absorber in low-cost photovoltaic cells: From the stoichiometric to the copper-poor compounds'. *Inorganic Chemistry* **51** (6), p.3346, (2012). DOI: 10.1021/ic202569q.

222 A. Khare et al. 'Calculation of the lattice dynamics and Raman spectra of copper zinc tin chalcogenides and comparison to experiments'. *Journal of Applied Physics* **111** (8), p.083707.1, (2012). DOI: 10.1063/1.4704191.

223 K. Yu & E.A. Carter. 'A strategy to stabilise kesterite CZTS for high-performance solar cells'. *Chemistry of Materials* **27** (8), p.2920, (2015). DOI: 10.1021/acs.chemmater.5b00172.

224 J.J.S. Scragg et al. 'A low-temperature order-disorder transition in Cu_2ZnSnS_4 thin films'. *Applied Physics Letters* **104** (4), p.041911.1, (2014). DOI: 10.1063/1.4863685.

225 P.A. Fernandes, P.M.P. Salomé, & A.F. da Cunha. 'Growth and Raman scattering characterisation of Cu_2ZnSnS_4 thin films'. *Thin Solid Films* **517** (7), p.2519, (2009). DOI: 10.1016/j.tsf.2008.11.031.

226 P. Xu et al. 'Stability and electronic structure of Cu_2ZnSnS_4 surfaces: First-principles study'. *Physical Review B* **88** (4), p.045427.1, (2013). DOI: 10.1103/physrevb.88.045427.

227 A. Ritscher, M. Hoelzel, & M. Lerch. 'The order-disorder transition in Cu_2ZnSnS_4: A neutron scattering investigation'. *Journal of Solid State Chemistry* **238**, p.68, (2016). DOI: 10.1016/j.jssc.2016.03.013.

228 G. Rey et al. 'The band gap of $Cu_2ZnSnSe_4$: Effect of order-disorder'. *Applied Physics Letters* **105** (11), p.112106.1, (2014). DOI: 10.1063/1.4896315.

229 L.T. Schelhas et al. 'Point defects in $Cu_2ZnSnSe_4$ (CZTSe): Resonant X-ray diffraction study of the low-temperature order/disorder transition'. *Physica Status Solidi B* **254** (9), p.1700156.1, (2017). DOI: 10.1002/pssb.201700156.

230 G.H. Vineyard. 'Theory of order-disorder kinetics'. *Physical Review* **102** (4), p.981, (1956). DOI: 10.1103/physrev.102.981.

231 C. Malerba, M. Valentini, & A. Mittiga. 'Cation disorder in Cu_2ZnSnS_4 thin films: Effect on solar cell performances'. *Solar RRL* **1** (9), p.1700101.1, (2017). DOI: 10.1002/solr.201700101.

232 M. Quennet et al. 'The order-disorder transition in Cu_2ZnSnS_4: A theoretical and experimental study'. *Journal of Solid State Chemistry* **250**, p.140, (2017). DOI: 10.1016/j.jssc.2017.03.018.

233 K. Rudisch et al. 'Order-disorder transition in B-type Cu_2ZnSnS_4 and limitations of ordering through thermal treatments'. *Applied Physics Letters* **108** (23), p.231902.1, (2016). DOI: 10.1063/1.4953349.

234 J.J.S. Scragg et al. 'Cu-Zn disorder and band gap fluctuations in $Cu_2ZnSn(S,Se)_4$: Theoretical and experimental investigations'. *Physica Status Solidi B* **253** (2), p.247, (2016). DOI: 10.1002/pssb.201552530.

235 D. Huang & C. Persson. 'Band gap change induced by defect complexes in Cu_2ZnSnS_4'. *Thin Solid Films* **535**, p.265, (2013). DOI: 10.1016/j.tsf.2012.10.030.

236 G.H. Moh. 'Tin-containing mineral systems'. *Chemie der Erde* **34**, p.1, (1975).

237 I.D. Olekseyuk, I.V. Dudchak, & L.V. Piskach. 'Phase equilibria in the Cu_2S-ZnS-SnS_2 system'. *Journal of Alloys and Compounds* **368** (1-2), p.135, (2004). DOI: 10.1016/j.jallcom.2003.08.084.

238 J. Just et al. 'Determination of secondary phases in kesterite Cu_2ZnSnS_4 thin films by X-ray absorption near edge structure analysis'. *Applied Physics Letters* **99** (26), p.262105.1, (2011). DOI: 10.1063/1.3671994.

239 K. Muska et al. 'Synthesis of Cu_2ZnSnS_4 monograin powders with different compositions'. *Energy Procedia* **10**, p.203, (2011). DOI: 10.1016/j.egypro.2011.10.178.

240 E.A. Pogue & A.A. Rockett. 'Phase stability of Cu_2ZnSnS_4-SnS_2 interfaces: $Cu_2ZnSn_3S_8$'. *Proceedings of the 43rd IEEE Photovoltaic Specialists Conference,* p.0471, (2016). DOI: 10.1109/pvsc.2016.7749638.

241 N. Johnson, E. Pogue, & A. Rockett. 'Multi-nuclear (^{119}Sn and ^{65}Cu) NMR and Raman spectroscopy to probe secondary phases in Cu_2ZnSnS_4'. *Proceedings of the 43rd IEEE Photovoltaic Specialists Conference,* p.3046, (2016). DOI: 10.1109/pvsc.2016.7750224.

242 C. Platzer-Björkman et al. 'Influence of precursor sulphur content on film formation and compositional changes in Cu_2ZnSnS_4 films and solar cells'. *Solar Energy Materials and Solar Cells* **98**, p.110, (2012). DOI: 10.1016/j.solmat.2011.10.019.

243 B.G. Mendis et al. 'The role of secondary phase precipitation on grain boundary electrical activity in Cu_2ZnSnS_4 (CZTS) photovoltaic absorber layer material'. *Journal of Applied Physics* **112** (12), p.124508.1, (2012). DOI: 10.1063/1.4769738.

244 P. Sarker, M.M. Al-Jassim, & M.N. Huda. 'Theoretical limits on the stability of single-phase kesterite Cu_2ZnSnS_4'. *Journal of Applied Physics* **117** (3), p.035702.1, (2015). DOI: 10.1063/1.4906065.

245 S. Schorr et al. 'Structure and phase relations in the 2($CuInS_2$)-Cu_2ZnSnS_4 solid solution system'. *Thin Solid Films* **517** (7), p.2508, (2009). DOI: 10.1016/j.tsf.2008.11.032.

246 S.H. Chaki, J.P. Tailor, & M.P. Deshpande. 'Covellite CuS: Single crystal growth by chemical vapour transport technique and characterisation'. *Materials Science in Semiconductor Processing* **27**, p.577, (2014). DOI: 10.1016/j.mssp.2014.07.038.

247 H. Sträter et al. 'Detailed photoluminescence studies of thin film Cu_2S for determination of quasi-Fermi level splitting and defect levels'. *Journal of Applied Physics* **114** (23), p.233506, (2013). DOI: 10.1063/1.4850955.

248 Y.C. Cheng et al. 'Raman scattering study of zinc blende and wurtzite ZnS'. *Journal of Applied Physics* **106** (12), p.123505.1, (2009). DOI: 10.1063/1.3270401.

249 T. Sorgenfrei et al. 'Synthesis and single crystal growth of SnS by the Bridgman-Stockbarger technique'. *Crystal Research and Technology* **48** (4), p.193, (2013). DOI: 10.1002/crat.201200484.

250 N.G. Deshpande et al. 'Growth and characterisation of tin disulphide (SnS_2) thin film deposited by successive ionic layer adsorption and reaction (SILAR) technique'. *Journal of Alloys and Compounds* **436** (1-2), p.421, (2007). DOI: 10.1016/j.jallcom.2006.12.108.

251 D.J. Singh. 'Optical and electronic properties of semiconducting Sn_2S_3'. *Applied Physics Letters* **109** (3), p.032102.1, (2016). DOI: 10.1063/1.4959104.

252 D.M. Berg et al. 'Thin film solar cells based on the ternary compound Cu_2SnS_3'. *Thin Solid Films* **520** (19), p.6291, (2012). DOI: 10.1016/j.tsf.2012.05.085.

253 H. Guan et al. 'Structural and optical properties of Cu_2SnS_3 and Cu_3SnS_4 thin films by successive ionic layer adsorption and reaction'. *Journal of Materials Science: Materials in Electronics* **24** (5), p.1490, (2013). DOI: 10.1007/s10854-012-0960-x.

254 V.P.G. Vani, M.V. Reddy, & K.T.R. Reddy. 'Thickness-dependent physical properties of co-evaporated Cu_4SnS_4 films'. *ISRN Condensed Matter Physics* **2013**, p.142029.1, (2013). DOI: 10.1155/2013/142029.

255 X. Chen et al. 'Synthesis, electrical conductivity, and crystal structure of $Cu_4Sn_7S_{16}$ and structure refinement of Cu_2SnS_3'. *Journal of Solid State Chemistry* **139** (1), p.144, (1998). DOI: 10.1006/jssc.1998.7822.

256 W. Bao & M. Ichimura. 'Influence of secondary phases in kesterite Cu_2ZnSnS_4 absorber material based on the first principles calculation'. *International Journal of Photoenergy* **2015**, p.1, (2015). DOI: 10.1155/2015/592079.

257 T. Unold et al. 'Correlation between composition and photovoltaic properties of Cu_2ZnSnS_4 thin film solar cells'. *Proceedings of the 37th IEEE Photovoltaic Specialists Conference,* p.002820, (2011). DOI: 10.1109/pvsc.2011.6186531.

258 X. Fontané et al. 'In-depth resolved Raman scattering analysis for the identification of secondary phases: Characterisation of Cu_2ZnSnS_4 layers for solar cell applications'. *Applied Physics Letters* **98** (18), p.181905.1, (2011). DOI: 10.1063/1.3587614.

259 D. Nam et al. 'Solar conversion efficiency and distribution of ZnS secondary phase in Cu_2ZnSnS_4 solar cells'. *Solar Energy Materials and Solar Cells* **149**, p.226, (2016). DOI: 10.1016/j.solmat.2016.01.025.

260 G. Chen et al. 'Formation mechanism of secondary phases in Cu_2ZnSnS_4 growth under different copper content'. *Materials Letters* **186**, p.98, (2017). DOI: 10.1016/j.matlet.2016.09.090.

261 Y. Ren et al. 'Evolution of Cu_2ZnSnS_4 during non-equilibrium annealing with quasi-in situ monitoring of sulphur partial pressure'. *Chemistry of Materials* **29** (8), p.3713, (2017). DOI: 10.1021/acs.chemmater.7b00671.

262 Y. Ren et al. 'Investigation of the SnS/Cu_2ZnSnS_4 interfaces in kesterite thin film solar cells'. *ACS Energy Letters* **2** (5), p.976, (2017). DOI: 10.1021/acsenergylett.7b00151.

263 J.P.F. Jemetio, P. Zhou, & H. Kleinke. 'Crystal structure, electronic structure and thermoelectric properties of $Cu_4Sn_7S_{16}$'. *Journal of Alloys and Compounds* **417** (1-2), p.55, (2006). DOI: 10.1016/j.jallcom.2005.09.030.

264 P.A. Fernandes, P.M.P. Salomé, & A.F. da Cunha. 'Precursors' order effect on the properties of sulphurised Cu_2ZnSnS_4 thin films'. *Semiconductor Science and Technology* **24** (10), p.105013.1, (2009). DOI: 10.1088/0268-1242/24/10/105013.

265 G.Y. Kim et al. 'Effects of $Cu_{2-x}S$ phase removal on surface potential of Cu_2ZnSnS_4 thin films grown by electroplating'. *Current Applied Physics* **14** (12), p.1665, (2014). DOI: 10.1016/j.cap.2014.09.009.

266 T. Nguyen et al. 'Raman scattering studies of Cu_2ZnSnS_4 thin films: Local distribution of the secondary phase $Cu_{2-x}S$ and the effect of KCN etching on $Cu_{2-x}S$'. *Journal of the Korean Physical Society* **66** (1), p.117, (2015). DOI: 10.3938/jkps.66.117.

267 M. Bär et al. 'Cliff-like conduction band offset and KCN-induced recombination barrier enhancement at the CdS/Cu_2ZnSnS_4 thin film solar cell heterojunction'. *Applied Physics Letters* **99** (22), p.222105.1, (2011). DOI: 10.1063/1.3663327.

268 A. Fairbrother et al. 'Development of a selective chemical etch to improve the conversion efficiency of Zn-rich Cu_2ZnSnS_4 solar cells'. *Journal of the American Chemical Society* **134** (19), p.8018, (2012). DOI: 10.1021/ja301373e.

269 Z. Wei et al. 'Raman mapping analysis for removal of surface secondary phases of CZTS films using chemical etching'. *Applied Physics Letters* **109** (12), p.123902.1, (2016). DOI: 10.1063/1.4963134.

270 J.B. Li, V. Chawla, & B.M. Clemens. 'Investigating the role of grain boundaries in CZTS and CZTSSe thin film solar cells with scanning probe microscopy'. *Advanced Materials* **24** (6), p.720, (2012). DOI: 10.1002/adma.201103470.

271 B.G. Mendis, L. Bowen, & Q.Z. Jiang. 'A contactless method for measuring the recombination velocity of an individual grain boundary in thin film photovoltaics'. *Applied Physics Letters* **97** (9), p.092112.1, (2010). DOI: 10.1063/1.3486482.

272 B.G. Mendis & K. Durose. 'Prospects for electron microscopy characterisation of solar cells: Opportunities and challenges'. *Ultramicroscopy* **119**, p.82, (2012). DOI: 10.1016/j.ultramic.2011.09.010.

273 A. Ennaoui et al. 'Cu_2ZnSnS_4 thin film solar cells from electroplated precursors: Novel low-cost perspective'. *Thin Solid Films* **517** (7), p.2511, (2009). DOI: 10.1016/j.tsf.2008.11.061.

274 U. Rau, K. Taretto, & S. Siebentritt. 'Grain boundaries in $Cu(In,Ga)(Se,S)_2$ thin-film solar cells'. *Applied Physics A* **96** (1), p.221, (2008). DOI: 10.1007/s00339-008-4978-0.

275 G.Y. Kim et al. 'Surface potential on grain boundaries and intragrains of highly efficient $Cu_2ZnSn(S,Se)_4$ thin films grown by two-step sputtering process'. *Solar Energy Materials and Solar Cells* **127**, p.129, (2014). DOI: 10.1016/j.solmat.2014.04.019.

276 Y. Jin & S.T. Dunham. 'The impact of charged grain boundaries on CdTe solar cell: EBIC measurements not predictive of device performance'. *IEEE Journal of Photovoltaics* **7** (1), p.329, (2017). DOI: 10.1109/jphotov.2016.2631298.

277 N.P. Klochko et al. 'Structure, optical, electrical and electronic parameters of a new thin film composition for kesterite solar cell'. *Solar Energy* **144**, p.818, (2017). DOI: 10.1016/j.solener.2016.11.054.

278 N. Muhunthan et al. 'Electrical characterisation of grain boundaries of CZTS thin films using conductive atomic force microscopy techniques'. *Materials Research Bulletin* **70**, p.373, (2015). DOI: 10.1016/j.materresbull.2015.05.002.

279 S. Chen et al. 'Defect physics of the kesterite thin film solar cell absorber Cu_2ZnSnS_4'. *Applied Physics Letters* **96** (2), p.021902.1, (2010). DOI: 10.1063/1.3275796.

280 A. Nagoya et al. 'Defect formation and phase stability of Cu_2ZnSnS_4 photovoltaic material'. *Physical Review B* **81** (11), p.113202.1, (2010). DOI: 10.1103/physrevb.81.113202.

281 T. Maeda, S. Nakamura, & T. Wada. 'First principles calculations of defect formation in In-free photovoltaic semiconductors Cu_2ZnSnS_4 and $Cu_2ZnSnSe_4$'. *Japanese Journal of Applied Physics* **50** (4S), p.04DP07.1, (2011). DOI: 10.1143/jjap.50.04dp07.

282 A. Walsh et al. 'Kesterite thin film solar cells: Advances in materials modelling of Cu_2ZnSnS_4'. *Advanced Energy Materials* **2** (4), p.400, (2012). DOI: 10.1002/aenm.201100630.

283 S. Chen et al. 'Classification of lattice defects in the kesterite Cu_2ZnSnS_4 and $Cu_2ZnSnSe_4$ Earth-abundant solar cell absorbers'. *Advanced Materials* **25** (11), p.1522, (2013). DOI: 10.1002/adma.201203146.

284 D. Mutter & S.T. Dunham. 'Calculation of defect concentrations and phase stability in Cu_2ZnSnS_4 and $Cu_2ZnSnSe_4$ from stoichiometry'. *IEEE Journal of Photovoltaics* **5** (4), p.1188, (2015). DOI: 10.1109/jphotov.2015.2430015.

285 W. Xiao et al. 'Intrinsic defects and Na doping in Cu_2ZnSnS_4: A density functional theory study'. *Solar Energy* **116**, p.125, (2015). DOI: 10.1016/j.solener.2015.04.005.

286 K. Yu & E.A. Carter. 'Elucidating structural disorder and the effects of Cu vacancies on the electronic properties of Cu_2ZnSnS_4'. *Chemistry of Materials* **28** (3), p.864, (2016). DOI: 10.1021/acs.chemmater.5b04351.

287 K. Yu & E.A. Carter. 'Determining and controlling the stoichiometry of Cu_2ZnSnS_4 photovoltaics: The physics and its implications'. *Chemistry of Materials* **28** (12), p.4415, (2016). DOI: 10.1021/acs.chemmater.6b01612.

288 X. Zhang et al. 'The instability of S vacancies in Cu_2ZnSnS_4'. *RSC Advances* **6** (19), p.15424, (2016). DOI: 10.1039/c5ra24585k.

289 V. Kosyak et al. 'Calculation of point defect concentration in Cu_2ZnSnS_4: Insights into the high-temperature equilibrium and quenching'. *Journal of Applied Physics* **122** (3), p.035707.1, (2017). DOI: 10.1063/1.4994689.

290 M. Courel, J.A. Andrade-Arvizu, & O. Vigil-Galán. 'Loss mechanisms influence on Cu_2ZnSnS_4/CdS-based thin film solar cell performance'. *Solid-State Electronics* **111**, p.243, (2015). DOI: 10.1016/j.sse.2015.05.038.

291 S. Shang et al. 'Cation disorder regulation by microstate configurational entropy in photovoltaic absorber materials $Cu_2ZnSn(S,Se)_4$'. *The Journal of Physical Chemistry C* **118** (43), p.24884, (2014). DOI: 10.1021/jp508840s.

292 C. Malerba et al. 'Stoichiometry effect on Cu_2ZnSnS_4 thin films morphological and optical properties'. *Journal of Renewable and Sustainable Energy* **6** (1), p.011404.1, (2014). DOI: 10.1063/1.4866258.

293 M. Grossberg et al. 'Photoluminescence study of disordering in the cation sublattice of Cu_2ZnSnS_4'. *Current Applied Physics* **14** (11), p.1424, (2014). DOI: 10.1016/j.cap.2014.08.013.

294 S. Chen et al. 'Abundance of $[Cu_{Zn} + Sn_{Zn}]$ and $[2Cu_{Zn} + Sn_{Zn}]$ defect clusters in kesterite solar cells'. *Applied Physics Letters* **101** (22), p.223901, (2012). DOI: 10.1063/1.4768215.

295 M. Paris et al. 'Solid-state NMR and Raman spectroscopy to address the local structure of defects and the tricky issue of the Cu/Zn disorder in Cu-poor, Zn-rich CZTS materials'. *Inorganic Chemistry* **53** (16), p.8646, (2014). DOI: 10.1021/ic5012346.

296 M. Paris et al. '^{119}Sn MAS NMR to assess the cationic disorder and the anionic distribution in sulphoselenide $Cu_2ZnSn(S_xSe_{1-x})_4$ compounds prepared from colloidal and ceramic routes'. *The Journal of Physical Chemistry C* **119** (48), p.26849, (2015). DOI: 10.1021/acs.jpcc.5b08938.

297 G. Gurieva et al. 'Structural characterisation of $Cu_{2.04}Zn_{0.91}Sn_{1.05}S_{2.08}Se_{1.92}$'. *Physica Status Solidi C* **12** (6), p.588, (2015). DOI: 10.1002/pssc.201400307.

298 L.E. Valle-Rios et al. 'Existence of off-stoichiometric single phase kesterite'. *Journal of Alloys and Compounds* **657**, p.408, (2016). DOI: 10.1016/j.jallcom.2015.09.198.

299 A. Ritscher et al. 'Off-stoichiometric CZTS: Neutron scattering investigations on mechanochemically synthesised powders'. *Journal of Alloys and Compounds* **689**, p.271, (2016). DOI: 10.1016/j.jallcom.2016.07.298.

300 A.A. Barragan et al. 'Grain-to-grain compositional variations and phase segregation in copper zinc tin sulphide films'. *ACS Applied Materials & Interfaces* **8** (35), p.22971, (2016). DOI: 10.1021/acsami.6b04982.

301 W.M. Hlaing Oo et al. 'Grain size and texture of Cu_2ZnSnS_4 thin films synthesised by cosputtering binary sulphides and annealing: Effects of processing conditions and sodium'. *Journal of Electronic Materials* **40** (11), p.2214, (2011). DOI: 10.1007/s11664-011-1729-3.

302 T. Prabhakar & J. Nagaraju. 'Alkali assisted enhancement of CZTS absorber layer characteristics'. *Proceedings of the 37th IEEE Photovoltaic Specialists Conference,* p.001357, (2011). DOI: 10.1109/pvsc.2011.6186209.

303 T. Prabhakar & N. Jampana. 'Effect of sodium diffusion on the structural and electrical properties of Cu_2ZnSnS_4 thin films'. *Solar Energy Materials and Solar Cells* **95** (3), p.1001, (2011). DOI: 10.1016/j.solmat.2010.12.012.

304 J.C. González et al. 'Influence of the sulphurisation time on the morphological, chemical, structural and electrical properties of Cu_2ZnSnS_4 polycrystalline thin films'. *Solar Energy Materials and Solar Cells* **123**, p.58, (2014). DOI: 10.1016/j.solmat.2014.01.005.

305 M. Johnson et al. 'Alkali-metal-enhanced grain growth in Cu_2ZnSnS_4 thin films'. *Energy & Environmental Science* **7** (6), p.1931, (2014). DOI: 10.1039/c3ee44130j.

306 A. Nagaoka et al. 'Effects of sodium on electrical properties in Cu_2ZnSnS_4 single crystal'. *Applied Physics Letters* **104** (15), p.152101.1, (2014). DOI: 10.1063/1.4871208.

307 A.D. Collord, H. Xin, & H.W. Hillhouse. 'Combinatorial exploration of the effects of intrinsic and extrinsic defects in $Cu_2ZnSn(S,Se)_4$'. *IEEE Journal of Photovoltaics* **5** (1), p.288, (2015). DOI: 10.1109/jphotov.2014.2361053.

308 T. Gershon et al. 'The role of sodium as a surfactant and suppressor of non-radiative recombination at internal surfaces in Cu_2ZnSnS_4'. *Advanced Energy Materials* **5** (2), p.1400849.1, (2015). DOI: 10.1002/aenm.201400849.

309 L.Q. Phuong et al. 'Photocarrier dynamics in undoped and Na-doped Cu_2ZnSnS_4 single crystals revealed by ultrafast time-resolved terahertz spectroscopy'. *Applied Physics Express* **8** (6), p.062303.1, (2015). DOI: 10.7567/apex.8.062303.

310 S. Tajima et al. 'Sodium distribution in solar-grade Cu_2ZnSnS_4 layers using atom-probe tomographic technique'. *Japanese Journal of Applied Physics* **54** (11), p.112302.1, (2015). DOI: 10.7567/jjap.54.112302.

311 Q. Wen et al. 'Crystal size-controlled growth of Cu_2ZnSnS_4 films by optimising the Na doping concentration'. *Materials Letters* **140**, p.16, (2015). DOI: 10.1016/j.matlet.2014.10.147.

312 K.-J. Yang et al. 'Two different effects of Na on Cu_2ZnSnS_4 thin film solar cells'. *Current Applied Physics* **15** (11), p.1512, (2015). DOI: 10.1016/j.cap.2015.08.021.

313 S.-Y. Li et al. 'Optical properties of reactively sputtered Cu_2ZnSnS_4 solar absorbers determined by spectroscopic ellipsometry and spectrophotometry'. *Solar Energy Materials and Solar Cells* **149**, p.170, (2016). DOI: 10.1016/j.solmat.2016.01.014.

314 O.P. Singh et al. 'Sodium induced grain growth, defect passivation and enhancement in the photovoltaic properties of Cu_2ZnSnS_4 thin film solar cell'. *Materials Chemistry and Physics* **177**, p.293, (2016). DOI: 10.1016/j.matchemphys.2016.04.030.

315 K. Sun et al. 'Influence of sodium incorporation on kesterite Cu_2ZnSnS_4 solar cells fabricated on stainless steel substrates'. *Solar Energy Materials and Solar Cells* **157**, p.565, (2016). DOI: 10.1016/j.solmat.2016.07.036.

316 L. Yuan et al. 'Investigation of sodium distribution in Cu_2ZnSnS_4 thin films and its effects on the performance of the solar cells'. *Materials Research Bulletin* **84**, p.314, (2016). DOI: 10.1016/j.materresbull.2016.08.003.

317 R. Aninat et al. 'Mapping and comparison of the shortcomings of kesterite absorber layers, and how they could affect industrial scalability'. *Thin Solid Films* **633**, p.146, (2017). DOI: 10.1016/j.tsf.2016.10.007.

318 J.P. Leitão et al. 'Photoluminescence and electrical study of fluctuating potentials in Cu_2ZnSnS_4-based thin films'. *Physical Review B* **84** (2), p.024120.1, (2011). DOI: 10.1103/physrevb.84.024120.

319 J.P. Leitão et al. 'Study of optical and structural properties of Cu_2ZnSnS_4 thin films'. *Thin Solid Films* **519** (21), p.7390, (2011). DOI: 10.1016/j.tsf.2010.12.105.

320 B.G. Mendis et al. 'Direct observation of Cu, Zn cation disorder in Cu_2ZnSnS_4 solar cell absorber material using aberration corrected scanning transmission electron microscopy'. *Progress in Photovoltaics: Research and Applications* **22** (1), p.24, (2012). DOI: 10.1002/pip.2279.

321 T. Gokmen et al. 'Band tailing and efficiency limitation in kesterite solar cells'. *Applied Physics Letters* **103** (10), p.103506.1, (2013). DOI: 10.1063/1.4820250.

322 D.P. Halliday et al. 'Luminescence of Cu_2ZnSnS_4 polycrystals described by the fluctuating potential model'. *Journal of Applied Physics* **113** (22), p.223503.1, (2013). DOI: 10.1063/1.4810846.

323 B.G. Mendis et al. 'The nature of electrostatic potential fluctuations in Cu_2ZnSnS_4 and their role on photovoltaic device performance'. *Journal of Physics: Conference Series* **471** (1), p.012014.1, (2013). DOI: 10.1088/1742-6596/471/1/012014.

324 L.Q. Phuong et al. 'Photocarrier localisation and recombination dynamics in Cu_2ZnSnS_4 single crystals'. *Applied Physics Letters* **103** (19), p.191902.1, (2013). DOI: 10.1063/1.4829063.

325 O. Gunawan, T. Gokmen, & D.B. Mitzi. 'Suns-V_{OC} characteristics of high-performance kesterite solar cells'. *Journal of Applied Physics* **116** (8), p.084504.1, (2014). DOI: 10.1063/1.4893315.

326 L.Q. Phuong et al. 'Temperature-dependent photocarrier recombination dynamics in Cu_2ZnSnS_4 single crystals'. *Applied Physics Letters* **104** (8), p.081907.1, (2014). DOI: 10.1063/1.4866666.

327 J.P. Teixeira et al. 'Comparison of fluctuating potentials and donor-acceptor pair transitions in a Cu-poor Cu_2ZnSnS_4-based solar cell'. *Applied Physics Letters* **105** (16), p.163901.1, (2014). DOI: 10.1063/1.4899057.

328 J.P. Teixeira et al. 'Radiative transitions in highly doped and compensated chalcopyrites and kesterites: The case of Cu_2ZnSnS_4'. *Physical Review B* **90** (23), p.235202.1, (2014). DOI: 10.1103/physrevb.90.235202.

329 A. Abelenda et al. 'Anomalous persistent photoconductivity in Cu_2ZnSnS_4 thin films and solar cells'. *Solar Energy Materials and Solar Cells* **137**, p.164, (2015). DOI: 10.1016/j.solmat.2015.02.001.

330 B.G. Mendis et al. 'Nanometre-scale optical property fluctuations in Cu_2ZnSnS_4 revealed by low temperature cathodoluminescence'. *Solar Energy Materials and Solar Cells* **174** (Supplement C), p.65, (2017). DOI: 10.1016/j.solmat.2017.08.028.

331 U. Rau & J.H. Werner. 'Radiative efficiency limits of solar cells with lateral band-gap fluctuations'. *Applied Physics Letters* **84** (19), p.3735, (2004). DOI: 10.1063/1.1737071.

332 M. Grossberg et al. 'The role of structural properties on deep defect states in Cu_2ZnSnS_4 studied by photoluminescence spectroscopy'. *Applied Physics Letters* **101** (10), p.102102.1, (2012). DOI: 10.1063/1.4750249.

333 A.P. Levanyuk & V.V. Osipov. 'Edge luminescence of direct-gap semiconductors'. *Soviet Physics Uspekhi* **24** (3), p.187, (1981). DOI: 10.1070/pu1981v024n03abeh004770.

334 N. Song et al. 'Heteroepitaxial growth of Cu_2ZnSnS_4 thin film on sapphire substrate by radio frequency magnetron sputtering'. *Applied Physics Letters* **104** (9), p.092103.1, (2014). DOI: 10.1063/1.4867093.

335 N. Song, X. Wen, & X. Hao. 'Radio frequency magnetron sputtered highly textured Cu_2ZnSnS_4 thin films on sapphire (0001) substrates'. *Journal of Alloys and Compounds* **632**, p.53, (2015). DOI: 10.1016/j.jallcom.2015.01.192.

336 N. Song et al. 'Diode laser annealing on sputtered epitaxial Cu_2ZnSnS_4 thin films'. *Physica Status Solidi Rapid Research Letters* **11** (5), p.1700033.1, (2017). DOI: 10.1002/pssr.201700033.

337 V. Chawla & B. Clemens. 'Inexpensive, abundant, non-toxic thin films for solar cell applications grown by reactive sputtering'. *Proceedings of the 35th IEEE Photovoltaic Specialists Conference,* p.001902, (2010). DOI: 10.1109/pvsc.2010.5616337.

338 G.K. Dalapati et al. 'Sputter grown sub-micrometer thick Cu_2ZnSnS_4 thin film for photovoltaic device application'. *Materials Letters* **160**, p.45, (2015). DOI: 10.1016/j.matlet.2015.07.089.

339 H.R. Jung et al. 'Evolution of detrimental secondary phases in unstable Cu_2ZnSnS_4 films during annealing'. *Electronic Materials Letters* **12** (1), p.139, (2016). DOI: 10.1007/s13391-015-5340-2.

340 S.K. Samji, R. Mannam, & M.S.R. Rao. 'Do defects get ordered in Cu_2ZnSnS_4?'. *Scripta Materialia* **117**, p.11, (2016). DOI: 10.1016/j.scriptamat.2016.02.009.

341 Z. Zhou et al. 'Fabrication of Cu_2ZnSnS_4 screen printed layers for solar cells'. *Solar Energy Materials and Solar Cells* **94** (12), p.2042, (2010). DOI: 10.1016/j.solmat.2010.06.010.

342 J. Xu et al. 'Fabrication of Cu_2ZnSnS_4 thin films on flexible polyimide substrates by sputtering and post-sulphurisation'. *Journal of Renewable and Sustainable Energy* **6** (5), p.053110.1, (2014). DOI: 10.1063/1.4896696.

343 C.-Y. Peng et al. 'Fabrication of Cu_2ZnSnS_4 solar cell on a flexible glass substrate'. *Thin Solid Films* **562**, p.574, (2014). DOI: 10.1016/j.tsf.2014.03.054.

344 J. Xu et al. 'Characterisation of Cu_2ZnSnS_4 thin films on flexible metal foil substrates'. *Journal of Materials Science: Materials in Electronics* **26** (2), p.726, (2015). DOI: 10.1007/s10854-014-2456-3.

345 S. Yazici et al. 'Growth of Cu_2ZnSnS_4 absorber layer on flexible metallic substrates for thin film solar cell applications'. *Thin Solid Films* **589**, p.563, (2015). DOI: 10.1016/j.tsf.2015.06.028.

346 A. Fairbrother et al. 'On the formation mechanisms of Zn-rich Cu_2ZnSnS_4 films prepared by sulphurisation of metallic stacks'. *Solar Energy Materials and Solar Cells* **112**, p.97, (2013). DOI: 10.1016/j.solmat.2013.01.015.

347 P.K. Sarswat & M.L. Free. 'An assessment of contact engineering for the Cu_2ZnSnS_4 alternative back contact'. *Materials Focus* **2** (4), p.244, (2013). DOI: 10.1166/mat.2013.1082.

348 O. Vigil-Galán et al. 'Toward a high Cu_2ZnSnS_4 solar cell efficiency processed by spray pyrolysis method'. *Journal of Renewable and Sustainable Energy* **5** (5), p.053137.1, (2013). DOI: 10.1063/1.4825253.

349 G. Altamura et al. 'Alternative back contacts in kesterite $Cu_2ZnSn(S_{1-x}Se_x)_4$ thin film solar cells'. *Journal of Renewable and Sustainable Energy* **6** (1), p.011401.1, (2014). DOI: 10.1063/1.4831781.

350 J.J. Scragg et al. 'A detrimental reaction at the molybdenum back contact in $Cu_2ZnSn(S,Se)_4$ thin film solar cells'. *Journal of the American Chemical Society* **134** (47), p.19330, (2012). DOI: 10.1021/ja308862n.

351 K. Wang et al. 'Structural and elemental characterisation of high-efficiency Cu_2ZnSnS_4 solar cells'. *Applied Physics Letters* **98** (5), p.051912.1, (2011). DOI: 10.1063/1.3543621.

352 J.T. Wätjen et al. 'Secondary compound formation revealed by transmission electron microscopy at the Cu_2ZnSnS_4/Mo interface'. *Thin Solid Films* **535**, p.31, (2013). DOI: 10.1016/j.tsf.2012.11.079.

353 P. Chelvanathan et al. 'Effects of transition metal dichalcogenide molybdenum disulphide layer formation in Copper-Zinc-Tin-Sulphur solar cells from numerical analysis'. *Japanese Journal of Applied Physics* **51** (10S), p.10NC32.1, (2012). DOI: 10.1143/jjap.51.10nc32.

354 J.J. Scragg et al. 'Rapid annealing of reactively sputtered precursors for Cu_2ZnSnS_4 solar cells'. *Progress in Photovoltaics: Research and Applications*, p.10, (2012). DOI: 10.1002/pip.2265.

355 P.A. Fernandes et al. 'Cu_2ZnSnS_4 solar cells prepared with sulphurised DC-sputtered stacked metallic precursors'. *Thin Solid Films* **519** (21), p.7382, (2011). DOI: 10.1016/j.tsf.2010.12.035.

356 D. Seo et al. 'Improvement of Cu_2ZnSnS_4 thin film properties by a modified sulphurisation process'. *Thin Solid Films* **591B**, p.289, (2015). DOI: 10.1016/j.tsf.2015.05.060.

357 B. Shin et al. 'Control of an interfacial $MoSe_2$ layer in $Cu_2ZnSnSe_4$ thin film solar cells: 8.9 % power conversion efficiency with a TiN diffusion barrier'. *Applied Physics Letters* **101** (5), p.053903.1, (2012). DOI: 10.1063/1.4740276.

358 X. Zhu et al. 'Determining factor of $MoSe_2$ formation in $Cu(In,Ga)Se_2$ solar cells'. *Solar Energy Materials and Solar Cells* **101**, p.57, (2012). DOI: 10.1016/j.solmat.2012.02.015.

359 A.D. Adewoyin, M.A. Olopade, & M. Chendo. 'Enhancement of the conversion efficiency of Cu_2ZnSnS_4 thin film solar cell through the optimisation of some device parameters'. *Optik: International Journal for Light and Electron Optics* **133**, p.122, (2017). DOI: 10.1016/j.ijleo.2017.01.008.

360 B. Vermang et al. 'Rear surface optimisation of CZTS solar cells by use of a passivation layer with nanosized point openings'. *IEEE Journal of Photovoltaics* **6** (1), p.332, (2015). DOI: 10.1109/jphotov.2015.2496864.

361 H. Cui et al. 'Boosting Cu_2ZnSnS_4 solar cells efficiency by a thin Ag intermediate layer between absorber and back contact'. *Applied Physics Letters* **104** (4), p.041115.1, (2014). DOI: 10.1063/1.4863951.

362 Z. Tong et al. 'Modification of absorber quality and Mo back contact by a thin Bi intermediate layer for kesterite Cu_2ZnSnS_4 solar cells'. *Solar Energy Materials and Solar Cells* **144**, p.537, (2016). DOI: 10.1016/j.solmat.2015.09.066.

363 F. Zhou et al. 'Improvement of J_{SC} in a Cu_2ZnSnS_4 solar cell by using a thin carbon intermediate layer at the Cu_2ZnSnS_4/Mo interface'. *ACS Applied Materials & Interfaces* **7** (41), p.22868, (2015). DOI: 10.1021/acsami.5b05652.

364 F. Liu et al. 'Enhancing the Cu_2ZnSnS_4 solar cell efficiency by back contact modification: Inserting a thin TiB_2 intermediate layer at Cu_2ZnSnS_4/Mo interface'. *Applied Physics Letters* **104** (5), p.051105.1, (2014). DOI: 10.1063/1.4863736.

365 J.J. Scragg et al. 'Effects of back contact instability on Cu_2ZnSnS_4 devices and processes'. *Chemistry of Materials* **25** (15), p.3162, (2013). DOI: 10.1021/cm4015223.

366 W. Li et al. 'Inhibiting MoS_2 formation by introducing a ZnO intermediate layer for Cu_2ZnSnS_4 solar cells'. *Materials Letters* **130**, p.87, (2014). DOI: 10.1016/j.matlet.2014.05.089.

367 X. Liu et al. 'Improving Cu_2ZnSnS_4 (CZTS) solar cell performance by an ultrathin ZnO intermediate layer between CZTS absorber and Mo back contact'. *Physica Status Solidi: Rapid Research Letters* **8** (12), p.966, (2014). DOI: 10.1002/pssr.201409052.

368 M.A. Green. 'The passivated emitter and rear cell (PERC): From conception to mass production'. *Solar Energy Materials and Solar Cells* **143**, p.190, (2015). DOI: 10.1016/j.solmat.2015.06.055.

369 F. Liu et al. 'Beyond 8 % ultrathin kesterite Cu_2ZnSnS_4 solar cells by interface reaction route controlling and self-organised nanopattern at the back contact'. *NPG Asia Materials* **9**, p.e401.1, (2017). DOI: 10.1038/am.2017.103.

370 Y. Ren et al. 'Influence of the Cu_2ZnSnS_4 absorber thickness on thin film solar cells'. *Physica Status Solidi A* **212** (12), p.2889, (2015). DOI: 10.1002/pssa.201532311.

371 T.P. Dhakal et al. 'Characterisation of a CZTS thin film solar cell grown by sputtering method'. *Solar Energy* **100**, p.23, (2014). DOI: 10.1016/j.solener.2013.11.035.

372 S. Tajima et al. 'Improvement of the open-circuit voltage of Cu_2ZnSnS_4 solar cells using a two-layer structure'. *Applied Physics Express* **8** (8), p.082302.1, (2015). DOI: 10.7567/apex.8.082302.

373 C. Yan et al. 'Boost V_{OC} of pure sulphide kesterite solar cells via a double CZTS layer stack'. *Solar Energy Materials and Solar Cells* **160**, p.7, (2017). DOI: 10.1016/j.solmat.2016.09.027.

374 O.K. Simya, A. Mahaboobbatcha, & K. Balachander. 'A comparative study on the performance of kesterite-based thin film solar cells using SCAPS simulation program'. *Superlattices and Microstructures* **82**, p.248, (2015). DOI: 10.1016/j.spmi.2015.02.020.

375 H. Arbouz, A. Aissat, & J.P. Vilcot. 'Simulation and optimisation of CdS-n/Cu_2ZnSnS_4 structure for solar cell applications'. *International Journal of Hydrogen Energy* **42** (13), p.8827, (2017). DOI: 10.1016/j.ijhydene.2016.06.185.

376 M. Courel, J.A. Andrade-Arvizu, & O. Vigil-Galán. 'Towards a CdS/Cu_2ZnSnS_4 solar cell efficiency improvement: A theoretical approach'. *Applied Physics Letters* **105** (23), p.233501.1, (2014). DOI: 10.1063/1.4903826.

377 M. Danilson et al. 'Temperature dependent current transport properties in Cu_2ZnSnS_4 solar cells'. *Thin Solid Films* **582**, p.162, (2015). DOI: 10.1016/j.tsf.2014.10.069.

378 L.Q. Phuong et al. 'Ultrafast free-carrier dynamics in Cu_2ZnSnS_4 single crystals studied using femtosecond time-resolved optical spectroscopy'. *Applied Physics Letters* **105** (23), p.231902.1, (2014). DOI: 10.1063/1.4903802.

379 T.K. Todorov, K.B. Reuter, & D.B. Mitzi. 'High-efficiency solar cell with Earth-abundant liquid-processed absorber'. *Advanced Materials* **22** (20), p.E156, (2010). DOI: 10.1002/adma.200904155.

380 A. Le Donne et al. 'Effects of CdS buffer layers on photoluminescence properties of Cu_2ZnSnS_4 Solar Cells'. *International Journal of Photoenergy* **2015**, p.1, (2015). DOI: 10.1155/2015/583058.

381 C. Yan et al. 'Band alignments of different buffer layers (CdS, Zn(O,S), and In_2S_3) on Cu_2ZnSnS_4'. *Applied Physics Letters* **104** (17), p.173901.1, (2014). DOI: 10.1063/1.4873715.

382 C. Yan et al. 'Boosting the efficiency of pure sulphide CZTS solar cells using the In/Cd-based hybrid buffers'. *Solar Energy Materials and Solar Cells* **144**, p.700, (2016). DOI: 10.1016/j.solmat.2015.10.019.

383 F. Liu et al. 'Light-bias-dependent external quantum efficiency of kesterite Cu_2ZnSnS_4 solar cells'. *ACS Photonics* **4** (7), p.1684, (2017). DOI: 10.1021/acsphotonics.7b00151.

384 J. Yu et al. 'Effect of deposited temperatures of the buffer layer on the band offset of CZTS/In_2S_3 heterostructure and its solar cell performance'. *Chinese Physics B* **26** (4), p.046802.1, (2017). DOI: 10.1088/1674-1056/26/4/046802.

385 N.E. Gorji. 'Quantitative analysis of the optical losses in CZTS thin film semiconductors'. *IEEE Transactions on Nanotechnology* **13** (4), p.743, (2014). DOI: 10.1109/tnano.2014.2318057.

386 F. Jiang et al. 'Preparation and properties of Cu_2ZnSnS_4 absorber and Cu_2ZnSnS_4/amorphous silicon thin film solar cell'. *Applied Physics Express* **4** (7), p.074101.1, (2011). DOI: 10.1143/apex.4.074101.

387 G. Yang et al. 'Band alignments at interface of Cu_2ZnSnS_4/ZnO heterojunction: An X-ray photoelectron spectroscopy and first-principles study'. *Journal of Alloys and Compounds* **628**, p.293, (2015). DOI: 10.1016/j.jallcom.2014.12.174.

388 A. Nagoya, R. Asahi, & G. Kresse. 'First-principles study of Cu_2ZnSnS_4 and the related band offsets for photovoltaic applications'. *Journal of Physics: Condensed Matter* **23** (40), p.404203.1, (2011). DOI: 10.1088/0953-8984/23/40/404203.

389 N. Sakai, H. Hiroi, & H. Sugimoto. 'Development of Cd-free buffer layer for Cu_2ZnSnS_4 thin film solar cells'. *Proceedings of the 37th IEEE Photovoltaic Specialists Conference,* p.003654, (2011). DOI: 10.1109/pvsc.2011.6185941.

390 A.I. Inamdar et al. 'Controlled growth of Cu_2ZnSnS_4 (CZTS) thin films for heterojunction solar-cell applications'. *Journal of the Korean Physical Society* **60** (10), p.1730, (2012). DOI: 10.3938/jkps.60.1730.

391 J. Kim et al. 'Optimisation of sputtered ZnS buffer for Cu_2ZnSnS_4 thin film solar cells'. *Thin Solid Films* **566**, p.88, (2014). DOI: 10.1016/j.tsf.2014.07.024.

392 S. Mahajan et al. 'Enhancement in the efficiency of crystalline Cu_2ZnSnS_4 thin film solar cell by using various buffer layers'. *Superlattices and Microstructures* **109**, p.240, (2017). DOI: 10.1016/j.spmi.2017.05.009.

393 H. Zhang et al. 'Prospects of Zn(O,S) as an alternative buffer layer for Cu_2ZnSnS_4 thin film solar cells from numerical simulation'. *IET Micro & Nano Letters* **11** (7), p.386, (2016). DOI: 10.1049/mnl.2016.0130.

394 X. Hao et al. 'Large V_{OC} improvement and 9.2 % efficient pure sulphide Cu_2ZnSnS_4 solar cells by heterojunction interface engineering'. *Proceedings of the 43rd IEEE Photovoltaic Specialists Conference,* p.2164, (2016). DOI: 10.1109/pvsc.2016.7750017.

395 K. Sun et al. 'Over 9 % efficient kesterite Cu_2ZnSnS_4 solar cell fabricated by using $Zn_{1-x}Cd_xS$ Buffer Layer'. *Advanced Energy Materials* **6** (12), p.1600046.1, (2016). DOI: 10.1002/aenm.201600046.

396 M. Bär et al. 'Soft X-rays shedding light on thin film solar cell surfaces and interfaces'. *Journal of Electron Spectroscopy and Related Phenomena* **190A**, p.47, (2013). DOI: 10.1016/j.elspec.2012.10.004.

397 A. Santoni et al. 'Valence band offset at the CdS/Cu_2ZnSnS_4 interface probed by X-ray photoelectron spectroscopy'. *Journal of Physics D: Applied Physics* **46** (17), p.175101, (2013). DOI: 10.1088/0022-3727/46/17/175101.

398 D. Zi-Yuan et al. 'An experimental and first-principles study on band alignments at interfaces of Cu_2ZnSnS_4/CdS/ZnO heterojunctions'. *Journal of Physics D: Applied Physics* **47** (7), p.075304.1, (2014). DOI: 10.1088/0022-3727/47/7/075304.

399 W. Xiao et al. 'Structural and electronic properties of the heterointerfaces for Cu_2ZnSnS_4 photovoltaic cells: a density functional theory study'. *Physical Chemistry Chemical Physics* **18** (17), p.12029, (2016). DOI: 10.1039/C6cp00817h.

400 S. Tajima et al. 'Cu_2ZnSnS_4 photovoltaic cell with improved efficiency fabricated by high-temperature annealing after CdS buffer layer deposition'. *Progress in Photovoltaics: Research and Applications* **25** (1), p.14, (2016). DOI: 10.1002/pip.2837.

401 J. Kim et al. 'High-efficiency $Cu_2ZnSn(S,Se)_4$ solar cells by applying a double In_2S_3/CdS emitter'. *Advanced Materials* **26** (44), p.7427, (2014). DOI: 10.1002/adma.201402373.

402 H.-H. Yang & G.-C. Park. 'A study on the properties of MgF_2 antireflection film for solar cells'. *Transactions on Electrical and Electronic Materials* **11** (1), p.33, (2010). DOI: 10.4313/teem.2010.11.1.033.

403 S.-Y. Kuo & M.-Y. Hsieh. 'Efficiency enhancement in Cu_2ZnSnS_4 solar cells with subwavelength grating nanostructures'. *Nanoscale* **6** (13), p.7553, (2014). DOI: 10.1039/c4nr00566j.

404 S. Ahmed et al. 'A high efficiency electrodeposited Cu_2ZnSnS_4 solar cell'. *Advanced Energy Materials* **2** (2), p.253, (2012). DOI: 10.1002/aenm.201100526.

405 R. Liu et al. 'Preparation of high-quality Cu_2ZnSnS_4 thin films for solar cells via the improvement of sulphur partial pressure using a static annealing sulphurisation approach'. *Solar Energy Materials and Solar Cells* **157**, p.221, (2016). DOI: 10.1016/j.solmat.2016.05.040.

406 T. Washio et al. '6 % efficiency Cu_2ZnSnS_4-based thin film solar cells using oxide precursors by open atmosphere type chemical vapour deposition'. *Journal of Materials Chemistry* **22** (9), p.4021, (2012). DOI: 10.1039/c2jm16454j.

407 Y. Kim et al. 'Highly concentrated synthesis of copper-zinc-tin-sulfide nanocrystals with easily decomposable capping molecules for printed photovoltaic applications'. *Nanoscale* **5** (21), p.10183, (2013). DOI: 10.1039/c3nr03104g.

408 A.V. Kumar, N.-K. Park, & E.-T. Kim. 'A simple chemical approach for the deposition of Cu_2ZnSnS_4 thin films'. *Physica Status Solidi A* **211** (8), p.1857, (2014). DOI: 10.1002/pssa.201330593.

409 K. Moriya, K. Tanaka, & H. Uchiki. 'Characterisation of Cu_2ZnSnS_4 thin films prepared by photochemical deposition'. *Japanese Journal of Applied Physics* **44** (Part 1, 1B), p.715, (2005). DOI: 10.1143/jjap.44.715.

410 A. Nagaoka et al. 'Growth and characterisation of Cu_2ZnSnS_4 single crystals'. *Physica Status Solidi A* **210** (7), p.1328, (2013). DOI: 10.1002/pssa.201200815.

411 D. Colombara et al. 'Crystal growth of Cu_2ZnSnS_4 solar cell absorber by chemical vapor transport with I_2'. *Journal of Crystal Growth* **364**, p.101, (2013). DOI: 10.1016/j.jcrysgro.2012.11.037.

412 M. Himmrich & H. Haeuseler. 'Far infrared studies on stannite and wurtzstannite type compounds'. *Spectrochimica Acta Part A: Molecular Spectroscopy* **47** (7), p.933, (1991). DOI: 10.1016/0584-8539(91)80283-O.

413 Y.-M. Li et al. 'High-pressure preparation of high-density Cu_2ZnSnS_4 Materials'. *Chinese Physics Letters* **33** (7), p.076101.1, (2016). DOI: 10.1088/0256-307x/33/7/076101.

414 H. Katagiri & K. K. Jimbo. 'Development of rare metal-free CZTS-based thin film solar cells'. *Proceedings of the 37th IEEE Photovoltaic Specialists Conference,* p.003516, (2011). DOI: 10.1109/pvsc.2011.6186707.

415 B.-T. Jheng, P.-T. Liu, & M.-C. Wu. 'A promising sputtering route for dense Cu_2ZnSnS_4 absorber films and their photovoltaic performance'. *Solar Energy Materials and Solar Cells* **128**, p.275, (2014). DOI: 10.1016/j.solmat.2014.05.033.

416 B.-T. Jheng et al. 'Effects of substrate temperature on the Cu_2ZnSnS_4 films deposited by radio-frequency sputtering with single target'. *Thin Solid Films* **564**, p.345, (2014). DOI: 10.1016/j.tsf.2014.05.053.

417 Y. Feng et al. 'A low-temperature formation path toward highly efficient Se-free Cu_2ZnSnS_4 solar cells fabricated through sputtering and sulphurisation'. *CrystEngComm* **18** (6), p.1070, (2016). DOI: 10.1039/c5ce02279g.

418 F. Liu et al. 'In situ growth of Cu_2ZnSnS_4 thin films by reactive magnetron co-sputtering'. *Solar Energy Materials and Solar Cells* **94** (12), p.2431, (2010). DOI: 10.1016/j.solmat.2010.08.003.

419 T. Ericson et al. 'Annealing behavior of reactively sputtered precursor films for Cu_2ZnSnS_4 solar cells'. *Thin Solid Films* **535**, p.22, (2013). DOI: 10.1016/j.tsf.2012.10.081.

420 T. Kubart et al. 'Reactive sputtering of Cu_2ZnSnS_4 thin films: Target effects on the deposition process stability'. *Surface and Coatings Technology* **240**, p.281, (2014). DOI: 10.1016/j.surfcoat.2013.12.042.

421 P.A. Cormier & R. Snyders. 'One-step synthesis of Cu_2ZnSnS_4 thin films by reactive magnetron co-sputtering'. *Acta Materialia* **96**, p.80, (2015). DOI: 10.1016/j.actamat.2015.06.001.

422 O.P. Singh et al. 'Synthesis and characterisation of petal type CZTS by stacked layer reactive sputtering'. *Superlattices and Microstructures* **88**, p.281, (2015). DOI: 10.1016/j.spmi.2015.09.020.

423 R. Nakamura et al. 'Cu_2ZnSnS_4 thin film deposited by sputtering with Cu_2ZnSnS_4 compound target'. *Japanese Journal of Applied Physics* **53** (2S), p.02BC10.1, (2014). DOI: 10.7567/JJAP.53.02BC10.

424 J. Wang et al. 'Cu_2ZnSnS_4 thin films: Facile and cost-effective preparation by RF magnetron sputtering and texture control'. *Journal of Alloys and Compounds* **552**, p.418, (2013). DOI: 10.1016/j.jallcom.2012.11.082.

425 M. Xie et al. 'Fabrication of Cu_2ZnSnS_4 thin films using a ceramic quaternary target'. *Vacuum* **101**, p.146, (2014). DOI: 10.1016/j.vacuum.2013.08.001.

426 N. Nafarizal, S. Kikuchi, & K. Sasaki. 'Sticking probabilities of Cu, Zn, Sn, and S atoms in magnetron sputtering plasmas employing a Cu_2ZnSnS_4 stoichiometric target'. *Vacuum* **121**, p.26, (2015). DOI: 10.1016/j.vacuum.2015.07.019.

427 Y.-P. Lin et al. 'Preparation of Cu_2ZnSnS_4 (CZTS) sputtering target and its application to the fabrication of CZTS thin-film solar cells'. *Journal of Alloys and Compounds* **654**, p.498, (2016). DOI: 10.1016/j.jallcom.2015.09.111.

428 R. Sun et al. 'Cu_2ZnSnS_4 ceramic target: Determination of sintering temperature by TG-DSC'. *Ceramics International* **42** (8), p.9630, (2016). DOI: 10.1016/j.ceramint.2016.03.048.

429 F. Yang et al. 'Fabrication of Cu_2ZnSnS_4 (CZTS) absorber films based on different compound targets'. *Journal of Alloys and Compounds* **689**, p.849, (2016). DOI: 10.1016/j.jallcom.2016.08.053.

430 G. Zoppi et al. 'Electrical, morphological and structural properties of RF magnetron sputtered Mo thin films for application in thin film photovoltaic solar cells'. *Journal of Materials Science* **46** (14), p.4913, (2011). DOI: 10.1007/s10853-011-5404-0.

431 J.H. Scofield et al. 'Sputtered molybdenum bilayer back contact for copper indium diselenide-based polycrystalline thin film solar cells'. *Thin Solid Films* **260** (1), p.26, (1995). DOI: 10.1016/0040-6090(94)06462-8.

432 Z.-S. Li et al. 'Cu_2ZnSnS_4 solar cells prepared by sulphurisation of sputtered ZnS/Sn/CuS precursors'. *Physica B: Condensed Matter* **502**, p.56, (2016). DOI: 10.1016/j.physb.2016.08.014.

433 K.-J. Yang et al. 'Effects of Na and MoS_2 on Cu_2ZnSnS_4 thin film solar cell'. *Progress in Photovoltaics: Research and Applications* **23** (7), p.862, (2015). DOI: 10.1002/pip.2500.

434 H. Cui et al. 'Impact of rapid thermal annealing of Mo coated soda lime glass substrate on device performance of evaporated Cu_2ZnSnS_4 thin film solar cells'. *Materials Letters* **125**, p.40, (2014). DOI: 10.1016/j.matlet.2014.03.122.

435 X. Liu et al. 'Rapid thermal annealed molybdenum back contact for Cu_2ZnSnS_4 thin film solar cells'. *Applied Physics Letters* **106** (13), p.131110.1, (2015). DOI: 10.1063/1.4916994.

436 K.-S. Lim et al. 'Comparison of Cu_2ZnSnS_4 thin films and solar cell performance using Zn target with ZnS target'. *Journal of Alloys and Compounds* **650**, p.641, (2015). DOI: 10.1016/j.jallcom.2015.08.056.

437 H. Katagiri. 'Cu_2ZnSnS_4 thin film solar cells'. *Thin Solid Films* **480-481**, p.426, (2005). DOI: 10.1016/j.tsf.2004.11.024.

438 S.M. Yu et al. 'Effect of the intermediate sulphide layer on the Cu_2ZnSnS_4-based solar cells'. *Journal of Materials Science: Materials in Electronics* **28** (7), p.5696, (2017). DOI: 10.1007/s10854-016-6241-3.

439 H. Yoo & J. Kim. 'Growth of Cu_2ZnSnS_4 thin films using sulphurisation of stacked metallic films'. *Thin Solid Films* **518** (22), p.6567, (2010). DOI: 10.1016/j.tsf.2010.03.058.

440 H.-J. Chen et al. 'Impact of SnS buffer layer at Mo/Cu_2ZnSnS_4 interface'. *Journal of the American Ceramic Society* **99** (5), p.1808, (2016). DOI: 10.1111/jace.14153.

441 H.-J. Chen et al. 'Comparative study of self-constituent buffer layers (CuS, SnS, ZnS) for synthesis Cu_2ZnSnS_4 thin films'. *Materials Letters* **169**, p.126, (2016). DOI: 10.1016/j.matlet.2016.01.030.

442 W. Li et al. 'The effect of ZnS segregation on Zn-rich CZTS thin film solar cells'. *Journal of Alloys and Compounds* **632**, p.178, (2015). DOI: 10.1016/j.jallcom.2015.01.205.

443 E.M. Mkawi et al. 'Influence of precursor thin films stacking order on the properties of Cu_2ZnSnS_4 thin films fabricated by electrochemical deposition method'. *Superlattices and Microstructures* **76**, p.339, (2014). DOI: 10.1016/j.spmi.2014.10.022.

444 N. Thota et al. 'Effect of metal layer stacking order on the growth of Cu_2ZnSnS_4 thin films'. *Applied Surface Science* **396**, p.644, (2017). DOI: 10.1016/j.apsusc.2016.11.001.

445 S.W. Shin et al. 'Studies on Cu_2ZnSnS_4 (CZTS) absorber layer using different stacking orders in precursor thin films'. *Solar Energy Materials and Solar Cells* **95** (12), p.3202, (2011). DOI: 10.1016/j.solmat.2011.07.005.

446 H. Yoo & J. Kim. 'Comparative study of Cu_2ZnSnS_4 film growth'. *Solar Energy Materials and Solar Cells* **95** (1), p.239, (2011). DOI: 10.1016/j.solmat.2010.04.060.

447 D.-H. Son et al. 'Influence of precursor sulphur content on film formation and the properties of sulphurised Cu_2ZnSnS_4 thin films for solar cells'. *Physica Status Solidi A* **211** (4), p.946, (2014). DOI: 10.1002/pssa.201330425.

448 M.A. Olgar et al. 'Effect of precursor stacking order and sulphurisation temperature on compositional homogeneity of CZTS thin films'. *Thin Solid Films* **615**, p.402, (2016). DOI: 10.1016/j.tsf.2016.07.058.

449 Y. Lu et al. 'Effects of sputtering period on the performance of Cu_2ZnSnS_4 solar cells'. *Physica B: Condensed Matter* **507**, p.35, (2017). DOI: 10.1016/j.physb.2016.11.019.

450 M.G. Sousa et al. 'Optimisation of post-deposition annealing in Cu_2ZnSnS_4 thin film solar cells and its impact on device performance'. *Solar Energy Materials and Solar Cells* **170**, p.287, (2017). DOI: 10.1016/j.solmat.2017.05.065.

451 C.-Y. Su, C. Yen Chiu, & J.-M. Ting. 'Cu_2ZnSnS_4 absorption layers with controlled phase purity'. *Scientific Reports* **5**, p.9291.1, (2015). DOI: 10.1038/srep09291.

452 R.A. Colina-Ruiz et al. 'Local atomic structure and analysis of secondary phases in non-stoichiometric Cu_2ZnSnS_4 using X-ray absorption fine structure spectroscopy'. *Journal of Alloys and Compounds* **714**, p.381, (2017). DOI: 10.1016/j.jallcom.2017.04.191.

453 X. Li et al. 'Investigation of Cu_2ZnSnS_4 thin films with controllable Cu composition and its influence on photovoltaic properties for solar cells'. *Journal of Alloys and Compounds* **694**, p.833, (2017). DOI: 10.1016/j.jallcom.2016.10.024.

454 M. Abusnina et al. 'Suppression of the $Cu_{2-x}S$ secondary phases in CZTS films through controlling the film elemental composition'. *IEEE Journal of Photovoltaics* **5** (5), p.1470, (2015). DOI: 10.1109/jphotv.2015.2447834.

455 J. Just et al. 'Secondary phases and their influence on the composition of the kesterite phase in CZTS and CZTSe thin films'. *Physical Chemistry Chemical Physics* **18** (23), p.15988, (2016). DOI: 10.1039/c6cp00178e.

456 S. Gupta et al. 'A low-cost, sulphurisation free approach to control optical and electronic properties of Cu_2ZnSnS_4 via precursor variation'. *Solar Energy Materials and Solar Cells* **157**, p.820, (2016). DOI: 10.1016/j.solmat.2016.08.004.

457 T. Tanaka et al. 'Influence of composition ratio on properties of Cu_2ZnSnS_4 thin films fabricated by co-evaporation'. *Thin Solid Films* **518** (21, Supplement), p.S29, (2010). DOI: 10.1016/j.tsf.2010.03.026.

458 K.U. Isah et al. 'Effect of different copper precursor layer thickness on properties of Cu_2ZnSnS_4 (CZTS) thin films prepared by sulphurisation of thermally deposited stacked metallic layers'. *Journal of Applied Physics* **2** (6), p.14, (2013). DOI: 10.9790/4861-0261419.

459 W. Li et al. 'Fabrication of Cu_2ZnSnS_4 thin film solar cells by annealing of reactively sputtered precursors'. *Journal of Alloys and Compounds* **701**, p.55, (2017). DOI: 10.1016/j.jallcom.2016.12.285.

460 N. Nakayama & K. Ito. 'Sprayed films of stannite Cu_2ZnSnS_4'. *Applied Surface Science* **92**, p.171, (1996). DOI: 10.1016/0169-4332(95)00225-1.

461 Y. Feng et al. 'The dependence of open-circuit voltage on the element component in Cu_2ZnSnS_4 film solar cells'. *Surface and Coatings Technology* **320**, p.65, (2017). DOI: 10.1016/j.surfcoat.2017.01.117.

462 H. Du et al. 'Investigation of combinatorial co-evaporated thin film Cu_2ZnSnS_4 (I): Temperature effect, crystalline phases, morphology, and photoluminescence'. *Journal of Applied Physics* **115** (17), p.173502.1, (2014). DOI: 10.1063/1.4871664.

463 C. Sripan et al. 'The effect of sulphur on the phase formation of Cu_2ZnSnS_4 solar cell material'. *Materials Letters* **180**, p.295, (2016). DOI: 10.1016/j.matlet.2016.05.027.

464 T. Ericson et al. 'Reactive sputtering of precursors for Cu_2ZnSnS_4 thin film solar cells'. *Thin Solid Films* **520** (24), p.7093, (2012). DOI: 10.1016/j.tsf.2012.08.002.

465 I.V. Bodnar et al. 'Transmittance spectra of Cu_2ZnSnS_4 thin films'. *Journal of Electronic Materials* **44** (10), p.3283, (2015). DOI: 10.1007/s11664-015-3909-z.

466 S.A. Khalate et al. 'Effect of deposition temperature on the properties of Cu_2ZnSnS_4 (CZTS) thin films'. *Superlattices and Microstructures* **103**, p.335, (2017). DOI: 10.1016/j.spmi.2017.02.003.

467 V. Robles et al. 'Cu_2ZnSnS_4 thin films obtained by sulphurisation of evaporated Cu_2SnS_3 and ZnS layers: Influence of the ternary precursor features'. *Applied Surface Science* **400**, p.220, (2017). DOI: 10.1016/j.apsusc.2016.12.186.

468 Q. Zhao et al. 'Fabrication and characterisation of Cu_2ZnSnS_4 thin films by sputtering a single target at different temperatures'. *Physica B: Condensed Matter* **523**, p.62, (2017). DOI: 10.1016/j.physb.2017.08.035.

469 M. Valdés, G. Santoro, & M. Vázquez. 'Spray deposition of Cu_2ZnSnS_4 thin films'. *Journal of Alloys and Compounds* **585**, p.776, (2014). DOI: 10.1016/j.jallcom.2013.10.009.

470 R. Touati, M. Ben Rabeh, & M. Kanzari. 'Effect of post-sulphurisation on the structural and optical properties of Cu_2ZnSnS_4 thin films deposited by vacuum evaporation method'. *Thin Solid Films* **582**, p.198, (2015). DOI: 10.1016/j.tsf.2014.12.032.

471 P. Bras, J. Sterner, & C. Platzer-Björkman. 'Investigation of blister formation in sputtered Cu_2ZnSnS_4 absorbers for thin film solar cells'. *Journal of Vacuum Science & Technology A: Vacuum, Surfaces, and Films* **33** (6), p.061201.1, (2015). DOI: 10.1116/1.4926754.

472 C. Malerba et al. 'Blistering in Cu_2ZnSnS_4 thin films: Correlation with residual stresses'. *Materials & Design* **108**, p.725, (2016). DOI: 10.1016/j.matdes.2016.07.019.

473 D.K. Kaushik, T.N. Rao, & A. Subrahmanyam. 'Studies on the disorder in DC magnetron sputtered Cu_2ZnSnS_4 (CZTS) thin films grown in sulfide plasma'. *Surface and Coatings Technology* **314**, p.85, (2017). DOI: 10.1016/j.surfcoat.2016.09.034.

474 F. Hergert & R. Hock. 'Predicted formation reactions for the solid-state syntheses of the semiconductor materials Cu_2SnX_3 and Cu_2ZnSnX_4 (X=S, Se) starting from binary chalcogenides'. *Thin Solid Films* **515** (15), p.5953, (2007). DOI: 10.1016/j.tsf.2006.12.096.

475 C.-Q. Liu et al. 'Phase evolution and sintering behaviors of Cu_2ZnSnS_4 powders synthesised by mechanochemical process with different milling parameters'. *Journal of Alloys and Compounds* **708**, p.428, (2017). DOI: 10.1016/j.jallcom.2017.03.008.

476 H.R. Jung et al. 'Phase evolution of Cu_2ZnSnS_4 (CZTS) kesterite thin films during the sulphurisation process'. *Ceramics International* **41** (10A), p.13006, (2015). DOI: 10.1016/j.ceramint.2015.06.145.

477 R.B.V. Chalapathy, G.S. Jung, & B.T. Ahn. 'Fabrication of Cu_2ZnSnS_4 films by sulphurisation of Cu/ZnSn/Cu precursor layers in sulphur atmosphere for solar cells'. *Solar Energy Materials and Solar Cells* **95** (12), p.3216, (2011). DOI: 10.1016/j.solmat.2011.07.017.

478 W. Li et al. 'Transmission electron microscopy analysis for the process of crystallisation of Cu_2ZnSnS_4 film from sputtered Zn/CuSn precursor'. *Nanotechnology* **25** (19), p.195701.1, (2014). DOI: 10.1088/0957-4484/25/19/195701.

479 N. Thota et al. 'Two step growth mechanism of Cu_2ZnSnS_4 thin films'. *Physica B: Condensed Matter* **449**, p.255, (2014). DOI: 10.1016/j.physb.2014.05.039.

480 H.R. Jung et al. 'Phase evolution pathways of kesterite Cu_2ZnSnS_4 and $Cu_2ZnSnSe_4$ thin films during the annealing of sputtered Cu-Sn-Zn metallic precursors'. *Solar Energy* **145**, p.2, (2017). DOI: 10.1016/j.solener.2016.09.043.

481 M.C. Johnson et al. 'Self-regulation of Cu/Sn ratio in the synthesis of Cu_2ZnSnS_4 films'. *Chemistry of Materials* **27** (7), p.2507, (2015). DOI: 10.1021/acs.chemmater.5b00108.

482 H. Yoo, J. Kim, & L. Zhang. 'Sulphurisation temperature effects on the growth of Cu_2ZnSnS_4 thin film'. *Current Applied Physics* **12** (4), p.1052, (2012). DOI: 10.1016/j.cap.2012.01.006.

483 T. Tanaka et al. 'Preparation of Cu_2ZnSnS_4 thin films by hybrid sputtering'. *Journal of Physics and Chemistry of Solids* **66** (11), p.1978, (2005). DOI: 10.1016/j.jpcs.2005.09.037.

484 A. Weber et al. 'Multi-stage evaporation of Cu_2ZnSnS_4 thin films'. *Thin Solid Films* **517** (7), p.2524, (2009). DOI: 10.1016/j.tsf.2008.11.033.

485 A. Weber, R. Mainz, & H.W. Schock. 'On the Sn loss from thin films of the material system Cu-Zn-Sn-S in high vacuum'. *Journal of Applied Physics* **107** (1), p.013516.1, (2010). DOI: 10.1063/1.3273495.

486 S.M. Pawar et al. 'Growth of void free Cu_2ZnSnS_4 (CZTS) thin films by sulphurisation of stacked metallic precursor films'. *Vacuum* **104**, p.57, (2014). DOI: 10.1016/j.vacuum.2014.01.007.

487 S. Harel et al. 'Surface composition deviation of Cu_2ZnSnS_4 derivative powdered samples'. *Applied Surface Science* **303**, p.107, (2014). DOI: 10.1016/j.apsusc.2014.02.096.

488 F. Geiger, C.A. Busse, & R.I. Loehrke. 'The vapour pressure of indium, silver, gallium, copper, tin, and gold between 0.1 and 3.0 bar'. *International Journal of Thermophysics* **8** (4), p.425, (1987). DOI: 10.1007/bf00567103.

489 O. Tukhlibaev & U.Z. Alimov. 'Laser photoionisation spectroscopy of the zinc atom and the study of zinc sulphide evaporation'. *Optics and Spectroscopy* **88** (4), p.506, (2000). DOI: 10.1134/1.626828.

490 D.-Y. Peng & J. Zhao. 'Representation of the vapour pressures of sulphur'. *The Journal of Chemical Thermodynamics* **33** (9), p.1121, (2001). DOI: 10.1006/jcht.2001.0835.

491 A.M. Klimova et al. 'Investigation of the saturated vapour pressure of zinc, selenium, and zinc selenide'. *Glass Physics and Chemistry* **31** (6), p.760, (2005). DOI: 10.1007/s10720-005-0124-7.

492 V. Piacente, S. Foglia, & P. Scardala. 'Sublimation study of the tin sulphides SnS_2, Sn_2S_3 and SnS'. *Journal of Alloys and Compounds* **177** (1), p.17, (1991). DOI: 10.1016/0925-8388(91)90053-x.

493 S. Abermann. 'Non-vacuum processed next generation thin film photovoltaics: Towards marketable efficiency and production of CZTS based solar cells'. *Solar Energy* **94**, p.37, (2013). DOI: 10.1016/j.solener.2013.04.017.

494 C. Yan et al. 'Kesterite Cu_2ZnSnS_4 solar cell from sputtered Zn/(Cu & Sn) metal stack precursors'. *Journal of Alloys and Compounds* **610**, p.486, (2014). DOI: 10.1016/j.jallcom.2014.05.004.

495 J.K. Larsen et al. 'Potential of CuS cap to prevent decomposition of Cu_2ZnSnS_4 during annealing'. *Physica Status Solidi A* **212** (12), p.2843, (2015). DOI: 10.1002/pssa.201532420.

496 A. Redinger et al. 'Route toward high-efficiency single-phase $Cu_2ZnSn(S,Se)_4$ thin film solar cells: Model experiments and literature review'. *IEEE Journal of Photovoltaics* **1** (2), p.200, (2011). DOI: 10.1109/jphotov.2011.2168811.

497 A. Redinger et al. 'The consequences of kesterite equilibria for efficient solar cells'. *Journal of the American Chemical Society* **133** (10), p.3320, (2011). DOI: 10.1021/ja111713g.

498 J.J. Scragg et al. 'Chemical insights into the instability of Cu_2ZnSnS_4 films during annealing'. *Chemistry of Materials* **23** (20), p.4625, (2011). DOI: 10.1021/cm202379s.

499 B. Pani et al. 'Enhancement of structural & opt-electronic properties of vacuum processed Cu_2ZnSnS_4 thin film by thiourea treatment'. *Journal of Alloys and Compounds* **708**, p.181, (2017). DOI: 10.1016/j.jallcom.2017.02.183.

500 A.-J. Cheng et al. 'Sulphurisation studies of the potential thin film solar absorber Cu_2ZnSnS_4'. *Proceedings of the 35th IEEE Photovoltaic Specialists Conference,* p.001906, (2010). DOI: 10.1109/pvsc.2010.5616339.

501 Y. Lin et al. 'Mechanistic aspects of preheating effects of electrodeposited metallic precursors on structural and photovoltaic properties of Cu_2ZnSnS_4 thin films'. *Solar Energy Materials and Solar Cells* **120A**, p.218, (2014). DOI: 10.1016/j.solmat.2013.09.006.

502 B. Pani, R.K. Singh, & U.P. Singh. 'Impact of pre-annealing temperature on the formation of Cu_2ZnSnS_4 absorber layer'. *Journal of Alloys and Compounds* **648**, p.332, (2015). DOI: 10.1016/j.jallcom.2015.05.207.

503 L. Vauche et al. 'Rapid thermal processing annealing challenges for large scale Cu_2ZnSnS_4 thin films'. *Physica Status Solidi A* **212** (1), p.103, (2015). DOI: 10.1002/pssa.201431387.

504 W. Wang et al. 'Effect of thermal pretreatment of metal precursor on the properties of Cu_2ZnSnS_4 films'. *Chinese Physics B* **24** (5), p.056805.1, (2015). DOI: 10.1088/1674-1056/24/5/056805.

505 S.-W. Fu et al. 'Impact of pre-alloying of sputtered Cu/Sn/Zn precursors for Cu_2ZnSnS_4 thin films'. *Materials Letters* **173**, p.1, (2016). DOI: 10.1016/j.matlet.2016.02.046.

506 M.A. Olgar et al. 'Cu_2ZnSnS_4-based thin films and solar cells by rapid thermal annealing processing'. *Thin Solid Films* **628**, p.1, (2017). DOI: 10.1016/j.tsf.2017.03.008.

507 M. Neuschitzer et al. 'Complex surface chemistry of kesterites: Cu/Zn reordering after low-temperature postdeposition annealing and its role in high-performance devices'. *Chemistry of Materials* **27** (15), p.5279, (2015). DOI: 10.1021/acs.chemmater.5b01473.

508 D. Fan et al. 'Three-step process improves crystal quality of Cu_2ZnSnS_4 absorber layer and efficiency of solar cell'. *Crystal Research and Technology* **50** (8), p.613, (2015). DOI: 10.1002/crat.201500025.

509 J.H. Lee et al. 'Effect of pre-annealing on the phase formation and efficiency of CZTS solar cell prepared by sulphurisation of Zn/(Cu,Sn) precursor with H_2S gas'. *Solar Energy* **136**, p.499, (2016). DOI: 10.1016/j.solener.2016.07.031.

510 N. Momose et al. 'Cu_2ZnSnS_4 thin film solar cells utilising sulphurisation of metallic precursor prepared by simultaneous sputtering of metal targets'. *Japanese Journal of Applied Physics* **50** (1S2), p.01BG09.1, (2011). DOI: 10.1143/jjap.50.01bg09.

511 A. Khalkar et al. 'Effect of growth parameters and annealing atmosphere on the properties of Cu_2ZnSnS_4 thin films deposited by cosputtering'. *International Journal of Photoenergy* **2013**, p.1, (2013). DOI: 10.1155/2013/690165.

512 J.J. Scragg, P.J. Dale, & L.M. Peter. 'Synthesis and characterisation of Cu_2ZnSnS_4 absorber layers by an electrodeposition-annealing route'. *Thin Solid Films* **517** (7), p.2481, (2009). DOI: 10.1016/j.tsf.2008.11.022.

513 V. Kheraj et al. 'Synthesis and characterisation of copper zinc tin sulphide (CZTS) compound for absorber material in solar cells'. *Journal of Crystal Growth* **362**, p.174, (2013). DOI: 10.1016/j.jcrysgro.2011.10.034.

514 M.G. Sousa et al. 'Cu_2ZnSnS_4 absorber layers obtained through sulphurisation of metallic precursors: Graphite box versus sulphur flux'. *Thin Solid Films* **535**, p.27, (2013). DOI: 10.1016/j.tsf.2012.11.080.

515 D.B. Mitzi et al. 'The path towards a high-performance solution-processed kesterite solar cell'. *Solar Energy Materials and Solar Cells* **95** (6), p.1421, (2011). DOI: 10.1016/j.solmat.2010.11.028.

516 E.A. Lund et al. 'Investigation of combinatorial co-evaporated thin film Cu_2ZnSnS_4 (II): Beneficial cation arrangement in Cu-rich growth'. *Journal of Applied Physics* **115** (17), p.173503.1, (2014). DOI: 10.1063/1.4871665.

517 J. He et al. 'Influence of sulphurisation pressure on Cu_2ZnSnS_4 thin films and solar cells prepared by sulphurisation of metallic precursors'. *Journal of Power Sources* **273**, p.600, (2015). DOI: 10.1016/j.jpowsour.2014.09.088.

518 J. Li et al. 'Influence of sulphurisation pressure on structural and electrical property of Cu_2ZnSnS_4 thin film and solar cell'. *Journal of Materials Science: Materials in Electronics* **27** (8), p.8688, (2016). DOI: 10.1007/s10854-016-4890-x.

519 A.U. Sheleg et al. 'Determination of the structural and optical characteristics of Cu_2ZnSnS_4 semiconductor thin films'. *Semiconductors* **48** (10), p.1296, (2014). DOI: 10.1134/s1063782614100273.

520 H. Cui et al. 'Fabrication of efficient Cu_2ZnSnS_4 solar cells by sputtering single stoichiometric target'. *Coatings* **7** (2), p.19.1, (2017). DOI: 10.3390/coatings7020019.

521 W. Wang et al. 'The effect of sulphur vapour pressure on Cu_2ZnSnS_4 thin film growth for solar cells'. *Solar Energy* **148**, p.12, (2017). DOI: 10.1016/j.solener.2017.03.071.

522 A. Alvarez, S. Exarhos, & L. Mangolini. 'Tin disulphide segregation on CZTS films sulphurised at high pressure'. *Materials Letters* **165**, p.41, (2016). DOI: 10.1016/j.matlet.2015.11.090.

523 T. Kobayashi et al. 'Investigation of Cu_2ZnSnS_4 based thin film solar cells using abundant materials'. *Japanese Journal of Applied Physics* **44** (Part 1, 1B), p.783, (2005). DOI: 10.1143/jjap.44.783.

524 S. Schorr et al. 'In-situ investigation of the kesterite formation from binary and ternary sulphides'. *Thin Solid Films* **517** (7), p.2461, (2009). DOI: 10.1016/j.tsf.2008.11.053.

525 W. Feng et al. 'Influence of annealing temperature on CZTS thin film surface properties'. *Journal of Electronic Materials* **46** (1), p.288, (2017). DOI: 10.1007/s11664-016-4873-y.

526 J. Han et al. 'Crystallisation behaviour of co-sputtered Cu_2ZnSnS_4 precursor prepared by sequential sulphurisation processes'. *Nanotechnology* **24** (9), p.095706.1, (2013). DOI: 10.1088/0957-4484/24/9/095706.

527 J.-S. Seol et al. 'Electrical and optical properties of Cu_2ZnSnS_4 thin films prepared by RF magnetron sputtering process'. *Solar Energy Materials and Solar Cells* **75** (1-2), p.155, (2003). DOI: 10.1016/S0927-0248(02)00127-7.

528 P. Bras, J. Sterner, & C. Platzer-Björkman. 'Influence of hydrogen sulphide annealing on copper zinc tin sulphide solar cells sputtered from a quaternary compound target'. *Thin Solid Films* **582**, p.233, (2015). DOI: 10.1016/j.tsf.2014.11.004.

529 U. Chalapathi, S. Uthanna, & V. Sundara Raja. 'Growth of Cu_2ZnSnS_4 thin films by a two-stage process: Effect of incorporation of sulphur at the precursor stage'. *Solar Energy Materials and Solar Cells* **132**, p.476, (2015). DOI: 10.1016/j.solmat.2014.09.035.

530 S. Rondiya et al. 'Effect of calcination temperature on the properties of CZTS absorber layer prepared by RF sputtering for solar cell applications'. *Materials for Renewable and Sustainable Energy* **6** (2), p.8.1, (2017). DOI: 10.1007/s40243-017-0092-6.

531 Z. Zakaria et al. 'Effects of sulphurisation temperature on Cu_2ZnSnS_4 thin film deposited by single source thermal evaporation method'. *Japanese Journal of Applied Physics* **54** (8S1), p.08KC18.1, (2015). DOI: 10.7567/jjap.54.08kc18.

532 A. Emrani et al. 'Cu_2ZnSnS_4 solar cells fabricated by short-term sulphurisation of sputtered Sn/Zn/Cu precursors under an H_2S atmosphere'. *Thin Solid Films* **577**, p.62, (2015). DOI: 10.1016/j.tsf.2015.01.051.

533 T. Toshihiko et al. 'Annealing-induced optical-bandgap widening of Cu_2ZnSnS_4 thin films with observation of simultaneous increase in local-structure ordering'. *Japanese Journal of Applied Physics* **54** (1), p.015503.1, (2014). DOI: 10.7567/JJAP.54.015503.

534 S.M. Pawar et al. 'Synthesis of Cu_2ZnSnS_4 (CZTS) absorber by rapid thermal processing sulphurisation of stacked metallic precursor films for solar cell applications'. *Materials Letters* **118**, p.76, (2014). DOI: 10.1016/j.matlet.2013.12.047.

535 K.-J. Yang et al. 'Effects of the compositional ratio distribution with sulphurisation temperatures in the absorber layer on the defect and surface electrical characteristics of Cu_2ZnSnS_4 solar cells'. *Progress in Photovoltaics: Research and Applications* **23** (12), p.1771, (2015). DOI: 10.1002/pip.2619.

536 Y. Yu et al. 'Close-space sulphurisation of sputtered metal precursors for Cu_2ZnSnS_4 thin film solar cells'. *Proceedings of the 43rd IEEE Photovoltaic Specialists Conference,* p.0539, (2016). DOI: 10.1109/pvsc.2016.7749652.

537 M. Yang et al. 'The Cu_2ZnSnS_4 solar cell with high open circuit voltage'. *Physica B: Condensed Matter* **509**, p.50, (2017). DOI: 10.1016/j.physb.2017.01.001.

538 G.K. Dalapati et al. 'Impact of molybdenum out-diffusion and interface quality on the performance of sputter-grown CZTS-based solar cells'. *Scientific Reports* **7** (1), p.1350.1, (2017). DOI: 10.1038/s41598-017-01605-7.

539 C.W. Hong et al. 'Comparative study on the annealing types on the properties of Cu_2ZnSnS_4 thin films and their application to solar cells'. *Applied Surface Science* **334**, p.180, (2015). DOI: 10.1016/j.apsusc.2014.09.050.

540 N. Thota et al. 'Growth and properties of Cu_2ZnSnS_4 thin films prepared by multiple metallic layer stacks as a function of sulphurisation time'. *Journal of Materials Science: Materials in Electronics* **28** (16), p.11702, (2017). DOI: 10.1007/s10854-017-6974-7.

541 T. Fukano, S. Tajima, & T. Ito. 'Enhancement of conversion efficiency of Cu_2ZnSnS_4 thin film solar cells by improvement of sulphurisation conditions'. *Applied Physics Express* **6** (6), p.062301.1, (2013). DOI: 10.7567/apex.6.062301.

542 M. Abusnina et al. 'Fabrication and characterisation of CZTS thin films prepared by the sulphurisation of RF-sputtered stacked metal precursors'. *Journal of Electronic Materials* **43** (9), p.3145, (2014). DOI: 10.1007/s11664-014-3259-2.

543 M.G. Sousa et al. 'Effect of rapid thermal processing conditions on the properties of Cu_2ZnSnS_4 thin films and solar cell performance'. *Solar Energy Materials and Solar Cells* **126**, p.101, (2014). DOI: 10.1016/j.solmat.2014.03.043.

544 J. Ge et al. 'Comparative study of the influence of two distinct sulphurisation ramping rates on the properties of Cu_2ZnSnS_4 thin films'. *Applied Surface Science* **258** (19), p.7250, (2012). DOI: 10.1016/j.apsusc.2012.02.141.

545 Z. Jiang et al. 'Effects of temperature-time profile on Cu_2ZnSnS_4 films and cells based on sulphur-contained precursors'. *Materials Science in Semiconductor Processing* **57**, p.239, (2017). DOI: 10.1016/j.mssp.2016.10.035.

546 A. Ritscher et al. 'Study of the mechanochemical process to crystalline Cu_2ZnSnS_4 powder'. *Materials Research Bulletin* **84**, p.162, (2016). DOI: 10.1016/j.materresbull.2016.08.006.

547 Y. Ren et al. 'Evolution of Na-S(-O) compounds on Cu_2ZnSnS_4 absorber surface and its effect on CdS growth'. *Proceedings of the 43rd IEEE Photovoltaic Specialists Conference,* p.2255, (2016). DOI: 10.1109/pvsc.2016.7750037.

548 M. Yasaka. 'X-ray thin film measurement techniques: X-ray reflectivity measurement'. *The Rigaku Journal* **26** (2), p.1, (2010).

549 R.F. Egerton. 'Physical Principles of Electron Microscopy'. Springer, (2005).

550 R. Thomasa. 'Practical Guide to ICPMS'. Marcel Dekker, (2004).

551 K. Durose et al. 'Physical characterisation of thin film solar cells'. *Progress in Photovoltaics: Research and Applications* **12** (2-3), p.177, (2004). DOI: 10.1002/pip.542.

552 H. Rietveld. 'A profile refinement method for nuclear and magnetic structures'. *Journal of Applied Crystallography* **2** (2), p.65, (1969). DOI: 10.1107/S0021889869006558.

553 B.H. Toby. 'R factors in Rietveld analysis: How good is good enough?'. *Powder Diffraction* **21** (1), p.67, (2006). DOI: 10.1154/1.2179804.

554 S.P. Thompson et al. 'Beamline I11 at Diamond: A new instrument for high resolution powder diffraction'. *Review of Scientific Instruments* **80** (7), p.075107.1, (2009). DOI: 10.1063/1.3167217.

555 'How Diamond Works'. The Diamond Light Source, (2017).

556 S. Brennan & P.L. Cowan. 'A suite of programs for calculating X-ray absorption, reflection, and diffraction performance for a variety of materials at arbitrary wavelengths'. *Review of Scientific Instruments* **63** (1), p.850, (1992). DOI: 10.1063/1.1142625.

557 A.-J. Cheng et al. 'Imaging and phase identification of Cu_2ZnSnS_4 thin films using confocal Raman spectroscopy'. *Journal of Vacuum Science & Technology A* **29** (5), p.051203.1, (2011). DOI: 10.1116/1.3625249.

558 D.M. Berg et al. 'Discrimination and detection limits of secondary phases in Cu_2ZnSnS_4 using X-ray diffraction and Raman spectroscopy'. *Thin Solid Films* **569**, p.113, (2014). DOI: 10.1016/j.tsf.2014.08.028.

559 V.F. Sears. 'Neutron scattering lengths and cross sections'. *Neutron News* **3** (3), p.26, (1992). DOI: 10.1080/10448639208218770.

560 'How ISIS Works'. The ISIS Pulsed Neutron and Muon Source, (2017).

561 E.D. Becker. 'High Resolution NMR: Theory and Chemical Applications', 3rd Edn. Academic Press, (2000).

562 G.W. Luther et al. 'Aqueous copper sulphide clusters as intermediates during copper sulphide formation'. *Environmental Science & Technology* **36** (3), p.394, (2002). DOI: 10.1021/es010906k.

563 N. Yamakawa, M. Jiang, & C.P. Grey. 'Investigation of the conversion reaction mechanisms for binary copper(II) compounds by solid-state NMR spectroscopy and X-ray diffraction'. *Chemistry of Materials* **21** (14), p.3162, (2009). DOI: 10.1021/cm900581b.

564 L. Choubrac et al. 'Multinuclear (^{67}Zn, ^{119}Sn and ^{65}Cu) NMR spectroscopy: An ideal technique to probe the cationic ordering in Cu_2ZnSnS_4 photovoltaic materials'. *Physical Chemistry Chemical Physics* **15** (26), p.10722, (2013). DOI: 10.1039/c3cp51320c.

565 T. Pietrass & F. Taulelle. '^{119}Sn solid-state NMR of tin sulphides. Evidence of polytypism in SnS_2'. *Magnetic Resonance in Chemistry* **35** (6), p.363, (1997). DOI: 10.1002/(sici)1097-458x(199706)35:6<363::aid-omr79>3.0.CO;2-p.

566 E. Smith & G. Dent. 'Modern Raman Spectroscopy: A Practical Approach'. Wiley, (2005).

567 P.K. Sarswat, M.L. Free, & A. Tiwari. 'Temperature-dependent study of the Raman A mode of Cu_2ZnSnS_4 thin films'. *Physica Status Solidi B* **248** (9), p.2170, (2011). DOI: 10.1002/pssb.201046477.

568 M. Altosaar et al. '$Cu_2Zn_{1-x}Cd_xSn(Se_{1-y}S_y)_4$ solid solutions as absorber materials for solar cells'. *Physica Status Solidi A* **205** (1), p.167, (2008). DOI: 10.1002/pssa.200776839.

569 T. Gürel, C. Sevik, & T. Çağın. 'Characterisation of vibrational and mechanical properties of quaternary compounds Cu_2ZnSnS_4 and $Cu_2ZnSnSe_4$ in kesterite and stannite structures'. *Physical Review B* **84** (20), p.205201.1, (2011). DOI: 10.1103/physrevb.84.205201.

570 X. Fontané et al. 'Vibrational properties of stannite and kesterite type compounds: Raman scattering analysis of $Cu_2(Fe,Zn)SnS_4$'. *Journal of Alloys and Compounds* **539**, p.190, (2012). DOI: 10.1016/j.jallcom.2012.06.042.

571 D. Dumcenco & Y.-S. Huang. 'The vibrational properties study of kesterite Cu_2ZnSnS_4 single crystals by using polarisation dependent Raman spectroscopy'. *Optical Materials* **35** (3), p.419, (2013). DOI: 10.1016/j.optmat.2012.09.031.

572 M.Y. Valakh et al. 'Raman scattering and disorder effect in Cu_2ZnSnS_4'. *Physica Status Solidi Rapid Research Letters* **7** (4), p.258, (2013). DOI: 10.1002/pssr.201307073.

573 R. Caballero et al. 'Non-stoichiometry effect and disorder in Cu_2ZnSnS_4 thin films obtained by flash evaporation: Raman scattering investigation'. *Acta Materialia* **65**, p.412, (2014). DOI: 10.1016/j.actamat.2013.11.010.

574 M. Dimitrievska et al. 'Raman scattering crystalline assessment of polycrystalline Cu_2ZnSnS_4 thin films for sustainable photovoltaic technologies: Phonon confinement model'. *Acta Materialia* **70**, p.272, (2014). DOI: 10.1016/j.actamat.2014.02.035.

575 M. Dimitrievska et al. 'Multiwavelength excitation Raman scattering study of polycrystalline kesterite Cu_2ZnSnS_4 thin films'. *Applied Physics Letters* **104** (2), p.021901.1, (2014). DOI: 10.1063/1.4861593.

576 O. Awadallah & Z. Cheng. 'In situ Raman monitoring of Cu_2ZnSnS_4 oxidation and related decomposition at elevated temperatures'. *IEEE Journal of Photovoltaics* **6** (3), p.764, (2016). DOI: 10.1109/jphotov.2016.2542479.

577 M. Guc et al. 'Polarised Raman scattering study of kesterite type Cu_2ZnSnS_4 single crystals'. *Scientific Reports* **6**, p.19414.1, (2016). DOI: 10.1038/srep19414.

578 W. Zhao et al. 'Low-temperature phase transformation of CZTS thin films'. *Chinese Physics B* **26** (4), p.046402.1, (2017). DOI: 10.1088/1674-1056/26/4/046402.

579 S.J. Sandoval et al. 'Raman study and lattice dynamics of single molecular layers of MoS_2'. *Physical Review B* **44** (8), p.3955, (1991). DOI: 10.1103/physrevb.44.3955.

580 P.A. Fernandes, P.M.P. Salomé, & A.F. da Cunha. 'Study of polycrystalline Cu_2ZnSnS_4 films by Raman scattering'. *Journal of Alloys and Compounds* **509** (28), p.7600, (2011). DOI: 10.1016/j.jallcom.2011.04.097.

581 C.G. Munce et al. 'A Raman spectroelectrochemical investigation of chemical bath deposited Cu_xS thin films and their modification'. *Colloids and Surfaces A: Physicochemical and Engineering Aspects* **295** (1-3), p.152, (2007). DOI: 10.1016%2fj.colsurfa.2006.08.045.

582 W.G. Nilsen. 'Raman spectrum of cubic ZnS'. *Physical Review* **182** (3), p.838, (1969). DOI: 10.1103/physrev.182.838.

583 L.S. Price et al. 'Atmospheric pressure chemical vapour deposition of tin sulphides (SnS, Sn_2S_3, and SnS_2) on glass'. *Chemistry of Materials* **11** (7), p.1792, (1999). DOI: 10.1021/cm990005z.

584 D.M. Berg et al. 'Raman analysis of monoclinic Cu_2SnS_3 thin films'. *Applied Physics Letters* **100** (19), p.192103.1, (2012). DOI: 10.1063/1.4712623.

585 T. He et al. 'The role of excess Sn in $Cu_4Sn_7S_{16}$ for modification of the band structure and a reduction in lattice thermal conductivity'. *Journal of Materials Chemistry C* **5** (17), p.4206, (2017). DOI: 10.1039/c7tc00420f.

586 S.P. Ramkumar et al. 'First-principles investigation of the structural, dynamical, and dielectric properties of kesterite, stannite, and PMCA phases of Cu_2ZnSnS_4'. *Physical Review B* **94** (22), p.224302.1, (2016). DOI: 10.1103/physrevb.94.224302.

587 J.M. Skelton et al. 'Vibrational spectra and lattice thermal conductivity of kesterite-structured Cu_2ZnSnS_4 and $Cu_2ZnSnSe_4$'. *APL Materials* **3** (4), p.041102.1, (2015). DOI: 10.1063/1.4917044.

588 O.P. Singh et al. 'Effect of temperature on thermal expansion and anharmonicity in Cu_2ZnSnS_4 thin films grown by co-sputtering and sulphurisation'. *Materials Chemistry and Physics* **146** (3), p.452, (2014). DOI: 10.1016/j.matchemphys.2014.03.052.

589 S. Van Duren et al. 'In situ monitoring of Cu_2ZnSnS_4 absorber formation with Raman spectroscopy during Mo/Cu_2SnS_3/ZnS thin film stack annealing'. *IEEE Journal of Photovoltaics* **7** (3), p.906, (2017). DOI: 10.1109/jphotov.2017.2686015.

590 G.D. Gilliland. 'Photoluminescence spectroscopy of crystalline semiconductors'. *Materials Science and Engineering: R Reports* **18** (3-6), p.99, (1997). DOI: 10.1016/S0927-796x(97)80003-4.

591 T. Schmidt, K. Lischka, & W. Zulehner. 'Excitation-power dependence of the near-band-edge photoluminescence of semiconductors'. *Physical Review B* **45** (16), p.8989, (1992). DOI: 10.1103/physrevb.45.8989.

592 M. Grossberg et al. 'Microphotoluminescence study of Cu_2ZnSnS_4 polycrystals'. *Journal of Photonics for Energy* **3** (1), p.030599.1, (2013). DOI: 10.1117/1.jpe.3.030599.

593 D. Bimberg, M. Sondergeld, & E. Grobe. 'Thermal dissociation of excitons bounds to neutral acceptors in high-purity GaAs'. *Physical Review B* **4** (10), p.3451, (1971). DOI: 10.1103/physrevb.4.3451.

594 J. Krustok, H. Collan, & K. Hjelt. 'Does the low-temperature Arrhenius plot of the photoluminescence intensity in CdTe point towards an erroneous activation energy?'. *Journal of Applied Physics* **81** (3), p.1442, (1997). DOI: 10.1063/1.363903.

595 M. Grossberg et al. 'Photoluminescence study of defect clusters in Cu_2ZnSnS_4 polycrystals'. *Current Applied Physics* **14** (3), p.447, (2014). DOI: 10.1016/j.cap.2013.12.029.

596 M.P. Salomé et al. 'Influence of CdS and ZnSnO buffer layers on the photoluminescence of Cu(In,Ga)Se_2 thin films'. *IEEE Journal of Photovoltaics* **7** (2), p.670, (2017). DOI: 10.1109/jphotov.2016.2639347.

597 K. Tanaka, T. Shinji, & H. Uchiki. 'Photoluminescence from Cu_2ZnSnS_4 thin films with different compositions fabricated by a sputtering-sulphurisation method'. *Solar Energy Materials and Solar Cells* **126**, p.143, (2014). DOI: 10.1016/j.solmat.2014.03.052.

598 H.J. Lee & S.I. Lee. 'Deposition and optical properties of nanocrystalline ZnS thin films by a chemical method'. *Current Applied Physics* **7** (2), p.193, (2007). DOI: 10.1016/j.cap.2006.03.005.

599 D. Kurbatov et al. 'Luminescent and optical characteristics of zinc sulphide thin films produced by close-spaced vacuum sublimation'. *Romanian Journal of Physics* **55** (1-2), p.213, (2010).

600 T.H. Sajeesh et al. 'Unveiling the defect levels in SnS thin films for photovoltaic applications using photoluminescence technique'. *Physica Status Solidi A* **207** (8), p.1934, (2010). DOI: 10.1002/pssa.200925593.

601 A.M. Saroja et al. 'Substrate temperature influence on the optical and electrical properties of spray deposited Sn_2S_3 thin films'. *Optik International Journal for Light and Electron Optics* **130**, p.245, (2017). DOI: 10.1016/j.ijleo.2016.08.083.

602 N. Tipcompor, S. Thongtem, & T. Thongtem. 'Effect of microwave radiation on the morphology of tetragonal Cu_3SnS_4 synthesised by refluxing method'. *Superlattices and Microstructures* **85**, p.488, (2015). DOI: 10.1016/j.spmi.2015.06.015.

603 K. Tanaka et al. 'Donor-acceptor pair recombination luminescence from Cu_2ZnSnS_4 bulk single crystals'. *Physica Status Solidi A* **203** (11), p.2891, (2006). DOI: 10.1002/pssa.200669545.

604 K. Hönes et al. 'Shallow defects in Cu_2ZnSnS_4'. *Physica B: Condensed Matter* **404** (23-24), p.4949, (2009). DOI: 10.1016/j.physb.2009.08.206.

605 S. Levcenko et al. 'Free-to-bound recombination in near stoichiometric Cu_2ZnSnS_4 single crystals'. *Physical Review B* **86** (4), p.045206, (2012). DOI: 10.1103/physrevb.86.045206.

606 T. Raadik et al. 'Low-temperature time-resolved photoluminescence in ordered and disordered Cu_2ZnSnS_4 single crystals'. *Physica B: Condensed Matter* **508**, p.47, (2017). DOI: 10.1016/j.physb.2016.12.011.

607 T. Gershon et al. 'Photoluminescence characterisation of a high-efficiency Cu_2ZnSnS_4 device'. *Journal of Applied Physics* **114** (15), p.154905.1, (2013). DOI: 10.1063/1.4825317.

608 T. Gershon et al. 'Relationship between Cu_2ZnSnS_4 quasi donor-acceptor pair density and solar cell efficiency'. *Applied Physics Letters* **103** (19), p.193903.1, (2013). DOI: 10.1063/1.4829920.

609 L. Van Puyvelde et al. 'Photoluminescence investigation of Cu_2ZnSnS_4 thin film solar cells'. *Thin Solid Films* **582**, p.146, (2015). DOI: 10.1016/j.tsf.2014.10.079.

610 M.J. Romero et al. 'Comparative study of the luminescence and intrinsic point defects in the kesterite Cu_2ZnSnS_4 and chalcopyrite $Cu(In,Ga)Se_2$ thin films used in photovoltaic applications'. *Physical Review B* **84** (16), p.165324.1, (2011). DOI: 10.1103/physrevb.84.165324.

611 D. Han et al. 'Deep electron traps and origin of p-type conductivity in the Earth-abundant solar cell material Cu_2ZnSnS_4'. *Physical Review B* **87** (15), p.155206.1, (2013). DOI: 10.1103/physrevB.87.155206.

612 K.S. Knight, W.G. Marshall, & S.W. Zochowski. 'The low-temperature and high-pressure thermoelastic and structural properties of chalcopyrite $CuFeS_2$'. *The Canadian Mineralogist* **49** (4), p.1015, (2011). DOI: 10.3749/canmin.49.4.1015.

613 'MSDS No. 002281: Nonflammable Gas Mixture Argon 96.5-99 % / Hydrogen Sulphide 10ppm-3.5 %'. Airgas Inc., (2010).

614 N. Muhunthan et al. 'Growth of CZTS thin films by co-sputtering of metal targets and sulphurisation in H_2S'. *International Journal of Photoenergy* **2013**, p.1, (2013). DOI: 10.1155/2013/752012.

615 'MSDS No. 002076: Toxic Flammable Gas Mixture Hydrogen Sulphide 14.24-99 % / Nitrogen 1-85.76 %'. Airgas Inc., (2013).

616 N. Song et al. 'Epitaxial Cu_2ZnSnS_4 thin film on Si (111) 4° substrate'. *Applied Physics Letters* **106** (25), p.252102.1, (2015). DOI: 10.1063/1.4922992.

Appendix 1: TOPAS input files

TOF neutron diffraction

The following is an example input file for Rietveld refinement of TOF neutron diffraction data from the HRPD beamline of the ISIS Pulsed Neutron and Muon Source (such as was used in Chapter 7) using two simultaneous data files for each refinement (from two detector banks), allowing antisite disorder of copper and zinc on all cation sites in the CZTS crystal structure, and using an independently measured sample composition. A macro is defined at the end to enable values of interest to be output to a .txt file during batch refinement. Red text indicates values that should be set (and fixed) to the correct or desired values before starting the refinement process. Green text indicates values that should be refined, consecutively in a sensible order, to arrive at a final model.

```
'================================================================================
'TOPAS input file for Rietveld refinement of TOF neutron diffraction data from HRPD, ISIS
'================================================================================


r_wp       1.00000000  r_exp       1.00000000  r_p       1.00000000
r_wp_dash  1.00000000  r_exp_dash  1.00000000  r_p_dash  1.00000000
weighted_Durbin_Watson             1.00000000  gof       1.00000000

iters 100000
chi2_convergence_criteria 0.001
do_errors
no_LIMIT_warnings
```

```
#define report

'------------------------------------------------------------------------------------------
'Information for b1 data file
'------------------------------------------------------------------------------------------
TOF_XYE(filename1, 10)
      start_X  31370
      finish_X 125000
      x_calculation_step = Yobs_dx_at(Xo); convolution_step 4
      bkg  0.00000000`_0.00000000 0.00000000`_0.00000000 0.00000000`_0.00000000
           0.00000000`_0.00000000 0.00000000`_0.00000000 0.00000000`_0.00000000

      TOF_LAM(0.001)
      scale_pks = D_spacing^4;
      weighting = If(SigmaYobs < .0001, 1, 1/SigmaYobs^2);

      TOF_x_axis_calibration(!t0_bs, 0.00000`_0.00000, !difc_bs, 48300.00000`_0.00000, !difa_bs, -4.00000`_0.00000)
      wifd_pkshape(!two_theta, 1.00000, !aprm,   1.00000, !tauf_2, 1.00000, !tauf_1, 1.00000, !tauf_0, 1.00000,
                   !taus_0,    1.00000, !taus_1, 1.00000, !t_eff,  1.00000, !hhh,    1.00000, !hhh_0,  1.00000)

      prm !mu_Si_bs  0.00000`_0.00000
      scale_pks = Exp(-mu_Si_bs*D_spacing);
      prm !fixb_bs   0.00000`_0.00000
      scale_pks = (Exp(-2*fixb_bs/(2 D_spacing)^2));

str
      r_bragg         1.00000000
      scale !scal_bs  1.00000`_0.00000
      tof_sample_peakshape(!lor_bs, 1.00000`_0.00000, !dsp_bs, 1.00000`_0.00000, !dspsq_bs, 0.00000`_0.00000)

'------------------------------------------------------------------------------------------
'Information for b2 data file
'------------------------------------------------------------------------------------------
TOF_XYE(filename2, 10)
      start_X  294200
      finish_X 135600
      x_calculation_step = Yobs_dx_at(Xo); convolution_step 4
```

```
      bkg  0.00000000`_0.00000000 0.00000000`_0.00000000 0.00000000`_0.00000000
           0.00000000`_0.00000000 0.00000000`_0.00000000 0.00000000`_0.00000000

      TOF_LAM(0.001)
      scale_pks = D_spacing^4;
      weighting = If(SigmaYobs < .0001, 1, 1/SigmaYobs^2);

      TOF_x_axis_calibration(!t0_90, 0.00000`_0.00000, !difc_90, 34800.00000`_0.00000, !difa_90, 0.00000`_0.00000)
      wifd_pkshape(!two_theta, 1.00000, !aprm,   1.00000, !tauf_2, 1.00000, !tauf_1, 1.00000, !tauf_0, 1.00000,
                   !taus_0,    1.00000, !taus_1, 1.00000, !t_eff,  1.00000, !hhh,    1.00000, !hhh_0,  1.00000)

      prm !mu_Si_90  0.00000`_0.00000
      scale_pks = Exp(-mu_Si_90*D_spacing);
      prm !fixb_90   0.00000`_0.00000
      scale_pks = (Exp(-2*fixb_90/(2 D_spacing)^2));

str
      r_bragg         1.00000000
      scale !scal_90  1.00000`_0.00000
      tof_sample_peakshape(!lor_90, 1.00000`_0.00000, !dsp_90, 1.00000`_0.00000, !dspsq_90, 1.00000`_0.00000)

'------------------------------------------------------------------------------------------
'Structural information
'------------------------------------------------------------------------------------------
for xdds {
for strs 1 to 1 {
      phase_name "CZTS (kesterite)"
      space_group "I-4"
      a !lpa  5.430000`_0.000000
      b =lpa;
      c !lpc  10.820000`_0.000000
      al 90.
      be 90.
      ga 90.
      volume  319.027`_0.000

      prm !tot_cu 2.00000
```

```
      prm !tot_zn 1.00000
      prm !tot_sn 1.00000
      prm !tot_s  4.00000

      site 2a x 0.                    y 0.                    z 0.
            occ Cu+1 !cu_2a                          1.00000`_0.00000 min 0 max 1 beq !b_2a 0.50000`_0.00000 min 0
            occ Zn+2 zn_2a =1-cu_2a;:                0.00000`_0.00000             beq =b_2a;

      site 2c x 0.                    y 0.5                   z 0.25
            occ Cu+1 !cu_2c                          1.00000`_0.00000 min 0 max 1 beq !b_2c 0.50000`_0.00000 min 0
            occ Zn+2 zn_2c =1-cu_2c;:                0.00000`_0.00000             beq =b_2c;

      site 2d x 0.                    y 0.5                   z 0.75
            occ Cu+1 cu_2d =tot_cu-cu_2a-cu_2c-cu_2b;: 0.00000`_0.00000           beq !b_2d 0.50000`_0.00000 min 0
            occ Zn+2 zn_2d =1-cu_2d;:                0.10000`_0.00000             beq =b_2d;

      site 2b x 0.                    y 0.                    z 0.5
            occ Sn+4 sn_2b =tot_sn;:                 1.00000                      beq !b_2b 0.50000`_0.00000 min 0
            occ Cu+1 !cu_2b                          0.00000`_0.00000 min 0 max =1-sn_2b; beq =b_2b;
            occ Zn+2 zn_2b =1-sn_2b-cu_2b;:          0.11305`_0.00000             beq =b_2b;

      site 8g x !Sx  0.24500`_0.00000  y !Sy  0.24500`_0.00000  z !Sz  0.12800`_0.00000
            occ S    s_8g  =tot_s/4;:                 1.00000                      beq !b_8g 0.50000`_0.00000 min 0
}
}

prm !temp_K 300 'Remove this line if a temperature is given by a batch file
prm chi_sq =Get(gof)^2;
prm lpc_h = lpc/2;
prm lpco2a = lpc/(2*lpa);
prm Sz2 = 2*Sz;

#ifdef report
out "Results.txt" append
'Out_String("Temp(K)\tRwp\tX^2\ta\terr_a\tc\terr_c\tc/2\terr_c/2\tc/2a\terrc/2a\tCu_2a\terr_C2a\tCu_2c\terr_C2c\tCu_
2d\terr_C2d\tCu_2b\terr_C2b\tSx\terr_Sx\tSy\terr_Sy\tSz\terr_Sz\t2*Sz\terr_2Sz\tbeq_2a\terr_b2a\tbeq2c\terr_b2c\tbeq
2d\terr_b2d\tbeq_2b\terr_b2b\tbeq_8g\terr_b8g")
```

```
Out(temp_K,     "\n%.0f")
Out(Get(r_wp), "\t%.1f")
Out(chi_sq,     "\t%.1f")
Out(lpa,        "\t%.5f", "\t%.5f")
Out(lpc,        "\t%.5f", "\t%.5f")
Out(lpc_h,      "\t%.5f", "\t%.5f")
Out(lpco2a,     "\t%.5f", "\t%.5f")
Out(cu_2a,      "\t%.2f", "\t%.2f")
Out(cu_2c,      "\t%.2f", "\t%.2f")
Out(cu_2d,      "\t%.2f", "\t%.2f")
Out(cu_2b,      "\t%.2f", "\t%.2f")
Out(Sx,         "\t%.5f", "\t%.5f")
Out(Sy,         "\t%.5f", "\t%.5f")
Out(Sz,         "\t%.5f", "\t%.5f")
Out(Sz2,        "\t%.5f", "\t%.5f")
Out(b_2a,       "\t%.4f", "\t%.4f")
Out(b_2c,       "\t%.4f", "\t%.4f")
Out(b_2d,       "\t%.4f", "\t%.4f")
Out(b_2b,       "\t%.4f", "\t%.4f")
Out(b_8g,       "\t%.4f", "\t%.4f")
#endif
```

Anomalous XRD

The following is an example input file for Rietveld refinement of anomalous XRD data from the I11 beamline of the Diamond Light Source (such as was used in Chapter 8) using three simultaneous data files for each refinement (at three different X-ray energies), including secondary phases (with ZnS as an example), allowing antisite disorder of copper and zinc on all cation sites and vacancies on all sites in the CZTS crystal structure, and using an independently measured overall sample composition. A macro is defined at the end to output hkl and d-spacing values of peaks to a .txt file. Red text indicates values that should be set (and fixed) to the correct or desired values before starting the refinement process. Orange text indicates values that must be reset to an output value iteratively with each refinement. Green text indicates values that should be refined, consecutively in a sensible order, to arrive at a final model.

```
'================================================================================================
'TOPAS input file for Rietveld refinement of anomalous scattering XRD data from I11, Diamond
'================================================================================================

r_wp       1.00000000  r_exp       1.00000000  r_p       1.00000000
r_wp_dash  1.00000000  r_exp_dash  1.00000000  r_p_dash  1.00000000
weighted_Durbin_Watson             1.00000000  gof       1.00000000

iters 100000
chi2_convergence_criteria 0.001
do_errors
no_LIMIT_warnings

#define output_peak_hkls

'------------------------------------------------------------------------------------------------
'Information for 15 keV data file
'------------------------------------------------------------------------------------------------
```

```
xdd filename1
      start_X  10
      finish_X 148
      x_calculation_step = Yobs_dx_at(Xo); convolution_step 4
      bkg  0.00000000`_0.00000000 0.00000000`_0.00000000 0.00000000`_0.00000000
           0.00000000`_0.00000000 0.00000000`_0.00000000 0.00000000`_0.00000000
           0.00000000`_0.00000000 0.00000000`_0.00000000 0.00000000`_0.00000000
           0.00000000`_0.00000000 0.00000000`_0.00000000 0.00000000`_0.00000000

      Zero_Error(!zero_1, 0.00000`_0.00000)
      Absorption(!abs_1,  100.00000`_0.00000)
      LP_Factor( 90)
      lam ymin_on_ymax 0.0001 la 1.0 lo 0.82600 lh 0.001
      Rp 48000
      Rs 430
      Slit_Width(0.015)
      Simple_Axial_Model(!axial_1, 5.00000`_0.00000)

str
      r_bragg      1.00000000
      scale !s1_1  9.00000e-005`_0.00000e-005
      TCHZ_Peak_Type(, 0.00001`_0.00000, , 0.00001`_0.00000, , 0.00001`_0.00000,, 0., , 0.00001`_0.00000,, 0.)

str
      r_bragg      1.00000000
      scale !s1_2  1.00000e-005`_0.00000e-005
      TCHZ_Peak_Type(, 0.00001`_0.00000, , 0.00001`_0.00000, , 0.00001`_0.00000,, 0., , 0.00001`_0.00000,, 0.)

'-------------------------------------------------------------------------------------------
'Information for 9.66 keV data file
'-------------------------------------------------------------------------------------------
xdd filename2
      start_X  10
      finish_X 148
      x_calculation_step = Yobs_dx_at(Xo); convolution_step 4
      bkg  0.00000000`_0.00000000 0.00000000`_0.00000000 0.00000000`_0.00000000
           0.00000000`_0.00000000 0.00000000`_0.00000000 0.00000000`_0.00000000
```

```
           0.00000000`_0.00000000 0.00000000`_0.00000000 0.00000000`_0.00000000
           0.00000000`_0.00000000 0.00000000`_0.00000000 0.00000000`_0.00000000

      Zero_Error(!zero_2, 0.00000`_0.00000)
      Absorption(!abs_2,  100.00000`_0.00000)
      LP_Factor( 90)
      lam ymin_on_ymax 0.0001 la 1.0 lo 1.28400 lh 0.001
      Rp 48000
      Rs 430
      Slit_Width(0.015)
      Simple_Axial_Model(!axial_2, 5.00000`_0.00000)

      local !s2  1.00000`_0.00000

str
      r_bragg           1.00000000
      scale =s2*s1_1;:  9.00000e-005`_0.00000e-005
      TCHZ_Peak_Type(, 0.00001`_0.00000, , 0.00001`_0.00000, , 0.00001`_0.00000,, 0., , 0.00001`_0.00000,, 0.)

str
      r_bragg           1.00000000
      scale =s2*s1_2;:  1.00000e-005`_0.00000e-005
      TCHZ_Peak_Type(, 0.00001`_0.00000, , 0.00001`_0.00000, , 0.00001`_0.00000,, 0., , 0.00001`_0.00000,, 0.)

'-------------------------------------------------------------------------------------------
'Information for 8.97 keV data file
'-------------------------------------------------------------------------------------------
xdd filename3
      start_X  10
      finish_X 148
      x_calculation_step = Yobs_dx_at(Xo); convolution_step 4
      bkg  0.00000000`_0.00000000 0.00000000`_0.00000000 0.00000000`_0.00000000
           0.00000000`_0.00000000 0.00000000`_0.00000000 0.00000000`_0.00000000
           0.00000000`_0.00000000 0.00000000`_0.00000000 0.00000000`_0.00000000
           0.00000000`_0.00000000 0.00000000`_0.00000000 0.00000000`_0.00000000

      Zero_Error(!zero_3, 0.00000`_0.00000)
```

```
      Absorption(!abs_3,  100.00000`_0.00000)
      LP_Factor( 90)
      lam ymin_on_ymax 0.0001 la 1.0 lo 1.38200 lh 0.001
      Rp 48000
      Rs 430
      Slit_Width(0.015)
      Simple_Axial_Model(!axial_3, 5.00000`_0.00000)

      local !s3  1.00000`_0.00000

str
      r_bragg           1.00000000
      scale =s3*s1_1;:  9.00000e-005`_0.00000e-005
      TCHZ_Peak_Type(, 0.00001`_0.00000, , 0.00001`_0.00000, , 0.00001`_0.00000,, 0., , 0.00001`_0.00000,, 0.)

str
      r_bragg           1.00000000
      scale =s3*s1_2;:  1.00000e-005`_0.00000e-005
      TCHZ_Peak_Type(, 0.00001`_0.00000, , 0.00001`_0.00000, , 0.00001`_0.00000,, 0., , 0.00001`_0.00000,, 0.)

'------------------------------------------------------------------------------------------
'Structural information
'------------------------------------------------------------------------------------------

prm !tot_cu 22.50000 'Overall sample composition
prm !tot_zn 16.25000 'Overall sample composition
prm !tot_sn 11.25000 'Overall sample composition
prm !tot_s  50.00000 'Overall sample composition

for xdds {
for strs 1 to 1 {
      phase_name "CZTS"
      space_group "I-4"
      a !lpa1  5.433000`_0.000000
      b =lpa1;
      c !lpc1  10.840000`_0.000000
      al 90.
```

```
be 90.
ga 90.
volume  319.969581`_0.000000

prm tot_cu1 =(tot_cu - 0.01*frac_2*tot_cu2)/(0.01*frac_1);:  25.00000`_0.00000 'Phase-specific composition
prm tot_zn1 =(tot_zn - 0.01*frac_2*tot_zn2)/(0.01*frac_1);:  12.50000`_0.00000 'Phase-specific composition
prm tot_sn1 =(tot_sn - 0.01*frac_2*tot_sn2)/(0.01*frac_1);:  12.50000`_0.00000 'Phase-specific composition
prm tot_s1  =(tot_s  - 0.01*frac_2*tot_s2) /(0.01*frac_1);:  50.00000`_0.00000 'Phase-specific composition

prm scal_1 = (cu1_2a+cu1_2c+cu1_2d+cu1_2b)/tot_cu1;:  0.08000`_0.00000 'Turns % composition into occupancy

site 1_2a x 0.                      y 0.                      z 0.
      occ Cu+1 !cu1_2a                          1.00000`_0.00000  min 0 max 1  beq !b1_2a  0.50000`_0.00000 min 0
      occ Zn+2 !zn1_2a                          0.00000`_0.00000  min 0 max 1  beq =b1_2a;
      prm      V1_2a   =1-cu1_2a-zn1_2a;:    0.00000`_0.00000

site 1_2c x 0.                      y 0.5                     z 0.25
      occ Cu+1 !cu1_2c                          1.00000`_0.00000  min 0 max 1  beq !b1_2c  0.50000`_0.00000 min 0
      occ Zn+2 !zn1_2c                          0.00000`_0.00000  min 0 max 1  beq =b1_2c;
      prm      V1_2c   =1-cu1_2c-zn1_2c;:    0.00000`_0.00000

site 1_2d x 0.                      y 0.5                     z 0.75
      occ Cu+1 !cu1_2d                          0.00000`_0.00000  min 0 max 1  beq !b1_2d  0.50000`_0.00000 min 0
      occ Zn+2 zn1_2d  =(tot_zn1*scal_1)-zn1_2a-zn1_2c-zn1_2b;:  1.00000`_0.00000 beq =b1_2d;
      prm      V1_2d   =1-cu1_2d-zn1_2d;:    0.00000`_0.00000

site 1_2b x 0.                      y 0.                      z 0.5
      occ Sn+4 sn1_2b  =tot_sn1*scal_1;:     1.00000`_0.00000                beq !b1_2b  0.50000`_0.00000 min 0
      occ Cu+1 !cu1_2b                          0.00000`_0.00000 min 0 max 1   beq =b1_2b;
      occ Zn+2 !zn1_2b                          0.00000`_0.00000 min 0 max 1   beq =b1_2b;
      prm      V1_2b   =1-sn1_2b-cu1_2b-zn1_2b;:  0.00000`_0.00000

site 1_8g x Sx1  0.24500`_0.00000  y Sy1  0.24500`_0.00000  z Sz1  0.12800`_0.00000
      occ S    s1_8g   =tot_s1*scal_1/4;:    1.00000`_0.00000                beq !b1_8g  0.50000`_0.00000 min 0
      prm      V1_8g   =1-s1_8g;:            0.00000`_0.00000

weight_percent  90.00000`_0.00000
```

```
      prm !frac_1     90.00000          'Iteratively set this equal to weight_percent
}
for strs 2 to 2 {
      phase_name "ZnS"
      space_group "F-43m"
      a !lpa2  5.413000`_0.000000
      b =lpa2;
      c =lpa2;
      al 90.
      be 90.
      ga 90.
      volume  158.603980`_0.000000

      prm !tot_cu2 0  'Phase-specific composition
      prm !tot_zn2 50 'Phase-specific composition
      prm !tot_sn2 0  'Phase-specific composition
      prm !tot_s2  50 'Phase-specific composition

      site 2_4a x 0.   y 0.   z 0.
            occ Zn+2 1.  beq b2_4a  0.50000`_0.00000 min 0


      site 2_4c x 0.25 y 0.25 z 0.25
            occ S    1.  beq b2_4c  0.50000`_0.00000 min 0

      weight_percent             10.00000`_0.00000
      prm !frac_2 =100-frac_1;:  10.00000
}
}

#ifdef output_peak_hkls
phase_out Peak_hkls.txt append load out_record out_fmt out_eqn
{
"%.0f\t" = H;
"%.0f\t" = K;
"%.0f\t" = L;
"%.5f\n" = D_spacing;
```

```
"%.5f\n" = 2 Rad Th;
}
#endif
```